Politecnico di Torino

ScuDo
Scuola di Dottorato ~ Doctoral School
WHAT YOU ARE, TAKES YOU FAR

Doctoral Dissertation
Doctoral Program in Aerospace Engineering (38^{th}cycle)

Design-to-Noise Methodologies for Future Supersonic Aircraft: Experimental, Numerical, and Analytical Approaches

By

Samuele Graziani

******

Supervisor(s):
Prof. Nicole Viola, Supervisor
Prof. Roberta Fusaro, Co-Supervisor

Doctoral Examination Committee:
Dr. Alexandra Loubeau, Referee, NASA Langley Research Center
Dr. Mattia Barbarino, CIRA Italian Aerospace Research Center
Dr. Victor W. Sparrow , Penn State University
Dr. Björn Nagel, German Aerospace Center DLR
Dr. Craig Lawson, Cranfield University

Politecnico di Torino
2026

Declaration

I hereby declare that, the contents and organization of this dissertation constitute my own original work and does not compromise in any way the rights of third parties, including those relating to the security of personal data.

Samuele Graziani
2026

* This dissertation is presented in partial fulfillment of the requirements for **Ph.D. degree** in the Graduate School of Politecnico di Torino (ScuDo).

To my beloved fiancè and future wife Giorgia and to all my family

Acknowledgements

First and foremost, I wish to express my deepest gratitude to my supervisors, Dr. Nicole Viola and Dr. Roberta Fusaro, for their constant guidance, support, and the valuable opportunities they provided throughout my doctoral journey. I am also sincerely thankful to the members of my committee for their time, constructive feedback, and dedication. My appreciation further extends to Dr. Davide Ferretto for his insightful suggestions and expertise.

I am particularly grateful to Dr. Steven A. E. Miller for hosting me at the University of Florida during my six-month visiting period, and to Dr. Francesco Petrosino and Dr. Marco Marini from CIRA for welcoming me between January and April 2023. Their mentorship, enthusiasm, and expertise have significantly contributed to my growth as a researcher. I would also like to thank all colleagues and collaborators who co-authored scientific publications with me during my PhD; their contributions and teamwork have been invaluable. I am equally grateful to the sonic boom research community, whose members warmly welcomed me from my very first conference and consistently inspired me through their expertise and dedication. I extend my gratitude to my colleagues involved in the EU-funded MORE&LESS project for their collaboration and support, particularly those at Politecnico di Torino and CIRA, with special thanks to Antimo Glorioso. I also thank my peers at the University of Florida—Fahad Nabid, Christian King, and Marie Rowe—for their stimulating discussions, collaborative spirit, and for making me feel welcome from the very beginning.

I am deeply thankful to my friends, especially Marco, Emanuele, and Federico, whose enduring friendship has been a constant source of strength and balance throughout this journey. Finally, and most importantly, I thank my parents, my family, and my fiancée for their unconditional love, patience, and unwavering support. This achievement would not have been possible without them.

Abstract

In the past twenty years, there has been a renewed interest in supersonic civil aircraft. The first generation of such configurations was forced to fly subsonically over land to avoid sonic boom annoyance, which contributed significantly to their commercial failure. Advances in aerodynamics, materials, and propulsion, together with a rising demand for fast long-distance travel, have driven this renewed interest. Consequently, there is a growing need for methods that support the design of high-speed aircraft while accounting for environmental impact. This work focuses on improving the prediction of sonic booms and providing guidance to both aircraft designers and regulatory agencies. The approach combines high-fidelity CFD simulations near the aircraft with the propagation of sonic boom signals through a stratified, non-uniform atmosphere. The numerical methods were tested against two experimental free-flight campaigns on sub-scaled models, showing deviations of around 1 dB between predictions and measurements, which confirms the accuracy of the proposed approach. The methodology covers the entire supersonic flight range, from Mach 1.5 to Mach 5.0 with several case studies. To assess the behavior of such configurations in off-design conditions, psychoacoustic, energy-based metrics and primary carpet extension were analyzed, providing quantitative data to inform the development of overland noise regulations for high-speed civil flights. The influence of different turbulence models in the CFD region on sonic boom metrics was also investigated to ensure robust and comprehensive assessments across diverse flight conditions. Since 1973, a ban for supersonic overland flight exists, but recently, President Trump signed an executive order to promote supersonic aviation in the United States. For that reason, it is important to work towards the definition of a specific certification standard, considering the whole supersonic flight envelope. Two practical tools were developed to support early-stage design. A sonic boom requirement was added to the Matching Chart tool for aircraft up to Mach 2, and a refined analytical method based on the simplified Carlson approach was proposed and validated. Together,

these tools allow designers without sonic boom knowledge to consider aeroacoustic requirements from the beginning of the design process, supporting future regulatory efforts on overland sonic boom standards.

Contents

List of Figures

List of Tables

Nomenclature

Roman Symbols

ΔH	Difference between the elevation of the gunshot trajectory and probe
C_D	Drag Coefficient
C_L	Lift Coefficient
C_{D_0}	Zero lift drag coefficient
C_{D_f}	Skin friction drag coefficient
C_{D_i}	Induced drag coefficient
$C_{D_{WV}}$	Wave drag due to volume coefficient
CO_2	Carbon Dioxide
F	Whitham F-Function
I_{SP}	Specific impulse
T/W	Thrust to Weight ratio
W/S	Wing Loading
c	Speed of Sound
G,B,C,D	Parameters in F-function
L	Distance parallel to the trajectory from the probe to the cannon outlet
M	Mach number

R	Ground projection of the perpendicular distance from the probe to the trajectory
r	Radial coordinate
R_S	Coefficient of determination
V	Velocity

Greek Symbols

α	angle of attack
β	Prandtl Glauert term, $\sqrt{M^2-1}$
β_i	Regression coefficients
χ	Retarded coordinate,$\chi = x - \beta r$
Γ	boundary cylinder
γ	Ratio of specific heat
γ_P	flight path angle
ι	Statistical error term
μ	Mach angle
μ_a	Dynamic viscosity
Ω_e	Linear domain outside Γ cylinder
Ω_i	non-linear domain outside Γ cylinder
ϕ	Roll angle projectile
ϕ_{CFD}	Radial angle of extraction, CFD
π	$\simeq 3.1415\ldots$
ρ	Air Density
θ	Azimuthal angle

θ_{CFD} Misalignment angle in the CFD grid

$\tilde{\nu}$ Kinematic turbulent viscosity

φ Roll angle during test campaigns

$\varpi_{i,j}$ Transport magnitude

Other Symbols

Δp Ground peak overpressure

Δt Ground signature duration

$\frac{dp}{p}$ Increase of static pressure

$\mathbf{d}_{\text{ac}}$ acoustically estimated trajectory vector

$\mathbf{d}_{\text{pen}}$ penetration estimated trajectory vector

$\Box$ d'Alembert operator

$A(x)$ Equivalent area due to volume

$A_e(x)$ Total effective area

$A_{e,1}$ Effective area

$A_{e,max}$ Maximum effective area

$B(x)$ Equivalent area due to lift

f source function

l_e Effective length of the aircraft

p_0 Free-stream ambient pressure

p_s Extracted static pressure

q_∞ Dynamic pressure $1/2\,\rho\,U^2$

x_0 launch position

x_1 shock detachment position

x_s sensor position

Acronyms / Abbreviations

h_e Effective altitude

K_P Pressure amplificator factor

K_R Reflection factor, 2.0

K_S Aircraft shape factor

K_t Time signature duration factor

M_e Effective Mach number

AIAA American Institute of Aeronautics and Astronautics

ASEL Sound Exposure Level, A-weighted

ASTRID Aircraft on-board Systems sizing and TRade-off analysis in Initial Design

ATR Air Turbo Rocket

AUSM Advection Upstream Splitting Method

BAC British Aircraft Corporation

BSEL Sound Exposure Level, B-weighted

CAD Computer Aided Design

CAEP Committee on Aviation Environmental Protection

CFD Computational Fluid Dynamics

CIRA Italian Aerospace Research Center

CS1 Case Study 1

CS2 Case Study 2

CS3 Case Study 3

CSEL Sound Exposure Level, C-weighted

DMR Dual Mode Ramjet

DNS Direct Numerical Simulations

DSEL Sound Exposure Level, D-weighted

EASA European Union Aviation Safety Agency

ESATTO Environmentally Sustainable AircrafT Trajectory and Operations

ESEL Sound Exposure Level, E-weighted

EU European Union

FAA Federal Aviation Administration

FDS Finite Difference Scheme

FFT Fast Fourier Transform

FVM Finite Volume Method

FVS Flux Vector Splitting

H/L Height over Length ratio for CFD extraction

HEFA Hydroprocessed Esters and Fatty Acids

HLLC Harten–Lax–van Leer–Contact

HTOL Horizontal Take-Off and Landing

ICAO International Civil Aviation Organization

ISA International Standard Atmosphere

ISBAP Indoor Sonic Boom Annoyance Predictor

ISL Institut Franco-Allemand Recherche Saint Louis

JAXA Japan Aerospace Exploration Agency

LEO Low Earth Orbit

LES Large Eddy Simulation

LTO Landing and Take-off cycle

MC Matching Chart

MDO Multidisciplinary Design Optimization

MORE&LESS MDO and Regulations for Low-boom and Environmentally Sustainable Supersonic aviation

MTOW Maximum Take-off Weight

MUSCL Monotonic Upstream-centered Schemes for Conservation Laws

NASA National Aeronautics and Space Administration

PL Perceived Level in dB

RADAR Radio direction and ranging

RANS Reynolds Average Navier Stokes

ROE-FDS Roe Flux Difference Splitting

SA Spalart Allmaras

SARPs Standards And Recommended Practices

SBJ Supersonic Business Jet

SBPW Sonic Boom Prediction Workshop

SEL Sound Exposure Level

SFC Specific Fuel Consumption

SSE Residual sum of squares

SSQ Total sum of squares

SST SuperSonic Transport

SU2 Stanford University Unstructured

TRL Technology Readiness Level

Context and scope of the research activity

The development of supersonic flight has always represented one of the most ambitious frontiers of aerospace engineering. Since the first supersonic flight in 1947, progress in aerodynamics, propulsion, and materials has made high-speed flight a reality. The introduction of commercial supersonic transport in the 1970s, symbolized by the Concorde and Tu-144, demonstrated the feasibility of passenger travel beyond the speed of sound. However, despite their pioneering achievements, these aircraft were withdrawn from service due to high operational costs, limited range efficiency, and the growing awareness of their environmental impact, particularly in terms of sonic boom and pollutant emissions.

For nearly two decades after the retirement of Concorde in 2003, supersonic flight remained confined to military and experimental research. In recent years, however, a renewed interest in civil supersonic transportation has emerged, motivated by both technological advancements and societal demand for faster, long-range mobility. Unlike past developments, current efforts are guided by new priorities: environmental sustainability, noise reduction, and compliance with stringent regulatory frameworks.

Over the last thirty years, the European Commission has actively supported numerous research programs aimed at pushing forward the maturity of Technology Readiness Level (TRL) for high-speed flights [5–8]. These programs not only reflect Europe's long-standing commitment to advancing high-speed aviation and reusable access to space, but also showcase how complex and interdisciplinary this field really is. Unlike traditional subsonic flight, flying at supersonic speeds demands closer collaboration across many disciplines and technologies. As flight Mach number increases, the coupling between these areas also increases, making integrated design approaches a mandatory rather than a choice. In the last few years, in alignment with

the European Union's vision for a greener and smarter future, increasing attention has been devoted to enhance the sustainability of the entire aviation sector, including civil supersonic. In this context, leading aerospace industries such as Airbus are actively developing next-generation technologies, including liquid hydrogen (LH_2)-powered aircraft [9], which could be used for application not only in conventional aviation but also in future supersonic and potentially hypersonic configurations [10]. In parallel, significant research efforts are focused on the optimization of propulsion systems, with particular attention to hybrid-electric architectures and advanced thermal management solutions to improve overall energy efficiency. At the same time, the aviation sector is investing heavily in the development of sustainable aviation fuels (SAFs) and alternative propulsion systems to significantly reduce CO_2 and NO_x emissions. Noise reduction is being pursued through innovative airframe designs, such as morphing wings and optimized landing gear fairings, as well as through quieter engine architectures like ultra-high-bypass ratio turbofans and open-rotor concepts. These combined efforts aim to accelerate the transition toward a more sustainable, low-emission, and low-noise aviation ecosystem.

However, current environmental regulations are insufficient to adequately address the challenges associated with high-speed flight. Since 1973, a regulatory ban on overland civil high-speed flights has been in place in the United States and most Western countries [11], mainly due to sonic booms. This restriction was introduced following the significant noise disturbances caused by Concorde during its supersonic cruise, which raised both public and political concerns. Despite notable progress in aircraft design and noise prediction technologies, the regulations governing civil supersonic flight have not changed in more than fifty years. In May 2025, however, the Senate Committee on Commerce, Science, and Transportation introduced the Supersonic Aviation Modernization (SAM) Act [12], mandating the Federal Aviation Administration (FAA) to develop regulations that would permit civil supersonic operations in the United States under specific conditions. At the same time, the Committee on Aviation Environmental Protection of the International Civil Aviation Organization (ICAO-CAEP) [13] is actively working on updating current regulations to accommodate future supersonic aircraft concepts, while maintaining sustainability and safety as primary priorities.

In this context, this thesis aims at introducing a comprehensive methodology, along with new tools, applications, and design guidelines to support the development of the next generation of quieter and environmentally sustainable supersonic

aircraft, specifically looking at sonic boom. To achieve this target, a multidisciplinary approach combining multiple levels of fidelity has been adopted—starting from conceptual aircraft design and progressing to detailed Computational Fluid Dynamics (CFD) simulations coupled with atmospheric propagation up to free-flight test campaigns. While CFD techniques for sonic boom prediction are well established at low-supersonic speeds, this work expands their application to higher Mach regimes—up to Mach 5. The numerical simulations results were validated thanks to two separate free-flight experimental campaigns carried out as part of the MORE&LESS project [14].

The numerical investigations that are carried out both in nominal and off-design conditions for two high-speed aircraft configurations highlights the need for new regulations. At the same time, numerous atmospheric profiles were employed, enabling an accurate assessment of the acoustic performance and footprint. Different noise metrics were analyzed to determine which could be more suitable for future sonic boom certification standards. In addition, the effects of including a turbulence model in the Computational Fluid Dynamics on psychoacoustics and energy-based metrics were investigated. This work has been done during a visiting collaboration at University of Florida, supervised by Dr. S.A.E. Miller. The noise metrics that were selected include PL, ISBAP and Sound Exposure Level (SEL), with different weighting functions.

Based on the simulation results, data-driven models and a set of design guidelines are developed to help mitigate sonic booms from the early stages of design. This is achieved, for example, by introducing a new requirement into the Matching Chart (MC) tool, thereby setting threshold values. To support this objective, existing analytical models are refined to improve the predictive accuracy of key sonic boom parameters, such as peak overpressure and signature duration. These enhancements are integrated into an existing holistic design framework developed at Politecnico di Torino, which aims to support the development of second-generation civil supersonic transport.

Finally, the thesis investigates an additional application involving the inverse estimation of flight dynamics for a supersonic vehicle prototype, derived from shock wave measurements. This novel methodology offers valuable insights into vehicle behavior during high-speed flight and presents an alternative validation strategy for aerodynamic modeling in complex flight regimes.

Chapter 1 presents an overview of the historical development and principal challenges of civil supersonic aviation. This chapter provides a brief overview of the first generation of supersonic aircraft and covers the basic physical principles and classical theories behind sonic booms. It also focuses on the environmental impact of high-speed flight, providing a preliminary overview on greenhouse gas emissions, pollutant emissions, noise during landing and take-off. The physical processes that generate sonic boom is then explained, along with how these sounds are perceived by people on the ground. Finally, an overview of the EU-funded MORE&LESS project [14] is provided, including the contribution of my thesis to its objectives.

Chapter 2 presents the case studies considered in this PhD thesis, which are presented as a function of increasing Mach number They are divided into two categories: full-scale supersonic aircraft concepts and scaled mock-ups used for experimental testing. The corresponding reference mission profiles for the full size aircraft are also introduced to offer a comprehensive understanding for each configuration and to support the rationale behind the selection of specific mission points analyzed for sonic boom. The free-flight sonic boom experiments provide fundamental data for the validation of the numerical methods employed throughout this work.

Chapter 3 presents the methodology and tools developed for this study. It begins with the definition of the bi-domain high-fidelity approach employed in the numerical simulations. First, the Computational Fluid Dynamics techniques are described in detail, emphasizing the adopted approach and the boundary conditions applied. Second, the methodology for modeling the propagation of shock waves through a non-uniform and stratified atmosphere is presented, along with the noise metrics used.
The chapter also describes the experimental setup implemented during the two free-flight test campaigns, including the acoustic equipment, its setup, and the reference conditions. Furthermore, an innovative methodology for inverse flight dynamics estimation based on shock wave recordings is highlighted. Finally, the high-fidelity simulations and experimental tests provide the foundation for the development of low-fidelity estimation methodologies and tools. A new constraint has been incorporated into the Matching Chart tool to account for sonic boom requirements at the conceptual design stage. Additionally, a refined analytical formulation based on Carlson's method is presented and validated.

Chapter 4 presents the application of the methodology to the case studies understudy . It begins with a numerical analysis of small off-design variations from the standard cruise conditions, focusing on noise metrics and primary carpet. These findings offer valuable information for regulators working on new guidelines for supersonic flight over land. Furthermore, the deviations of the noise metrics due to the consideration of different turbulence scheme is presented. Next, the chapter presents the experimental results from the free-flight test campaigns and compares them with the numerical simulations. It discusses in detail the differences observed between the two aircraft configurations and suggests ways to improve the numerical predictions. The chapter also introduces a new approach using inverse flight dynamics estimation—based on shock wave data and CFD simulations—applied to one of the two experimental tests. The integration of new sonic boom-related equations into the Matching Chart tool—derived from high-fidelity simulations—is discussed, along with their implications for the design of a Mach 1.5 case study. Refinements to existing analytical formulations for sonic boom prediction are also presented and implemented within a comprehensive conceptual design framework for future supersonic aircraft.

Finally, a discussion of the main research achievements is presented in Chapter 5, along with recommendations for potential improvements and suggestions for future research activities. Chapter 6 then summarizes the key findings, highlights the original contributions of this work, and outlines the broader implications for future supersonic aircraft design.

In addition, Appendix A presents the methodology employed for the correct computation of the roll angle during the experimental test. Lastly, Appendix B presents the results of the high-fidelity bi-domain approach for two hypersonic concepts. These results serve the development of the refined analytical methodologies.

Chapter 1

Introduction

The demand for faster and greener air travel is pushing the aerospace industry to develop a new generation of high-speed aircraft, that aims to cut down environmental impacts without sacrificing safety or public acceptance. Over the last twenty years, interest in supersonic civil aviation has grown, fueled by advances in technology and changing market demands [15–18]. Designers are currently considering supersonic civil planes as a concrete solution, as long as they meet key operational, environmental, and regulatory standards. The retirement of Concorde in 2003 closed the first generation era of commercial supersonic civil flights.

This chapter gives an overview of the current landscape of supersonic civil aviation, with a focus on the sonic boom challenges. Section 1.1 reviews key milestones in supersonic flight. Section 1.2 looks at ongoing efforts to design quieter and more efficient supersonic aircraft, and highlights major international programs. Section 1.3 addresses some of the main technical and regulatory challenges of high-speed aviation. Section 1.4 describes how physical mechanisms generate and propagate sonic booms, and discusses the key parameters involved. Section 1.5 outlines the first models used to estimate sonic booms during the first supersonic generation civil aircraft era. Finally, Section 1.6 introduces the EU-funded project that frames the present research.

1.1 Historical background of supersonic flight

In 1947, Chuck Yeager became the first pilot to break the sound barrier in level flight, piloting the Bell X-1—an experimental rocket-powered aircraft designed specifically for high-speed research [19, 20], which was released from a B-29 mother ship at high altitude, the X-1 reached approximately 700 mph (Mach 1.06) at 42,000 feet. Earlier attempts to reach Mach 1 encountered intense aerodynamic buffeting in the transonic regime, but on its ninth powered flight, the X-1 achieved the first sustained and controlled supersonic flight. Data from this program proved fundamental to understanding transonic and supersonic aerodynamics, laying the groundwork for future advances in both military and civil supersonic aviation. Following that period, supersonic flight became a crucial aspect of military aviation. Both the United States and the Soviet Union dedicated significant resources to developing supersonic fighters [21]. The 1950s marked significant progress in jet propulsion—especially with afterburners—enabling higher speeds and altitudes. At the same time, engineers worked through tough aerodynamic and structural problems like improving wing and fuselage shapes using the area rule, designing smarter variable-geometry inlets, and handling the heat and stress that come with flying at high speeds. These challenges led to the use of new materials like titanium alloys and sparked fresh innovations in how aircraft are built. During the Cold War, militaries developed several supersonic aircraft alongside civil aviation. The Convair B-58 Hustler, the first Mach 2-capable bomber, featured a low thickness-to-chord delta wing, an area-ruled fuselage, and lightweight honeycomb construction. At the same time, the Soviet MiG-19 became the first supersonic fighter to be produced in large numbers, achieving speeds of up to Mach 1.35 with a range of 800 nautical miles. The Lockheed SR-71 Blackbird, designed for high-altitude reconnaissance, consistently maintained speeds above Mach 3. First flown in December 1964 [22, 23], it operated at altitudes around 80,000 feet, powered by Pratt & Whitney J58 engines that functioned increasingly like ramjets at high speeds. The SR-71 and similar aircraft contributed significantly to advances in high-speed aerodynamics, thermal protection systems and propulsion integration. Another key program was the XB-70 Valkyrie, a Mach 3-capable prototype bomber and SST testbed. It used a delta wing, slab-sided fuselage, six jet engines, and hinged outer wing panels that deflected downward at high speeds for better aerodynamics. Despite stability issues above Mach 2.5, the second prototype achieved stable Mach 3 cruise in 1966. Between 1966 and 1967, the XB-70 joined

the National Sonic Boom Program, showing that large supersonic aircraft could generate damaging ground overpressures [24]. During this era, the first generation of long-range, high-subsonic civil jets entered commercial service, ushering in a new age of global air travel. This environment spurred interest in supersonic civil transport, driven by ambitions to drastically reduce intercontinental flight times and broaden air travel's appeal [25, 26]. Four major nations—France, the United Kingdom, the United States, and the Soviet Union—studied the viability of supersonic passenger aircraft [27]. In the U.S., Boeing, in partnership with General Electric, led development of the Boeing 2707, the country's first supersonic passenger aircraft [28, 29]. Designed to carry up to 300 passengers at cruise speeds near Mach 3, the 2707 represented an ambitious project, but due to economic pressures and shifting political priorities ultimately it was cancelled in 1971.

In the 1960s and 1970s, the British Aircraft Corporation (BAC) and France's Aérospatiale developed Concorde, the first commercial supersonic aircraft in regular service [30–32]. Environmental concerns—especially sonic booms and high noise during takeoff and landing—sparked public opposition and regulatory restrictions. In 1970, the U.S. Senate banned commercial supersonic overland flights. Although briefly lifted in 1976 for Concorde landings at Washington Dulles, opposition persisted. A New York ban was overturned by the U.S. Supreme Court in 1977, allowing transatlantic flights to JFK. Concorde was powered by four Rolls-Royce/Snecma Olympus 593 turbojet engines with afterburners and featured a slender ogive delta wing. To increase aerodynamic performance, variable-geometry inlets and nozzles were employed, while the droop-nose design improved pilot visibility during take-off and landing. In the same period, the Soviet Union developed the Tupolev Tu-144 [33], the first commercial aircraft to exceed Mach 2. Larger and heavier than its competitor, it flew first in 1968 but faced technical issues and a fatal crash in 1973, ending commercial service by 1978. Figure 1.1 shows Concorde (Subfigure 1.1a) and Tu-144 (Subfigure 1.1b) configurations.

(a) Concorde aircraft

(b) TU144 aircraft

Fig. 1.1 Concorde and TU 144 civil supersonic aircraft

Since Concorde's retirement, interest in a second generation of supersonic transport has remained strong. Current designs are prioritizing fuel efficiency, noise reduction and passenger comfort. These efforts show how the industry is committed to making high-speed travel both environmentally friendly and cost-effective.

1.2 Most recent concepts of supersonic aircraft

Reintroducing supersonic flight faces significant challenges due to environmental concerns and public opposition. Decades of low-boom research [34–39] have shown that aerodynamic shaping and control of off-body pressure can significantly reduce sonic boom intensity on the ground. Modern designs generate low-amplitude, shaped sonic booms that differ markedly from the harsh N-wave signatures of first-generation jets such as the Tu-144 and Concorde, reducing high-frequency sound pressure levels by up to 60 dB [40].

Since 2018, NASA and Lockheed Martin have developed the X-59 demonstrator [41–45] to lower sonic boom levels and measure community annoyance, to enable new regulations for supersonic commercial flights over land. Flight test data and public feedback will guide regulators such as ICAO, FAA, and EASA in setting certification standards and acoustic limits for overland high-speed civil operations [46]. Figure 1.2 shows the X-59 demonstrator during the rollout ceremony in 2024.

Fig. 1.2 X-59 demonstrator rollout ceremony, 12^{th} Jan. 2024 [47]

Starting in January 2025, Boom Supersonic began flight testing its XB-1 demonstrator under boomless flight conditions, at Mach number up to 1.15 [48]. At transonic speeds, the Mach cone widens and atmospheric effects can refract shock waves upward, preventing them from reaching the ground. This phenomenon occurs below a specific Mach number, usually referred to as the cut-off Mach number [49–51]. This allow the reduction of sonic boom impact while allowing cruise speeds about 25% faster than current subsonic aircraft. These tests are an important step toward the launch of Boom's upcoming Overture airliner [52], which is designed to carry between 64 and 80 passengers at speeds reaching Mach 1.7. The aircraft is built around a slender delta wing optimized for supersonic cruise and is powered by four medium-bypass turbofan engines that operate without afterburners. The Overture range is just above 4,000 nm (7,870 km), operating with Sustainable Aviation Fuel (SAF). Unlike low-boom demonstrators, the Overture focuses on efficient supersonic flight while meeting current noise regulations. Both Boom's aircraft appear in Figure 1.3.

(a) Boom XB-1 demonstrator

(b) Boom Overture passenger aircraft concept

Fig. 1.3 Boom XB-1 and Overture configurations.

In addition, Japan and Europe are actively exploring innovative supersonic aircraft concepts, mostly at the design stage. Under the S4 program, JAXA developed a conceptual small supersonic transport with a cruise speed of Mach 1.6, carrying about 50 passengers with a range of 6,300 km [53, 54] (Figure 1.4). The project aims to reduce sonic boom levels below 85 dB in PL and meet ICAO Chapter 14 noise standards for takeoff and landing. Europe is actively advancing supersonic research through EU-funded projects such as MORE&LESS [14] and SENECA [55]. The MORE&LESS project focuses on supporting Europe in defining ambitious environmental standards for future supersonic aviation in collaboration with the international community, while the SENECA project aims to develop detailed models of carbon emissions and landing and take-off (LTO) noise in the vicinity of airports.

Fig. 1.4 JAXA S4 low-boom concept

1.3 Challenges of supersonic aviation

1.3.1 Aerodynamics and design

The design of a supersonic aircraft presents numerous challenges due to the aerodynamics, propulsion, and aerothermodynamics that at high speeds are different from subsonic regime. As a result, these aircraft tend to be more complex and expensive to develop [56, 57]. In addition, during supersonic flight phases the center of pressure tends to shift rearward, which affect the longitudinal stability. Furthermore, shock waves cause sudden changes in pressure, temperature, and density. Engineers work to design wings that reduce drag and keep the aircraft stable at high Mach numbers, while still providing enough lift for takeoff and landing [58]. To reduce wave-drag, supersonic configurations often have highly swept delta wings with low aspect ratios, which help make the wing thinner and delay the formation of shock waves. While they are efficient at supersonic speeds, these wings tend to produce reduced lift during subsonic flight operations [59]. In addition, zero-lift drag (C_{D_0}) behaves differently when flying supersonically, as visible in Figure 1.5. At lower Mach numbers, drag is primarily due to skin friction. As speed increases, however, wave drag becomes more pronounced and eventually emerges as the dominant component of total aerodynamic drag.

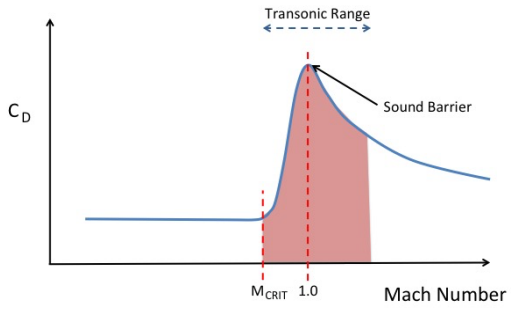

Fig. 1.5 Aerodynamic drag coefficient C_D as a function of Mach number

Lift-induced drag results from the uneven lift distribution along the wing. The pressure difference between the upper and lower surfaces creates vortices, especially near the wingtips. As the lift coefficient C_L increases, lift-induced drag grows proportionally to $C_{D_i} = KC_L^2$.

1.3.2 Propulsion

Designing supersonic propulsion presents significant challenges, as the propulsion system must accelerate the aircraft from takeoff to cruise and maintain efficiency during supersonic flight. Specific impulse (I_{sp}), measuring thrust per propellant weight, indicates efficiency. Turbofan and turbojet engines operate efficiently up to about Mach 3: beyond this speed, ramjet or scramjet engines must take over. Integrating multiple engine types into one propulsion system adds significant design complexity. Since engine performance depends heavily on Mach number, both specific impulse (I_{sp}) and available thrust generally decrease as speed increases. Future propulsion systems may use Sustainable Aviation Fuel (SAF) or liquid hydrogen (LH_2). LH_2 offers high specific energy—about 143 MJ/kg, over three times that of Jet-A1 fuel—so it can deliver up to three times the specific impulse of hydrocarbons. However, LH_2 has roughly ten times lower volumetric energy density than kerosene, and it would require more complex storage tanks about four times the volume of conventional systems, increasing production costs and demanding airport infrastructure upgrades [60]. Yet, the lower fuel mass reduces the aircraft's gross weight. Because LH_2 is extremely cold, tanks need special insulation to prevent boil-off [61]. Designers maximize tank volume-to-surface ratio to limit heat loss, often integrating fuel storage within the fuselage. It allows compact, thermally efficient tank shapes but increases fuselage size and wetted area [62, 63]. However, supersonic aircraft face strict aerodynamic and noise constraints, making it difficult to accommodate the additional volume needed for LH_2 tanks. Current and upcoming international regulations further compound this challenge by limiting aircraft geometry and performance.

1.3.3 Implications for climate change and pollutant emissions

The aviation sector is an important contributor to global greenhouse gas emissions, responsible for approximately 2–3% of global CO_2 emissions [1]. While mitigation strategies have largely focused on conventional subsonic aircraft, the advent of supersonic transport (SST) presents distinct challenges due to higher speeds, altitudes, and fuel consumption per passenger-kilometer. These operational characteristics not only increase CO_2 emissions but also amplify non-CO_2 effects, such as stratospheric

water vapor, contrail formation, and NO_X-induced ozone perturbations, which may persist for years at typical supersonic cruising altitudes [64].

Implications for climate change

In December 2019, the European Commission launched the Green Deal, aiming for climate neutrality by 2050 [65]. Complementing this, the Air Transport Action Group (ATAG) proposed a roadmap to achieve net-zero carbon emissions in aviation by 2050 [1], and visible in Figure 1.6. Although primarily focused on subsonic operations, these scenarios highlight technological pathways that could partially benefit supersonic aviation:

- Scenario 1: Rapid technology breakthroughs, including unconventional airframes and hybrid-electric or fully electric short-haul aircraft. While these concepts are not directly applicable to current supersonic designs, advancements in lightweight materials and efficient propulsion could indirectly reduce SST emissions.
- Scenario 2: Airframe optimization (e.g., blended-wing bodies) combined with conventional engines. For supersonic aircraft, this approach could inspire aerodynamic refinements to reduce drag and fuel burn at high Mach numbers.
- Scenario 3: Deployment of hydrogen-powered or fully electric aircraft alongside widespread use of Sustainable Aviation Fuels (SAF). Hydrogen combustion, being carbon-free, is especially promising for SST, though volumetric and cryogenic storage requirements impose significant design challenges [66, 67].

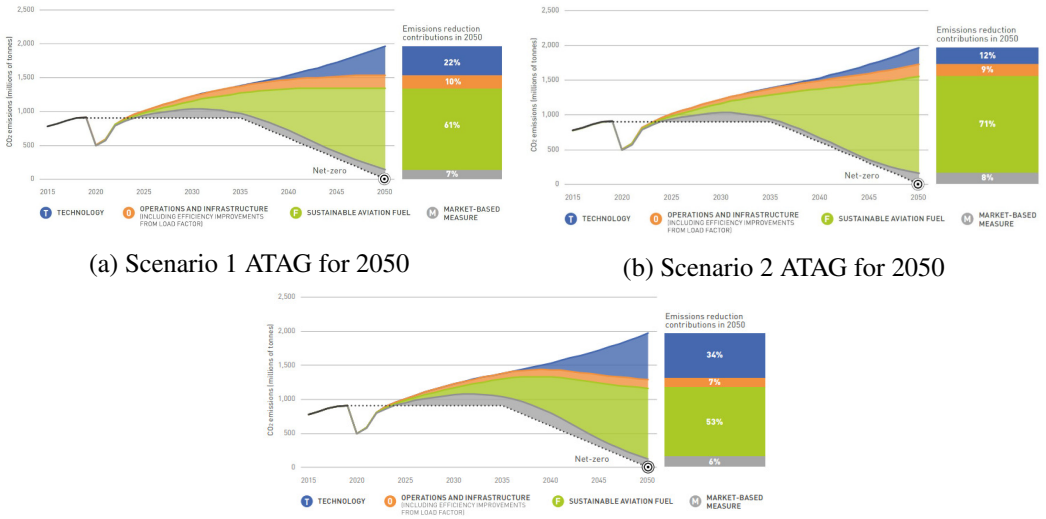

(a) Scenario 1 ATAG for 2050

(b) Scenario 2 ATAG for 2050

(c) Scenario 3 ATAG for 2050

Fig. 1.6 ATAG scenarios for aviation in 2050 [1]

One of the key advantages of biofuel is its drop-in characteristics, as it can be used in existing airports with the current infrastructure. However, most of them require blending with conventional jet fuel, and moreover biofuels still emit not negligible pollutants in the atmosphere. Hydroprocessed Esters and Fatty Acids (HEFA) biofuels mainly consist of paraffinic hydrocarbons, while jet fuel standards require at least 8% aromatics. As of today, there are no clear regulations that standardize how different biofuel types can be blended together, which complicates operations at airports where airlines may use various blends. In the evaluation of biofuels, the carbon abatement cost remains the most practical way to measure their environmental benefit. However, challenges vary depending on the production method: for example, Fischer–Tropsch synthesis involves high capital costs, whereas hydrotreated vegetable oils (HVO) are more sensitive to feedstock prices. Beyond carbon dioxide emissions, the impact of aviation's non-CO_2 effects on the climate are still not fully understood. The European Commission has set a target for Sustainable Aviation Fuels (SAF) to make up 63% of aviation fuel by 2050, but currently, global production reaches just 1% [68]. Scaling up SAF production significantly will be critical to meeting climate goals. At the same time, concerns remain about the use of common biofuel feedstocks like corn, palm, soy, and sugarcane, due to their potential effects on food security and the environment [69].

Liquid hydrogen (LH_2) offers a promising alternative with major climate benefits. Being carbon-free, LH_2 combustion produces no CO_2. Its higher flame speed shortens combustion time and lowers flame temperature, cutting nitrogen oxide (NO_X) emissions by up to 90% compared to kerosene engines [66, 67]. However, LH_2 combustion emits significantly more water vapor, and the climate impact of it depends on altitude. Grewe et al. [64] estimate that water vapor emitted below 12,000 meters of altitude can persist from one hour up to six months. At the altitudes typical of supersonic flight (15,000 to 20,000 meters), water vapor can stay in the atmosphere for as long as five years.

Pollutant emissions

Pollutant emissions remain a critical obstacle in the development of supersonic aviation. ICAO Annex 16, Volume II [70] defines current emission standards for subsonic aircraft engines, regulating the following pollutants [71]:

- Nitrogen oxides (NO_X);
- Carbon monoxide (CO);
- Unburned hydrocarbons (HC);
- Non-volatile particulate matter (nvPM);
- Fuel venting.

While CO_2 is the main cause of climate change, it doesn't have a direct impact on local air quality, which is regulated separately under ICAO Annex 16, Volume III [72]. Regulators evaluate emissions for each pollutant over a standardized Landing and Take-Off (LTO) cycle, which includes several defined operating modes, each specifying thrust settings and durations, as detailed in Table 1.1. Unlike noise and CO_2 emissions regulated on a whole-aircraft basis, regulators apply air quality standards directly to engines. These standards currently affect subsonic aircraft engines with rated sea-level static thrust exceeding 26.7 kN.

Table 1.1 Landing and Take-Off (LTO) cycle definition for subsonic and supersonic aircraft

Mode	Subsonic aircraft		Supersonic aircraft	
	Thrust level (%)	Duration (min)	Thrust level (%)	Duration (min)
Take-off	100	0.7	100	1.2
Climb	85	2.2	65	2.0
Descent	-	-	15	1.2
Approach	30	4.0	34	2.3
Taxi/ground idle	7	26	5.8	26

1.3.4 Noise

LTO Noise

One of the most controversial aspects of Concorde was its high community noise during airport operations, mainly due to the high thrust and jet velocity required for take-off [73]. Future supersonic aircraft aim to reduce noise during landing and take-off (LTO), but meeting current subsonic noise regulations remains difficult due to the inherently higher speeds and thrust levels involved. ICAO defines subsonic aircraft noise limits in Annex 16, Volume I [72]. However, regulators continue developing standardized procedures for supersonic aircraft [74], while researchers assess whether current subsonic procedures can suit future SSTs [75, 76]. Noise certification relies on three ground measurement locations as visible in Figure 1.7:

- sideline (peak lateral noise during full take-off thrust)
- flyover (6,500 m from brake release)
- approach (2,000 m from the runway threshold)

If an aircraft exceeds the noise limit at one or two points, it may still comply if:

- The total exceedance does not surpass 3 EPNdB;
- No single point exceeds by more than 2 EPNdB;
- Any excess is balanced by reductions at the remaining points.

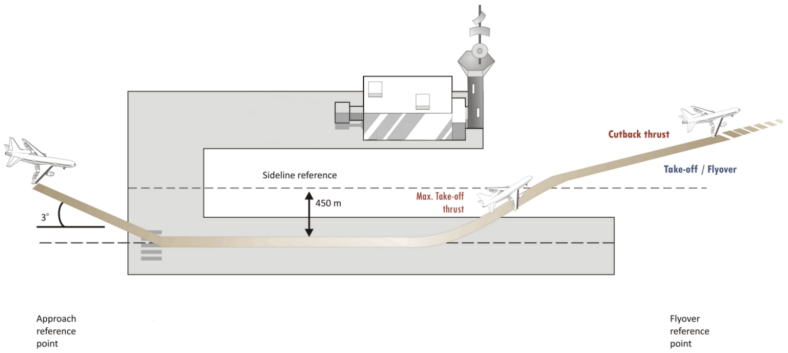

Fig. 1.7 Aircraft LTO noise certification measurement points [77]

Regulators require that the takeoff flight path be calculated assuming the aircraft is at its Maximum Take-Off Mass (MTOM) at brake release. Operators must maintain average engine thrust up to a certain altitude, which depends on the number of engines. Beyond this altitude, thrust must be sufficient to sustain a 4% climb gradient. Reference procedures use standard atmospheric conditions: 1 atm pressure, 25°C temperature, 70% relative humidity, and no wind. Concorde began flying in 1976, and a few years later, in 1981, noise regulations were introduced that limited supersonic transport (SST) noise to Concorde's levels. Since no new SST planes have been certified since then, these rules remain outdated and don't fully match today's aircraft designs. Still, they remain useful as historical reference points [71]. At the same time, there is a clear need for updated noise standards that specifically address the unique challenges of supersonic aircraft. The high-speed aviation community is actively working to support the development of new and upgraded regulations.

Sonic Boom

Sonic boom remains one of the main challenges in supersonic flight. Unlike conventional aircraft noise—primarily generated during take-off and landing—sonic boom results from sustained supersonic cruise and affects larger population areas. Sonic booms have historically raised public concerns due to their sudden, sharp nature and the potential to cause annoyance to population on ground and structural damage to buildings. While the physical mechanisms behind sonic booms are well understood, their societal impact and the negative perception they generate continue to pose significant challenges to the widespread adoption of civil supersonic travel. As today, supersonic aircraft designers treat sonic boom as one of the main issues

to minimize. The development of low-boom configurations highlights this need, focusing on reshaping the pressure signature to reduce perceived loudness and improve public acceptance. This aim now drives much of the current research and regulatory debate on supersonic flight. Psychoacoustic studies indicate that listeners perceive pressure signatures with slower rise times as less disturbing than traditional N-waves. To mitigate community impact, supersonic flights over land have been prohibited for civil purposes since 1973 [11], restricting operations to oceanic routes. However, concerns have been raised about potential effects on marine ecosystems. Consequently, researchers have developed models to investigate how sonic booms propagate through and interact with the ocean [78].

1.4 Physical principles of sonic boom generation

Sonic boom occurs when an object travels through the atmosphere faster than the local speed of sound, generating shock waves from sudden air compression. These shock waves form a near-conical pattern spreading outward from the aircraft. Simple shapes like projectiles create a bow shock at the front and a tail shock at the rear, but full-scale aircraft produce more complex shock patterns due to multiple aerodynamic surfaces. In the proximity of the aircraft, shock waves form at the nose, engine inlets, wing leading edges, and tail. These shocks interact as they travel through the atmosphere to the ground. By the time they reach the ground—the far-field region—the shocks merge into a simpler pattern, typically two main shocks: the bow shock and the tail shock, producing the classic N-wave pressure profile of sonic booms. At ground level, the pressure signature starts with a sharp rise from ambient pressure caused by the bow shock, followed by a gradual expansion, and finally a second abrupt rise to restore to ambient pressure. Both shocks have brief rise times during which the pressure changes, creating the N-wave shape. However, this ideal shape is often altered as the shock waves travel through the atmosphere, indeed turbulence and atmospheric gradients can smooth out the sharp transitions or introduce small spikes and irregularities in the pressure profile. Figure 1.8 illustrates the sonic boom's evolution from the near field region in proximity of the aircraft to the far field domain at ground level. This bi-domain approach will be used in the following sections to properly evaluate the signal.

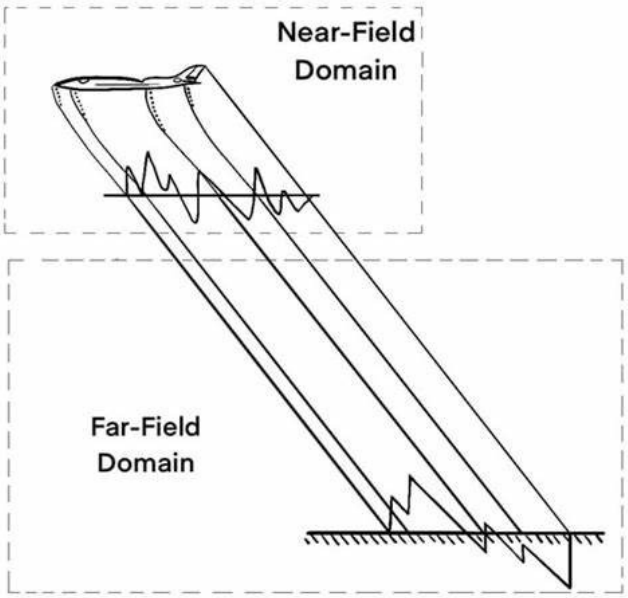

Fig. 1.8 Sonic boom bi-domain regions

Aircraft designers can alter the shape acting on the distribution of volume and lift along the airframe to change the sonic boom signature on the ground. Darden [79] showed that optimizing these parameters reduces the maximum overpressure, lowering boom loudness. A flat-top signature, for example, has a more constant and less intense overpressure than a traditional N-wave, improving community acceptance. Modern low-boom supersonic demonstrators are designed with carefully shaped airframes and optimized flight trajectories to minimize the intensity of sonic booms experienced on the ground. The human ear senses rapid pressure changes. When two pressure peaks occur closely, it hears them as a single sharp noise. It explains why small supersonic projectiles produce a single "boom," while large supersonic aircraft at high altitude create a "double boom" characterized by two distinct pressure peaks separated by over 0.1 seconds [80–82].

A range of atmospheric effects may influence sonic boom propagation. Large-scale factors like temperature gradients, wind speed and direction, humidity, and atmospheric pressure can refract and distort acoustic rays. Negative temperature gradients (temperature decreasing with altitude) bend rays upward, creating shadow zones where the boom is not heard (Figure 1.9). Positive gradients bend rays downward, increasing boom intensity. Wind shear significantly influences the propagation of sonic boom rays. Headwinds tend to deflect them upward, reducing their impact

at ground level, while tailwinds bend them downward, potentially intensifying the perceived boom. Crosswinds add further complexity by distorting both the shape and intensity of the boom footprint. On a smaller scale, atmospheric turbulence can smooth or scatter the shock fronts, modifying the pressure signature that ultimately reaches the ground.

The sonic boom carpet refers to the area on the ground beneath the flight path where the shock waves combine to create the sonic boom heard by observers. Figure 1.9 depicts the typical sonic boom carpet for a civil supersonic aircraft, highlighting two exposure zones. Firstly, the primary boom carpet, caused by direct propagation of shock waves from the aircraft, and secondary carpets produced by reflection and refraction in atmospheric layers above and below the primary zone. A shadow zone exists between these two carpets where no boom is detected.

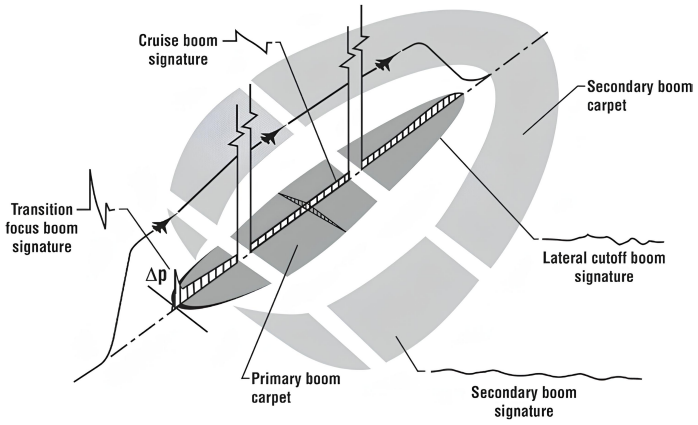

Fig. 1.9 Schematic of sonic boom ground exposures [2]

Although secondary boom carpets have lower overpressure and loudness than the primary carpet, they can still be annoying due to low-frequency vibrations or rumbles. These secondary booms, with frequencies between 0.1 and 1 Hz, are often inaudible outdoors but can induce building vibrations felt indoors. To better characterize sonic boom phenomena, initially several physical parameters were used. The key factors that describe a sonic boom include peak overpressure (Δp), rise time, duration, slope, and overpressure impulse. When the rise time is longer, the sudden pressure changes feel less sharp, which tends to reduce annoyance. Because these acoustic characteristics influence how people perceive and tolerate sonic booms, several large-scale studies have investigated public reactions, since the Concorde era. Human studies have clarified public responses: the 1964 Oklahoma City study exposed

500,000 residents to up to eight booms daily for six months [83–85], generating complaints and damage claims. In contrast, the 1961-1962 St. Louis study exposed 2.5 million residents to 76 flights in a year [86, 87], with no unexpected health effects and population habituation, though lower flight frequency suggests tolerance limits. In Europe, research at the Institut de Saint-Louis (ISL) using sonic boom simulators found that the startle effect drives annoyance [88]. This effect decreases as the rise time increases for the same peak overpressure. Modern studies use high-fidelity simulators like JAXA's [3], which reproduces realistic booms indoors and outdoors with multi-speaker setups and acoustic treatments (Figures 1.10a–1.10c), including walls and windows to mimic reflections and transmission paths for accurate perception studies.

(a) Simulator door closed (b) Outdoor simulator (c) Indoor simulator

Fig. 1.10 JAXA indoor and outdoor sonic boom simulators [3]

NASA has also developed indoor and outdoor sonic boom simulators for psychoacoustic research [89]. The original outdoor facility, built in the 1990s, features an acoustically treated chamber and a multi-speaker array that accurately reproduces boom signatures with rise times down to 2 milliseconds. A new indoor sonic boom simulation facility at NASA allow controlled studies on indoor boom perception and potential mitigation strategies.

1.5 Classical Theories

Since the first supersonic flight in 1947, numerous theories have been developed to understand the sonic boom phenomenon. In the 1950s, research efforts focused on both the theoretical foundations of sonic boom generation [90, 91] and its primary

effects on human perception and the environment. In parallel, mathematical formulations were derived to predict key characteristics, particularly the overpressure. These theories, while reliable and forming the foundation of sonic boom prediction, present inherent limitations and uncertainties. With the advent of Computational Fluid Dynamics (CFD) and High-Performance Computing (HPC), such classical theories are no longer used as the primary methodology for reliable estimation. Moreover, these approaches do not account for the psychoacoustic aspects of the signal, which currently represent the main focus of research in the field.

1.5.1 Whitham Theory

Before the first supersonic flights, the nature of the sonic boom was not really understood. Research in the 1940s and 1950s began to clarify that these booms are caused by shock waves from objects traveling faster than sound [92, 93].Early studies of ballistic projectiles were particularly valuable, as they provided the first quantitative insight into the behavior of these disturbances and contributed to the development of first reliable analytical models.

In 1952, Whitham [94] introduced a theoretical framework for wave disturbances generated by slender, axisymmetric bodies at supersonic speeds. His analysis showed that linearized solutions reliably predict first-order pressure amplitudes along approximate characteristic paths. For simple slender bodies, such as projectiles, the shock structure typically consists of a bow shock at the nose and a tail shock aft. More complex aircraft generate multiple shocks that merge downstream into an N-wave. Whitham's method, though originally for smooth, slender bodies, can accommodate slope discontinuities, extending its applicability. The theory assumes small disturbances, inviscid, homogeneous, supersonic flow, and observation at sufficient distance from the body. Whitham's linear theory provides correct first-order pressure values along a Mach characteristic, but the characteristic location itself is only zeroth-order accurate. Whitham developed a procedure to correct the characteristic location to the first order, obtaining a first order solution. The acoustic solution for the flow-field around a supersonic projectile is written in Equation 1.1:

$$\delta p(x-\beta r) = p_0 \frac{\gamma M^2 F(x-\beta r)}{\sqrt{2\beta r}} \tag{1.1}$$

Which could also be written as:

$$\delta p(\chi) = p_0 \frac{\gamma M^2 F(\chi)}{\sqrt{2\beta r}} \tag{1.2}$$

where new coordinate χ represents the Mach waves generated at the axial position x along the body, β is the Prandtl Glauert term, r is the radial distance and p_0 the free-stream pressure.

Equations 1.1 and 1.2 describe the acoustic propagation of a locally axisymmetric source. This implies that r is sufficiently large for near-field cross effects to be negligible, and that the amplitudes are small enough for propagation to remain linear. Under these conditions, the source function $F(x)$ depends on geometry:

$$F(x) = \frac{1}{2\pi} \int_0^x \frac{A''(\bar{x})}{\sqrt{x-\bar{x}}} d\bar{x}, \tag{1.3}$$

where $A(x)$ is the cross-sectional area distribution along a plane inclined at the local Mach angle, $A''(x)$ is its second derivative, and x is the distance along the body axis from the nose ($\bar{x} = 0$) to the station of interest. For slender bodies, A is often approximated by the cross-sectional area. Equation 1.3 provides a first-order estimate of the pressure disturbance.

Walkden [95] determined the directional component of lift dependence for a wing–body combination, accounting for fuselage volume, wing volume and lift, as well as body–wing interference. His result for the F-function can be expressed as the sum of a single volume term, which includes interference effects, and a single lift term, which likewise includes lift–interference contributions.

$$F(x,\theta) = \frac{1}{2\pi} \int_0^x \frac{A_v''(\bar{x},\theta) + \frac{\beta}{2q_\infty} L'(\bar{x},\theta)}{\sqrt{x-\bar{x}}} d\bar{x}, \tag{1.4}$$

with:

- $A_v''(\bar{x},\theta)$ – second derivative of local volume cross-section along the Mach plane,
- $L'(\bar{x},\theta)$ – derivative of the lift distribution,
- $q_\infty = \frac{1}{2}\rho_\infty U_\infty^2$ – free-stream dynamic pressure,

- $\beta = \sqrt{M_\infty^2 - 1}$ – Prandtl-Glauert Mach factor,
- θ – directional component along the lift distribution.

The total lift contribution is:

$$L(x,\theta) = \cos\theta \int_0^x L'(\bar{x},\theta)\, d\bar{x}. \tag{1.5}$$

The A_v'' term is the volume contribution, and is determined by the cross sections measured by cutting planes aligned with the Mach angle. The L term is the contribution due to lift and it is determined along Mach cutting planes. Except for slender wing planforms, Equation 1.5 is a more rigorous approximation than the use of simple cross sectional areas for the volume part.

The equation for the derivation of the effective area A_e is written as Equation 1.6:

$$F(x,\theta) = \frac{1}{2\pi} \int_0^x \frac{A_e''(\bar{x},\theta)}{\sqrt{x-\bar{x}}}\, d\bar{x}, \tag{1.6}$$

For a slender body, $A_v(x,\theta)$ can be approximated by the normal cross-sectional area at station x. For an aircraft in level flight or in a coordinated turn, the lift acts normal to the wing span, directed upward, and θ is zero in the downward direction. The total lift is given by the integral of $\cos\theta\, L'(x)$ over the vehicle length.

Whitham's theory is more reliable for slender bodies flying at low to moderate supersonic speeds ($1 < M \lesssim 2.5$), where disturbances remain small and linearization is valid. Its accuracy deteriorates for blunt shapes, strong shocks, or flows with separation, where nonlinear effects become significant. Environmental factors such as turbulence, temperature gradients, and wind are not included. Consequently, practical sonic boom predictions often combine Whitham's framework with numerical simulations or empirical corrections to account for nonlinearities and atmospheric effects. Despite these limitations, Whitham's theory provides a solid foundation for understanding how shock waves are generated and for estimating far-field pressures based on geometry and flight conditions. Later extensions, like Walkden's formulation, try to make it work for more realistic aircraft shapes, which helps to connect the idealized theory to actual sonic boom predictions.

1.5.2 Sonic boom minimization theories

Whitham's formulation laid the theoretical groundwork for predicting far-field sonic boom signatures under ideal conditions. Building on this foundation, researchers have applied the theory toward practical sonic boom reduction. Minimizing sonic boom has been a core design goal since the early days of supersonic flight, starting with Busemann's foundational studies [96]. Numerous mitigation strategies arise from understanding pressure wave physics, aircraft shape, and flight altitude. A key insight is that merging shock waves produce stronger pressure peaks than individual shocks, that led early designs to focus on weakening shocks near the aircraft to reduce the boom perceived on the ground. However, reducing sonic boom intensity often causes aerodynamic penalties, notably increased drag. Suppressing shock interactions near the aircraft typically requires rounded noses that spread shock energy and reduce wave reinforcement. While this reduces the far-field pressure signature, it generates a strong bow shock, increasing wave drag. On the other hand, slender noses produce stronger trailing shocks that merge with and amplify the bow shock, raising the far-field pressure signature. Thus, the design of a supersonic aircraft requires balancing low-boom objectives with aerodynamic efficiency. Carlson [97] proposed one of the first sonic boom minimization methods by calculating a theoretical lower bound on far-field boom pressure. Theoretical advances continued with Jones's work [98], who developed propagation equations based on Whitham's and Walkden's area rule F-function integral. Jones recognized that this equation could be treated as an Abel integral, and since $A_v^{''}(x)$ and $L(x)$ are continuous over $0 \leq x \leq l$, its inverse is given by Equation 1.7:

$$A_v''(x) + \frac{\beta}{2q_\infty} L'(x) = 2\frac{d}{dx}\int_0^x \frac{F(y)}{\sqrt{(x-y)}} dy \tag{1.7}$$

Integrating the equation it is possible to obtain 1.8:

$$A_v'(x) + \frac{\beta}{\rho V^2} L(x) = 2\int_0^x \frac{F(y)}{\sqrt{(x-y)}} dy \tag{1.8}$$

Integrating expression 1.8 once more it is possible to obtain, after changing the order of integration on the right-hand side, Equation 1.9.

$$A_e(x) = A_y(x) + \frac{\beta}{2q_\infty}\int_0^x L(y)dy = 4\int_0^x F(y)\sqrt{x-y}dy \tag{1.9}$$

Equation 1.9 forms the basis of Jones's key work on minimizing sonic boom by optimizing lift and area distributions [99]. His focus was on far-field booms, modeled as N-waves, while near-field booms appear as sharp delta pulses since shocks lose energy faster than acoustic waves. Although minimizing sharp shocks is possible, such signatures are usually undesirable. George and Seebass [28, 100, 101] built on Jones's theory, showing his delta function solution works well in the region where the sonic boom keeps its N-wave shape. They extended the model to include the full near-field pressure pattern, creating smooth lift and area shapes that reduce overpressure for given weight, altitude, and speed. The authors find that smooth pressure distributions reduce boom intensity by delaying or softening shock merging, resulting in reduced N-waves far from the aircraft. In their work they included realistic cruise conditions, setting a theoretical lower limit for boom strength. To reduce the intensity of sonic booms at ground level, aircraft designers aim to concentrate the F-function near the nose — ideally shaping it to resemble a Dirac delta. Jones later extended far-field analysis to include the rear shock [102].

George and Seebass gave a specific F-function form in Equation 1.10 that minimizes pressure perturbations. This sharp front peak ensures a dominant effect at the leading edge.

$$F(y) = \begin{cases} G\delta(y) + By + C & 0 \leq y \leq \gamma \\ By - D & \gamma \leq y \leq l \end{cases} \tag{1.10}$$

Seebass and George [100, 101] showed that shaping the equivalent area of a body of revolution can reduce sonic boom. They used the F-function to derive an expression for area A, based on parameters B,C,D and G, given in Equation 1.11.

$$A_e(x) = 4Gx^{\frac{1}{2}} + \frac{16}{15}Bx^{\frac{5}{2}} + \frac{8}{3}Cx^{\frac{3}{2}} - l(x-\lambda)\frac{8}{3}(x-\lambda)^{\frac{3}{2}}(C+D) \tag{1.11}$$

To determine optimal coefficients of the F-function for sonic boom mitigation, George and Seebass [103] imposed conditions aimed at minimizing key features of the boom signature. Their solutions showed that, under certain assumptions, the intensity of both front and rear shocks could be significantly reduced—especially for sufficiently long and lightweight aircraft. Their work provided a rigorous mathematical framework for shaping the F-function to achieve the lowest possible ground-level overpressures, determining the foundation for low-boom supersonic aircraft design.

1.5.3 Carlson simplified method

Carlson [104] developed a practical handbook procedure in the 1970s to estimate key features of N-wave sonic boom signatures. His method rapidly predicts bow shock overpressure, time signature duration, and primary carpet dimensions—both longitudinal and lateral—using minimal input data. Compared to high-fidelity methods, it offers fast, low-cost estimates suited for early conceptual design and applies to steady or moderately climbing/descending supersonic flight up to 76km altitude. The core simplification reformulates Whitham's F-function [94] using a shape factor K_S, which encapsulates vehicle geometry and performance. The handbook provides charts linking K_S to a lift parameter K_L for various studied configurations, enabling quick sonic boom predictions without intensive computation.

However, the method applies only to N-wave signatures, like those of first generation high-speed civil era. It cannot model the shaped, low-boom signatures targeted by next-generation supersonic designs, which aim to reduce public annoyance [71].

Evaluating the peak overpressure and time signature duration using Carlson's method begins with the analysis of the equivalent area due to volume, A(x), which represents the cross-sectional area perpendicular to the Mach cone. While generally reliable, this approximation tends to lose accuracy at high angles of attack or when applied in the hypersonic regime. The calculation explicitly subtracts the airstream tube entering the engines inlet. The second step evaluates the equivalent area due to lift, B(x), approximated by the aircraft's lift planform distribution. This distribution is derived using established theoretical methods [50, 105] and is expressed in Equation 1.12:

$$B(x) = \frac{\sqrt{M^2-1}\, W \cos\gamma \cos\theta}{1.4\, p_v M^2 S} \int_0^x b(x)\, dx \tag{1.12}$$

where W is the aircraft weight in $[kg]$ and $b(x)$ is the local span of aircraft planform at a given value of x-coordinate. The third step combines the previously evaluated equivalent area due to volume and lift to compute the total effective area, which is then used to determine the aircraft shape factor K_S.

Once K_S is known, it is possible to derive the propagation parameters M_e and h_e from the operating conditions and obtains the atmospheric factors K_p and K_t from reference charts. To extend the use of atmospheric propagation factors to off-track and non-zero flight-path-angle conditions, the method evaluates the effective Mach

number and effective altitude. The effective Mach number corresponds to the level-flight Mach value that yields the same ray-path inclination in the flight-track plane as the actual condition, offering a consistent way to characterize ray angles in complex trajectories. It is defined in Equation 1.13:

$$M_e = \frac{1}{\sin(\gamma + \cot^{-1}\sqrt{M^2-1})} \tag{1.13}$$

The effective altitude is the ray-path distance measured perpendicular to the flight path, and it is defined as Equation 1.14:

$$h_e = h\cos\gamma + d_x \sin\gamma \tag{1.14}$$

With d_x defined as the component of the distance between the aircraft ground-track position at the time of sonic boom generation and the ground impact location, projected along the direction of the aircraft ground track.

$$d_x = K_d\left(\frac{h}{\sqrt{M_e^2-1}}\right)$$

Complete equations for the more general off-track case are presented, and the effective Mach number is illustrated in equation 1.15

$$M_e = \sqrt{1 + \frac{\left[\frac{1}{\cos\gamma\sqrt{M^2-1}}\left(1 - \frac{\tan\gamma}{\cos\theta\sqrt{M^2-1}}\right)\right]^2}{\left[\left(\tan\gamma + \frac{1}{\cos\theta\sqrt{M^2-1}}\right)\frac{1}{\cos\gamma\sqrt{M^2-1}}\right]^2 + \left[\frac{\tan\theta}{\sqrt{M^2-1}}\left(\tan^2\gamma+1\right)\right]^2}} \tag{1.15}$$

While the effective altitude is illustrated in Equation 1.16:

$$h_e = \sqrt{d_y^2 + (h\cos\gamma + d_x\sin\gamma)^2} \tag{1.16}$$

In Equation 1.16, the parameter d_y is the sideways distance between where the aircraft was when the sonic boom formed and where it hits the ground, measured perpendicular to the flight path. The method also includes two correction factors to handle atmospheric effects: K_P adjusts for uneven atmospheric conditions, and K_R, usually set to 2.0, accounts for ground reflection. Using these, Equations 1.17

and 1.18 calculate the bow shock overpressure and the duration of the signature.

$$\Delta p_{\max} = K_P K_R \sqrt{p_v p_g} \, (M^2 - 1)^{1/8} \, h_e^{-3/4} \, l^{3/4} \, K_S \tag{1.17}$$

$$\Delta t = K_t \frac{3.42}{a_v} \frac{M}{(M^2 - 1)^{3/8}} \, h_e^{1/4} \, l^{3/4} \, K_S \tag{1.18}$$

Here, $\Delta p_{\max}$ represents the peak overpressure, and Δt is the duration of the signature. The factors K_P and K_R adjust for atmospheric and ground effects, while K_t corrects the duration. K_S stands for the aircraft shape factor. The parameter l is the characteristic aircraft length, M the Mach number, and h_e the effective altitude. The ambient speed of sound is a_v, and p_v and p_g are the atmospheric pressures at the reference altitude and ground level, respectively.

1.6 MORE&LESS project

This thesis has been carried out in strong collaboration with the H2020 MORE&LESS project. Therefore, this section provides an overview of the project, its major objectives and how the thesis has benefit from the collaboration as well as the contributions of the thesis to the project itself. The European Union funded the H2020 MORE&LESS project under the Horizon 2020 Research Programme, started in 2021 [14, 66] and concluded in April 2025. The project addresses the challenge of supporting Europe in shaping ambitious environmental standards for future supersonic aviation, working alongside the international community. In line with ICAO Assembly Resolution A39-1, it performs a comprehensive assessment of the environmental impacts of supersonic flight. Advances in key fields—such as aerodynamics, jet noise, sonic boom, propulsion, pollutant emissions, and overall environmental impact—are systematically translated into practical guidelines for regulatory authorities.

Fig. 1.11 MORE&LESS project logo

MORE&LESS explores the future of supersonic aviation, addressing both near- and long-term scenarios across a range of aircraft types and mission profiles. A core goal is to protect communities and the environment by evaluating emissions—greenhouse gases and pollutants—as well as noise impacts, including those from landing and take-off (LTO) and sonic boom. These insights contribute directly to shaping future regulations, either by updating existing standards or proposing new ones in line with next generation supersonic aircraft operations. The project reviews current and anticipated environmental regulations, identifying key areas where the regulatory framework needs to evolve—especially in light of ongoing bans on supersonic over-land flights and the challenge of adapting CO_2 standards to supersonic aircraft. The work begins with conceptual designs for aircraft flying at speeds between Mach 2 and Mach 5, and combines low- and high-fidelity modeling with experimental testing. This process validates simulation tools, which are then integrated into a multidisciplinary design framework called ESATTO [106]. MORE&LESS also explores alternatives to conventional hydrocarbon fuels, including biofuels and cryogenic options. Through a range of case studies—spanning different configurations, performance targets, and fuel types—the project improves the versatility and applicability of the developed tools.

Numerous benefits have arisen in this thesis from the collaboration within the MORE&LESS project. First, the ability to evaluate the available case studies, developed in line with the next generation of supersonic civil aircraft, allowed for a comprehensive assessment. Second, the proposed methodologies and tools were validated through experimental test campaigns and additional case studies. Moreover, collaboration with internationally recognized experts in the field enhanced the quality of the research, fostering continuous interactions and constructive feedback.

This thesis also made several contributions to the project. First, the numerical generation of sonic booms for all project case studies was assessed under on-design

flight conditions. Additionally, within some partner organizations, the setup, data acquisition, and numerical validation of two free-flight experimental tests were performed. Finally, the developed and validated design-oriented tools were integrated into the holistic multidisciplinary design framework to incorporate sonic boom constraints for the next generation of supersonic aircraft.

Chapter 2

Case studies

This research analyzes various case studies to test and validate the proposed methodologies and tools, ranging from low-supersonic wing-body business jets to hypersonic cruise waveriders. In addition to the full-scale case-studies, this thiesis also analyses two experimental free-flight test sub-scale models, used in experimental test campaigns inside the MORE&LESS project [107] derived from the hypersonic concepts. These mock-up configurations are similar but not identical to the original ones to ensure negligible lift for safety purposes and to facilitate stress and thermal analyses.

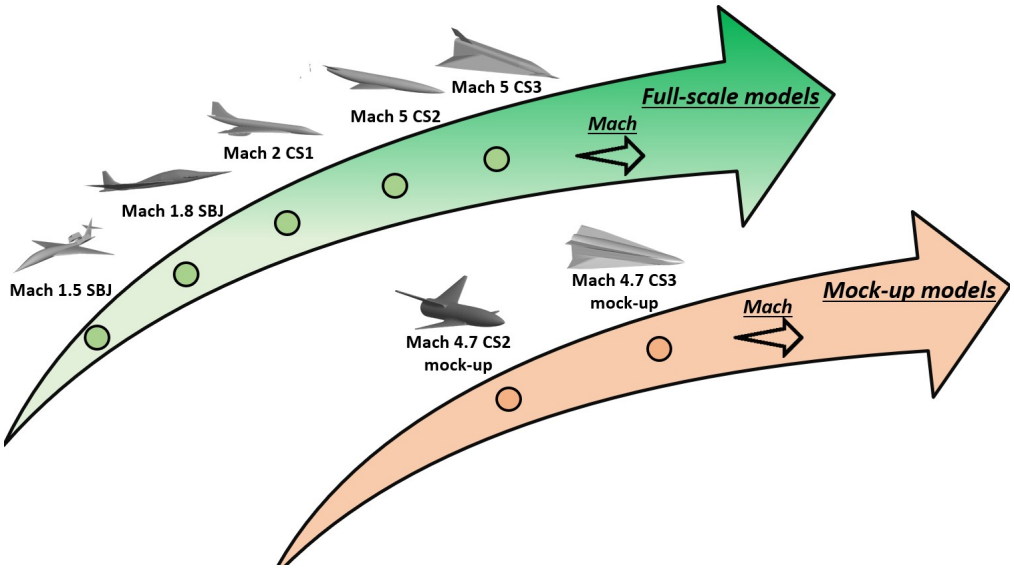

Fig. 2.1 Case studies evaluated in the PhD thesis

Figure 2.1 summarises the configurations analysed in this doctoral work. The aircraft displayed along the green arrow represent the full-scale models, spanning from a Mach 1.5 business jet to a Mach 5 hypersonic waverider with antipodal flight routes. The sequence follows increasing cruise Mach number. Complementarily, the second (orange) arrow illustrates the mock-up configurations employed in the experimental campaigns. As both correspond to Mach 4.7 conditions, they are arranged in the same order as their respective full-scale counterparts. However, for the CS3 mock-up case study, additional simulations at Mach 4.58 were employed for the derivation of inverse flight dynamics estimation, based on the recorded speed at the end of aeroacoustic area.

The first family of aircraft analyzed in this thesis are those of the MORE&LESS project, and denominated in this thesis as CS1, CS2 and CS3. The *CS1* configuration is a Mach 2 Concorde-like configuration with similar performance and geometric characteristics. Secondly, the *CS2* is a hypersonic demonstrator developed in collaboration with UK company Reaction Engine [108, 109] for flight test of the SABRE engine. Lastly, the *CS3* is a hypersonic waverider developed by Politecnico di Torino, and consisted in a redesign of the STRATOFLY aircraft [6]. The aim of the latter configuration is to sustain antipodal routes while flying hypersonically at Mach 5. In addition, the two sub-scaled configurations used in the experimental test are also presented. The differences between the full scale and mock-up models are evident from Figure 2.1.

However, none of the above mentioned configurations satisfied prospective sonic boom standards for future civil overland high-speed flights. To strengthen collaboration with colleagues in the ICAO-WG1 group, two additional configurations were developed within this thesis. The first is a Mach 1.5, 15-passenger supersonic business jet, created in collaboration with the Universitat Politècnica de Catalunya (UPC) and referred to here as *Mach 1.5 SBJ* or *CS4* concept. The second is a Mach 1.8, 20-passenger business jet developed internally to improve sonic boom performance and align with possible future regulatory limits. For this configuration, the effects of different turbulence models in the near-field Computational Fluid Dynamics domain were also assessed.

2.1 Mach 1.5 Supersonic Business Jet, Case Study 4

The first configuration was developed ad hoc for the purposes of this thesis and specifically to align with future possible supersonic overland flights. It is a Mach 1.5 business jet, hereafter referred to as the *Mach 1.5 SBJ (Supersonic Business Jet)*.The aircraft is designed using the internal proprietary tool ASTRID-H 2.0 software [110]. The design accommodates 15 passengers and incorporates two rear-mounted turbofan engines that operate without afterburners. This would reduce fuel consumption as well as noise during landing and take-off (LTO) operations. It features a double-delta wing configuration, which enhances aerodynamic efficiency in the supersonic regime and improves lift and maneuverability during both transonic and supersonic flight phases. Table 2.1 reports the main geometric and performance parameters of the selected aircraft.

Table 2.1 Mach 1.5 SBJ main geometric and performance characteristics

Aircraft parameter	Value
Cruise Mach number	1.5 [−]
Wing surface	117.4 [m^2]
Aircraft length	41.5 [m]
Range	5,500 [km]
Passengers	15 [−]
Maximum take-off weight	49,434 [kg]
Fuel Mass	21,260 [kg]
Wing loading	438 [kg/m^2]
Thrust to weight ratio	0.46 [−]

The initial configuration was designed to meet a preliminary set of performance and boom-related requirements. However, the resulting range of 5,500 km falls short of the minimum needed for transatlantic operations, prompting a redesign aimed at extending the range without compromising aerodynamic efficiency and sonic boom performance. Two sketches of the Mach 1.5 Supersonic Business Jet configuration are visible in Figure 2.2.

(a) Sketch Mach 1.5 Supersonic Business Jet (b) Top view Mach 1.5 Supersonic Business Jet

Fig. 2.2 Mach 1.5 Supersonic Business Jet case study views

The study also involves the preliminary aerodynamic database using inviscid CFD simulations and then corrects the results with engineering-based formulations [111]. It considers a broad range of Mach numbers and angles of attack to comprehensively characterize the clean configuration, as shown in Table 2.2. However, the effects of control surfaces remain to be investigated. The aircraft includes three elevons on each wing and a tail rudder composed of two separate surfaces.

Table 2.2 Test Matrix clean configuration SBJ

Mach [-]	Clean α [deg]
0.30	$-5^\circ \rightarrow 20^\circ$, step 5°
0.60	$-5^\circ \rightarrow 20^\circ$, step 5°
0.80	$-5^\circ \rightarrow 20^\circ$, step 5°
0.95	$-5^\circ \rightarrow 20^\circ$, step 5°
1.05	$-5^\circ \rightarrow 20^\circ$, step 5°
1.20	$-5^\circ \rightarrow 20^\circ$, step 5°
1.50	$-5^\circ \rightarrow 20^\circ$, step 5°

An in-house tool specifically designed for mixed-flow turbofan engines, as presented by Piccirillo et al. [112], created the propulsive database. Figure 2.3 illustrates the mission profile for the configuration. The aircraft completes the mission at a cruise Mach number of 1.5, maintaining altitudes between 16 and 19 kilometers, as shown in Figure 2.3a. Figure 2.3b shows the variation in angle of attack during the mission, as it remains nearly constant at approximately 2.5° throughout the supersonic cruise phase. The significant altitude increase observed during the mission highlights the configuration's excess lift. As fuel consumption reduces the aircraft's weight and the angle of attack stays almost constant, the surplus lift causes a substantial altitude gain during cruise.

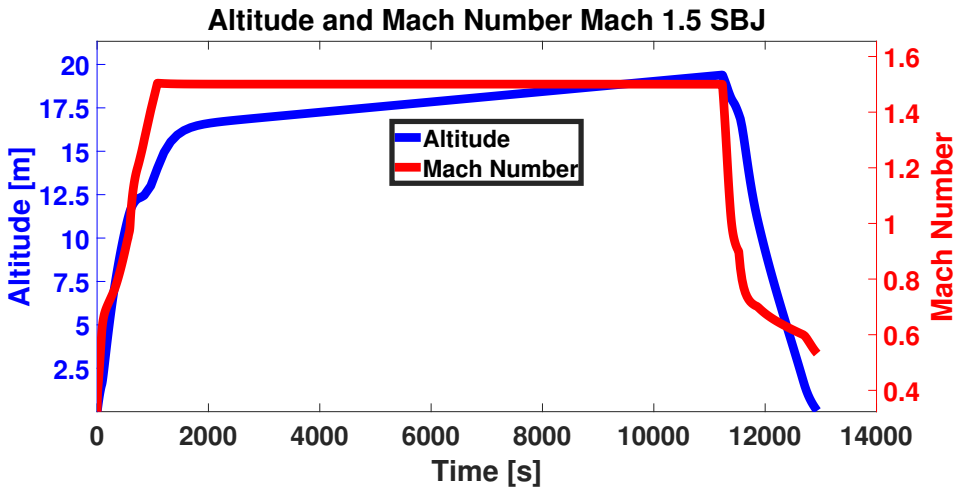

(a) Mach 1.5 SBJ mission profile

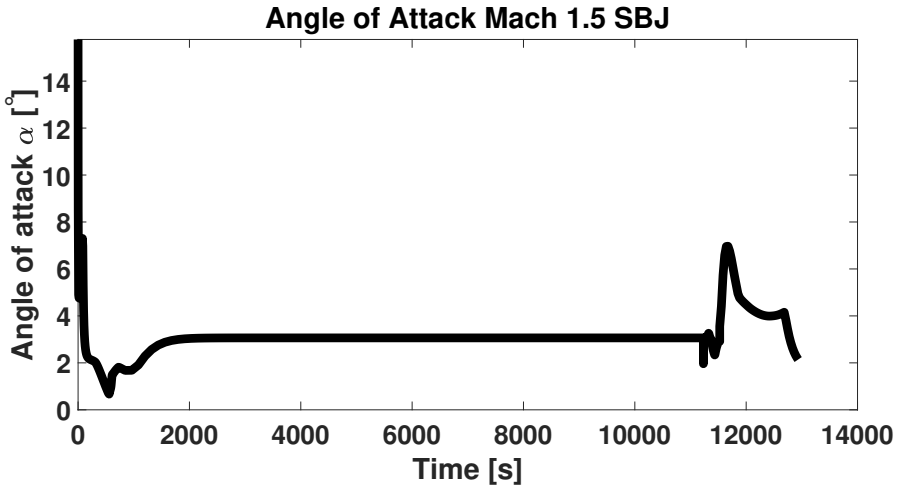

(b) Mach 1.5 SBJ angle of attack excursion

Fig. 2.3 Mach 1.5 SBJ mission profile and angle of attack excursion

2.2 Mach 1.8 Supersonic Business Jet, Case Study 5

The Mach 1.8 business jet configuration originates from an internal project at Politecnico di Torino, and it was developed using ASTRID-H 2.0 software [110, 113]. The design accommodates 20 passengers and uses two rear-mounted turbofan engines without afterburners, as the previous concept. The aircraft features a double-delta wing planform combined with a canard layout to improve longitudinal stability and maneuverability. The fuselage shape follows the area rule, reducing the effective

cross-sectional area and minimizing wave drag. Engine nacelles are integrated into the tail section, positioned above the trailing edge of the main wing, with the exhaust partially shielded by a pair of aerodynamic fins. Placing the canards forward reduces the required volume of the rear fuselage and ensures a smoother aerodynamic transition. Moreover, the canards enhance control authority during low-speed, high-angle-of-attack phases typical of takeoff and landing.

Table 2.3 highlights the main geometric and performance characteristics of the selected configuration.

Table 2.3 Mach 1.8 Business jet main characteristics

Aircraft parameter	Value
Length	39.0 [m]
Wingspan	13.0 [m]
Wing area	114.96 [m^2]
Aspect ratio	1.41 [$-$]
Fuselage height	2.5 [m]
MTOW	43,950 [kg]
Fuel weight	21,000 [kg]
Cruise altitude	18,000 [m]
Cruise Mach number	1.8 [$-$]

This PhD thesis analyzes two distinct mission points at a constant Mach number of 1.8, corresponding to angles of attack of 0° and 4°. At this stage, the study does not yet provide a complete aerodynamic and propulsive characterization, relying instead on a low-fidelity preliminary assessment for the mission profile.

Figure 2.4 highlights the lateral and top views of the configuration.

(a) Lateral view Mach 1.8 Supersonic Business Jet

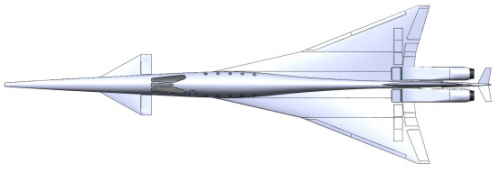

(b) Top view Mach 1.8 Supersonic Business Jet

Fig. 2.4 Lateral and top view Mach 1.8 Business jet

2.3 Mach 2 Concorde-like, Case Study 1 (CS1)

The third aircraft evaluated derives from the MORE&LESS project [14], and represents a Mach 2 passenger aircraft. This configuration is a redesign of the previously described Concorde, and will be referred to in this PhD thesis as *CS1* [114, 111]. The geometric and performance characteristics of CS1 are comparable to those of the original Concorde, featuring a cruise Mach number of 2.0 at an altitude of 59,000 ft, as highlighted in Table 2.4. The characterization of the aircraft encompasses several key aspects, including vehicle design, aerodynamic, propulsive analysis, and mission simulation. Table 2.4 highlights the main geometric and performance features of the vehicle.

Table 2.4 CS1 geometric and mass characteristics

Aircraft parameter	Value
Length	61.7 [m]
Wingspan	25.80 [m]
Wing surface	358 [m^2]
Range	6,500 [km]
Payload capacity	15,200 [kg]
Maximum take off weight	179,850 [kg]
Fuel Mass	85,289 [kg]

The aerodynamic [111] and propulsive databases support the development of a detailed mission profile. Table 2.5 presents the aerodynamic database test matrix performed with CFD methods. Initially, viscous effects were included through engineering formulations [111] and later refined using viscous simulations. The propulsive database, developed with EcoSimPro [115] software in collaboration with Von Karman Institute of Fluid Dynamics (VKI) , considers initially four turbojet engines with afterburner, while later studies proved the feasibility of the mission with four turbofan engines without afterburner.

Table 2.5 Aerodynamic database Test Matrix CS1

Mach [-]	Clean α [deg]	Flap effect δ
0.30	$-5° \rightarrow 20°$, step 5°	$-25° \rightarrow 25°$, step 10°
0.60	$-5° \rightarrow 20°$, step 5°	$-25° \rightarrow 25°$, step 10°
0.80	$-5° \rightarrow 20°$, step 5°	$-25° \rightarrow 25°$, step 10°
0.95	$-5° \rightarrow 20°$, step 5°	$-25° \rightarrow 25°$, step 10°
1.05	$-5° \rightarrow 20°$, step 5°	$-25° \rightarrow 25°$, step 10°
1.20	$-5° \rightarrow 20°$, step 5°	$-25° \rightarrow 25°$, step 10°
1.60	$-5° \rightarrow 20°$, step 5°	$-25° \rightarrow 25°$, step 10°
2.00	$-5° \rightarrow 20°$, step 5°	$-25° \rightarrow 25°$, step 10°

The three views of the CS1 aircraft are shown in Figure 2.5, and the shape similar to the original Concorde configuration is clearly visible.

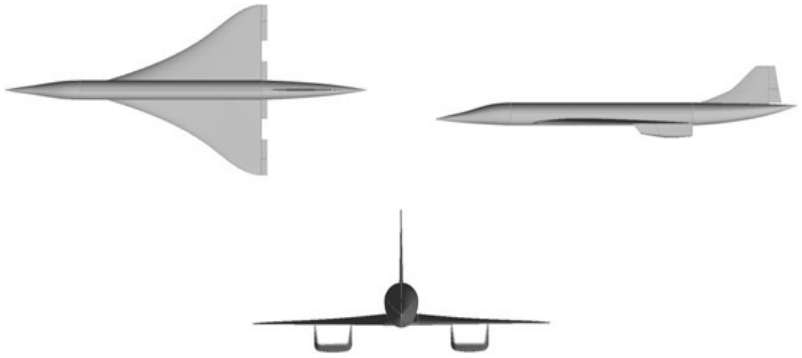

Fig. 2.5 Lateral, Upper and Side view of the CS1 aircraft

The flight control system includes three elevons on each wing and a split rudder on the tail, composed of two separate surfaces. Table 2.6 reports the control surfaces main data of the CS1 configuration.

Table 2.6 CS1 control surfaces

Surface	Chord [m]	Span [m]	Deflections [deg]	Surface [m^2]
Internal elevon	2.38	2.95	$\pm$ 25	7.02
Central elevon	1.93	2.35	$\pm$ 25	4.54
External elevon	1.63	3.45	$\pm$ 25	5.63
Upper rudder	1.56	3.25	$\pm$ 15	5.07
Lower rudder	2.07	2.05	$\pm$ 15	4.24

Figure 2.6 highlights the differences between this configuration and the original Concorde one, in particular the dihedral angle is set to 0° for the upgraded configuration and the wing shape has some minor differences.

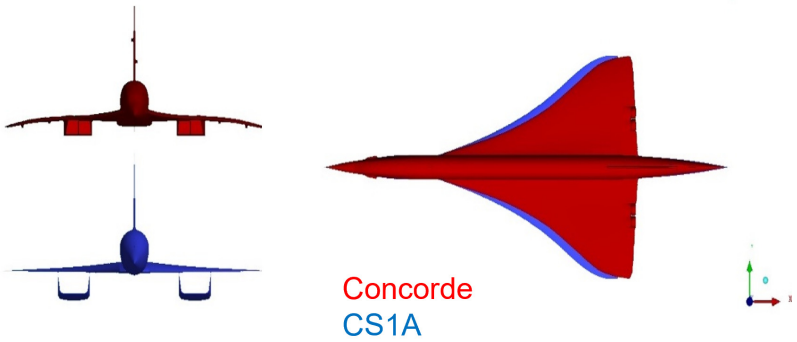

Fig. 2.6 Geometric comparison between CS1 and Concorde

The reference mission profile is displayed in Figure 2.7a, with a cruise Mach number of 2.0, and altitudes between 15.5 and 18 km. Across the cruise mission, the angle of attack has values around 4°, with a small visible decrease. As its predecessor, the mission profile safely connects the cities of Paris and New York, ensuring the required transatlantic range of 6,500 km.

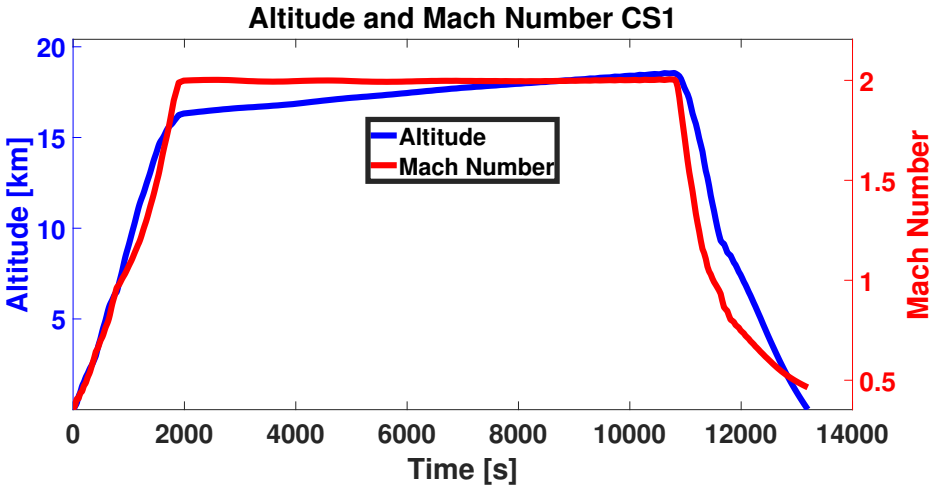

(a) CS1 mission profile

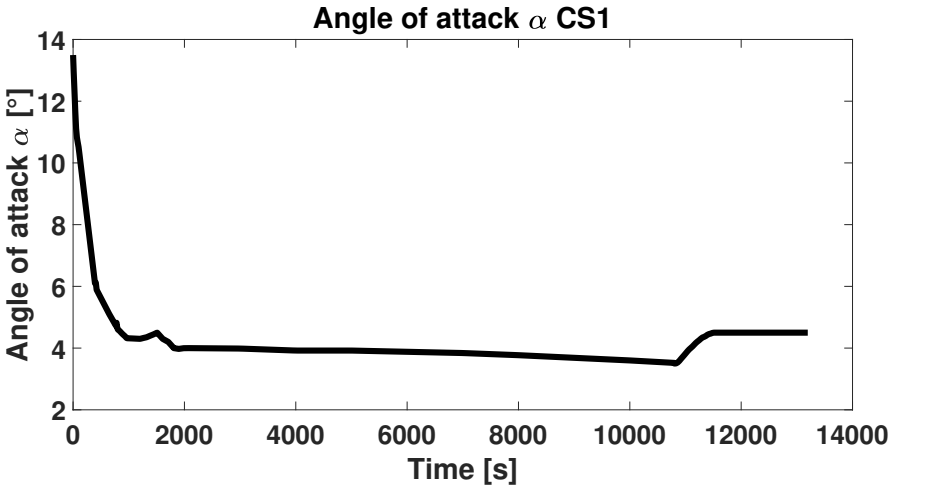

(b) CS1 angle of attack excursion

Fig. 2.7 CS1 mission profile and angle of attack excursion

2.4 Mach 5 hypersonic demonstrator Case Study 2 (CS2)

The CS2 and CS3 concepts are also included in this thesis. Although their cruise Mach numbers fall outside the feasible design space of second generation of sustainable supersonic civil aircraft, they provide valuable data for characterizing sonic booms in the hypersonic regime and for validating the numerical procedure through experimental test campaigns. One of the case studies evaluated in the MORE&LESS

project is a Mach 5 hypersonic test bed. This research collaborates with the former UK company Reaction Engines on the configuration named HTB (Hypersonic Test Bed), referred to as CS2 throughout this PhD thesis. The configuration served as a test bed for the SABRE engine flight demonstrator [108, 109]. The vehicle takes off and lands on a runway like a conventional aircraft, classifying it as a Horizontal Take-Off and Landing (HTOL) system, offering significant advantages in operational logistics. To improve the achievable mass ratio for a single-stage-to-orbit (SSTO) mission, SKYLON employs SABRE engine technology. This combined-cycle LO_X/LH_2 propulsion system operates in both airbreathing and rocket modes, enabling seamless propulsion throughout the entire flight envelope. During the initial mission phase, the engine runs in airbreathing mode, supporting take-off and the initial ascent until the vehicle reaches Mach 5.14 at an altitude of 28.5 km. At this point, the engine transitions to pure rocket mode to continue the climb and complete insertion into Low Earth Orbit (LEO). Figure 2.8 presents a representation of the CS2 aircraft. The design positions the SABRE engine on top of the fuselage, while the rocket engine is located at the rear end.

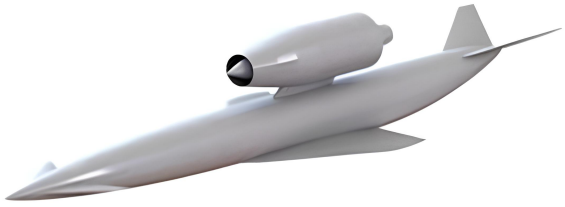

Fig. 2.8 Layout of the CS2 configuration with engine mounted

The simulations omit explicit modeling of the engine components. Since the SABRE engine is mounted on top of the aircraft's fuselage, it minimally influences the shock waves generated beneath the aircraft. Consequently, the primary sonic boom is not significantly affected by the presence of the engine. This simplification allows for a more focused analysis of the aerodynamic shock structures without compromising the accuracy of the predicted sonic boom signature.

The main geometric and performance characteristics of the aircraft are reported in Table 2.7.

Table 2.7 CS2 main characteristics

Aircraft parameter	Value
Cruise Mach number	5.0 $[-]$
Wing surface	40.77 [m^2]
Aircraft length	24.53 [m]
Wingspan	8.67 [m]
Height	3.81 [m]
Engine Diameter	1.66 [m]
Fuselage diameter	1.902 [m]

2.4.1 CS2 mock-up

As previously mentioned, the research involved two distinct experimental free-flight test campaigns carried out in collaboration with ISL (Institut Franco-Allemand de Recherches de Saint-Louis) and CIRA (Italian Aerospace Research Center). The tested configurations consist of sub-scaled versions of the original case studies developed within the MORE&LESS project, modified as needed to fit the available launch systems. Section 3.3 describes these experimental setups in detail. The first configuration, a sub-scaled model of the CS3 model is described in Section 2.5.1, and it was tested during the campaign on October 4th and 5th, 2022. Next, the focus shifts to the sub-scaled mock-up of CS2 aircraft.

ISL developed the mock-up configuration of the CS2 vehicle for the second outdoor free-flight experimental test campaign conducted in November 2023 at the ISL facility. The team designed the subscaled CS2 model for launch from a 91 mm smooth-bore launcher. However, critical limitations in the original configuration required significant redesign work. Two key requirements guided the redesign: firstly, the vehicle had to withstand the mechanical loads experienced during launch and free flight without sustaining structural damage. Secondly, for safety reasons, the configuration had to minimize aerodynamic lift generation during flight. To meet these objectives, structural reinforcements were introduced to reduce body deformation during launch, as shown in Figure 2.9a. Slight modifications to the pusher plate from previous test firings accommodated the updated geometry of the CS2 configuration, as shown in Figure 2.9b.

(a) CS2 mock-up

(b) Sabot package CS2 mock-up

Fig. 2.9 CS2 mock-up configuration and sabot package

The characteristics of the aircraft are visible in Table 2.8. For stability, different materials were employed: the nose of the aircraft was constructed with WNiFe(D176), while the body with AL7075. The use of materials with different density was needed to ensure longitudinal stability and operational safey during the experimental free-flight. The total weight of the projectile is 437 grams and the projectile was built to be have a fixed static margin to be on a safe side.

The sabot has been studied with 5-petals plus a pusher plate, similar to the CS3 mock-up configuration discussed later. The materials of the sabot is Onyx and Carbon Fiber, while the pusher plate is composed by AL7075 and high-density polyethylene, which has high strength-to-density ratio. The average density of this material ranges from 930 to 970 kg/m^3 giving stronger inter-molecular forces and tensile strength compared to low-density polyethylene.

Table 2.8 CS2 mock-up main characteristics

Aircraft Characteristics	Value
Reference Length	0.2337 $[m]$
Weight	0.437 $[kg]$
Center of gravity position	0.1300 $[m]$
Wingspan	0.0843 $[m]$
Fuselage diameter	0.0081 $[m]$
Maximum acceleration	35.0 $[kg/s]$
Part in AL7075	0.1338 $[m]$
Weight pusher plate	0.312 $[kg]$
Weight petals	0.434 $[kg]$

Filament deposition using a Markforged Mark Two 3D printer formed the petals. This manufacturing method incorporates a lightweight honeycomb infill that significantly lowers the component's mass. The reduced inertia helps minimize stresses from volumetric forces, especially under high acceleration. Continuous carbon fiber reinforcements embedded within an Onyx matrix—a nylon-based composite—align with the internal geometry to strengthen the outer shell, improving stiffness and overall strength without adding significant weight.

During the development of the CS2 mock-up configuration, two main structural problems arise. The first derives from the asymmetric layout of the wings and fins, which created uneven aerodynamic and inertial loads. These loads caused significant bending along the projectile's main body, especially during launch phase. To fix this, structural reinforcements were added to reduce deformation. The second problem involved a localized stress concentration near the projectile's base, which raised concerns about possible plastic deformation under operational conditions. Finite element analyses revealed that failure might occur around 35 g acceleration. To address this, the aft section received additional reinforcement to resist axial and radial loads better.

2.5 Mach 5 hypersonic waverider Case Study 3 (CS3)

Building on the analysis of supersonic configurations, this section introduces the CS3 Hypersonic Waverider, highlighting design modifications for efficient Mach 5 cruise. Although the previously described CS2 aircraft reaches Mach 5 during segments of its mission profile, it does not sustain hypersonic velocities for extended portions of its flight. Waverider configurations keep the bow shock attached to the leading edge at the design condition, maximizing lift-to-drag ratio and hypersonic efficiency [116]. However, their large wetted area requires early consideration of skin friction drag [117]. This thesis examines a modified version of the STRATOFLY MR3, adapted within the MORE&LESS project for Mach 5 cruise with antipodal range over 19,000 km [118]. To address issues at this speed—excess lift, intake spillage, and nozzle overexpansion— a redesign was needed [119]. In particular, the fuselage was shortened while retaining the wingspan and making geometric refinements to restore aerodynamic balance and stability. Figure 2.10 highlights the CS3 waverider configuration.

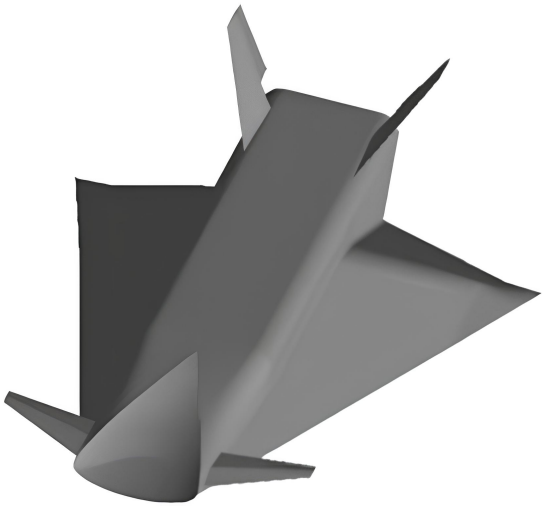

Fig. 2.10 Layout of the CS3 Mach 5 waverider configuration

Propulsive powerplant for the CS3 aircraft relies on a combination of six Air Turbo Rockets (ATRs) and a Dual Mode Ramjet (DMR), both fueled by liquid hydrogen. Table 2.9 summarizes the main geometric and performance characteristics of the configuration.

Table 2.9 CS3 main geometric and performance characteristics

Aircraft parameter	Value
Cruise Mach number	5.0 $[-]$
Planform surface	2,000 [m^2]
Aircraft length	75.16 [m]
Wingspan	41 [m]
Internal volume	8,000 [m^3]
Range	19,000 [km]
Maximum take-off weight	288,000 [kg]
Operative empty weight	150,000 [kg]
Payload	30,000 [kg]
Cruise altitude	28,000 [km]

Mission profile of the CS3 aircraft is shown in Figure 2.11a. During the hypersonic cruise phase, the aircraft maintains a constant Mach number of 5.0 while operating at altitudes ranging between 28 and 31 km. The vehicle meets its mission

range requirement of 19,000 km. Figure 2.11b shows how the angle of attack varies throughout the mission, highlighting that the cruise phase is set at an angle of attack of approximately – 0.3°.

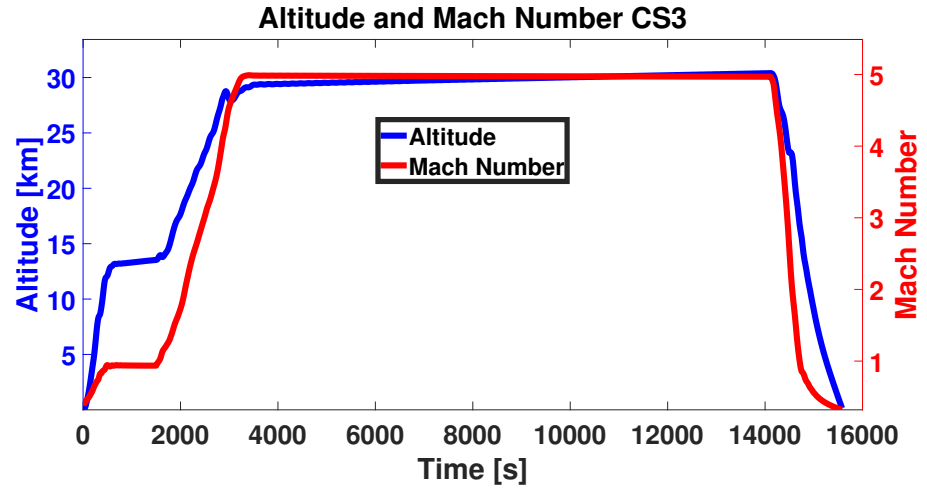

(a) CS3 mission profile

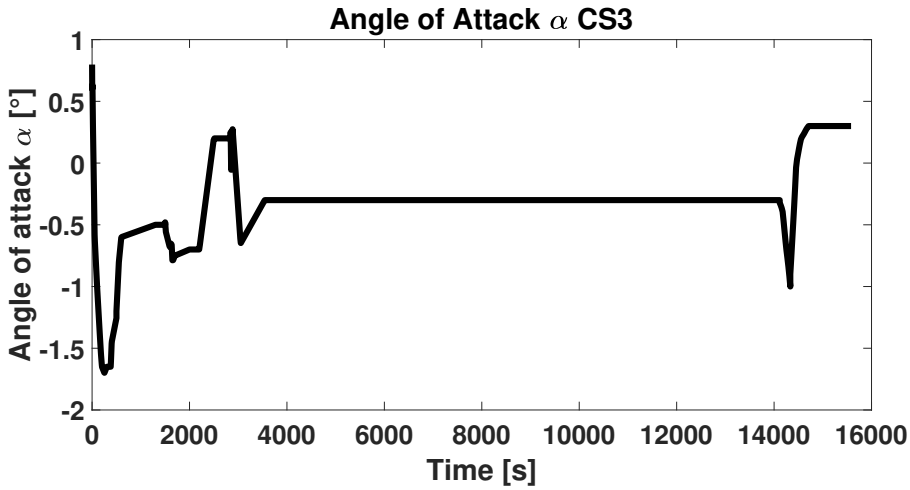

(b) CS3 angle of attack excursion

Fig. 2.11 CS3 mission profile and angle of attack excursion

2.5.1 CS3 mock-up

The thesis also develops the mock-up configuration of the CS3 aircraft to support the first MORE&LESS outdoor free-flight experimental test campaign on sonic boom [120, 121], conducted in October 2022 at the ISL facility in Saint-Louis,

France. The work includes the design and fabrication of a sub-scale model intended for launch from a 91 mm smooth-bore powder gun at the ISL proving ground. A key challenge was balancing the need for high-fidelity pressure measurements with maintaining aerodynamic stability during free flight—that is, avoiding significant pitching, rolling, or yawing motions. Because of the configuration's geometric features, the model required modifications to suit gun-launched testing. In particular, the design minimizes the lift coefficient, bringing it as close to zero as possible to reduce aerodynamic forces during flight and ensure accurate sonic boom signature measurements. The geometric changes focus primarily on the lee-side surface, as shown in Figure 2.12a. This choice reflects the fact that the windward side primarily governs shock wave generation and ground propagation, and therefore must remain as close as possible to the original aircraft. To reduce the risk of asymmetric lift during free-flight tests, the lower fuselage contour was mirrored onto the upper side, creating geometric symmetry along the longitudinal plane. This adjustment effectively suppresses lift at zero angle of attack, improving the model's dynamic stability.

Model simplification and launch facilitation required the removal of non-essential aerodynamic features, including canards and fins. Sealing the frontal air intake had no significant effect on the sonic boom signature. These modifications preserved the representativeness of the measured overpressure relative to the full-scale vehicle while enhancing the model's durability.

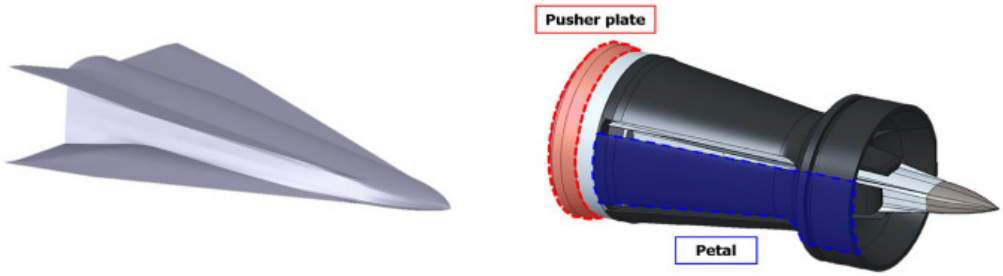

(a) CS3 mock-up

(b) Sabot package CS3 mock-up

Fig. 2.12 CS3 mock-up configuration and sabot package

The study combined numerical simulations and experimental tests to examine the aerodynamic behavior of the mock-up configuration. CFD simulations predicted flow characteristics, while wind tunnel tests validated those predictions. High-speed cameras recorded the model's free-flight motion inside the tunnels during testing.

To extract quantitative data, a custom image-processing algorithm developed at ISL processed the footage frame by frame to extract key aerodynamic coefficients such as lift, drag, and momentum. These tests focused on evaluating the aerodynamic stability of the mock-up design at different roll angles, ensuring the model maintained stability across the flight envelope.

Table 2.10 highlight the main characteristics of the CS3 mock-up configuration.

Table 2.10 CS3 mock-up geometric characteristics

Aircraft Characteristics	Value
Projectile mass	0.5017 $[kg]$
Length	0.203 $[m]$
CG/Nose	0.1326 $[m]$
Wingspan	0.0779 $[m]$
Height	0.0494 $[m]$
Sabot & projectile mass	≈ 1 $[kg]$

Figure 2.12b shows the sabot package designed to launch the mock-up configuration. The assembly includes four individual petals, created with a Markforged Mark II filament-based 3D printer, and a machined aluminum pusher plate. The pusher plate plays a key role during launch by effectively sealing the propellant gases and transmitting pressure evenly to both the sabot and the projectile. This design helps keep the structural integrity and ensures the model follows a stable, accurate free-flight path.

Chapter 3

Methodology & tools

This chapter lays out the methodology and tools implemented and used throughout this research. It gives a thorough overview of the multi-fidelity methodology and describes the design and implementation of the computational tools developed by the candidate. The emphasis is placed on the improvements and refinements made to the numerical methods and their implementation, highlighting the original contributions of this thesis. In addition to the computational developments, this chapter also outlines the experimental activities conducted and validated by the numerical results to provide reference data for model calibration. These tests, performed on scaled configurations under controlled conditions, allowed for a direct assessment of the accuracy of the near-field and propagation models. Furthermore, new and refined analytical models were formulated to improve the prediction of key sonic-boom-related quantities, such as peak overpressure and signature duration. These models are integrated within the broader multi-fidelity design environment, ensuring consistency between low- and high-fidelity tools and enabling a comprehensive assessment of the physical phenomena. Figure 3.1 provides a schematic representation of the research workflow that supports this work. The diagram outlines the scope of the research activities:

- White blocks indicate foundational activities or validated computational modules that were available prior to the start of the PhD in 2022.
- Green rectangles represent the development and investigative work carried out by the candidate as part of the doctoral research.

- Blue blocks correspond to the non-technical outcomes and broader societal impacts of this work.

These non-technical outcomes show the practical impact of the PhD candidate research. They contribute to improving sonic boom experimental campaigns, provide regulators (such as ICAO, FAA, EASA, and ENAC) with a reliable evidence base, and offer guidance for designers of future supersonic aircraft.

In addition, the types of arrows used in the same Figure convey specific meanings:

- Simple arrows: connect blocks to tools or methodologies available prior to the start of the PhD in 2022.
- Thick arrows: connect blocks to new tools or methodologies developed by the candidate during the PhD.
- Dashed arrows: indicate potential future work for further validation that does not require the development of new methodologies.
- Dotted arrows: show how the outcomes of the thesis can support agencies, aircraft designers, and the planning of future test campaigns.

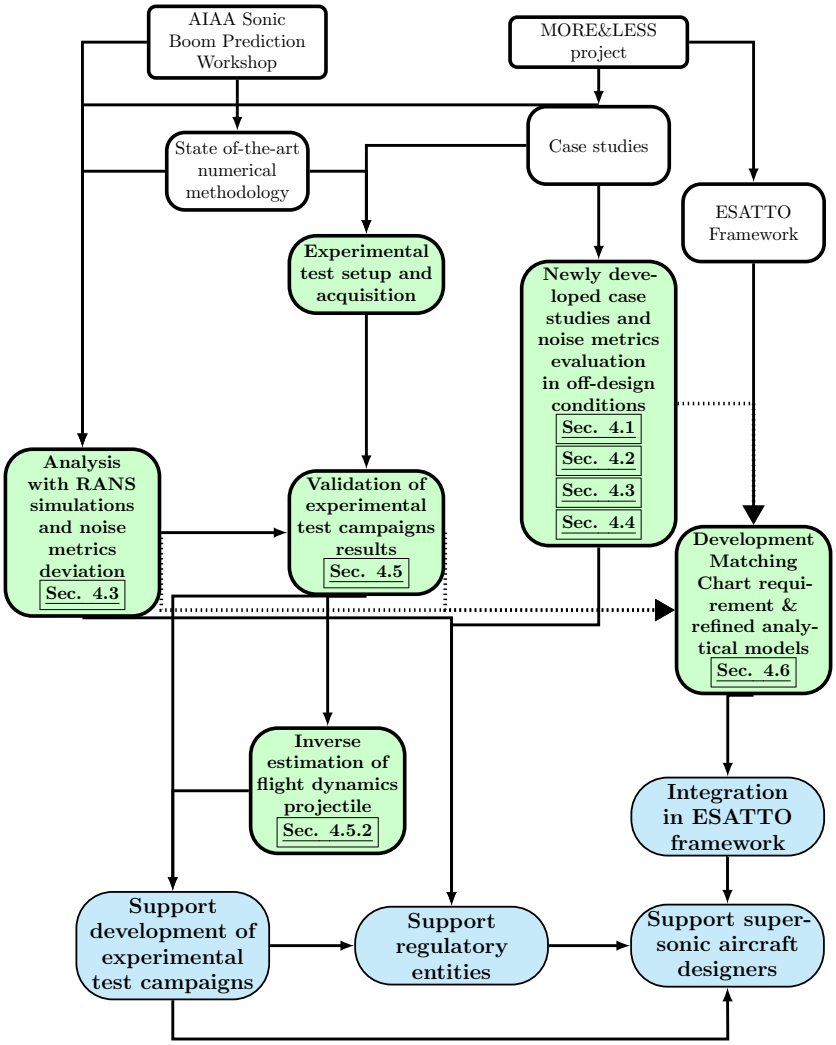

Fig. 3.1 Workflow of the PhD activities

This work, conducted within the MORE&LESS project, builds upon the findings of the three AIAA Sonic Boom Prediction Workshops held between 2014 and 2020 [122–124] and Propagation Workshops [125, 126], widely recognized as the state-of-the-art in sonic boom modeling. In this thesis, the bi-domain methodology, originally developed for low supersonic configurations, is extended to cases up to Mach 5. The numerical approach, including the applied boundary conditions, has been validated against two independent experimental campaigns. Beyond numerical validation, these experiments enable an innovative inverse estimation of the flight dynamics of one configuration from shock wave measurements.

As part of the research activity, two low-boom configurations were developed to support future supersonic civil overland operations. A set of noise metrics under on & off-design conditions were analyzed for a supersonic business jet and the Concorde-like configuration, providing evidence to support regulatory assessments. Realistic atmospheric profiles were also evaluated to examine the sensitivity of the selected metrics to varying atmospheric gradients. While Euler simulations are generally employed due to their lower computational cost, the impact of incorporating turbulence modeling in the Computational Fluid Dynamics analysis has also been investigated for a low-boom concept.

High-fidelity simulations and experimental results were further employed to improve sonic boom estimation at the conceptual design stage. Currently, reliable low-fidelity tools for preliminary sonic boom assessment are lacking. One of the aims of this thesis is to provide early-stage robust analytical tools to support aircraft designers without specialized expertise in aeroacoustics. Specifically, a new matching chart requirement based on peak overpressure is derived for configurations up to Mach 2, and a refined, simplified Carlson method is proposed and validated. Both tools have been incorporated into the ESATTO Framework [106], a holistic multidisciplinary design environment, to support the design of the next generation of high-speed civil aircraft. Figure 3.2 highlights a proposed workflow derived as a outcome of the proposed methodology for future high-speed civil aircraft designers. While it would be highly explained in Section 5.3, a brief description is here provided.

The tools developed in Section 3.4 are included within the workflow. Firstly, the updated Matching chart of Section 3.4.3 is included within the first and second layer of ASTRID-H 2.0 software, the research group property tool for aircraft design. Secondly, the refined analytical Carlson method of Section 3.4.4 is used to verify if the low-fidelity sonic boom requirements are met. Subsequently, high-fidelity numerical simulations are employed as well as experimental test on sub-scaled configurations. The latter would be performed with the suggestions given in Section 5.5, derived from the experimental test campaigns findings described in Section 3.3.

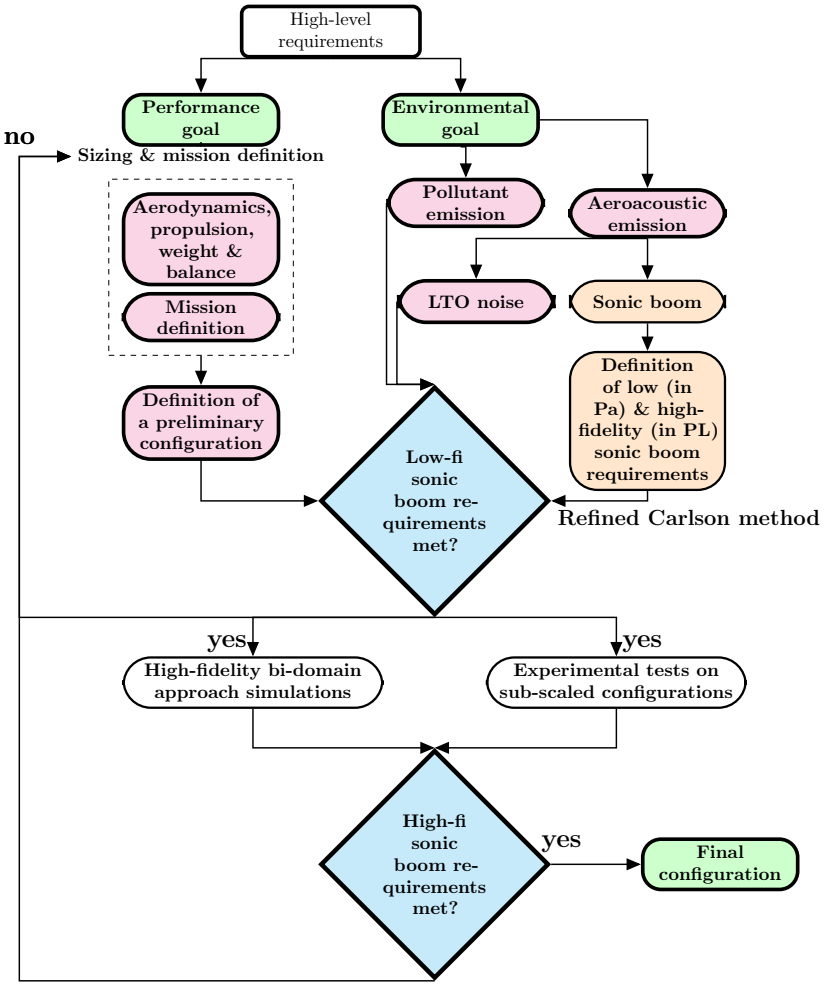

Fig. 3.2 Proposed workflow for future high-speed civil aircraft design

This chapter is organized to guide the reader through the methodologies and tools employed in this research. As stated in Chapter 1, sonic boom is generally numerically resolved by a bi-domain high-fidelity approach, visible in Figure 1.8. Firstly, the near-field region is resolved with Computational Fluid Dynamics techniques, while the far-field domain is computed with a dedicated propagation solver to account the effects of a non-uniform and stratified atmosphere. Section 3.1 focuses on the near-field approach, discussing the governing equations, the numerical strategies adopted, grid generation, boundary conditions, and the computational tools utilized. Section 3.2 addresses the far-field methodology, describing the two propagation solvers used, the atmospheric profiles considered, and the noise metrics applied. In Section 3.3, the experimental setup is presented, starting with the configuration

and acoustic instrumentation and then providing a detailed account of the two test campaigns. Section 3.3.4 explains the procedure used for the inverse estimation of flight dynamics. Finally, Section 3.4 reviews the ESATTO Framework, introduces the new sonic boom requirement in the Matching Chart, and presents the refined Carlson method.

3.1 Near-field

3.1.1 Governing Equations

In Computational Fluid Dynamics, the governing equations describe the conservation of mass, momentum, and energy in a viscous, compressible fluid [127]. The problem depends on four independent variables—space (x, y, z) and time t—and six primary dependent variables: pressure p, density ρ, temperature T, and the three components of velocity (u, v, w). Each of these variables varies with both position and time. These equations can be written in either conservative or non-conservative form. Unlike continuous analytical approaches, numerical methods approximate the flow-field over a discrete grid, and the equivalence between conservative and non-conservative forms no longer holds in practice. Non-conservative formulations may accumulate errors in the proximity of discontinuities, such as shock waves, which may ultimately result in nonphysical solutions or numerical instabilities. This limitation is particularly critical in the context of sonic boom prediction, where discontinuities and shock waves are inherently present. The control volume fixed in space leads to the conservative form of the governing equations, whereas a moving control volume corresponds to the non-conservative form. This distinction underlies the numerical relevance discussed above. A general flow field is evaluated , in which a finite region of the flow is enclosed within a closed control volume V, bounded by a control surface S, considering the control volume fixed in space with the fluid moving through it.

Continuity Equation

A brief evaluation of the three governing equations in the conservative form is here presented. Considering the model of a finite control volume fixed in space, at a specific point on the control surface, the flow velocity is $\vec{V}$ and the vector elemental

surface area is $d\vec{S}$. The net mass flow out of the control volume through the control surface S is the summation over S of the elemental mass, and it is the surface integral highlighted in Equation 3.1a. The mass contained within the elementary volume $d\mathscr{V}$ is $\rho\ d\mathscr{V}$, and so the total mass inside the control volume is therefore evaluated in Equation 3.1b.

$$\iint_S \rho\vec{V}\cdot d\vec{S}, \tag{3.1a}$$

$$\iiint_{\mathscr{V}} \rho\, d\mathscr{V}. \tag{3.1b}$$

The integral form then could be written as Equation

$$\iiint_{\mathscr{V}} \frac{\partial\rho}{\partial t}, d\mathscr{V} + \iint_S \rho\vec{V}\cdot d\vec{S} = 0. \tag{3.2}$$

Applying the Divergence Theorem and noting that the volume is arbitrary, it is possible obtain the differential, conservative form of the continuity equation:

$$\frac{\partial\rho}{\partial t} + \nabla\cdot(\rho\vec{V}) = 0. \tag{3.3}$$

Momentum Equation

Momentum conservation is essentially Newton's second law applied to a fluid element, in which the net force equals mass times acceleration. Forces include body forces $\vec{F}_B$ and surface forces from pressure p and viscous stresses τ. In conservative vector form, the momentum equation is written as Equation 3.4:

$$\frac{\partial(\rho\vec{V})}{\partial t} + \nabla\cdot(\rho\vec{V}\otimes\vec{V}) = -\nabla p + \nabla\cdot\tau + \vec{F}_B. \tag{3.4}$$

For the viscous stress tensor τ, several assumptions are commonly made: the fluid is isotropic; pure translation or rigid-body rotation does not generate viscous stresses, which is linearly proportional to the rate of strain. Moreover, the viscous force acts tangentially on the surfaces of fluid elements. For an isotropic Newtonian fluid, the viscous stress tensor in Cartesian coordinates is given by Equation 3.5:

$$\tau_{i,j} = 2\mu_a\left(\varepsilon_{i,j} - \frac{1}{3}(\nabla\cdot\vec{V})\delta_{i,j}\right), \tag{3.5}$$

where μ_a is the dynamic viscosity and $\delta_{i,j}$ the Kronecker delta. Finally, the momentum equation for the x component is given in as Equation 3.6:

$$\frac{\partial(\rho u)}{\partial t} + \nabla \cdot (\rho \vec{V} u) = -\frac{\partial p}{\partial x} + \nabla \cdot \left[\mu \left(\frac{\partial \vec{V}}{\partial x} + \nabla u \right) - \frac{2}{3} \mu (\nabla \cdot \vec{V}) \hat{i} \right] + F_{B,x} \tag{3.6}$$

Analogous expressions for y and z components can be easily derived, but are clearly outside the aim of this thesis.

Energy equation

The energy equation expresses the first law of thermodynamics, in which the total energy change in a system equals the difference between the heat transferred to the system and the work done by the system itself. The energy per unit mass contained is composed by three parts: internal, kinetic and potential. The primary mechanism for heat transfer $\dot{Q}$ to the fluid is thermal conduction. Since the heat is transferred to the system across the boundary surface it can be represented as a surface integral of the heat flux, and related to the temperature gradient via Fourier's law $\dot{q}^{"} = -k\,\nabla T$. The two main mechanisms of work that is done by a system are the pressure work done by the pressure acting normal to the system boundary, and the viscous work done by the action of the fluid viscous shear. Incorporating the pressure work term in the convective flux, introducing Fourier's law for heat conduction, and by applying the divergence theorem, the energy equation can be expressed in its conservative form as Equation 3.8:

$$\iiint_{\mathscr{V}} \frac{\partial(\rho e_t)}{\partial t} d\mathscr{V} + \iiint_{\mathscr{V}} \nabla \cdot \left[\rho \vec{V} \left(e_t + \frac{p}{\rho} \right) \right] d\mathscr{V} = \tag{3.7}$$

$$\iiint_{\mathscr{V}} \nabla \cdot \left[k \nabla T + (\tau \cdot \vec{V}) \right] d\mathscr{V} + \iiint_{\mathscr{V}} \dot{S}_g d\mathscr{V} \tag{3.8}$$

The control volume is arbitrary, hence the sum of all the integrands must be zero to satisfy the equilibrium. So it is possible to obtain the differential form of the conservation of energy Equation in 3.9:

$$\frac{\partial(\rho e_t)}{\partial t} + \nabla \cdot [\vec{V}(\rho e_t + p)] = \nabla \cdot \left[k \nabla T + (\tau \cdot \vec{V}) \right] + \dot{S}_g \tag{3.9}$$

3.1.2 Near-field CFD investigation

In this thesis, Computational Fluid Dynamics (CFD) techniques are used to study the flow around a supersonic aircraft due to the strong non-linearities and three-dimensional interactions near the fuselage. In this region, aerodynamic effects dominate, while atmospheric refraction has little impact. Section 3.2 shows that refraction becomes relevant in the far-field, influencing acoustic wave propagation. Over the past decade, CFD techniques for simulating sonic boom generation have improved significantly [122]. In this PhD thesis, two CFD solvers, three numerical schemes, and two different turbulence models were used to study the pressure fields around various supersonic and hypersonic configurations. The selection of methods was guided by recommendations and improvements found in the literature, combined with the results obtained. This work uses solvers based on the finite volume method (FVM), which approximates the integral form of the governing conservation laws—mass, momentum, and energy—by dividing the computational domain into many small control volumes. Each control volume enforces the conservation laws, making FVM a robust and intuitive way to discretize time-dependent conservation equations.

In aerospace, one of the earliest applications of finite volume methods was made by MacCormack [128], who applied these techniques to problems involving compressible flow. Outside aerospace, finite volume methods have been widely developed and improved to simulate turbulent flows across various industries [129], becoming a common approach in Computational Fluid Dynamics. Using this method on an unstructured mesh composed by quadrilateral elements means setting up a system to index the cells and keep track of each cell's neighbors. If the mesh has both triangular and quadrilateral cells, the number of neighbors changes depending on the type of cell. Since each edge is shared by two cells, it's easier to calculate fluxes by going over the edges instead of the cells themselves. After finding the flux through an edge, the flux contributions are updated for the two cells it connects: the flux is added to one cell's balance and subtracted from the other's, which keeps the fluid properties conserved [130].

Finite volume methods work well for solving conservation laws in Fluid Dynamics, especially in compressible and supersonic flows. They use the integral form of the equations, which handles shock waves and other discontinuities better than differential methods, and this makes them suitable for with sharp gradients. Finite volume

methods handle complex shapes well, including unstructured and mixed-element meshes, often with less effort than finite element methods. They also make it easier to build upwind schemes, which are crucial for accurately capturing the direction of wave propagation in convection-dominated flows. Furthermore, under uniform flow conditions, the discrete flux balances naturally vanish, leading to exact preservation of constant states—an important property that contributes to the overall numerical fidelity of the method. A significant challenge of the finite volume method lies in achieving accuracy beyond second order. Enhancing the order of accuracy requires the use of higher-order quadrature techniques to accurately evaluate the integrated fluxes over each face or edge of the control volumes. Additionally, it is necessary to implement reconstruction procedures that provide higher-order approximations of the flux vectors at the quadrature points, derived from the known averaged state variables within a stencil of neighboring cells [130].

At the same time, considerable effort has been devoted to exploring various numerical schemes in order to identify the most suitable approach for simulating sonic boom generation [4, 131]. Numerical schemes are critical for converting the governing equations from continuous formulations into discrete forms that can be implemented within computational solvers. Considering the flow regimes investigated in this PhD thesis, ANSYS Fluent provides the second-order upwind implicit ROE scheme [132], which employs Flux-Difference Splitting (ROE-FDS) [133]. Since all the waves travel in the same direction in a supersonic flow, it is natural to use an upwind scheme. The Roe Flux-Difference Splitting scheme is a popular numerical method used to solve hyperbolic conservation laws, especially when dealing with compressible flows. It was first introduced by Roe back in 1981 [132], and later improved with techniques based on characteristic flux splitting [133] to make it more stable and accurate when handling shock-heavy flows. ROE-FDS belongs to the class of approximate Riemann solvers, designed to estimate the solution of the Riemann problem at cell interfaces by linearizing the governing equations using locally computed Jacobians. The ROE-FDS method decomposes the flux differences into characteristic waves by analyzing the Jacobian matrix of the flux function. To ensure consistency and conservation of quantities between adjacent cells, the Jacobian matrix is appropriately averaged. The resulting eigenvalues and eigenvectors determine the propagation speeds and directions of the corresponding waves. Subsequently, the method separates the fluxes according to the sign of the eigenvalues, enabling the reconstruction of the solution in an upwind direction,

consistent with the natural propagation of information within the flow. The ROE-FDS scheme effectively preserves sharp flow features more accurately than simpler methods, such as central or first-order upwind schemes, making it well-suited for the simulation of high-speed aerodynamic flows with steep gradients. However, the scheme can occasionally produce non-physical expansion shocks, particularly in transonic or hypersonic regimes. This limitation arises from the method's reliance on a linearized approximation and the absence of an entropy correction in its original formulation.

Along with Roe's flux-difference splitting (ROE-FDS), ANSYS Fluent includes the second-order Advection Upstream Splitting Method (AUSM), first introduced by Liou [134]. AUSM does not require eigen-decomposition of the flux Jacobian, which makes it easier to implement compared to Roe's approach. Furthermore, the scheme avoids differentiation of fluxes, and the flux formulations do not explicitly involve pressure derivatives concerning density and internal energy. This feature is especially helpful when working with gases that follow complex equations of state, since sharp changes in thermodynamic properties can often cause numerical problems. AUSM splits the inviscid flux into convective and pressure components. The convective terms are treated like passive scalars and moved at a specified velocity across cell interfaces. The pressure terms depend on acoustic wave speeds and help AUSM capture shocks clearly and reduce numerical noise. Fluxes at cell faces are calculated using an upwind scheme, ensuring correct propagation of information through the domain. The AUSM method adjusts the flux-splitting coefficients based on local flow conditions. This helps improve stability and accuracy for many different flow regimes. Maintaining the simplicity and computational efficiency characteristic of Flux Vector Splitting methods, AUSM achieves a level of accuracy comparable to the previously defined ROE-FDS. AUSM has been used widely in sonic boom prediction [4, 135–137]. The algorithm is notably straightforward, requiring only $O(n)$ operations, which makes it both computationally efficient and easy to implement in numerical codes.

In SU2 (Stanford University Unstructured), several numerical schemes are available. Following the work of Glorioso et al. [131] for sonic boom estimation, the HLLC numerical scheme was selected. The HLLC Riemann solver, introduced by Toro [138] for the compressible Euler equations, is widely used in supersonic flow simulations. While the original HLL method does not account for intermediate waves, the HLLC solver restores the missing contact wave, allowing accurate

capture of contact discontinuities. This feature is particularly important in one-dimensional unsteady flows, where contact waves strongly influence the solution. In two-dimensional steady supersonic flows, HLLC can accurately model slip lines due to its ability to resolve contact discontinuities. In multidimensional, time-dependent flows, the solver improves the resolution of shear layers and vortical structures compared to HLL, although it does not explicitly resolve all transverse waves. By including these additional characteristic waves, the HLLC solver provides a more accurate representation of key flow features while maintaining computational efficiency.

Both ANSYS Fluent & SU2 employ an unstructured finite-volume approach to solve the Reynolds-Averaged Navier–Stokes (RANS) equations, with gradients evaluated using the Green–Gauss method [139], with an ideal gas model for the air phase. ANSYS Fluent controls convergence by adaptively adjusting the Courant–Friedrichs–Lewy (CFL) number, thereby modifying the time step to enhance stability and accelerate convergence. Conversely, SU2 performs simulations with a constant CFL number. Maintaining a constant CFL value prevents oscillations that may arise when it is gradually varied, a common issue in central-difference schemes. The CFL condition itself is a fundamental criterion for the stability of numerical methods applied to hyperbolic partial differential equations, ensuring that information does not propagate faster than the numerical grid can resolve. Due to the geometry of the different case studies, only half of the aircraft was modeled, and a symmetry boundary condition was imposed along the longitudinal plane to reduce computational cost. Additionally, all remaining external boundaries of the mesh — excluding the inlet and outlet — were modeled as slip walls to confine the domain without introducing significant flow disturbances.

Turbulence model

In this thesis, two turbulence models were employed to assess the deviations in the noise metrics relative to the classical inviscid equations. The analysis was carried out for the low-boom Mach 1.8 Supersonic Business Jet, considering two representative flight conditions. For consistency with best practices given by NASA, the turbulence model selected are k$-\omega$ and Spalart–Allmaras. This provide a comparison between two widely used approaches for simulating viscous effects in compressible flows, in which the convective terms are discretized using a first-

order upwinding. The remaining simulations were conducted under steady state and inviscid flow assumptions to streamline the analysis and limit the computational effort. This approach was adopted to enable a broader parametric exploration, since the large number of flight conditions considered in the following case studies would make fully viscous simulations computationally impractical for the intended level of accuracy.

$\mathbf{k}-\omega$

The k-ω turbulence model, inspired by Kolmogorov's theory of turbulence [140], was developed by Saffman [141] and later refined by Wilcox [142–144]. It belongs to the family of two-equation eddy-viscosity models and is used to simulate turbulent flows by solving transport equations for the turbulent kinetic energy k, and the specific dissipation rate, ω. The variable ω is related to the turbulence frequency, while k measures the energy contained within the turbulent fluctuations. One advantage of the k-ω formulation is its ability to accurately capture near-wall behavior without relying on empirical wall functions, making it particularly useful for flows with strong boundary layers, separation, or adverse pressure gradients. Wilcox later refined the model [142–144], providing a formulation that balances predictive accuracy with computational efficiency.

Spalart-Allmaras

The Spalart–Allmaras (SA) turbulence model is a one-equation eddy-viscosity model that solves a transport equation for a modified turbulent kinematic viscosity, usually represented as $\tilde{\nu}$. Introduced by Spalart and Allmaras in 1992 [145], the model was designed to offer a good balance between computational efficiency and robustness. Unlike more complex two-equation models such as the k–ε and k–ω formulations, the SA model does not attempt to resolve the turbulence kinetic energy explicitly. Instead of solving multiple transport equations, the model uses a single variable to represent turbulent viscosity. This makes the equations easier to solve while still capturing essential features like boundary layer development, skin friction, and limited separation under adverse pressure gradients. Because of this balance, it's widely used in aerospace applications. Its stability and relatively low computational cost also make it a good fit for turbomachinery cases, where complex geometries

and dense grids often rule out more advanced turbulence models. But the original Spalart–Allmaras formulation works as a low-Reynolds-number model, which means it needs the viscous sublayer to be fully resolved. If the mesh near the wall is too coarse, accuracy drops—sometimes significantly—especially in regions where boundary layer behavior matters most.

Alternative numerical approaches

A variety of methods exist for carrying out high-fidelity analyses of sonic boom, beside the bi-domain approach briefly described in Section 1.4. Over the past few decades, the development of new Computational Fluid Dynamics techniques (CFD) and the increasing availability of High-Performance Computing (HPC) have fundamentally changed the way these simulations are performed, making it possible to obtain far more detailed and accurate predictions than before. In a typical workflow for estimating sonic boom signatures at ground level, the first step is to model the flow field around the aircraft to capture the generation of the pressure disturbance. The resulting waveform is then propagated from a reference altitude down to the ground, taking into account the effects of a non-uniform, stratified atmosphere along the way. The near-field region is the area in the proximity of the aircraft where shock waves form and complex nonlinear effects take place, which include interactions between shock waves, the curvature of shock fronts, and the impact of crossflow. For relatively small configurations, wind tunnel experiments can offer valuable insights into the shock wave patterns generated by a supersonic vehicle. The far-field modeling phase starts by taking the pressure signature from the near-field region as input. It then considers the effects of atmospheric changes, acoustic absorption, and turbulence as the wave travels through the atmosphere. As a consequence, the overall accuracy of sonic boom predictions strongly depends on the fidelity of the near-field simulation, which provides the initial conditions for the propagation analysis .

Several alternative approaches have been explored in the literature. Yamashita et al. [146] carried out full-field direct simulations using a time-marching scheme, but the high computational cost makes this method impractical for early-stage design. To address this issue, the same author introduced a more efficient space-marching technique with semi-adapted structured grids in a vertically stratified atmosphere [147]. In a subsequent study, Yamashita et al. applied full-field simulations to more

complex urban settings, capturing the interactions between the sonic boom wavefront and surrounding buildings [148].

JAXA developed an additional CFD method that uses a multi-block structured mesh framework based on the Euler equations to capture jet-on effects explicitly [149]. Their approach discretizes the convective terms with the AUSMDV scheme, which they enhance using MUSCL extrapolation and a min-mod limiter to boost numerical stability and accuracy.

Wintzer and Kroo [150] employed an adjoint-based mesh refinement strategy to enable rapid and automated generation of volume grids for analyzing the near-field region of low-boom configurations. Emmanuelli et al. [151] studied sonic boom propagation over realistic terrain by solving the full two-dimensional Euler equations using finite-difference time-domain (FDTD) methods. Dragna used a similar method [152], running numerical simulations to examine sonic boom reflections in urban environments. These simulations considered both classical N-waves and low-boom signatures. Kandil [153] proposed a hybrid CFD approach combining Euler and Full Potential solvers with grid adaptation and shock fitting, enabling efficient and accurate prediction of near-field sonic boom signatures. Lastly, Ma et al. [154] analyzed near-field sonic boom signatures using the HUNS3D solver, showing that it can accurately and efficiently predict the pressure disturbances near a delta wing–body aircraft. They validated their results by comparing them with wind tunnel experiments.

3.1.3 Grid generation and boundary conditions

In this PhD thesis, the numerical methodology developed and suggested by NASA during the AIAA Sonic Boom Prediction Workshop was adopted [123, 124, 155, 156]. The cross-validated methods and results provided by workshop participants represent the current state of the art in near-field sonic boom prediction. The computational grid follows a hybrid topology, as shown in Figure 3.3. The setup divides the mesh into two regions: an unstructured zone around the aircraft geometry and a structured region covering the rest of the domain. The unstructured zone has the shape of a half-cylinder, while the structured region is created using a blocking strategy aligned with the Mach cone angle μ. Since the structured mesh depends on the Mach number, even slight variations require the generation of a new mesh

[157]. The mesh elements are tetrahedral in the unstructured region, hexahedral in the structured area, and pyramidal in the transition zone between them. Unlike Ma et al. [158], who split the hexahedral elements into prisms to improve grid alignment and better follow curved surfaces, this thesis uses only hexahedral elements in the structured region.

The present grid-generation strategy follows the principles of the Mach Cone Aligned Prism (MCAP) method developed by Cliff et al. [157], but it is adapted to a hybrid unstructured–structured framework. In this approach, the near-body region is discretized using an unstructured tetrahedral mesh suitable for both viscous and inviscid simulations, while the outer region consists of a structured hexahedral mesh aligned with the local Mach cone angle. The transition between the two regions is achieved through a thin interface layer of pyramidal elements, ensuring grid conformity and preserving cell quality. The hexahedral collar grid is generated so that its cell faces are sheared relative to the freestream direction by an angle corresponding to the Mach cone, thereby minimizing numerical dissipation during the propagation of shock waves. The alignment of the structured region with the Mach angle enables accurate capture of pressure disturbances convected downstream while maintaining computational efficiency over long propagation distances. The cylindrical outer boundary of the near-body tetrahedral domain defines the interface surface from which the structured Mach-aligned grid originates. The mesh density in this collar region is refined within the Mach cone and downstream of the vehicle over approximately one third to one half of the body length, to resolve the formation and coalescence of the bow and tail shocks. This configuration provides a robust and efficient framework for accurate near-field sonic boom prediction while remaining compatible with standard CFD solvers for hybrid meshes. The vehicles geometry are rotated to the required angle of attack in place so that the off-body grids can remain aligned with the Mach angle for any given flight condition, with the incoming flow at incidence α=0°.

The hybrid grid configuration adopted in this work has been rigorously validated by NASA through the Sonic Boom Prediction Workshop (SBPW), demonstrating its reliability and accuracy for near-field sonic boom simulations.

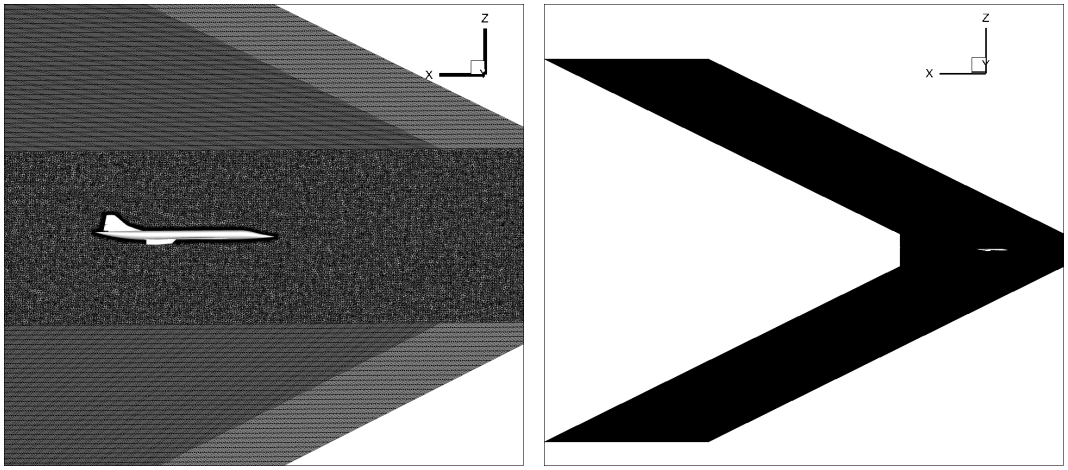

(a) Unstructured & structured grid employed (b) Domain of the near-field CFD simulation

Fig. 3.3 Detail of the grid generation and extension

Compared to fully unstructured or fully structured grids, the mixed-grid approach offers an effective compromise between accuracy and computational efficiency [158]. Previous studies have emphasized the importance of grid alignment [157], particularly in the z direction, since even small misalignments can cause noticeable differences in the sonic boom signature.

Anderson [159] showed that Cartesian meshes can predict out-of-body signatures effectively, provided they align well with the Mach angle μ. When properly oriented, these grids limit numerical dissipation and reduce the number of elements needed. As a result, it is possible to extract pressure signatures up to $H/L = 5$ distances without excessive computational cost. The H/L ratio is defined as the radial distance in relation to the aircraft's characteristic body length, such that H/L = 3 describes a radial distance of 3 body lengths. Figure 3.4 shows the radial extraction position for a selected case study. Moschetta [160] highlights the need to avoid the sonic glitch phenomenon—a numerical artifact that appears as spurious oscillations or sudden jumps in the near-field pressure signature during supersonic CFD simulations. This glitch distorts the otherwise smooth N-wave signature. To reduce numerical errors, this work uses a fine-enough mesh, aligns the grid closely with the local Mach cone angle, and applies smoothing or hybrid meshing where needed. To handle sonic glitches specifically, a slight angular offset—$\mu \pm \theta$, with $\theta \ll \mu$—is introduced. Together, these steps help minimize artifacts and improve the accuracy of the simulated flow field.

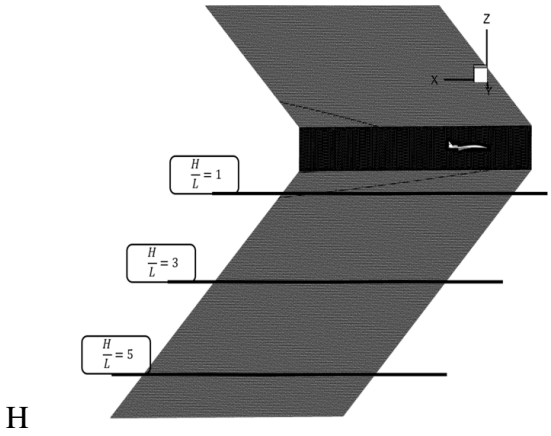

Fig. 3.4 CFD extraction points, H/L

As an example, the number of cells in the complete domain is approximately 21.5 million for the CS1 case study (Section 2.3), while for a low-fidelity aerodynamic grid, it is about 2.1 million elements [114]. The goal of the simulations presented in this work is to propagate the pressure variations of the shock waves produced by the aircraft in the whole computational domain, avoiding numerical artifacts like artificial dissipation. The differences between an aerodynamic simulation and an aeroacoustic computation are pointed out in Figure 3.5, where the flow fields evaluated using those two different approaches are compared. While the aerodynamic solution yields good agreement for global coefficients, with lift and drag matching the reference values [112], the associated pressure flow field differs significantly from that of the reference aircraft [114]. The pressure variations are dissipated by the computational grid used in the aerodynamic simulation, while they are perfectly visible in the aeroacoustic simulation up to the far-field of the domain.

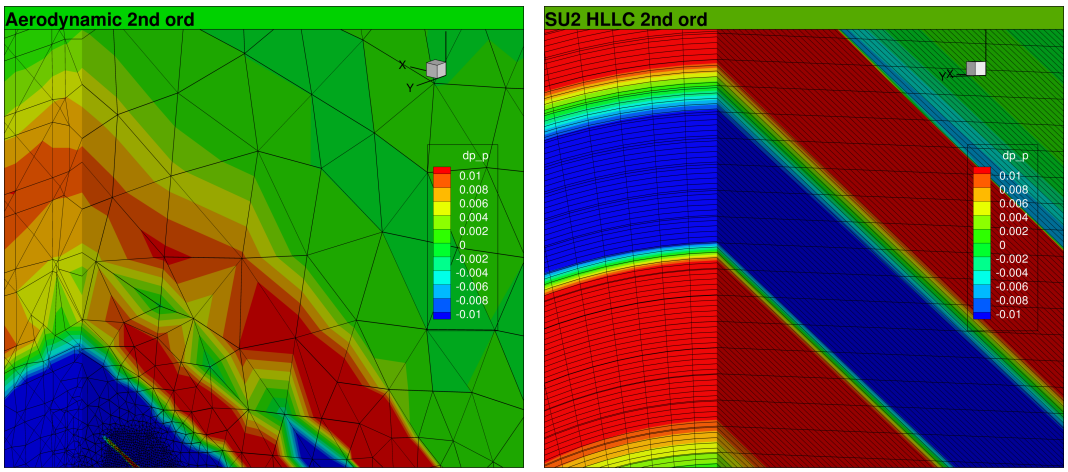

(a) Aerodynamic grid slice

(b) Sonic boom grid slice

Fig. 3.5 Aerodynamic and sonic boom grid [4]

Furthermore, this thesis investigates the interaction between shock waves and the boundary layer to assess its influence on the accuracy of flow predictions. Turbulence modeling was employed to provide a more realistic representation of the flow field and to quantify the discrepancies arising from neglecting viscosity in sonic boom generation and propagation. In general, Euler simulations demand significantly less computational effort than Reynolds-Averaged Navier–Stokes (RANS) approaches. However, previous studies have shown that neglecting the boundary layer in the near-field region has a limited impact on sonic boom generation [4, 131, 161–164]. Despite this, estimating the order of magnitude of the error introduced in the psychoacoustics and energy-based metrics due to boundary layer exclusion was necessary to validate the Euler simulations performed. The variation of these metrics across the different fidelity levels provides a valuable means to quantify their sensitivity to viscous effects, thereby supporting the assessment of the accuracy and applicability of each simulation approach.

For the selected configuration—representative of a Mach 1.8 low-boom concept introduced in Section 2.2 and assessed in Section 4.1.3—38 prism layers were generated. The first layer height is 10^{-5} m with a constant height ratio of 1.18. This setup produced a turbulent boundary-layer thickness of approximately 5.4 cm, in line with the expected values for the present Reynolds-number regime. The selected mesh is visible in Figure 3.6, with the nose boundary layer highlighted in Subfigure

3.6a for the RANS simulation, while Subfigure 3.6b highlights the same point of the geometry for the Euler simulations.

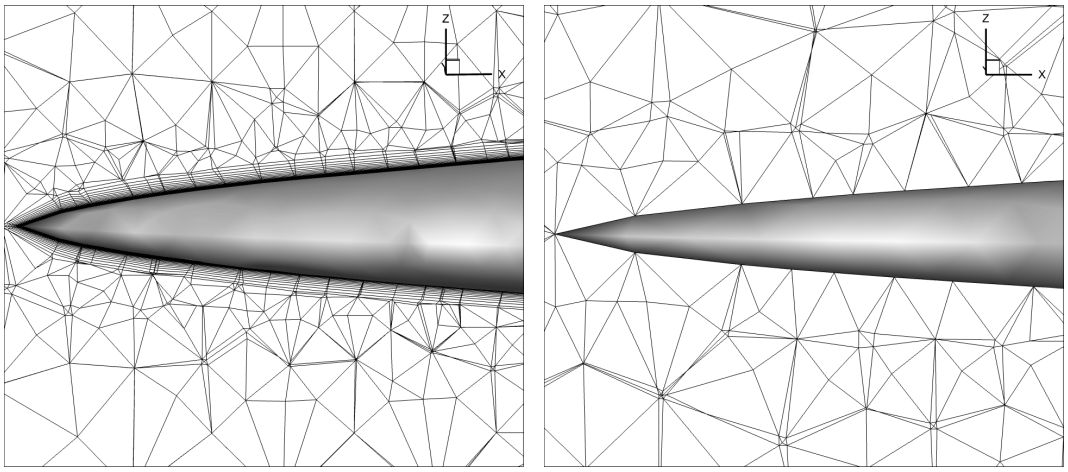

(a) Boundary Layer RANS simulations (b) Unstructured grid Euler simulations

Fig. 3.6 Analysis of the differences between Euler and RANS grids

3.1.4 Overview of the computational tools for near-field generation and post processing

ANSYS Fluent

As introduced in Section 3.1, two CFD solvers were used for the near-field sonic boom simulations. The first solver is ANSYS Fluent [165], for which versions 2021 R2 and later 2023 R2 were employed. ANSYS Fluent, developed by ANSYS Inc., runs primarily on C and uses a client–server setup that supports parallel computing. Thanks to this architecture, it is possible to run simulations interactively—whether on a local desktop or a high-performance computing environment—allowing for both flexibility and efficiency.

A key advantage of Fluent is its support for a wide range of mesh types, including 2D triangular and quadrilateral, as well as 3D tetrahedral, hexahedral, pyramidal, wedge, polyhedral, and hybrid meshes. It also offers adaptive meshing, refining or coarsening the grid locally based on flow gradients, which improves accuracy without excessive computational cost. Fluent's versatility extends to modeling diverse physical phenomena such as laminar and turbulent flows, heat transfer,

chemical reactions, and multiphase flows. Those features makes it particularly suited for aerospace applications, including accurate prediction of shock waves in sonic boom simulations. ANSYS Fluent provides a full suite of post-processing tools through ANSYS Workbench, allowing users to generate contour plots, vector fields, streamlines, isosurfaces, and animations for detailed visualization.

SU2

SU2 or *Stanford University Unstructured*, is an open-source CFD software developed at Stanford University for solving partial differential equations, with a focus on aerospace applications [166]. Written mainly in C++, it handles both steady and unsteady compressible and incompressible flows across a wide range of regimes, from subsonic to hypersonic. Its use of unstructured meshes allows accurate modeling of complex geometries. SU2 uses several numerical methods, such as finite volume and finite element approaches, and includes advanced turbulence models such as RANS with the SST k-ω model and hybrid RANS/LES. One of its standout features is the adjoint-based optimization, which makes sensitivity analysis and gradient-based aerodynamic shape design much more efficient. Its modular setup facilitates customization and integration into automated workflows, including mesh deformation and refinement to boost accuracy. Outputs from SU2 are compatible with visualization tools such as ParaView and Tecplot. SU2 also provides a Python interface (SU2py), which allows users to script workflows and automate simulations, making extensive parametric studies easier to run and results easier to reproduce. As an open-source platform, SU2 continues to evolve through contributions from a global community.

ICEM CFD

ANSYS developed ICEM CFD [167] to help generate high-quality meshes. It works with multiple geometric file types, which makes it easier to handle complex or large models. The software includes interactive tools to build both structured and unstructured meshes, and it also offers thorough mesh diagnostics and editing features to ensure accuracy.

ICEM CFD can handle geometries from virtually any source—commercial CAD, universal databases, scan data, or point clouds—and can mesh imperfect or dirty CAD

models using patch-independent algorithms without requiring fully defined solids or flow volumes. Its rich set of geometry manipulation, blocking, and refinement tools enables the creation of high-quality meshes suitable for CFD, finite element analysis, and other numerical simulations.

3.2 Far-field investigation

With increasing radial distance from the supersonic vehicle, the three-dimensional effects of the fluid motion weaken, and the shock waves originating from different parts of the configuration merge into a single conical shock front. As the distance from the aircraft increases, the resulting shock front gradually approaches the shape of the Mach cone surrounding the vehicle. From this perspective, the propagation of the Mach-cone shock front can be described using a ray-tracing method. This approach allows modeling the refraction of shock waves due to gradients in sound speed and wind. Although the ray-tracing method relies on the assumption of locally planar waves (i.e., a far-field approximation), its main advantage lies in its ability to capture the refraction effects of the stratified atmosphere, which become predominant in the far-field regime. For far-field ground propagation, the augmented Burgers equation [168] is widely employed. This model incorporates thermo-viscous losses and molecular relaxation processes, which play a key role in shaping the rise time and steepening of sonic boom shocks [169–171]. Pierce [172] originally formulated the equation assuming planar, small-amplitude waves to incorporate relaxation effects in nonlinear acoustic propagation. A more general derivation from the fluid dynamic equations, explicitly including molecular relaxation in a moving, stratified medium, was provided by Cleveland [168].

In an inhomogeneous and moving medium, the augmented Burgers equation along a ray tube accounting for relaxation effects can be expressed as Equation 3.10:

$$\frac{\partial p^{'}}{\partial s} = -\frac{p^{'}}{2G}\frac{\partial G}{\partial s} + \varphi\psi\frac{\beta p^{'}}{\rho_0 c_0^3}\frac{\partial p^{'}}{\partial t^{'}} + \varphi\psi^2\frac{\delta}{2c_0^3}\frac{\partial^2 p^{'}}{\partial t^{'2}} + \varphi\psi^2\sum_{\nu}\frac{(\Delta c)\nu}{c_0^2} + \frac{\tau_\nu\frac{\partial^2}{\partial t^{'2}}}{1+\psi\tau_\nu\frac{\partial}{\partial t^{'}}}p^{'} \tag{3.10}$$

More details on the equation are reported in the work of Cleveland [168], Rallabhandi [173] and Lonzaga [174]. In this expression, $p^{'}$ denotes the acoustic pressure

perturbation, s is the arc length along the ray path, and $t^{'}$ is the retarded time. The equation includes geometric spreading effects, nonlinear steepening, thermo-viscous dissipation, and molecular relaxation contributions. The parameter c_0 refers to the ambient speed of sound in the atmosphere, while ρ_0 is the ambient air density. The non-linearity coefficient β characterizes the strength of nonlinear effects in the propagation of the shock wave. Additionally, δ represents the diffusivity of sound due to both viscosity and heat conduction. The final summation terms accounts for frequency-dependent attenuation and relaxation effects in the medium, where (Δc) refers to changes in sound speed due to different physical mechanisms, and τ is the relaxation time constant for each mechanism.

This PhD research investigates the far-field pressure signature and noise metrics by adopting two separate computational tools based on different approaches. The first is propaBoom, a simulation tool developed in-house within the MORE&LESS project by TUHH [164]. The second is NASA's PCBoom solver (version 7.1), a well-established tool in the field of sonic boom prediction [175, 174, 176, 177]. The atmospheric profile between the reference altitude of the aircraft and the ground has an important role in the determination of the sonic boom carpet and in the intensity of the shock, as highlighted in Section 3.2.3. Although a radial distance of H/L = 3 is typically used for pressure signal extraction, prior studies have shown that H/L = 1 introduces negligible differences in sonic boom predictions [178]. An investigation of the variation of noise metrics due to different positions of extraction has been conducted, focusing on the variation between H/L=3 and H/L=1. Figure 3.7 illustrates the results of ray-tracing propagation in a non-uniform, stratified atmosphere. The propagation starts from the near-field source obtained through the previous methodology and continues until the corresponding ground waveform is computed.

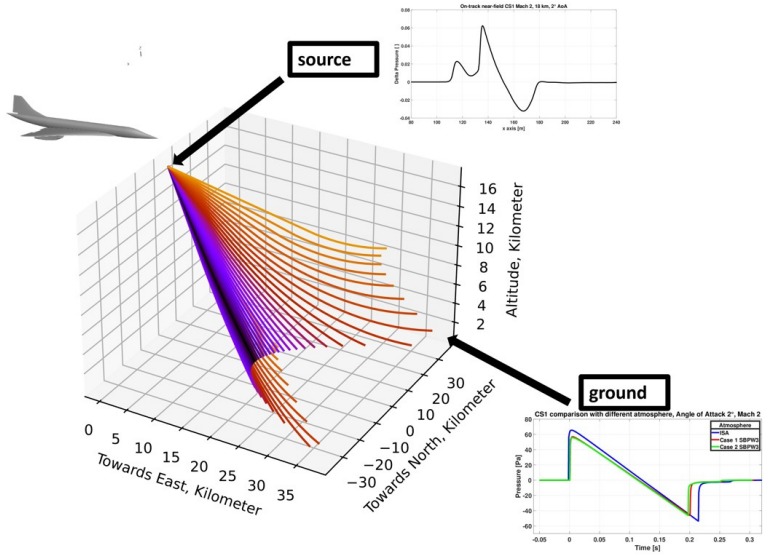

Fig. 3.7 Ray tracing propagation of the signal through the atmosphere

3.2.1 propaBoom solver

propaBoom is an in-house tool of the MORE&LESS project [14] developed by TUHH [179, 164]. The first assumption is that the aircraft is heading towards east. The extracted pressure signatures from the CFD are interpolated on a two-dimensional domain defined by the streamwise coordinate x and the azimuthal angle ϕ. This procedure allow a smooth variation of the acoustic field across azimuthal angles, ensuring the reconstruction of intermediate signatures. To focus the analysis on the propagation of shock waves, the near-field pressure data are selectively filtered to exclude regions of the CFD solution that do not contribute significantly to the acoustic footprint, and this is achieved through a transformation of the pressure signals from the physical (spatial) domain to a non-dimensional variable τ, which is aligned with the Mach cone geometry.

The normalized parameter τ is defined such that $\tau = 0$ corresponds to the aircraft's nose and $\tau = 1$ to its aft end. Its formulation incorporates the characteristic length L, the axial position x, and the Mach angle μ, as detailed in Equation 3.11:

$$\tau = \frac{1}{L}\Big(x - r\mu\Big) \tag{3.11}$$

The normalized signal is first cut at $\tau_1 = -0.2$ and $\tau_2 = 1.7$, before a linear fading over the duration of $\tau = 0.2$ at the start and end of the signal is applied to guarantee zero pressure at the signal borders. To allow sufficient room for non-linear evolution of the waveform during propagation, the signal is further extended by zero-padding, covering an enlarged domain from $\tau_1 = -1$ to $\tau_2 = 2.5$. Following this preprocessing step, the pressure signature associated with a specific azimuthal direction is converted into the frequency domain. This conversion accounts for the aircraft's flight speed at the corresponding operating condition and is carried out using a sampling frequency of 200 kHz.

The azimuthal angle sets both the starting position and orientation of each propagation ray on the Mach cone's surface. Each ray starts from a point along the aircraft's flight path, positioned directly above a reference point on the ground at the reference flight altitude. The initial direction is perpendicular to the Mach cone surface and aligned with the velocity vector of the configuration. The main goal of the ray-tracing simulation is to find where the shock wave front hits the ground. This involves figuring out which azimuthal angles produce rays that reach the ground directly and separating those from rays that bend upward and never intersect the surface. The results are limiting azimuth angles and the geometric position of the ground intersection for every ray. With propaBoom [164], rays are emitted over a structured azimuthal distribution. Within the azimuth range of between -40° and 40°, rays are sent out at intervals of 10°, while beyond this region, a finer resolution of 5° is adopted to improve accuracy near the limit azimuth angles. A bisection method evaluates the critical azimuth angle where rays shift from ground intersection to refracting upward. The method determines the limiting azimuth angle and reports it with a precision of two decimal places.

The governing equations for the ray-tracing, including wind effects, are twofold. One equation describes the shock wave front position, while the second one describes the orientation of the shock wave front normal vector. Onyeonwu originally formulated the ray tracing equations [180], and Yamamoto later presented them in a consolidated form [181]. Equation 3.12 shows the version used.

$$\begin{cases} \dfrac{d\mathbf{R}}{dt} = c\mathbf{N} + \mathbf{W} \\ \dfrac{d\mathbf{N}}{dt} = \left(\mathbf{I} - \mathbf{N} \otimes \mathbf{N}^\top\right) \nabla \left(c_0 - \mathbf{W} \cdot \mathbf{N}\right) \end{cases} \tag{3.12}$$

In Equation 3.12, **R** represents the position vector of the ray in space, the term c represents the speed of sound, **N** is the unit vector in the direction of the ray's propagation, vector **W** refers to the wind velocity in the atmosphere, which affects the propagation speed of the ray, **I** is the identity matrix, and the dyadic product $\mathbf{N} \otimes \mathbf{N}^{\top}$ constructs a projection operation. Ray tracing models wave paths but not amplitude; a 1D nonlinear equation accounts for shock attenuation and distortion. This equation is the Augmented Burgers equation [168, 181, 173]. The solution is performed in the time domain and excludes Doppler shift effects. Nevertheless, it incorporates geometrical spreading, variations in the atmosphere, nonlinear steepening, classical damping, and molecular relaxation phenomena.

3.2.2 PCBoom solver

PCBoom is a comprehensive suite of tools developed by NASA for simulating the propagation of sonic booms through the atmosphere [175, 174, 176, 177]. It applies full three-dimensional ray tracing based on geometrical acoustics to predict ground-level sonic boom signatures and their spatial footprints resulting from supersonic flight. Additionally, PCBoom provides estimates of selected noise metrics. The codebase originated more than 50 years ago with the work of Thomas [182], and its predictive capabilities have since been continuously improved through successive developments [175, 183–185].

The theoretical basis for predicting sonic boom signatures derives from the work of Whitham [94] and Walkden [95]. They developed models based on the F-function and the equivalent area distribution of the aircraft. These classical approaches assume a horizontally stratified atmosphere over a flat Earth—a simplification that remains adequate for modeling primary booms, where propagation distances are typically limited to around 100 km and thus small compared to the Earth's curvature.

In this PhD thesis, the Enhanced Burgers Solver was adopted to simulate the nonlinear propagation of sonic booms in the atmosphere, incorporating full wind effects as described by Lonzaga et al. [175]. This solver accounts for the Doppler shifting of wave frequencies due to the relative motion between the atmospheric medium and the ground-based frame of reference. The model's governing equation is expressed in the frequency domain as follows:

$$\frac{\partial U}{\partial s} = \frac{i\omega\tilde{\beta}}{4\pi}\int U(\omega')U(\omega-\omega')d\omega' - \alpha_t(\omega)U(\omega) \tag{3.13}$$

In Equation 3.13, U is the Fourier transform of the scaled acoustic pressure u. The symbol ω indicates the angular frequency. The coefficient $\tilde{\beta}$ relates to nonlinearity, while $\alpha_t(\omega)$ represents the Doppler-shifted and convected absorption.

The Enhanced Burgers Solver decouples the nonlinear and absorptive components of wave propagation at each time step. Nonlinear effects are computed in the time domain, while thermoviscous and relaxation-based absorption are evaluated in the frequency domain. The split-step pseudospectral method separates the problem by reformulating Equation 3.13 into two sub-problems, each solved with a closed-form analytical solution.

Compared to the older Legacy Burgers Solver in PCBoom, the Enhanced Burgers Solver runs much faster and is more stable numerically. It eliminates the need for anti-Gibbs filtering, which was previously applied to suppress spurious oscillations near discontinuities. On top of that, the Enhanced Solver includes the convective index—a measure of how wind changes the actual path the wavefront takes. This index quantifies the difference between the actual path of the ray through moving air and the path perceived by a stationary observer.

Atmospheric turbulence results from small-scale fluctuations in wind and temperature, which create irregularities in the air. These variations cause sonic booms to focus and defocus unpredictably, altering their acoustic signatures. Turbulence influences sonic booms in two notable ways: it introduces random disturbances trailing the shock fronts and leads to unpredictable increases in shock rise times. These effects are typically most significant within the atmospheric boundary layer. For overland propagation, solar heating and time of day generally influence the height of the atmospheric boundary layer (ABL) and the intensity of turbulence. Generally, turbulence tends to be weakest during the early morning hours, while it typically reaches its maximum intensity in the afternoon due to stronger solar radiation.

PCBoom incorporates three models to account for the effects of atmospheric turbulence on sonic boom propagation. The first model employ a three-dimensional turbulent scattering framework developed by Crow [186], which characterizes random signature distortions. The second approach uses a two-dimensional turbulence

representation implemented through finite impulse response (FIR) filtering techniques developed by Locey and Sparrow [187, 188] end extended by Bradley et al. [189], Stout [190] and Downs et al. [191]. However, in this PhD thesis, no atmospheric turbulence was considered.

Additional technical details about PCBoom, including implementation and solver configuration, are documented in the official PCBoom Technical Reference [174].

3.2.3 Atmospheric modelling

High-fidelity prediction of ground sonic boom disturbances requires consideration of atmospheric modelling. In particular, temperature, humidity, wind, and pressure gradients affect the way shock waves travel and dissipate over large distances. These variations influence the extension of the sonic boom carpet and the noise metrics, which are crucial for community response evaluations. The International Standard Atmosphere (ISA) is frequently used due to its simplicity. This model provides a simplified vertical structure of the atmosphere gradients, including a fixed rate of -6.5 K/km for the temperature profile within the troposphere and the absence of wind components [192]. While effective for general purposes, the ISA atmosphere does not capture the complexity of a real atmosphere.

Improvements to the ISA atmospheric model has been introduced to increase the modeling fidelity. A standardized humidity profile, outlined in ANSI S1.26 Annex C [193], has been integrated for this work. In addition, the upgraded ISA profile was used during the Sonic Boom Prediction Workshop to provide a more representative reference atmosphere.

Despite the improvements, the International Standard Atmosphere retains significant limitations that may result in overly simplified predictions. Therefore, to better replicate the real atmospheric conditions affecting sonic boom propagation, this study incorporates atmospheric profiles provided by the second and third Sonic Boom Prediction Workshops (SBPW2 [194], SBPW3 [195]). The selected atmospheric profiles used are highlighted in Figure 3.8.

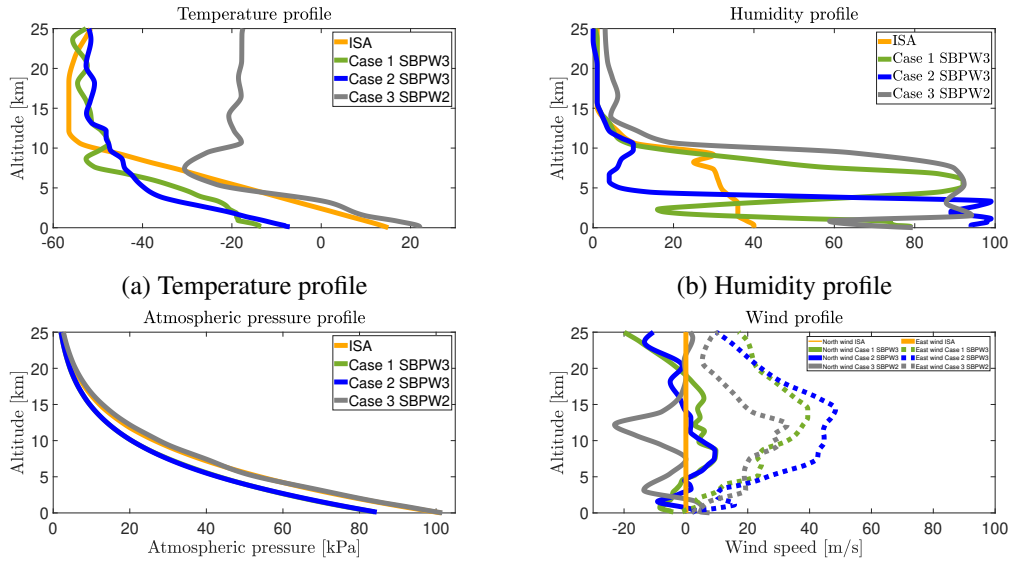

(a) Temperature profile

(b) Humidity profile

(c) Atmospheric pressure profile

(d) Wind profile

Fig. 3.8 Temperature, humidity, atmospheric pressure and wind profiles evaluated.

Three representative atmospheric profiles have been selected from previous Sonic Boom Prediction Workshops. The first, referred in this thesis as *Case 1 SBPW3* [196], corresponds to an atmospheric profile that allows a wide range of azimuth angles for an eastward-flying aircraft to generate ground-reachable sonic booms. The second, denominated in this work *Case 2 SBPW3* [197], represents conditions that produce a vast sonic boom footprint. The third profile, named *Case 3 SBPW2* [198], is derived from the second Sonic Boom Prediction Workshop and is associated with the axibody configuration.

3.2.4 Psychoacoustics and energy-based metrics

In literature, numerous noise metrics are available to characterize sound disturbance properly. In addition to acoustic factors, many non-acoustic variables also influence human annoyance. For example, studies have reported conflicting results between different genders regarding noise perception [199, 200]. Age is another significant factor, with annoyance generally increasing with age [199]. Moreover, startle reactions—involuntary responses such as flinching, jumping, or a rapid shift in attention triggered by sudden onset, high peak overpressure, or sharp waveform—have been shown to influence annoyance responses to sonic booms [199].

The metrics selected for this PhD thesis were chosen based on their strong correlation with human perception data related to sonic boom annoyance, as well as their widespread use and availability within the sonic boom research community. As recently highlighted by Loubeau [201], the Sound Exposure Level *SEL* (with various weighting functions, Figure 3.9), Perceived Level *PL*, and the Indoor Sonic Boom Annoyance Predictor *ISBAP* are among the most suitable metrics for analyzing sonic booms for future overland certification standards.

PL

Perceived Level (PL) is a psychoacoustic measure of the loudness of a sound, and Stevens developed the Mark VII method for its calculation in the early 1970s [202]. One important advancement compared to the earlier Mark VI method is the extension of the frequency range, especially toward lower frequencies. This change is particularly significant for sonic boom studies, where waveforms often contain considerable acoustic energy between 1 Hz and 10,000 Hz. In this approach, measured sound pressure levels (SPL) are converted into perceived loudness values expressed in sones. The loudness values in each frequency band are then combined into a total loudness, S_t, using the formulation shown in Equation 3.14:

$$S_t = S_m + F \cdot \left(\sum (S - S_m)\right) \tag{3.14}$$

In Equation 3.14, F represents the fractional loudness contribution of each band, and S_m is the maximum band loudness. After obtaining the total loudness in sones, it is converted into Perceived Level (PL) in decibels using Equation 3.15:

$$\mathrm{PL} = 32 + 9 \log_2 S_t \tag{3.15}$$

This conversion reflects the nonlinear human perception of loudness, where each doubling of loudness in sones corresponds to an increase of 9 dB in PL.

Sound Exposure Level

The Sound Exposure Level (SEL) quantifies the total sound energy of a waveform, normalized to a standard reference duration. It captures the time-integrated squared

acoustic pressure, making it possible to compare sounds that differ in duration. In all SEL calculations presented here, the reference pressure p_0 is equal to $20 \cdot 10^{-6}$Pa. Sound Exposure Level is calculated according to ANSI/ASA S1.4-2014, as shown in Equation 3.16:

$$L_{E,T} = 10\log_{10}\left(\frac{\int_{t_1}^{t_2} p^2(t), dt}{p_0^2 T_0}\right) \tag{3.16}$$

Different frequency weighting functions (e.g., A, B, C, D, E-weightings) were applied to the waveforms [203]. Comparing these weightings is essential for evaluating metric robustness under off-design conditions, as some of those better capture the low-frequency energy content characteristic of sonic booms. The weighting functions used in this study are shown in Figure 3.9.

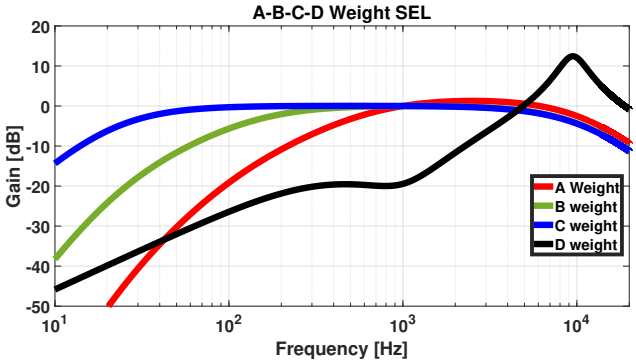

Fig. 3.9 Frequency weighting functions used for Sound Exposure Level (SEL) calculation

ISBAP

The Indoor Sonic Boom Annoyance Predictor (ISBAP) is a recent metric developed by NASA over the past decade [201]. Notably, ISBAP is designed to quantify and assess the indoor annoyance caused by sonic boom, while relying just on outdoor acoustic measurements. ISBAP metric integrates three outdoor measures of acoustic impact:

- Perceived Loudness Level (PL)
- A-weighted Sound Exposure Level (ASEL)
- C-weighted Sound Exposure Level (CSEL)

These noise metrics are weighted and combined to reflect how the indoor sonic boom is perceived in terms of annoyance. The ISBAP formulation was developed by Loubeau et al. [201] appears in Equation 3.17.

$$\text{ISBAP} = \text{PL} + 0.42\,(\text{CSEL} - \text{ASEL}) \tag{3.17}$$

The analysis uses the difference between CSEL and ASEL to quantify the impact of low-frequency content, which plays a significant role in perceived annoyance due to rattling and structure-borne transmission indoors.

3.3 Experimental test

This PhD thesis benefits from two separate experimental outdoor free-flight sonic boom test campaigns conducted as part of the MORE&LESS project. These test campaigns allow the validation of the proposed methodology for sonic boom estimation up to Mach 5. In addition, the main limitations and several recommendations for improving both the numerical modelling and the experimental setup are discussed in Chapter 5. These campaigns involved two sub-scale configurations, which were described in Sections 2.4.1 and 2.5.1. The tests were performed at the ISL proving ground in Baldersheim, located about 25 km north of Saint-Louis, France. The first campaign was conducted from October 3$^{\text{rd}}$ to 6$^{\text{th}}$, 2022, using the CS3 mock-up configuration, followed by a second campaign from November 6$^{\text{th}}$ to 9$^{\text{th}}$, 2023, which employed the CS2 mock-up. Each campaign involved a full day of setting the facility, with an additional half-day required for dismantling the equipment.

The primary objective of these experiments was to acquire a comprehensive dataset from free-flight tests to characterize the sonic boom signatures generated by novel configurations. The study also uses the resulting data to validate numerical simulation methodologies up to Mach 5 and to refine both established and novel analytical models for sonic boom prediction. In addition, the last aim of the campaign was to study experimentally the sonic boom signature and metrics at high Mach numbers. As previously discussed, conventional wind tunnel testing was deemed unsuitable for capturing pressure signatures, primarily due to practical limitations [204]. One of the primary constraints lies in the requirement for a facility large enough to capture pressure signature profiles several body lengths downstream of

the model—an objective that is unachievable within the spatial limitations of a conventional wind tunnel. The use of small-scale models mounted on supported stings presents several non-negligible challenges. Firstly, the vibrations induced by the sting can distort the pressure signature, while the support structure may disturb the flow, leading to nonphysical results. Secondly, wind tunnel pressure probes are subject to boundary layer buildup [205], which tends to blunt the steep pressure gradients associated with shock waves, leading to reduced measured discontinuities. Due to these factors, the data must be empirically corrected, which introduces extra uncertainties and can reduce the accuracy of the physical representation.

Free-flight subscaled ballistic range testing overcomes most of these limitations. In fact, by eliminating support structure interference and boundary layer effects on sensors, the free-flight approach provides more accurate and physically representative measurements. Ballistic ranges offer several practical benefits: they are relatively affordable to operate [206], allow for quick turnaround between tests, and their modular gun barrels and sabots make it easy to test different geometries without extensive re-instrumentation. However, the main drawback is the uncertainty in the manufacturing of the different projectile, which can cause unexpected dynamic behavior during free flight.

The ISL team implemented numerous safety procedures during the test to ensure the safety of all personnel involved. The protocol involved the following steps:

1. Test preparation, with cannon setup and all equipment inspection.
2. Initialization of microphones, cameras, and radars. Microphone calibration.
3. Deployment of the three stationary UAVs, if used in the selected specific test.
4. Integration of the model with the sabot package, and installation in the cannon.
5. Starting data recording.
6. Execution of the test.
7. Stopping data recording, followed by recovery of the frames and measurement of the roll angle.

3.3.1 Outdoor sonic boom measurement setup

The ISL facility in Baldersheim allows projectile free-flight testing for distances up to 1 km by employing both rifled and smooth-bore powder guns. The calibers range from 12.7 to 105.0 mm, and the flight Mach number spans from compressible subsonic flows (Mach 0.6) to hypersonic flows (Mach 6.0). Within this PhD thesis, two sub-scaled mock-up configurations were launched using a 91 mm smooth-bore powder gun. The two tests were performed under atmospheric conditions, covering flight distances of 112 m for the CS2 mock-up configuration and 210 m for the CS3 mock-up, with rectilinear trajectories and known initial Mach numbers and angles of attack. For each shot, measurements of the Mach number, angle of attack, and roll angle of the projectile characterized the flight conditions.

After the release from the smooth-bore cannon, the sabot petals of the projectile detached due to its initial velocity. The sabot petals generally separate within the first meters of the flight, and a dedicated sabot catcher wall made with wood is located between 5 to 10 meters from the launcher, as visible in Figure 3.10. The model is considered to be in undisturbed free-flight after the sabot catcher, where disturbances from the gun or sabot do not occurs anymore [207].

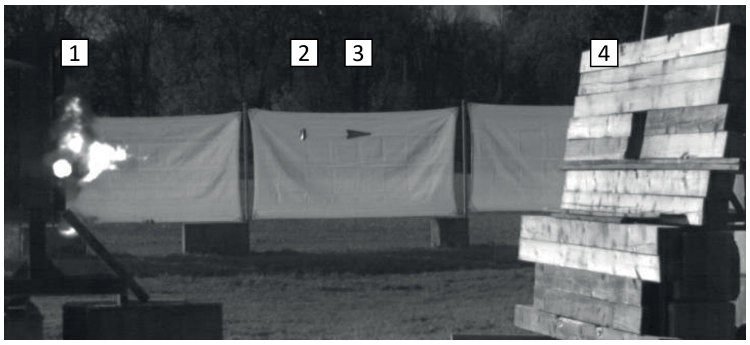

Fig. 3.10 Projectile in proximity of the sabot catcher [207]

A continuous Doppler radar operating in the X-band at 10.52 GHz measured the velocity profile and associated drag near the launcher along the trajectory. The acquired data are processed by employing a Fast Fourier Transform (FFT) analysis, with a 3D high-speed optical tracking system developed by Specialised Imaging Ltd. [208] used to record videos of the projectile from the release from the cannon until reaching the sand bay. The system employs a trajectory tracker, comprising a high-speed camera and a motorized mirror, to continuously and accurately follow

the projectile along its trajectory [209]. These complementary measurement techniques bring additional output signals which could yield to the determination of the 3D positions along the trajectory. The roll angles were explicitly evaluated using two paper frames positioned at the entrance and exit of the acoustic measurement zone—the segment of the fireline where the acoustic sensors measured the data. Figure 3.11a shows the two paper frames, and Appendix A details CIRA's procedure for computing the roll angle along the trajectory, that was necessary for the numerical validation of the experimental test. Further details of the acoustic zone for each flight test are available in Section 3.3.2 and 3.3.3.

(a) Paper frames for roll angle estimation

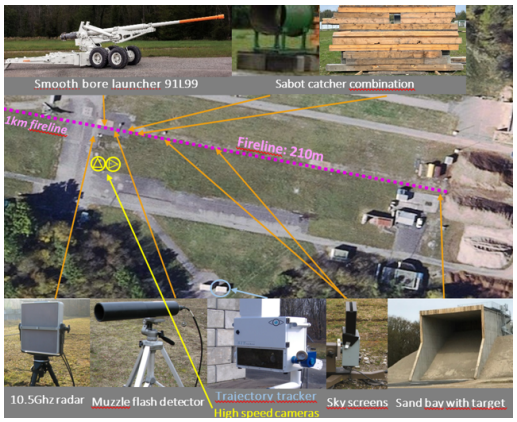

(b) Instrumentation adopted for the experimental test

Fig. 3.11 Paper frames for roll angle estimation and instrumentation adopted for the experimental test .

Besides the instrumentation already mentioned, two sky screens were installed along the firing line to regulate the scanning speed of the trajectory tracker, thereby maintaining tracking accuracy, and a muzzle flash detector was employed to initiate the experiments.

Acoustic equipment

During the two experimental test campaigns, CIRA and ISL used a variety of acoustic instruments to capture detailed pressure field measurements. Specifically, ISL deployed fifteen 1/4-inch Brüel & Kjær model 4938 microphones [210], which were mounted about 30 cm above the ground. The ISL microphones operate with a 200 V polarization voltage and have a typical sensitivity of 1.6 mV/Pa, with a

frequency response from 4 Hz to 70 kHz, making them particularly well-suited for sonic boom analysis, with a dynamic range of 172 dB. In the first campaign, the microphones were arranged along three lines located 70, 85, and 100 meters from the cannon outlet, with the five closest points of approach *CPA* placed between 5 and 30 meters. The microphone layout changed between the first and second test phases; further details can be found in Sections 3.3.2 and 3.3.3.

In addition, CIRA integrated four 1/4-inch PCB prepolarized pressure field microphones for the first test campaign and six in the second [211]. Compared to the ISL instrumentation, these microphones have a sensitivity of 0.25 mV/Pa and their frequency response spans from 4 Hz to 20 kHz, with a tolerance of ± 2 dB, and a dynamic range of 182 dB. CIRA placed its acoustic setup about 1 meter and 1 meter and a half above the ground, at distances of 5, 10, and 15 meters from the fireline. The higher position helped reduce overlapping signals and made it easier to compare acoustic signatures at different roll angles for both configurations tested. In contrast, ISL set its microphones closer to the ground to reduce interference between direct and reflected acoustic signals and to capture the direct sonic boom signal with high fidelity. This difference is altitude location allows cross-validation of sonic boom results as a function of roll angles.

In addition to the fifteen previously described microphones, to have a three-dimensional measurement of the shock wave propagation, the ISL's team deployed three unmanned aerial vehicles (UAVs), each equipped with onboard acoustic instruments and maintaining stationary flight. During each flight, the three drones have been set in stationary flight above the position of the microphones deployed on the field, perpendicularly to the shooting line, at heights varying from 10 to 50m depending on the drone and the recorded shot. In the second experimental test campaign, drone usage was limited to a single test. Each UAV is equipped with a Real-Time Kinematic GPS, ensuring positional accuracy of about 10 cm. Each drone was equipped with an RTK-GPS (Real-Time Kinematic Global Positioning System), providing position estimates with a maximal error on the order of 10 cm at a sampling rate of 5 Hz. The drones also carried a Roland R-07 data recorder and a Sennheiser KE4-211-9 electret microphone, capable of measuring peak pressures above 160 dB without distortion. The microphone sensitivity is approximately 0.3 mV/Pa. Data acquisition was manually triggered on each of the three drones. To synchronize the recordings, a transient acoustic signal was generated 2 m from the three drones positioned on the ground. This transient event was subsequently used

to align the time histories from the individual measurements. The aerial recording platforms consisted of two DJI Phantom 3 Pro drones and one DJI Phantom 4 Pro, and their microphones are referred to as P3O3, P3OASyS, and P4, respectively. As part of the safety protocol, each drone had to maintain a stable hover at its assigned position before the projectile was transferred from storage to the launch platform. A representation of the position of the drones is visible in Figure 3.12.

Fig. 3.12 Microdrones position

The TEAC Corp. data recorder captured data from the ground-based ISL equipment, operating via a personal computer at a sampling frequency of 192 kHz. The beginning and the ending of the acquisition of the signals was performed manually during the countdown process of the recorded shot, and once the shot was triggered. At the same time, CIRA microphones were collected by an eight-channel real-time sound level integrator and analyzed from IMC Corp., at a sampling rate of 51.2 kHz per channel [209].

3.3.2 Test campaign 1: setup and environmental conditions

In October 2022, ISL carried out its first outdoor free-flight sonic boom test at the open range facility in Baldersheim, France. The first campaign employed the CS3 mock-up configuration described in Section 2.5.1, derived from the CS3 configuration (Section 2.5) and STRATOFLY [6]. The experimental test was organized by ISL, CIRA, and Politecnico di Torino, with approximately fifteen people participating

in the tests. Figure 3.13 provides a snapshot of the group who took part in the campaign.

Fig. 3.13 Personnel involved in the first test campaign

To properly ensure reliable and comprehensive data collection for post-processing analysis, a structured test matrix has been employed. This approach enables a complete characterization of the aircraft's behavior, considering both horizontal and vertical flight. The test matrix included five different shots, completed over two consecutive days:

- Three vertical launches performed on October 4th, with the model's wings oriented perpendicular to the ground (Subfigure 3.14b).
- Two horizontal launches performed on October 5th, with the wings aligned parallel to the ground (Subfigure 3.14a).

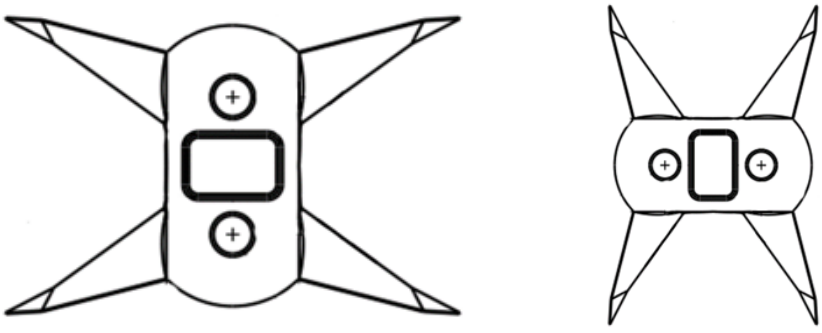

(a) Horizontal shot CS3 mock-up (b) Vertical shot CS3 mock-up

Fig. 3.14 Horizontal and vertical shot CS3 mock-up

Table 3.1 summarizes the key data recorded for each shot during the test campaign using ISL's atmospheric equipment, positioned just behind the cannon. These parameters—initial projectile velocity, speed of sound, atmospheric pressure, temperature, and relative humidity—are essential for accurately estimating and interpreting the sonic boom pressure signatures recorded by the microphones. By understanding how these conditions interact, it is possible contextualize the test results within the atmospheric environment at the time and use this information to set up and validate numerical simulations.

Table 3.1 Test matrix for the first experimental campaign

Shot	Speed [m/s]	Mach	Pressure [hPa]	Temperature [°C]	Humidity [%]
1	1616	4.70	995.4	19	69
2	1617	4.70	995.2	20	59
3	1605	4.68	995.7	14	89
4	1609	4.69	995.2	18	72
5	1612	4.70	994.9	23	51

The ground instrumentation for the first test campaign included a distribution of an array of microphones, provided by both ISL and CIRA, as stated in Section 3.3.1. The layout of the acoustic sensor for the first test campaign is visible in Figure 3.15. The naming convention identifies ISL devices as *Mic* and CIRA instrumentation as *Ch*, while it omits the positions of the three UAVs.

Fig. 3.15 Microphones layout for the CS3 mock-up test campaign [207]

The projectile free-flight distance from the end of the cannon to the sand bay area is approximately 210 meters with a rectilinear trajectory, with an initial Mach number of around 4.70. Due to the symmetric wing design adopted, the configuration achieved a near-zero lift coefficient at exit angle of attack (around 0°), contributing to a stable and predictable free-flight trajectory. Beyond the primary technical goals, the first test campaign also helped to understand better how to conduct the measurements in practice. It offered a chance to test the whole experimental setup, from data acquisition to instrumentation handling, laying the groundwork for the second test campaign. This campaign also created a reference dataset under controlled launch conditions and offered important insights into how wing orientation affects the sonic boom signature. The data collected form a crucial basis for validating numerical prediction models and for guiding future experiments. An overview of the instrumentation adopted in the first test campaign is visible in Figure 3.16.

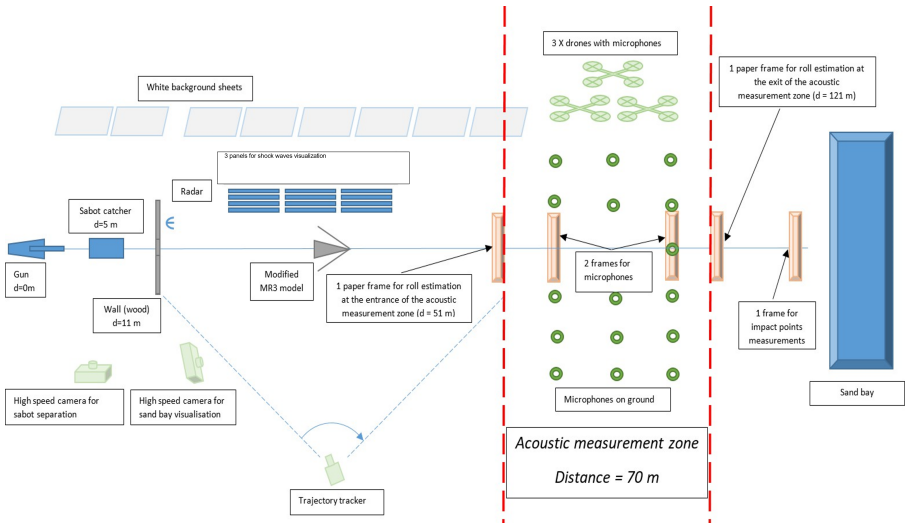

Fig. 3.16 Setup first test campaign

To validate the numerical results against the experimental data, it is necessary to compute the geometric distance between the acoustic equipment and the projectile for each shot. In this PhD thesis, this distance is referred to as the closest point of approach (CPA), defined as the minimum distance between the firing line and the acoustic equipment. The assumption of a constant CPA is considered acceptable across all shots, even though small variations in the projectile trajectory may occur due to wind gusts or manufacturing tolerances. These variations are estimated to be no more than a few centimetres and do not affect the quality of the results. In order to assess and validate the experimental results against the numerical simulations performed with both ANSYS Fluent and SU2 for the CS3 mock-up case study, it was necessary to determine closest point of approach. The CPA distance for the ground-based microphones remained constant across all test shots. Table 3.2 lists the closest Point of Approach values for each test, distinguishing between the acoustic equipment deployed by ISL (Subtable 3.2a) and the one used by CIRA (Subtable 3.2b).

Table 3.2 CPA microphones

(a) ISL microphones

Microphone	CPA[m]
Mic1	14.7
Mic2	4.9
Mic3	10.4
Mic4	20.3
Mic5	30.3
Mic6	14.8
Mic7	5.0
Mic8	10.3
Mic9	20.4
Mic10	30.2
Mic11	15.0
Mic12	5.0
Mic13	10.2
Mic14	20.1
Mic15	30.1

(b) CIRA microphones

Microphone	CPA[m]
Ch1	5.4
Ch2	10.1
Ch3	4.2
Ch4	9.9

The locations of the ISL and CIRA measurement systems are summarised in Table 3.3. Subtable 3.3a reports the latitude, longitude, and altitude of the ISL instrumentation, whereas Subtable 3.3b presents the corresponding information for the CIRA instrumentation. However, to enable accurate investigation of sonic boom data, GPS coordinates are used to accurately estimate perpendicular distances from the trajectory to the probes and parallel distances from the probes to the cannon outlet. To achieve a good level of accuracy, the haversine formula was chosen to determine the great-circle distance between two points on a sphere, given their longitudes and latitudes. Both parallel and perpendicular distances, are then evaluated using the cosine formula.

Table 3.3 Position of the ground sensor

(a) ISL's instrumentation

Mic.	Lat. [°]	Long. [°]	h [m]
#1	47.81914	7.43332	281.6
#2	47.81913	7.43345	281.7
#3	47.81910	7.43364	281.9
#4	47.81909	7.43378	281.9
#5	47.81907	7.43391	281.9
#6	47.81894	7.43387	281.9
#7	47.81895	7.43374	281.8
#8	47.81897	7.43361	281.8
#9	47.81899	7.43341	281.8
#10	47.81901	7.43328	281.6
#11	47.81888	7.43324	281.6
#12	47.81886	7.43337	281.8
#13	47.81884	7.43357	281.9
#14	47.81882	7.43370	281.9
#15	47.81880	7.43383	281.9

(b) CIRA's instrumentation

Ch.	Lat. [°]	Long. [°]	h [m]
#1	47.81904	7.43356	282.5
#2	47.81903	7.43362	282.5
#3	47.81894	7.43340	282.4
#4	47.81895	7.43333	282.3

Similarly, the position of the three UAVs is displayed in Table 3.4, in which latitude, longitude and elevation are represented for each microphone and shot.

Table 3.4 Position of UAVs

(a) P3O3

Shot	Lat. [°]	Long. [°]	h [m]
# 1	47.81911	7.43371	22.6
# 2	47.81909	7.43348	33.6
# 3	47.81902	7.43346	29
# 4	47.81900	7.43314	15.3
# 5	47.81908	7.43312	26

(b) P4

Shot	Lat. [°]	Long. [°]	h [m]
#1	47.81893	7.43402	8.1
#2	47.81895	7.43390	26.2
#3	47.81891	7.43344	19.5
#4	47.81897	7.43339	20.4
#5	47.81902	7.43337	43.2

(c) P3OASyS

Shot	Lat. [°]	Long. [°]	h [m]
#1	47.81883	7.43381	30.2
#2	47.81889	7.43407	24.8
#3	47.81910	7.43357	26.2
#4	47.81914	7.43343	21
#5	47.81928	7.43409	0.5

Numerical grid and boundary conditions

Due to the reduced dimensions of the CS3 mock-up projectile, particular care must be taken when modeling the aircraft. The mesh definition, in terms of refinement and adaptation strategy, requires specific effort to properly capture discontinuities. The reduced radius of curvature necessitates careful grid generation, especially in regions such as the wing section and the aircraft nose, where finer meshing is needed. Compared with other case studies, the grid contains a higher number of elements, and the vertical domain length is set to 5.5 body lengths. The increased vertical length is necessary for the application of the Whitham formulation in experimental test comparisons, which requires a fully developed N-wave, and for the inverse flight estimation problem discussed in Section 3.3.4. A sketch of the numerical grid employed is shown in Figure 3.17.

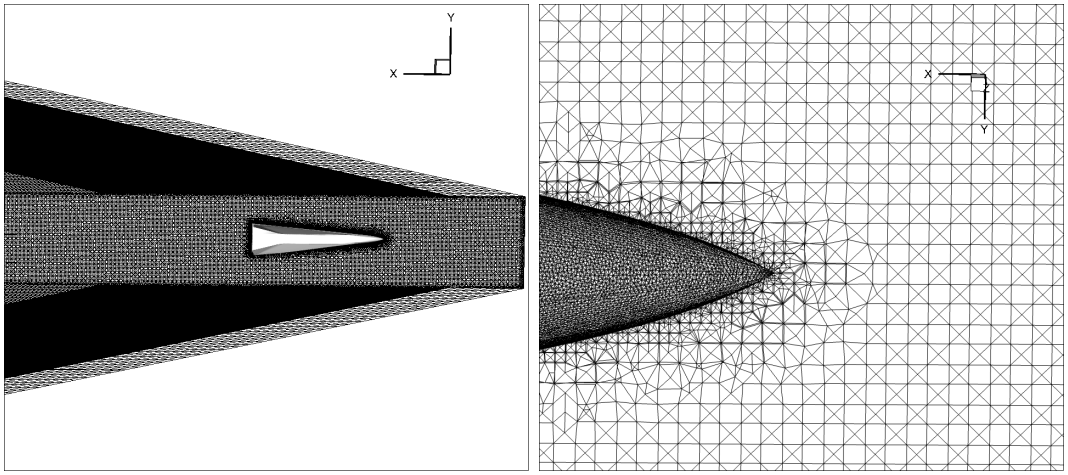

(a) CS3 mock-up structured-unstructured grid (b) CS3 mock-up nose mesh detail

Fig. 3.17 Details of the numerical grid CS3 mock-up projectile

3.3.3 Test campaign 2: setup and environmental conditions

The second outdoor free-flight test campaign took place in November 2023 at the same location in the Baldersheim open range facility. The collaboration again involved ISL, CIRA, and Politecnico di Torino. The second campaign focused on the CS2 mock-up configuration (Section 2.4.1), and the test matrix for this configuration was designed as:

- Two shots, made on Tuesday the 7^{th} of November
- Two shots, made on Wednesday the 8^{th} of November

In contrast to the first experimental campaign, the second one featured exclusively horizontal shots, dictated by the projectile's aerodynamic shape. Table 3.5 highlights the test matrix used in the experimental campaign, detailing the atmospheric parameters recorded for each shot. These parameters were essential for accurately estimating the sonic boom pressure signatures captured by the microphones.

Table 3.5 Test matrix CS2 mock-up performance experimental campaigns

Shot	V_0 [m/s]	M_0	V_{impact}	M_{impact}	Acc (G)	P_{max} (bar)	P_{muzzle}(bar)
#1	1577	4.67	1540	4.56	35870	1100	89
#2	1587	4.70	1549	4.58	36000	1100	90
#3	1590	4.72	1553	4.61	35580	1092	95
#4	1592	4.72	1543	4.57	36630	1120	95

For the CS2 test campaign, CIRA employed two additional microphones, with a total of six ground recorders. In addition, a Head and Shoulder Unit (HSU) artificial head was integrated into the CIRA setup to improve the acoustic data acquisition capabilities [212]. ISL for the second campaign deployed the same number of microphones, and two drone-supported microphones. Table 3.6 summarizes the atmospheric conditions recorded during the two days of testing.

Table 3.6 Test matrix atmospheric conditions CS2 mock-up

Shot	Temperature [° C]	Humidity [%]	Pression [hPa]
#1	10	82	989.5
#2	10	83	989.6
#3	8	86	990.3
#4	9	87	994.1

The fireline in this campaign was notably shorter compared to the previous campaign, mainly because of the configuration's aerodynamic shape. The lift distribution in the design leads to a fireline distance of about 100 meters. Unlike the previous configuration, the CS2 mock-up does not have a near-zero lift coefficient at the cannon exit, due to its wing shape and tail fin design. Table 3.7 shows the simulated altitude gain at different fireline distances as a function of Mach number.

Table 3.7 CS2 mock-up fireline analysis

Mach	C_{N_a}	Lift [N]	Z_c(m) @50m	Z_c(m) @100m	Z_c(m) @250m
4	32.1	169.9	0.2	0.9	5.7
5	28.7	238.0	0.2	0.8	5.1

Figure 3.18 shows the flight path of the CS2 mock-up. The nominal path represents the desired trajectory, while the deviated path accounts for the influence of lift.

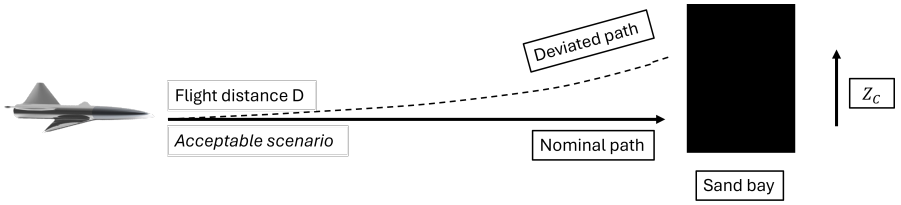

Fig. 3.18 CS2 safety acceptable flight path

The fireline for the second test campaign is little above 112 meters, with the two paper frames employed for the roll angle estimation based at 36.7 and 112.0 meters from the gun muzzle.

With the help of CIRA personnel, the position of their microphones and artificial head were precisely documented to enable a direction comparison between numerical simulations and experimental results. Table 3.8 highlights the coordinates of the acoustic equipment deployed by CIRA.

Table 3.8 CIRA acoustic equipment second test campaign

	x[m]	y [m]	z[m]
Ch 1	56.72	6.66	1.50
Ch 2	56.32	11.41	1.50
Ch 3	56.05	16.61	1.50
Ch 4	66.75	7.35	1.50
Ch 5	66.67	12.05	1.50
Ch 6	76.41	7.54	1.50
HSU, test 1-3	49.98	63.20	1.50
HSU, test 4	46.26	53.04	2.40

The position of the acoustic equipment deployed by CIRA is visible in Figure 3.19a. As in the previous test campaign, CIRA placed the microphones at altitude of 1.5 meter above the ground, while ISL deployed his instrumentation at roughly 0.30 meters to minimize the influence of ground reflections and better isolate the direct sonic boom signal. Figure 3.19 highlights the position of the acoustic equipment for both CIRA and ISL.

(a) CIRA acoustic equipment position

(b) ISL acoustic equipment position

Fig. 3.19 CIRA & ISL acoustic equipment position

3.3.4 Inverse estimation of the flight dynamics

This PhD thesis includes a collaboration with ISL to investigate the inverse estimation of the flight dynamics of projectiles, in particular for the CS3 mock-up configuration. Inverse problems—long studied in acoustics—pose significant challenges, even in the case of stationary sources [213–215]. Accurately estimating the trajectory and velocity of supersonic bodies from their shock wave signatures continues to be a key research area in military acoustics [216]. While the forward problem of shock wave emission by supersonic bodies has been thoroughly explored in both aerospace and acoustical literature [217, 218], the inverse problem—particularly for non-axisymmetric geometries—remains relatively underexplored when the wave nature of the pressure field is preserved. This approach is especially relevant in applications where the spatio-temporal evolution of the pressure field, including amplitude variations, can reveal meaningful information of the source. Previous studies have shown that the inverse problem can be rendered tractable by linearizing the governing equations of shock wave propagation. In particular, Whitham [94, 217] demonstrated that the shock strength depends only weakly on the Mach number, scaling as $(M^2-1)^{1/8}$. In typical inverse estimation scenarios involving supersonic projectiles, the shock propagation distances to the sensors are on the order of 50 meters or less, thus justifying the neglect of thermoviscous losses. In this thesis, the acoustic field beyond a bounded nonlinear domain is extrapolated using an adjoint Green's function formulation with equivalent time-harmonic sources. The

methodology enables an amplitude-based inverse estimation of the projectile's flight dynamics, relying on linearized wave propagation models and precomputed pressure fields obtained from Euler CFD simulations on a cylindrical surface of radius five times the projectile's characteristic length.

The proposed inverse estimation framework is validated using experimental data from free-flight tests. Reconstructed flight parameters are quantitatively compared with ground-measurements obtained through RADAR tracking, high-speed imaging, and terminal impact analysis.

Problem statement

Lighthill demonstrated that the equations governing fluid motion with fluctuating stresses can be reformulated to resemble wave equations in a stationary, homogeneous medium [219]. Ffowcs, Williams and Hawkings (FWH) extended the approach to describe the acoustic field generated by moving bodies, including those traveling at supersonic speeds [220]. Their reformulation of the mass and momentum conservation laws leads to Equation 3.18:

$$\frac{\partial \rho}{\partial t} + \frac{\partial (\rho u_i)}{\partial x_i} = \rho_0 v_i \delta(g) \frac{\partial g}{\partial x_i}, \quad \frac{\partial (\rho u_i)}{\partial t} + \frac{\partial (\rho u_i u_j + p_{ij})}{\partial x_j} = p_{ij} \delta(g) \frac{\partial g}{\partial x_i}. \quad (3.18)$$

By eliminating the momentum term ρu_i, these can be rearranged into an inhomogeneous wave equation:

$$\Box(\rho - \rho_0) = \frac{\partial^2 T_{ij}}{\partial x_i \partial x_j} - \frac{\partial}{\partial x_i}\left(p_{ij}\delta(g)\frac{\partial g}{\partial x_j}\right) + \frac{\partial}{\partial t}\left(\rho_0 v_i \delta(g)\frac{\partial g}{\partial x_i}\right), \quad (3.19)$$

where $\Box$ is the d'Alembert operator, δ is the Dirac delta distribution, and T_{ij} is the stress-energy tensor. The operator is defined as:

$$\Box = \left(\frac{\partial^2}{\partial x_i^2} - \frac{1}{c^2}\frac{\partial^2}{\partial t^2}\right), \quad (3.20)$$

with the stress tensor components given by:

$$T_{ij} = \rho u_i u_j + p_{ij} - c^2 \rho \delta_{ij}, \quad p_{ij} = p\delta_{ij} + \mu_a \left(-\frac{\partial u_i}{\partial x_j} - \frac{\partial u_j}{\partial x_i} + \frac{2}{3} \left(\frac{\partial u_k}{\partial x_k} \right) \delta_{ij} \right). \tag{3.21}$$

The Ffowcs Williams and Hawkings (FWH) analogy is also valid for the pressure wave field and has been involved in aeroacoustic study, especially in the context of rotating blades [221, 222]. While Ospel and Graziani present a more rigorous mathematical treatment in [223], the analogy is powerful in the sense that it posits aerodynamic noise to be modeled as the pressure field emitted by an equivalent distribution of acoustic multipole moments. In this context, the retarded Green's function defines the simplest multipole—the monopole—and characterizes its source through Equation 3.22:

$$G(x,y,t) = \frac{1}{4\pi|x-y|} \delta \left(t - \frac{|x-y|}{c} \right), \tag{3.22}$$

Which satisfies the inhomogeneous wave equation for a point source located at y emitting at time t. While this formulation provides accurate representations in the far-field, estimating the time-dependent source strengths of multipoles may introduce errors in the near-field, especially due to nonlinear interactions and overlapping shock fronts close to the projectile.

Flight dynamic estimation

A conventional method for solving the inverse supersonic flight problems is the estimation of the velocity and position of the projectile by employing the Time Difference of Arrival (TDOA) of the shock waves recorded by a microphone array. These TDOAs are typically computed by using the shock fronts of the N-waves, and due to the projectile's unsymmetrical rotation, the question arises as to whether the method is still suitable. The result section highlights that the highest time differences introduced by the roll angle of the projectile are around $2 \cdot 10^{-5} s$. Considering the adopted sampling frequency of 192 kHz, which results in a sample duration of $5.2 \cdot 10^{-6}$ s, the roll angle orientation leads to a time difference of one to four samples, which corresponds to a positioning error of around 7 mm. It is possible to conclude that the solely usage of TDOAs of the shock fronts is sufficient for

the position, velocity and trajectory computation, but may unsuitable for the roll angle estimation. It was decided to adopt a two-step approach: initially, the problem of trajectory and velocity estimation of the supersonic body is solved by TDOAs. Subsequently, once the trajectory and velocity are established, the roll angle was estimated based on the space-time boundary condition computed with computational fluid dynamics.

Acoustic trajectory and velocity estimation

The trajectory of the projectile was assumed to be a straight line in the acoustic measurement zone. Because the Mach cone angle—and consequently the shock front's time of arrival—depends on the projectile's velocity, and the trajectory vector also influences arrival times, it is necessary to estimate both velocity and trajectory simultaneously.

The simulated time of arrival t_s^{sim} of the N-wave at a sensor is defined as the sum of the time t_s^v the projectile travels from its initial position $x_0 \in \mathbb{R}^3$ to the shock detachment point $x_1 \in \mathbb{R}^3$, and the time t_s^c the shock wave to propagate from x_1 to the sensor location $x_s \in \mathbb{R}^3$. This relationship is given by Equation 3.23:

$$t_s^{\text{sim}} = t_s^v + t_s^c = \frac{||x_1 - x_0||}{v_0 - v_1} \log \frac{v_0}{v_1} + \frac{||x_s - x_1||}{c} \tag{3.23}$$

where c is the speed of sound, assumed to be constant in time and space, and $v_0, v_1 \in \mathbb{R}$ are the unknown velocities. The detachment point x_1 can be computed by parameterizing the trajectory as visible in Equation 3.24:

$$\begin{aligned} \mathbf{L}(\varepsilon) &= \mathbf{x}_0 + \varepsilon \mathbf{d} \\ \mu_2 &= \frac{\pi}{2} - \mu \\ \cos(\mu_2) &= \frac{(\mathbf{L}(\varepsilon) - \mathbf{x}_0) \cdot \mathbf{d}}{\|\mathbf{L}(\varepsilon) - \mathbf{x}_0\| \, \|\mathbf{d}\|} \end{aligned} \tag{3.24}$$

Assuming the launch point $\mathbf{x}_0$ lies at the origin, after rearranging, the scalar trajectory parameter ε can be determined analytically as:

$$
\begin{aligned}
E &= \|\mathbf{d}\|^2(\cos^2\mu_2 - 1) \\
F &= 2(\mathbf{x_s}\cdot\mathbf{d})(1-\cos^2\mu_2) \\
H &= \cos^2\mu_2\|\mathbf{x_s}\|^2 - \frac{(\mathbf{x_s}\cdot\mathbf{d})^2}{\|\mathbf{d}\|^2} \\
\varepsilon &= \frac{-F \pm \sqrt{F^2 - 4EH}}{2E}
\end{aligned}
\tag{3.25}
$$

Care must be taken when interpreting the solution due to the space-time cone spanned by the Mach angle μ in the direction of the trajectory starting at the launch point, as shown in Figure 3.20. The solution of the time of arrival propagation equations is plotted for a projectile launched at the origin moving at a speed of 1030 m/s along the x-axis. The magenta line in Figure 3.20 mark the surface of the causality cone, in which the right side shows the causal solution and the top and the bottom left side shows the acausal solution.

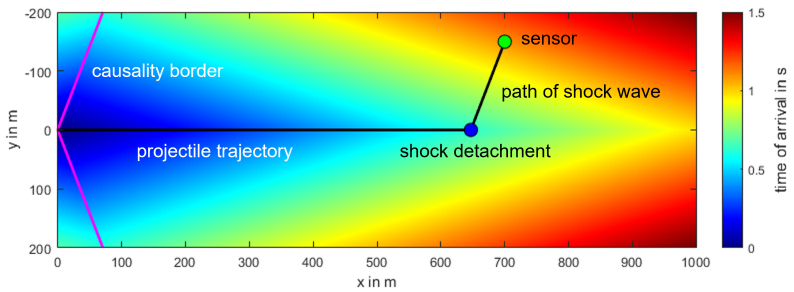

Fig. 3.20 Time of arrival of the ballistic shock wave for a supersonic body along the x-axis with causality borders

Due to the dependence of the Mach angle μ on the time-dependent velocity, a finite difference scheme for given $v = [v_0, v_{end}]^T \in \mathbb{R}^2$ where v_{end} is the projectile velocity at 122 meters, was employed to compute the forward time of the time of arrival TOA. To estimate the trajectory and velocity from the time difference of arrival (TDOA) measurements, the minimization problem shown in Equation 3.26 was formulated and solved for the unknown vectors $\mathbf{v}$ and $\mathbf{d}$.

$$\begin{aligned}
&\min_{\mathbf{v},\mathbf{d}} \left\| \mathbf{t}_{\text{tdoa}}^{\text{exp}} - \mathbf{t}_{\text{tdoa}}^{\text{sim}} \right\|_q \\
&= \min_{\mathbf{v},\mathbf{d}} \left\| \begin{bmatrix} t_1^{\text{exp}} \\ t_2^{\text{exp}} \\ \vdots \\ t_N^{\text{exp}} \end{bmatrix} - \min(\mathbf{t}^{\text{exp}})\mathbf{1} - \left(\begin{bmatrix} t_1^{\text{sim}} \\ t_2^{\text{sim}} \\ \vdots \\ t_N^{\text{sim}} \end{bmatrix} - \min(\mathbf{t}^{\text{sim}})\mathbf{1} \right) \right\|_q
\end{aligned} \tag{3.26}$$

Here, t_s^{exp} denotes the experimentally measured time of arrival of the shock at sensor s measured in the experiment. Due to the nonlinear nature of the problem and the nonconvex shape of the cost function, a reasonable initial guess is fundamental for the solver to converge properly. In this work, the Nelder-Mead algorithm [224] was used, with initial guesses $\mathbf{v} = [1600, 1500]^T$ m/s and $\mathbf{d} = [0, 1, 0]$.

Acoustic roll angle estimation

The time delay and amplitude decay of the emitted shock wave is modeled using equivalent acoustic multipole moments such as the retarded Green's function of the d'Alembertian shown in Equation 3.22. The geometry of the acoustic multipole simulation is highlighted in Figure 3.21, in which Subfigure Figure 3.21a shows a sketch of the original multipole solution and Subfigure Figure 3.21b the equivalent source approximation used in this work.

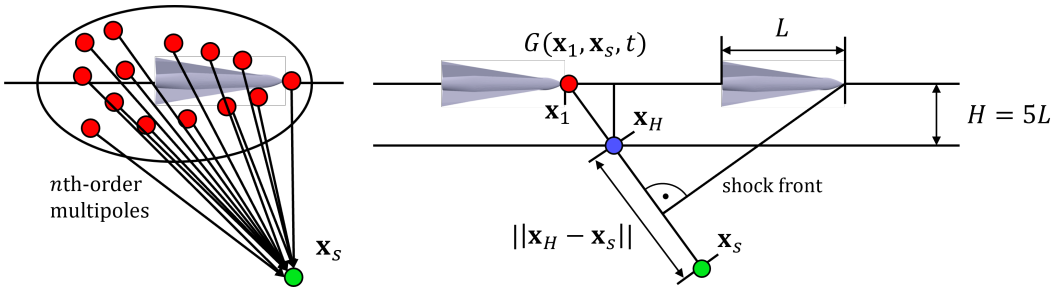

(a) Original multipole solution (b) Equivalent source approximation

Fig. 3.21 Computation of the pressure wave propagation in the far field

The method uses collective sources inherent to the fast multipole method [225], in which the n^{th}-order multipole solution of the FWH equation is substituted given

collective sources positioned along the line of the trajectory. This assumption is valid considering that the propagation distance greatly exceeds the body length of the projectile. Assuming that the shock wave propagates at a constant speed outside the nonlinear domain, and that the sound velocity remains uniform in space and time, the shock front forms a constant-phase surface governed by the Eikonal equation.

$$(\nabla\Phi)^2 = \frac{1}{c^2}$$

The propagation is modeled as normal acoustic rays with respect of the shock front, with an angle described as:

$$\mu_2 = \frac{\pi}{2} - \sin^{-1}\left(\frac{1}{M}\right)$$

Rays are defined originating from the shock detachment point x_1, which represents the location of the equivalent point source along the trajectory. The blue point marks the intersection at H/L=5 cylinder for which the pressure time source terms were determined with computational fluid dynamics. The green point is the evaluation point in the field, respectively the pressure sensor and end of the ray. Within the linear domain, the acoustic response can be approximated by integrating multipole sources distributed along the trajectory. Because the strength of the shock depends on the azimuthal angle, it is necessary to account for the angular variation in the linearized shock wave emission function. The pressure field in the linear domain can be expressed as Equation 3.27:

$$p(x,t) = \int_0^t \int_0^L \frac{f(\mathbf{y},\tau,\phi)}{4\pi||x-y||}\delta\left(t-\tau-\frac{|\mathbf{x}-\mathbf{y}|}{c}\right)\mathrm{d}l\mathrm{d}\tau \tag{3.27}$$

In which $y \in$ L. However, due to the normal ray assumption, the integral collapses, since the source function is to be emitted by a corresponding equivalent shock detachment point on the trajectory, which results in Equation 3.28:

$$p(\mathbf{x_s},t) = \int_0^t \frac{f(\mathbf{x_1},\mathbf{x_H},\tau)}{4\pi\,|\mathbf{x_s}-\mathbf{x_1}|}\delta\left(t-\tau-\frac{|\mathbf{x_1}-\mathbf{x_s}|}{c}\right)d\tau \tag{3.28}$$

Here, $f(\mathbf{x_1},\mathbf{x_H},\tau)$ is the CFD-derived shock wave source term. To estimate the roll angle ϕ, having known the pressure values from the sensor array, one approach

involves comparing the simulated and experimental differences in the amplitude of the shock fronts at the sensor positions. The comparison is highlighted in Equation 3.29.

$$\min_{\phi} \left\| \mathbf{p}^{\text{exp}}_{\text{adoa}} - \mathbf{p}^{\text{exp}}_{\text{sim}} \right\|_q = \min_{\phi} \left\| \frac{\mathbf{p}^{\text{exp}}}{\max(\mathbf{p}^{\text{exp}})} - \frac{\mathbf{p}^{\text{sim}}}{\max(\mathbf{p}^{\text{sim}})} \right\|_q \tag{3.29}$$

Where p_s^{sim} is the simulated magnitude of the shock front computed with Equation 3.28 at the sth sensor, and p_s^{exp} is the experimentally determined magnitude of the shock front at the sth sensor. However, including the temporal evolution of the shock wave introduces the challenge of comparing pairs of transient time functions representing short-term dynamic events. A suitable way to resolve this problem is the Wasserstein distance W_s^q [226], even if not renowned in acoustics. The temporal and amplitude differences of a shock pair can be quantified as:

$$W_s^q(\mathbf{p}_s^{\text{sim}} - \mathbf{p}_s^{\text{exp}}) = \left(\min_{\varpi \in \Pi(\mathbf{p}_s^{\text{sim}}, \mathbf{p}_s^{\text{exp}})} \sum_{i,j} d(\mathbf{p}_s^{\text{sim}}[i], \mathbf{p}_s^{\text{exp}}[j])^q \varpi_{ij} \right)^{\frac{1}{q}}, \tag{3.30}$$

Where $W_s^q(\mathbf{p}_s^{\text{sim}} - \mathbf{p}_s^{\text{exp}})$ is the qth Wasserstein distance of the two shocks, $d(\mathbf{p}_s^{\text{sim}}[i], \mathbf{p}_s^{\text{exp}}[j])$ is the distance of the ith and jth pressure samples in the underlying space, $\Pi(\mathbf{p}_s^{\text{sim}}, \mathbf{p}_s^{\text{exp}})$ is the set of joint distributions ϖ of the N-wave shocks of the s-th sensor and ϖ_{ij} is the magnitude transported from sample $\mathbf{p}_s^{\text{sim}}[i]$ to sample $\mathbf{p}_s^{\text{exp}}[j]$.

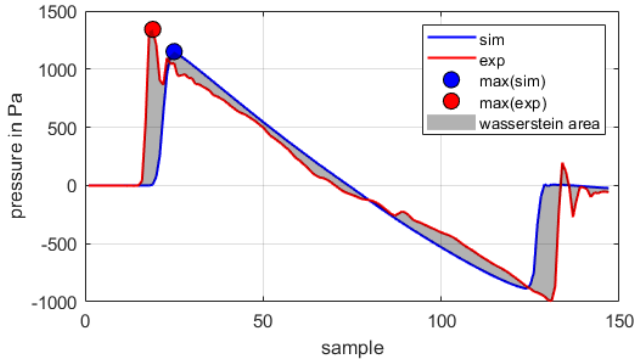

Fig. 3.22 Illustration of the shock front and Wasserstein distance based cost function basis

Figure 3.22 shows the two cost functions used for the determination of the inverse problem for a given N-wave shock pair. The blue marked results are those related

to the numerical simulations, while the red one are related to the experimentally determined shock front.
The roll angle estimation, based on the Wasserstein distance, corresponds to the minimum of all potential transport planes between the two N-wave shocks, and captures the temporal evolution of the pressure. Defined the overall fitness of the estimated roll angle by summing the Wasserstein distances across all pairs of experimental and simulated shock waves for the given sensor array to minimize Equation 3.31.

$$\min_{\phi} \sum_{s=1}^{N} W_s^q \left(\mathbf{p}_s^{\text{sim}}, \mathbf{p}_s^{\text{exp}} \right) \tag{3.31}$$

3.4 Sonic boom preliminary estimation methodologies and tools

Evaluating the sonic boom impact in the early phases of aircraft design is far from straightforward. At this stage, only limited data are usually available, while high-fidelity numerical simulations—although reliable—remain too computationally costly to be used. Designers, however, need to explore a wide portion of the design space quickly, which calls for methods that trade some accuracy for efficiency. For this reason, valuable effort has been directed toward the development of simplified prediction tools that can generate ground-level signatures with acceptable precision at a fraction of the cost. These tools are typically derived from higher-fidelity simulations of representative configurations, which are then reduced to simplified models or empirical correlations. It should be noted that these results, as an initial approximation, are primarily based on the maximum peak overpressure and do not rely on acoustic or noise metrics. By integrating such models into the conceptual design process, it becomes possible to evaluate potential environmental impacts and assess regulatory compliance at an earlier stage of development.

3.4.1 ESATTO Framework

The aim of the MORE&LESS project, within which this PhD research has been conducted, is to provide the scientific community with an integrated, multidisciplinary framework composed of validated and widely accepted tools for the holistic

assessment of the environmental impact of future supersonic aircraft within the global air navigation system. ESATTO, the holistic multidisciplinary framework developed as the main outcome of the project, is structured based on the different work package results and the tools developed within it.

The ESATTO Framework integrates multiple specialized modules into a cohesive process for the design and assessment of environmentally sustainable supersonic aircraft.

3.4.2 ESATTO Framework modules

ASTRID-H 2.0

Astrid-H 2.0 is the first tool to be launched during a run of the ESATTO Framework, and it is a proprietary tool of the research group. The version of the software implemented within the Framework requires three input files in .yaml format:

- The Configuration file (Config.yaml), which defines the case study by specifying the type of fuel (Biofuel/Hydrogen) and the type of engine (Turbofan/Turbojet)
- The file containing the High-Level Inputs for the Biofuel-powered aircraft (HLInputs_Mach2_Biofuel.yaml)
- The file containing the High-Level Inputs for the Hydrogen-powered aircraft (HLInputs_Mach2_lH2.yaml)

The tool will take approximately one minute to complete the preliminary design of the case study. Four main outputs are generated and displayed:

- The list of the main geometric and weight variables representing the preliminary design of the selected aircraft
- The low-fidelity estimation of emissions for each mission segment
- The propulsive database used for the mission
- The clean aerodynamic database used for the mission

The latest version, ASTRID-H 2.0 consists of three distinct layers. The first layer uses high-level requirements and statistical data to perform the initial sizing and guides the iteration process based on low-fidelity algorithms. At the same time, the Matching Chart tool [110, 113] is used to estimate thrust-to-weight and wing-loading ratios, taking into account both performance and environmental requirements. Including environmental constraints ensures that candidate designs remain feasible with future environmental standards within the ESATTO framework. A dedicated sonic boom equation for the Matching Chart is presented in Section 3.4.3. The second layer refines these results using surrogate aerodynamic and propulsive models derived from high-fidelity numerical analyses and experimental data. These models offer greater accuracy than conventional analytical formulations found in the literature, while maintaining low computational demands. The third and last layer, the Mission Concept Validation, is carried out using the ASTOS simulation tool [227], which is employed to validate the mission profile. Since ASTRID-H 2.0 is intended to support the conceptual design of a broad range of aircraft, the framework incorporates a degree of flexibility. For speeds between Mach 1.5 and Mach 4, a conventional wing and fuselage configuration is used, while at higher Mach numbers, a waverider layout is adopted. Regarding propulsion, a turbojet or turbofan architecture is applied from Mach 1.5 to Mach 3, whereas combined-cycle engines are selected for higher-speed regimes. A sketch of the three layers of ASTRID-H 2.0 is highlighted in Figure 3.23.

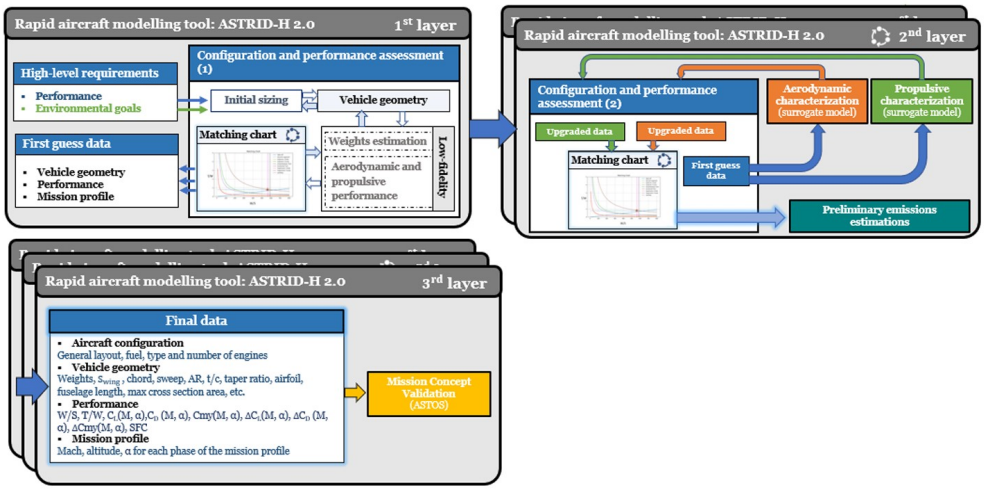

Fig. 3.23 Subdivision of the three layers in ASTRID-H 2.0

Pollutants and GHGs Emissions Module

The Emission Module operationalizes the multi-tier combustion and emission-estimation methodology. The proposed multi-layer modeling framework integrates multiple chemical-kinetic simulation strategies to capture the complex dynamics of combustion under varying operational conditions. All modeling approaches are implemented within a single simulation environment, Cantera [228], which is employed to simulate the combustion phenomena. Upon selection of the case study and the corresponding propulsive database, the module performs the emission analyses and generates the Emission Database (EDB) in CSV format. These emission data are subsequently processed by the Emission Inventory Generator module to produce a georeferenced Emission Inventory for use in environmental impact assessments. All thermodynamic and chemical-kinetic combustion simulations are executed through a shared Python executable, which automates the parsing of fuel-specific chemical-kinetic mechanisms imported via Cantera. This modular architecture enables automatic management of modeling tiers and kinetic mechanisms without requiring further user intervention.

Emission Inventory Module

The Emission Inventory Module is a Python-based tool that maps engine emissions into a flight trajectory to create a spatially and temporally resolved emission inventory. It takes as input a non-georeferenced Emission Database (EDB) generated by the ESATTO Emission Module. Separately, reference mission profiles are computed using any flight analysis software (e.g. ASTOS), resulting in a 4D trajectory (time, latitude, longitude, altitude). Each point on the trajectory is associated with a corresponding fuel flow and thrust profile. The full georeferenced inventory (4D emissions) is subsequently used for climate impact assessment, where the spatial and temporal pattern of emissions influences contrail formation and atmospheric chemistry.

Environmental Impact Module

The Environmental Impact Module quantifies the climate and atmospheric effects of flight emissions using two specialized software tools, both interfaced within Python:

- **OpenAirClim (OAC)** [229]: a climate–chemistry response model developed by DLR for aviation applications. OAC uses the 4D annual emission inventory as input and computes global climate metrics by applying precomputed, non-linear response functions that emulate detailed climate–chemistry simulations.

- **Supersonic Effects** [230]: a Python package designed to provide rapid estimates of stratospheric ozone and radiative impacts from supersonic transport (SST) operations. Unlike OAC, this tool does not require a full georeferenced inventory. Instead, it operates on aggregated emissions over a specified flight corridor and cruise altitude. Supersonic Effects employs empirical sensitivity datasets, where ozone column changes (in Dobson Units) and radiative forcing (in mWm^{-2}) are modeled as linear functions of emissions at given altitudes and regions. Inputs include the annual total mass of emitted species (e.g., NO, SO_2, H_2O), the flight corridor region—which defines the background atmospheric state—and the cruise altitude. The model interpolates among tabulated ozone and forcing sensitivities to estimate the resulting atmospheric response.

OpenAirClim (OAC) is a comprehensive and global model capable of processing the annual 4D emission inventories of any aircraft fleet, including both subsonic and supersonic operations. It produces long-term climate metrics representative of large-scale atmospheric responses. In contrast, Supersonic Effects is specialized for supersonic transport (SST) corridors and neglects spatial details other than the specified region and cruise altitude.

Optimization Process

The ESATTO optimization process integrates the aforementioned modules to identify the cruise altitude that minimizes the overall environmental impact. Specifically, the state-of-the-art optimizer is implemented as a Python executable that:

- ingests the key performance parameters obtained from the impact analyses.

- combines the resulting impact metrics and determines the cruise altitude at which their cumulative effect is minimized.

In this optimization process, the contribution of the *atmospheric response*—evaluated through the Supersonic Effects model—is decisive. The OpenAirClim (OAC) contribution, representing the climate impact, is assessed using the reference mission derived from ASTOS-based feasibility studies. This mission assumes a fixed cruise altitude and employs the georeferenced emissions provided by the Emission Inventory. Conversely, the Supersonic Effects contribution is computed for six distinct cruise altitudes, ranging from 13 km to 18 km, using propulsive parameters from the Propulsive Database (PDB) and emission data from the Emission Database (EDB). Future developments of the ESATTO optimization process will introduce an iterative loop to verify and ensure that, by adopting the cruise altitude identified by the optimizer based on Supersonic Effects results, the updated mission indeed achieves the minimum overall environmental impact, including climate effects evaluated through OAC.

ESATTO Framework formalization

To ensure a clear and structured representation of the framework's operation, its formalization was performed within the MDAx (MDAO Workflow Design Accelerator) environment [231]. MDAx is a software platform designed to support multidisciplinary design processes in a modular and visual manner, facilitating the integration of diverse tools into a single automated workflow. Its use enables a precise definition of the connections among the various modules of the framework, specifying inputs, outputs, and logical dependencies. Furthermore, the graphical representation provided by MDAx illustrates the optimization cycle governed by the optimizer. The formalization within MDAx also represents a key step toward the subsequent implementation and deployment of the framework in RCE, an environment that allows for its remote and integrated execution. Figure 3.24 presents the ESATTO Framework as formalized in MDAx.

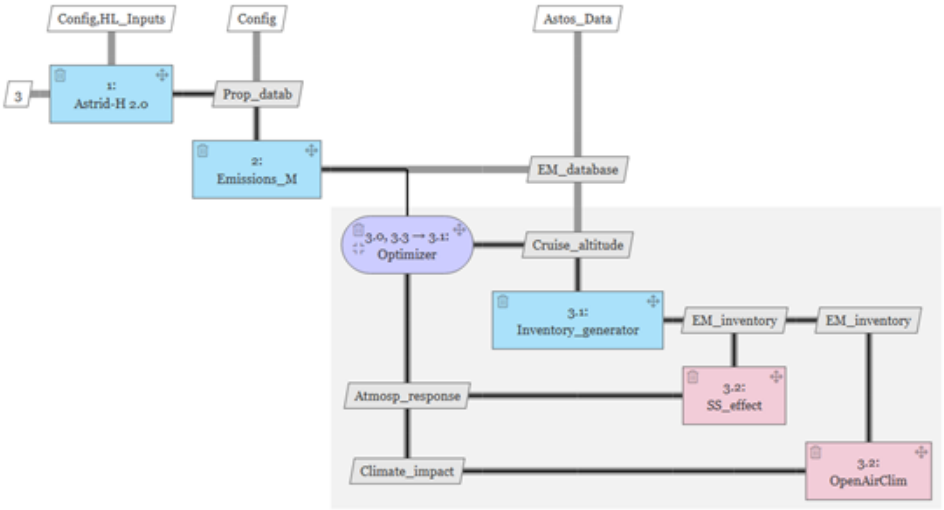

Fig. 3.24 ESATTO Framework on MDAx

ESATTO Framework execution

The ESATTO Framework is executed within the RCE Environment [232]. The first step involves configuring the input provider by specifying the paths to the required input files on the local machine. The ASTRID-H 2.0 tool, labeled Design in Figure 3.25, requires connections to all three source files. In contrast, the Emission Module, labeled Emissions in Figure 3.25, only needs to be linked to its configuration file. The second input required by the Emission Module is the Propulsive Database, which is generated by ASTRID-H 2.0 as an output in .xlsx format. The Emission Database produced by the Emission Module is then provided as input to both the Emission Inventory Module (labeled Inventory) and the Supersonic Effects tool (SS_effects).

The Inventory Module, together with the reference mission provided by the input provider, generates an emission inventory containing georeferenced emissions along the reference flight path. Concurrently, the Supersonic Effects tool supplies the optimizer with evaluations of the annual atmospheric response produced by the fleet of case-study aircraft. In parallel, the OpenAirClim (OAC) tool quantifies the climate impact of the same fleet. Finally, the optimizer combines the impact metrics obtained from OAC and Supersonic Effects at the reference cruise altitude and determines the cruise altitude that minimizes their combined effect. In future developments, an iterative optimization loop is envisaged. In the first iteration, the climate impact

assessed by OpenAirClim is linked exclusively to the user-defined reference mission, corresponding to a single fixed cruise-altitude condition. In subsequent iterations, the reference mission will be updated to adopt the cruise altitude identified by the optimizer. The georeferenced emission inventory, the relative climate impacts of the reference aircraft fleet, and the overall environmental impact will then be re-evaluated. This process will iterate until convergence, ensuring that the selected cruise altitude effectively minimizes the total environmental impact across both climate and atmospheric response metrics.

Figure 3.25 shows the Framework implemented in RCE.

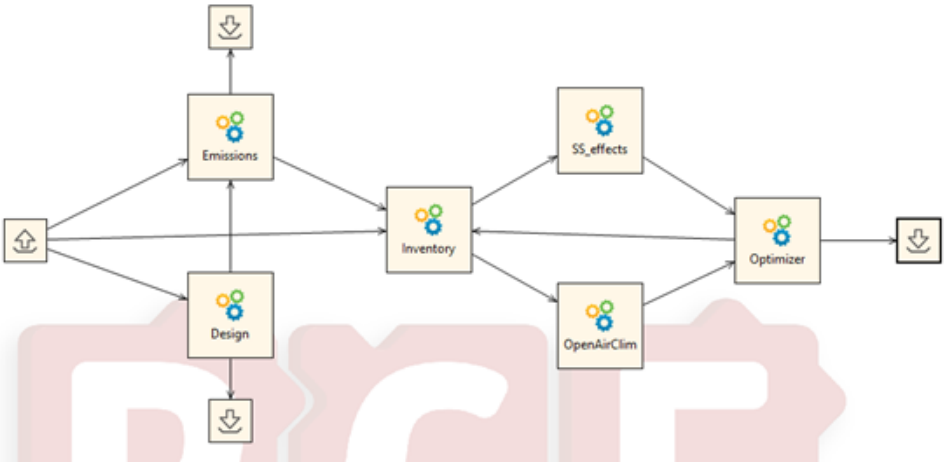

Fig. 3.25 ESATTO Framework on RCE

3.4.3 Sonic boom requirement in the Matching Chart

Supersonic aircraft must satisfy performance requirements that are broader and more demanding than those of conventional subsonic airplanes. The main challenge comes from operating for sustained periods at supersonic speed, where wave drag increases rapidly. In this regime, it becomes the largest contributor to aerodynamic drag, so its reduction is a central design goal. To address it, designers often turn to highly swept or delta wing planforms. These choices, however, create difficulties at the other mission segments. During airport operations, supersonic aircraft usually need longer runways because of higher stall speeds and their lower aerodynamic efficiency in LTO operations. Addressing these challenges requires an integrated design approach that balances aerodynamic and propulsion efficiencies, while ensuring compliance with airport and environmental regulatory constraints.

The conceptual design phase usually starts by defining the main mission requirements, focusing on the relationship between payload and range within a specific mission profile. The profile outlines different flight segments and defines a cruising Mach number at a given altitude. The design process follows an iterative approach to estimate the maximum take-off weight [233–235]. In this process, geometric and configuration parameters are used to estimate the empty weight, while analytical models calculate the fuel weight by assessing fuel consumption during each mission segment. The iteration process is monitored by checking the convergence of the final mass across successive iterations. The hypotheses on the type of propulsion plant used and on the category of the aircraft are also important to estimate first guesses data about the Specific Fuel Consumption (SFC) as well as aerodynamic characteristics.

Defining performance requirements across the various flight segments enables the determination of both the wing area needed to generate sufficient lift and the thrust necessary to balance the aerodynamic drag under all different flight conditions. This analysis is facilitated by the Matching Chart tool, which relates the required thrust and wing area to the take-off mass during each part of the mission profile. A graphical output of this method is provided in Figure 3.26, where the green region highlights the set of feasible design solutions for a specified configuration.

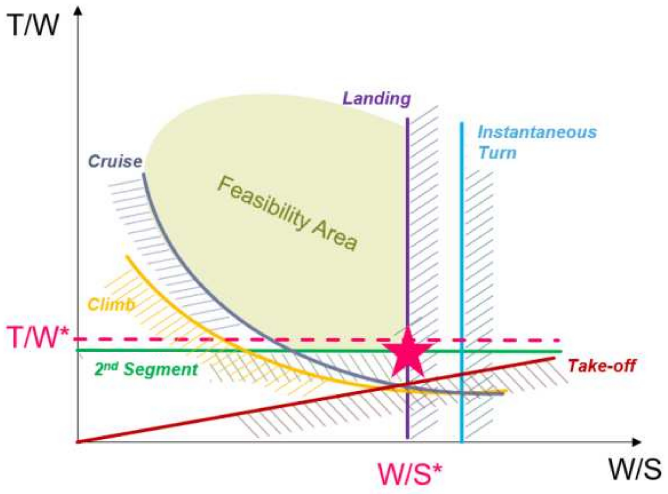

Fig. 3.26 Example of a Matching Chart [110]

The methodology selects specific thrust-to-weight ratio (T/W) and wing loading (W/S) pairs, facilitating the identification of baseline configurations for more in-

depth analysis. This approach streamlines the aircraft sizing process by allowing different flight conditions and propulsion performance to be evaluated in a single plot. To ensure comparability, the equations are adjusted to reflect equivalent conditions at sea level. This approach, originally proposed by [236], is still valid today, being flexible enough to support different kinds of aircraft design studies [110, 113], with proper updates to tune the method as a function of the aircraft category. The feasible design space results from the intersection of different constraint curves, with the design point generally selected at the lowest T/W value while maintaining a consistent W/S. Available thrust shall then be slightly higher, considering a proper margin, and in Figure 3.26 is represented by the dashed pink line.

The integration of sonic boom constraints into the Matching Chart tool is a novel contribution in this PhD thesis. This allows early evaluation of numerous trade-offs between performance and noise limits and supporting a more balanced conceptual design. The simplified methodology uses a statistical analysis to estimate ground-level peak overpressure for case studies with a cruise Mach number lower than 2.0.

Linear regression and correlation analysis

The linear regression was performed using the CS1 and CS2 configurations. For both, the model fitting considered a maximum Mach number of 2. The model is intended to show how aerodynamic and geometric input variables influence the positive and negative peaks in the ground pressure signature, while relying on simplified assumptions. The relationship is captured with a multiple linear regression, presented in Equation 3.32.

$$y = \beta_0 + \beta_1 x_1 + \beta_2 x_2 + \beta_3 x_3 + \ldots + \beta_i x_i + \iota \tag{3.32}$$

In Equation 3.32, y represents the dependent variable, and $x_1, x_2, \ldots, x_i$ are the independent variables. The intercept is β_0, and the regression coefficients are $\beta_1, \beta_2, \ldots, \beta_i$. The term ι accounts for the statistical error. The coefficients are estimated by minimizing the sum of squared differences between observed and predicted values, according to the least squares method.

It is assumed that the relationship between the variables is linear, that observations are independent, that errors have constant variance, and that residuals follow a normal distribution. The goal is to determine how each independent variable affects the dependent variable, make predictions for new data based on the identified relationships, and provide an interpretable equation that describes the system.

The independent variables are six in total, plus two dependent variables, corresponding to the positive and negative pressure peaks of the ground signature. Consequently, two separate regression equations are required, each relating the set of input variables to one of the output variables. Three independent variables relate to the aircraft geometric dimensions and show interdependence. To improve model accuracy, a correlation analysis was performed thanks to MATLAB's corrcoef function [237] to identify variables that can be excluded. The input data consists of a matrix where each column represents a variable, and each row corresponds to an observation. The dimensional parameters considered are aircraft length, wingspan, and wing surface, while the flight condition parameters include Mach number, altitude, and angle of attack. The Pearson correlation coefficient [238] was used to measure the linear relationship between each pair of variables. The result is a symmetric correlation matrix. Values range from -1 (perfect negative correlation) to 1 (perfect positive correlation), with 0 meaning no linear correlation. Figure 3.27 presents the heatmap of the correlation matrix.

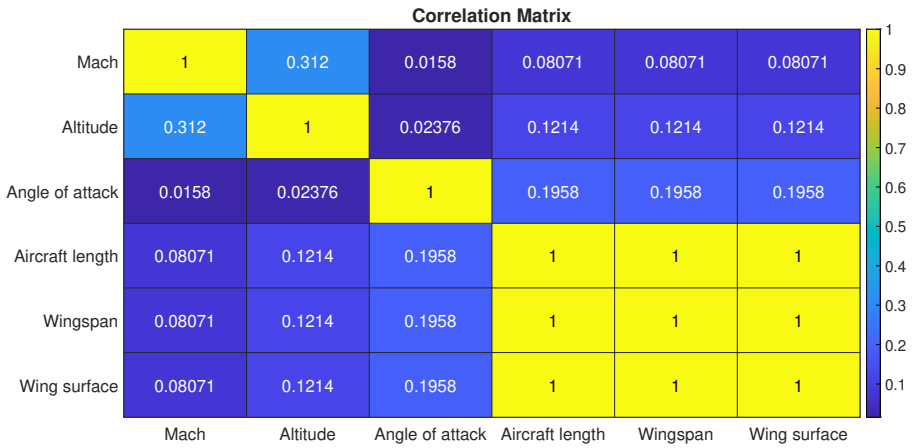

Fig. 3.27 Correlation matrix

As expected, aircraft in the same category show strong correlations among length, wingspan, and wing surface, while other variables are partially correlated, likely due

to the small dataset employed. To ensure effective linear regression, only one of the highly correlated variables is kept. Wing surface is chosen because it is a key sizing parameter and a direct output of the Matching Chart tool whereas length and wingspan are excluded.

Mathematical model

All the parameters necessary for the application of the mathematical model are defined and constitute the two matrices X and Y:

- inputs X: Mach, altitude, angle of attack, wing surface.
- outputs Y: Δp_1, the positive pressure peak, and Δp_2, the negative pressure peak.

First the model adds a unit column to the inputs matrix X, modeling the regression intercept. In the second step, the model performs the linear regression, computing two linear vectors $b_{1,linear}$ and $b_{2,linear}$ for Δp_1 and Δp_2 respectively, through the least squares method as highlighted in Equation 3.33:

$$b = \left(X^T X\right)^{-1} X^T y \tag{3.33}$$

These vectors contain the regression coefficients, β. The predicted values of Δp_1 and Δp_2, denoted as $y_{\text{pred},1}$ and $y_{\text{pred},2}$ respectively, are then obtained by multiplying the coefficient vectors with the input matrix X. Finally, the model evaluates the residual sum of squares (SSE) from equation 3.34 and the total sum of squares (SSQ) from equation 3.35:

$$\text{SSE} = \sum_{i=1}^{m} \left(y_i - y_{\text{pred},i}\right)^2 \tag{3.34}$$

$$\text{SSQ} = \sum_{i=1}^{m} \left(y_i - \tilde{y}\right)^2 \tag{3.35}$$

In Equation 3.35 $\tilde{y}$ is the mean of the observed values Y. From these parameters, the coefficient of determination (R_S^2) is derived, which measures the goodness of fit of the model, taking values between 0 and 1, and can be expressed as Equation 3.36:

$$R_S^2 = 1 - \frac{\text{SSE}}{\text{SSQ}} \tag{3.36}$$

3.4.4 Refinement of available analytical methods

Section 1.5.3 introduced the original simplified Carlson methodology [104], developed for the first generation of supersonic civil configurations in the late '70s. Although the method is suitable for the objectives of the conceptual design phase, it requires detailed input data that are often unavailable in the earliest stages. In particular, a complete CAD model is needed to compute the equivalent area distribution due to volume, $A(x)$. For specific configurations, however, the methodology in Section 1.5.3 can be further simplified by using shape factor charts, as shown in Figure 3.28.

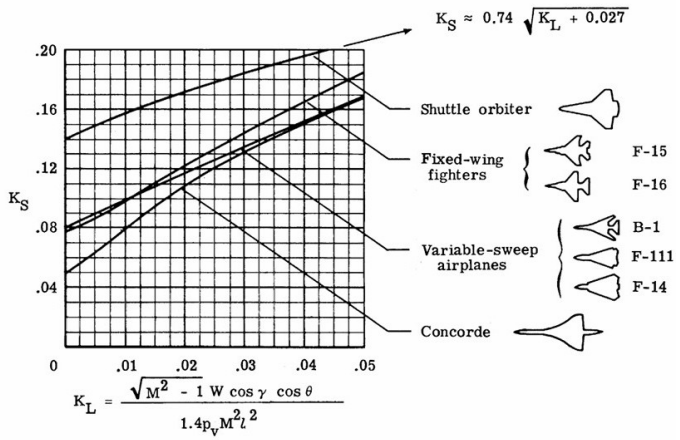

Fig. 3.28 Shape factor K_S original charts, Simplified Carlson method

In the abscissa in Figure 3.28 is the so called lift parameter K_L described as Equation 3.37:

$$K_L = \frac{\sqrt{M^2 - 1}\, W \cos\gamma \cos\theta}{1.4\, p_v M^2 l^2} \tag{3.37}$$

In which W is the aircraft weight, γ is the flight path angle, θ is the azimuth angle, p_v is the atmospheric pressure at the selected altitude, l is the aircraft reference length. To use Figure 3.28, a user must first identify the aircraft type, compute Equation 3.37, and then read the corresponding shape factor directly. The Figure shows that larger aircraft are generally more slender and thus associated with lower shape factor values. Fighter aircraft, owing to their particular geometries, tend to exhibit higher shape factor values. It should be noted that the configurations represented in Figure 3.28 correspond to first-generation supersonic civil transports and military fighters. In contrast, second-generation designs are expected to be more slender

and to operate at lower Mach numbers. Within this PhD work, the original Carlson formulation has therefore been extended for application to the conceptual design of second-generation supersonic civil aircraft.

To extend the applicability of low-fidelity methodologies, a new framework for estimating the aircraft shape factor K_S was developed. This framework combines high-fidelity simulations with experimental data [120, 239] from the MORE&LESS project, covering Mach numbers from 1.5 to 5.0 across a variety of aircraft configurations.

The methodology addresses specific limitations of the research group's proprietary tool, ASTRID-H 2.0. At the present stage, the software cannot produce a complete 3D CAD model at the end of the iterative design process, and relying on simplified sketches can introduce non-negligible errors. Because the goal of the conceptual design phase is to identify feasible configurations for more detailed follow-on studies, reliable estimation methods are essential.

The methodology was applied to four different aircraft categories:

- Supersonic Business Jet (Section 2.1)
- Concorde-like layout (Section 2.3)
- Hypersonic Waverider (Section 2.5)
- Hypersonic demonstrator (Section 2.4)

The aircraft's used are visible in Figure 4.69.

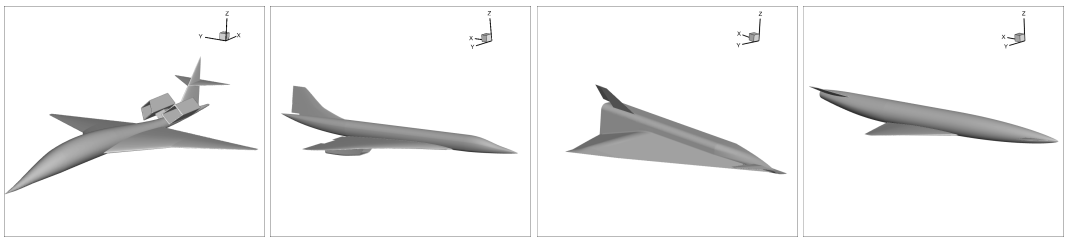

(a) Supersonic Business Jet (b) Mach 2 Concorde-like layout (c) Mach 5 Hypersonic waverider (d) Hypersonic wing and fuselage

Fig. 3.29 Aircraft evaluated for refined analytical method

The dataset includes both numerical simulations and experimental results. In particular, the experimental data correspond to the Hypersonic Waverider (Section

3.3.2) and the Hypersonic Demonstrator (Section 3.3.3). For each numerical or experimental point, the peak overpressure Δp and the lift parameter K_L of Equation 3.37 were calculated. The aircraft shape factor for each specific flight condition was determined by inverting Equation 1.17 as:

$$K_S = \frac{\Delta p}{K_P \, K_R \, \sqrt{p_v \, p_g} \, (M^2 - 1)^{\frac{1}{8}} h_e^{-\frac{3}{4}} l^{\frac{3}{4}}}$$

By evaluating the lift parameter for each selected numerical simulation or experimental test, a set of abscissa and ordinate points was obtained. Simulations were grouped by aircraft category following the approach proposed by Carlson. Table 3.9 provides a summary of representative data points for each category.

Table 3.9 Representative dataset for the refinement of current analytical methods

Aircraft	Mach	Test type	angle of attack [deg]
Business Jet	$1.2 \rightarrow 1.5$	numerical	$-2^\circ \rightarrow 4^\circ$
Concorde-like	$1.5 \rightarrow 2$	numerical	$-2^\circ \rightarrow 4^\circ$
Hypersonic Waverider	$4 \rightarrow 5$	numerical	0°
Hypersonic Wing-Fuselage	$1.2 \rightarrow 5$	numerical	0°
Hypersonic Waverider	4.7	experimental	0°
Hypersonic Wing-Fuselage	4.7	experimental	0°

For each aircraft family, analytical curve fitting was performed to describe the relationship between the aircraft shape factor K_S and the lift parameter K_L. To achieve this, the cubic smoothing spline function `csaps` [240] was used. In this implementation, `csaps(x,y)` returns a cubic smoothing spline in `ppform`, where x represents the lift parameter K_L and y the corresponding aircraft shape factor K_S. This spline provides an approximation of the data such that, for each point x_j, the value of the spline satisfies $f(x_j) \approx y_j$, with $j = 1, \ldots, n$.

The smoothing spline f minimizes

$$p \sum_{j=1}^{n} w_j |y_j - f(x_j)|^2 + (1-p) \int \lambda(t) \, |D^2 f(t)|^2 dt,$$

In the spline formulation, the first term measures the fitting error, while the second term penalizes roughness. Here, n is the number of data points, $D^2 f$ denotes the

second derivative, w_j are the error weights (default 1), and $\lambda(t)$ is the roughness weight function (default constant 1). By default, `csaps` selects a smoothing parameter p based on the distribution of the data points x. In this work, `csaps` is applied separately to each aircraft family to model the relationship between K_S and K_L for conceptual design cases. The resulting spline produces a smooth, analytical curve that can be used to estimate shape factors for intermediate K_L values without performing additional high-fidelity simulations. This approach ensures consistency with the proposed framework and allows seamless integration with the ESATTO workflow.

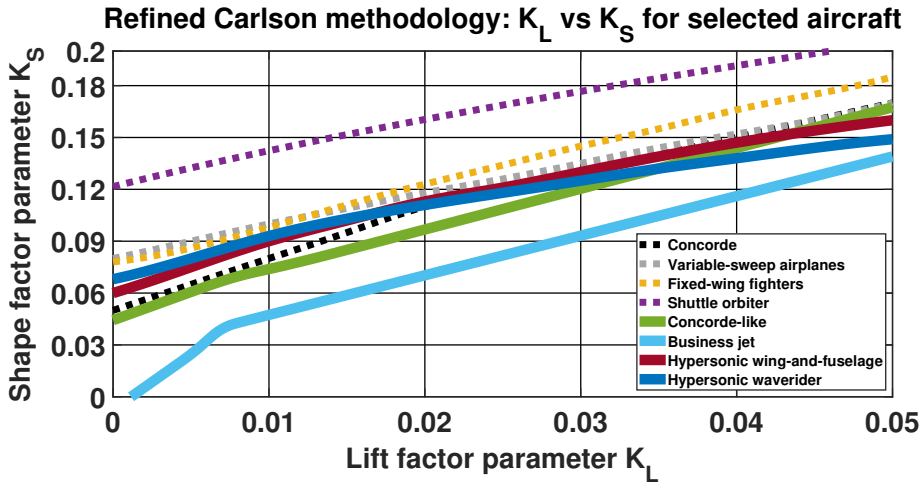

Fig. 3.30 Correlation between lift parameter K_L and aircraft shape factor K_S according to the refined Carlson methodology.

Figure 3.30 presents the refined shape factor charts derived from the high-fidelity simulations and experimental test campaigns conducted within the MORE&LESS project. Configurations represented by dotted markers correspond to previously developed designs, whereas solid markers indicate the new designs introduced in this PhD thesis. The configurations evaluated appear to have a noticeable reduced shape factor parameter compared to the case studies evaluated by Carlson in his original work. This difference arises because the newly studied configurations are more slender than those reported in the original handbook.

The method used to derive the business jet curve is described here. Table 3.10 reports the correlation between K_L and K_S for the simulated flight conditions. The values shown refer to an azimuth angle θ of 0°; however, the complete range between 0 and 50° was examined using a 5° increment.

Table 3.10 Lift and shape factor parameter correlation, business jet

K_L lift parameter	K_S shape factor
0.00408	0.0186
0.00456	0.0216
0.00513	0.02519
0.00659	0.0368
0.00713	0.0401
0.00779	0.0413
0.00813	0.0432
0.0135	0.0559
0.0148	0.0578
0.0197	0.0717
0.0292	0.0919
0.0442	0.1229

Consistent with the formulation proposed by Carlson [104], an analogous expression has been derived for the business jet category. Figure 3.31 presents the interpolated trend together with the high-fidelity data and the associated 95% prediction interval.

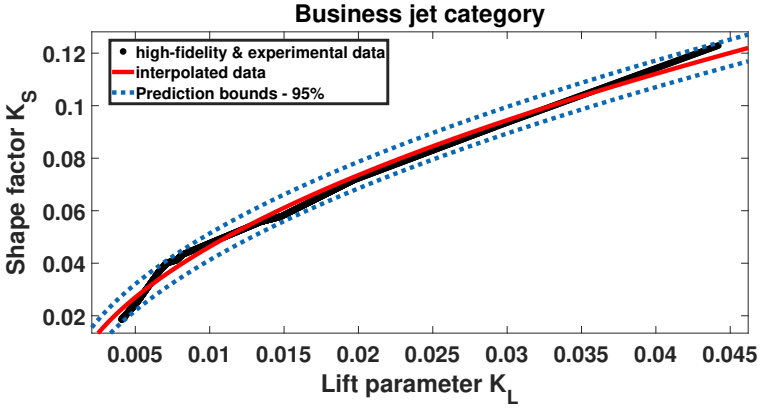

Fig. 3.31 Correlation between lift parameter K_L and aircraft shape factor K_S, business jet

All original data fall within the 95% prediction bounds. Before deriving the final expression, the possibility of using a relation of the form $K_S{=}\alpha\ \sqrt{K_L}\ +\beta$, consistent with Carlson's prediction for the Space Shuttle configuration, was first

verified. Equation 3.38 summarizes the resulting formulation for the business jet category.

$$K_S = \alpha \cdot \sqrt{K_L} + \beta = 0.6593 \cdot \sqrt{K_L} - 0.0196 \tag{3.38}$$

The physical interpretation of the coefficients α and β is detailed. The parameter β represents the value of the shape factor when the lift parameter is zero. It characterizes the intrinsic sonic-boom performance of the configuration: lower β values indicate shapes that inherently generate lower peak overpressures for a given lift parameter, thereby improving low-boom capability. Conversely, the coefficient α quantifies how the sonic-boom performance of the aircraft category varies with changes in flight conditions. It reflects the ability of the configuration to maintain comparable Δp values despite variations in operating parameters. Smaller α values indicate reduced sensitivity to flight-condition changes.

Additionally, the lower and upper bound of the α and β parameters are presented in Table 3.11. The high coefficient of determination ($R^2 = 0.9896$) confirms the strong correlation between the lift parameter and the derived shape factor formulation for the business jet category.

Table 3.11 Lift and shape factor parameter correlation, business jet

	lower	upper
α	0.6498	0.6687
β	-0.0207	-0.0186

Similarly, the correlation between the lift parameter K_L and the aircraft shape factor K_S has been evaluated for the other aircraft categories in Table 3.12. Specifically, Table 3.12a reports the values for the Concorde-like configuration, Table 3.12b lists the results for the hypersonic wing–fuselage configuration, and Table 3.12c provides the corresponding data for the hypersonic waverider.

Table 3.12 Lift and shape factor parameter correlation for the three categories.

(a) Concorde-like

K_L	K_S
0.00494	0.0598
0.00539	0.0619
0.00605	0.0642
0.00652	0.0656
0.00707	0.0674
0.00839	0.0703
0.00889	0.0718
0.00903	0.0723
0.0105	0.0748
0.0113	0.0767
0.0118	0.0779
0.0134	0.0814
0.0141	0.0829
0.0195	0.0989
0.0257	0.1105

(b) Hypersonic wing–fuselage

K_L	K_S
0.0013	0.0641
0.0028	0.0687
0.00489	0.0741
0.00542	0.0754
0.00664	0.0798
0.00731	0.0832
0.0103	0.0921
0.0121	0.0963
0.0162	0.1044
0.0191	0.111
0.0276	0.124
0.0305	0.132
0.0371	0.146

(c) Hypersonic waverider

K_L	K_S
0.0019	0.07233
0.0025	0.0733
0.00313	0.0748
0.00452	0.0787
0.00504	0.0811
0.00625	0.0841
0.00696	0.0863
0.00795	0.0891
0.00984	0.0939
0.01219	0.0978
0.01397	0.1013
0.01481	0.1029
0.01713	0.1071
0.0218	0.1152
0.0287	0.1214
0.0335	0.128
0.0421	0.1412

Figure 3.32 illustrates the correlation between the original data, the interpolated trend, and the associated 95% prediction interval for each aircraft category. Figure 3.32a corresponds to the Concorde-like configuration, Figure 3.32b to the hypersonic wing–fuselage configuration, and Figure 3.32c to the hypersonic waverider.

All configurations fall within the 95% prediction interval, with the sole exception of the highest K_L values of the Concorde-like configuration, which lie outside the typical design flight envelope.

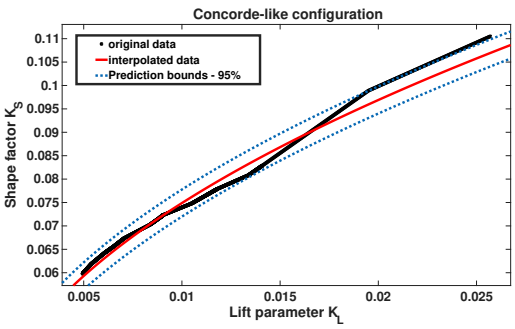

(a) Concorde-like

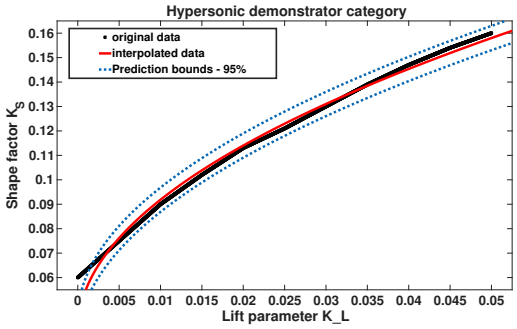

(b) Hypersonic wing–fuselage

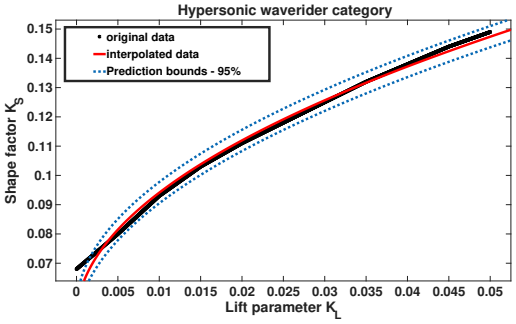

(c) Hypersonic waverider

Fig. 3.32 Correlation between K_L and K_S with interpolated data and 95% prediction boundary

The resulting formulations for the three aircraft categories are reported below:

$$K_S = 0.5316\sqrt{K_L} + 0.02172 \qquad \text{Concorde-like,} \tag{3.39}$$

$$K_S = 0.5352\sqrt{K_L} + 0.03833 \qquad \text{Hypersonic wing–fuselage,} \tag{3.40}$$

$$K_S = 0.4310\sqrt{K_L} + 0.05101 \qquad \text{Hypersonic waverider.} \tag{3.41}$$

Unlike the business-jet category, the β parameter is positive for all three configurations. This trend reflects their intrinsic geometrical characteristics: these vehicles are not designed for low-boom performance and therefore exhibit higher baseline values of the shape factor. The corresponding lower and upper bounds of the α and β parameters are provided in Table 3.13.

Table 3.13 Lower and upper bounds for the α and β parameters

(a) Concorde-like

	lower	upper
α	0.5286	0.5346
β	0.02141	0.02203

(b) Hypersonic wing–fuselage

	lower	upper
α	0.5331	0.5373
β	0.03800	0.03866

(c) Hypersonic waverider

	lower	upper
α	0.4294	0.4326
β	0.05076	0.05125

Finally, Table 3.14 reports the R^2 values obtained for each category. The consistently high coefficients of determination confirm the strong correlation between the lift parameter and the derived shape-factor formulation across all selected configurations.

Table 3.14 Coefficient of determination (R^2)

(a) Concorde-like

R^2	0.9834

(b) Hypersonic wing–fuselage

R^2	0.992

(c) Hypersonic waverider

R^2	0.9908

A new routine was developed to estimate peak overpressure and sonic boom carpet extents based on aircraft typology and performance. This routine is fully compatible with the ESATTO Framework [106], the holistic multi-disciplinary framework for developed within the project.

Once a design iteration is completed, the expected sonic boom overpressure across multiple azimuth angles can be assessed by selecting the aircraft typology and the corresponding K_L lift parameter for the specific flight condition. This approach allows early-stage evaluation of sonic boom impacts without the need for high-fidelity, computationally expensive simulations during the first phases of the conceptual design. The methodology has been validated for the Mach 1.8 Supersonic Business Jet (Section 2.2), with results benchmarked against both high-fidelity simulations and the original Carlson methodology.

Integration in ASTRID-H 2.0

The two methodologies presented in Sections 3.4.3 and 3.4.4 are implemented in ASTRID-H 2.0. The first layer draws on high-level requirements and statistical data, relying on low-fidelity algorithms to perform the initial sizing. Within this step, the methodologies developed in this thesis are used to introduce the preliminary

sonic boom constraint. The second layer builds on these results by employing surrogate aerodynamic and propulsion models based on high-fidelity simulations and experimental data. This approach raises the level of accuracy while keeping the computational cost low. Taken together, the two layers create a progressive process: the fidelity of the analysis increases, and the final design outcomes become more consistent and reliable.

Chapter 4

Results

Chapter 4 presents the principal outcomes of this doctoral research, obtained thanks to the methodologies introduced in Chapter 3. The analyses covered the various case studies described in Chapter 2, enhancing the capability to apply the developed methodologies and tools to a broad spectrum of supersonic configurations. Computational Fluid Dynamics simulations were carried out using the High Performance Computing infrastructure of Politecnico di Torino [241]. Two clusters were employed in this work. Initially, the ISOLA 1 cluster (used between 2022 and 2024) provided 58 compute nodes, including 6 equipped with NVIDIA V100 GPUs. Following a major upgrade in 2024, simulations were performed on the ISOLA 2 cluster, which offers 73 compute nodes, 26 equipped with NVIDIA A40 GPUs and 1 with an NVIDIA A100 GPU. Additionally, during the research visit at University of Florida, the HiPerGator Research Computing cluster has been used [242], and it has a total of 66,000 cores. Specifically, the work leveraged the HiPerGator AI SuperPod, which features 1,120 NVIDIA Ampere A100 GPUs and 2.5 PB of all-flash storage, providing 13.75 Petaflops of double-precision LinPack performance and 0.7 Exaflops for AI workloads.

The chapter is organized into specific sections. Section 4.1 evaluates the main outcomes from Computational Fluid Dynamics simulations. Firstly, the effects of off-design conditions in the near-field region were evaluated for both the Mach 1.5 Supersonic Business Jet (Section 2.1) and the Mach 2 Concorde-like configuration (Section 2.3). These results serves as input for the propagation module later described. This work was conducted during a six-month research period at the Department

of Mechanical and Aerospace Engineering (MAE) at University of Florida, under the supervision of Dr. S.A.E. Miller and Dr. Sivaramakrishnan Balachandar. In addition, Section 4.1.3 compares the numerical results of the inclusion of turbulence modelling in the near-field region for the Mach 1.8 Supersonic Business Jet 2.2.

Secondly in Section 4.2 the results obtained for in the previous Section are propagated within a non-uniform and stratified atmosphere down to the ground. The influence of variations in angle of attack, Mach number, and near-field turbulence model is examined. In addition, the impact of different atmospheric profiles is also discussed. The effects of off-design conditions on the noise metrics for the Mach 1.5 Supersonic Business Jet and Mach 2 Concorde-like configurations are evaluated in Section 4.3. PL, ISBAP and A-E Sound Exposure Level (SEL) metrics are employed. In addition, the influence of k-ω and Spalart-Allmaras turbulence models in the Computational Fluid Dynamics simulations on the noise metrics is assessed. The effects on the primary carpet extension and limiting azimuth angle in off-design conditions for the Mach 1.5 Supersonic Business Jet and CS1 configurations is assessed in Section 4.4.

Validation of the high-fidelity numerical methodologies against experimental data is reported in Subsections 4.5.1 and 4.5.3. Both Sections highlights limitations and uncertainties of the results, which would be later and deeply discussed in Section 5.2. In addition, an innovative approach for the inverse flight dynamics estimation, developed in collaboration with ISL, is presented in Section 4.5.2 for the CS3 mock-up configuration. The high-fidelity results serves as a foundation for the development of refined low-fidelity methodologies. Section 4.6.1 introduces a low-fidelity constraint for sonic boom peak overpressure within the framework of conceptual aircraft design. Refinements to existing analytical methods are also detailed in Section 4.6.2. These results are validated with the Mach 1.8 supersonic business jet, and later included within the holistic multidisciplinary design framework.

4.1 Near-field result

As previously pointed out in Figure 1.8, in sonic boom research it is standard practice to extract the pressure signature at a vertical distance that is representative of the characteristic length of the aircraft, and it is typically expressed by the non-dimensional ratio H/L. H is the vertical extraction height, while, L represents the

reference length of the configuration under investigation. Throughout this thesis, several values of H/L were considered depending on the purpose of the analysis. For conventional configurations, H/L = 1 and H/L = 3 are sufficiently far from the noise-source to capture the relevant features of the near-field pressure distribution. This condition represents the point at which the shock wave has fully developed, and the aerodynamic effects most clearly characterize the transition from near-field to mid-field behavior. As a result, it provides a more robust and physically consistent basis for the subsequent propagation analysis. The influence of the position of extraction in the noise metrics is assessed in this thesis, with variations within 0.3 dB observed across different extraction points. These results justify the use of a reduced CFD domain, which decreases the computational cost and enables localized mesh refinements in regions of interest. However, in the case of numerical validation against experimental data and for the inverse estimation of flight dynamics, a higher extraction distance of H/L=5 was required. This choice was motivated by the requirement to ensure a fully developed N-wave pressure signature, which is a key assumption for the corresponding post-processing and validation steps.

To analyze the ground disturbance with sufficient coverage, the near-field pressure signatures were extracted at radial angles between ϕ_{CFD} 0° and 90°. The study selects this range based on the thesis's focus on evaluating the primary carpet boom. A complete analysis of the secondary boom carpet would require data up to 180°, which was outside the objectives of this work. The choice of angular resolution depended on the nature of each analysis. Generally, a step size of 5° ensure a good compromise between resolution and computational cost. In contrast, for the validation of the experimental campaign, a coarser step of 7.5° was sufficient to accurately validate the results. Lastly, for the inverse estimation of flight dynamics, however, a finer angular resolution of 2.5° was necessary due to the higher sensitivity of the reconstructed trajectory to directional pressure variations. However, in this Chapter the plots of the pressure signature in both near-field and far-field are presented generally with a 10° step to ensure adequate visibility to all signals recorded or simulated. Figure 4.1 illustrates the radial extraction angles model used. In particular, the extracted angle at 0° is positioned beneath the aircraft, while 180° above it; this notation is commonly used in sonic boom research, and adopted to maintain consistency.

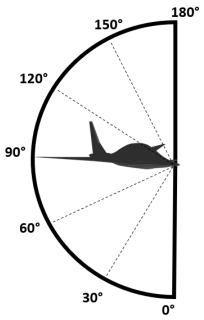

Fig. 4.1 Extraction angles ϕ_{CFD} from Computational Fluid Dynamics

The notation dp/p, defined in Equation 4.1, denotes the normalized increment in static pressure and is used extensively throughout this Chapter.

$$\frac{dp}{p} = \frac{p_s - p_0}{p_0} \tag{4.1}$$

Here, p_s denotes the extracted static pressure value at the specific H/L ratio used, while p_0 is the free-stream static pressure. Portion of the domain with positive dp/p means compression regions, while negative dp/p expansion portions.

4.1.1 Mach 1.5 Supersonic Business Jet

The first configuration analyzed is the Mach 1.5 Supersonic Business Jet introduced in Section 2.1. Figures 2.3a and 2.3b shows the mission profile and angle of attack variations for the reference flight. The representative on-design cruise condition is defined at Mach 1.5, angle of attack set to 2°, and altitude 16.15 km (53,000 ft). Table 4.1 summarizes the simulated Mach–angle of attack cases, with the cruise point highlighted by a green solid ✓. A total of twelve simulations were performed for this configuration, and all of them solve the Euler equations without turbulence modeling.

Table 4.1 Mach 1.5 Supersonic Business Jet simulations, green ✓ scheduled design point

Mach	**-2°**	**0°**	**2°**	**4°**
1.20	✓	✓	✓	✓
1.35	✓	✓	✓	✓
1.50	✓	✓	✓	✓

As shown in Table 4.1, the simulations employ different Mach numbers, and each case required a dedicated structured grid, as previously described. The details of the three grids used for the Mach 1.5 Supersonic Business Jet are presented in Table 4.2.

Table 4.2 Supersonic Business Jet grids detail

	Mach 1.20	Mach 1.35	Mach 1.50
Nodes	6,143,235	6,560,657	7,125,330
Elements	11,947,665	12,666,625	13,172,505
Tetra	6,421,145	6,758,123	6,702,359
Hexa	4,875,552	5,228,280	5,804,344
Tri	473,430	474,180	474,140
Penta	0	0	0
Quad	125,664	146,016	139,160
Pyra	42,768	50,760	43,316

Consistent with the increase of the domain size due solely to the widening Mach angle μ, the grid for the highest Mach number contains a slight increase of number of elements—particularly hexahedral elements—that compose the structured Mach cone aligned grid. Computational time for the simulations span between 21 and 24 hours on the HPC cluster of Politecnico di Torino with 48 processors, and between 11 to 13 hours with the HiPerGator cluster by using 108 processors.

Figure 4.2 shows the near-field static pressure increase contours at the reference cruise Mach number condition for angles of attack ranging from -2° to 4°. These contours reveal how shock structures vary with incidence.

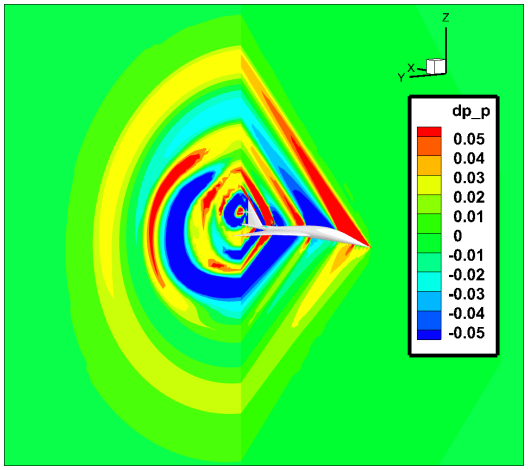

(a) Mach 1.5 SBJ, angle of attack $\alpha = -2°$, Mach 1.5

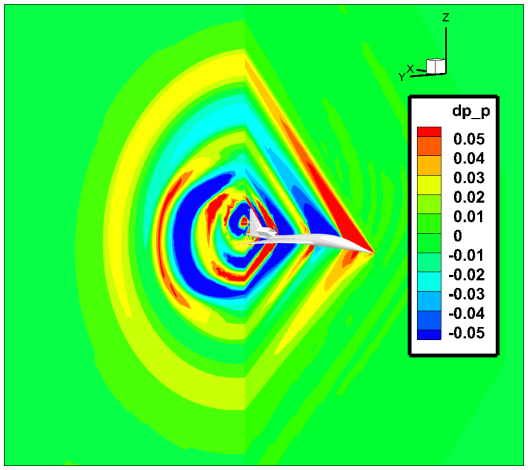

(b) Mach 1.5 SBJ, angle of attack $\alpha = 0°$, Mach 1.5

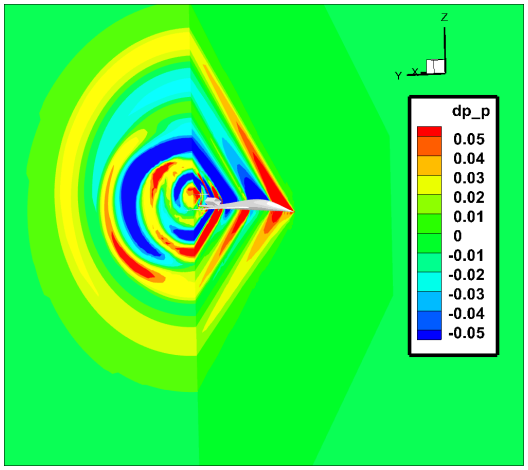

(c) Mach 1.5 SBJ, angle of attack $\alpha = 2°$, Mach 1.5

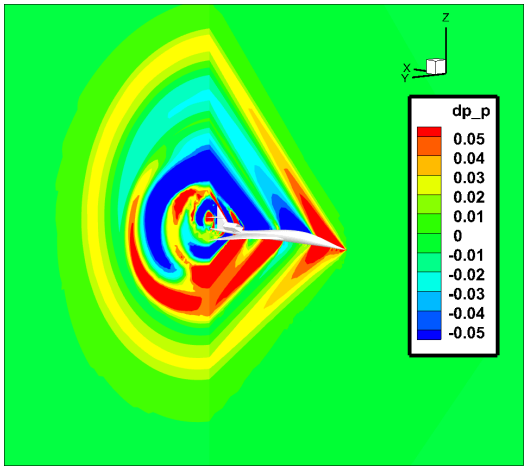

(d) Mach 1.5 SBJ, angle of attack $\alpha = 4°$, Mach 1.5

Fig. 4.2 Increase of static pressure contour Mach 1.5 SBJ, flight Mach number 1.5

The shock pattern for this configuration changes noticeably with the angle of attack. At $-2°$, four distinct compression regions appear, corresponding to shocks from the nose, wing, engine nacelles, and horizontal tail, with the flow clearly asymmetric. At $0°$, the shocks become more defined, and interactions emerge among those originating from the fuselage, wing leading edge, and nacelles. By $2°$, the wing shock remains relatively weak but shifts slightly upstream, closer to the fuselage, which increases compression beneath the aircraft. At $4°$, the wing shock dominates, merging with the nacelle shock and producing a more pronounced and extended pressure rise under the fuselage. Overall, the contours indicate that

the nose shock position is largely insensitive to angle-of-attack changes, while the strength and interactions of the wing and nacelle shocks vary considerably, enhancing the asymmetry of the flow field. Mach contours for the same flight conditions are presented in Figure 4.3.

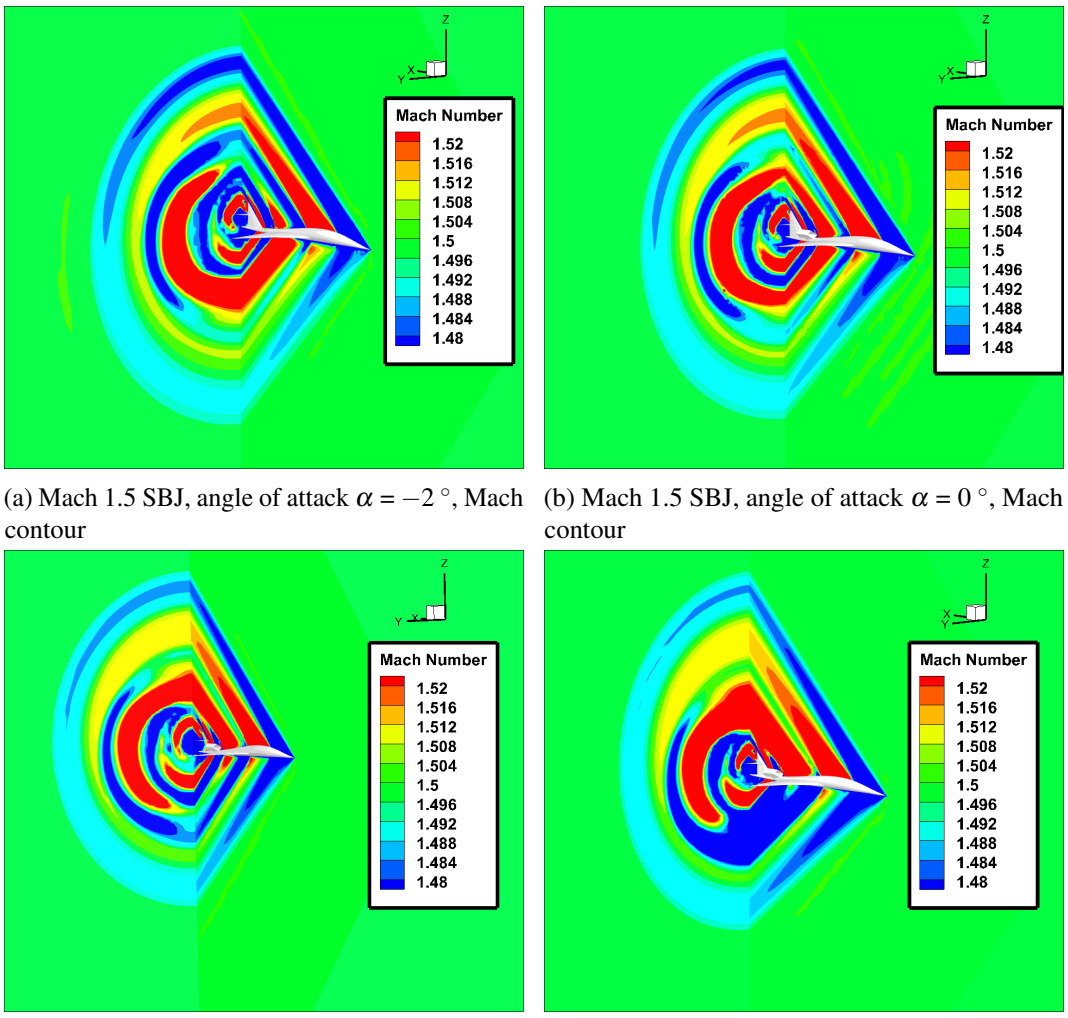

(a) Mach 1.5 SBJ, angle of attack $\alpha = -2\,^{\circ}$, Mach contour

(b) Mach 1.5 SBJ, angle of attack $\alpha = 0\,^{\circ}$, Mach contour

(c) Mach 1.5 SBJ, angle of attack $\alpha = 2\,^{\circ}$, Mach contour

(d) Mach 1.5 SBJ, angle of attack $\alpha = 4\,^{\circ}$, Mach contour

Fig. 4.3 Mach number contour Mach 1.5 SBJ configuration

The Mach number contours demonstrated the same trend visible for the increase of static pressure, highlighting coherency in the numerical simulations. The four extracted pressure signature at H/L=1 are visible in Figure 4.4 for the different simulated angle of attack conditions. The flight Mach number is equal to reference one in cruise, and coherent with the one of the previously displayed contours.

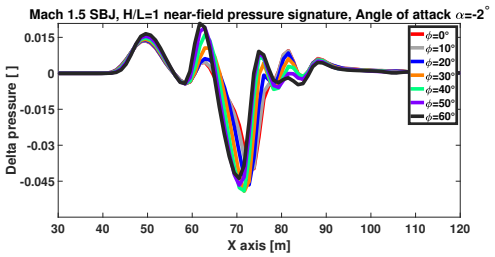

(a) Extracted H/L= 1 pressure signature, α= -2°

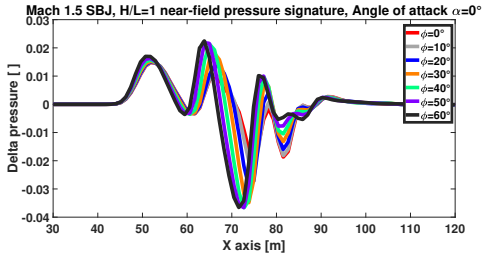

(b) Extracted H/L= 1 pressure signature, $\alpha = 0^\circ$

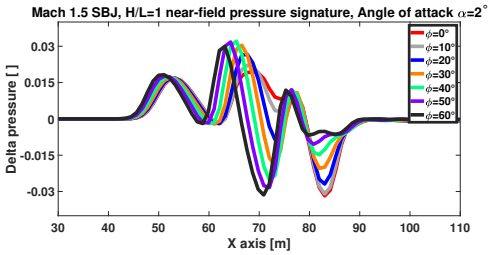

(c) Extracted H/L= 1 pressure signature, $\alpha = 2^\circ$

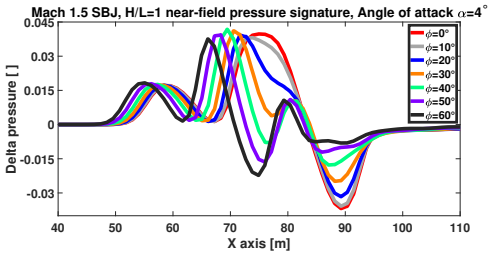

(d) Extracted H/L= 1 pressure signature, $\alpha = 4^\circ$

Fig. 4.4 Extracted pressure signature H/L=1 Mach 1.5 Supersonic Business Jet

The influence of the angle of attack on the extracted near-field pressure signature is evident in the ϕ_{CFD} 0–60° range. It was decided to show this range to ensure adequate visibility of the extracted pressure signature. At an angle of attack of 4°, the shock waves generated by the wing, the engine nacelle and horizontal tail have already merged in the near-field region for extracted azimuth angles. In contrast, as observed in the static pressure contours, at a flight condition with an angle of attack of -2°, four distinct shocks—originating from the nose, wing, engine, and horizontal tail—remain visible. In addition, the four extracted pressure signature confirms the previous statement regarding the intensity of the nose shock with variations in angle of attack, which is essentially constant. Finally, for azimuthal angles of 0, 10 & 20° the shape of the extracted pressure signature varies, highlighting a shock interaction that is not visible in the other simulated angles. This is particularly visible in the extracted pressure signatures highlighted in Figure 4.5c and 4.5d.

The extracted pressure signature are also evaluated at a vertical ratio of H/L=3 in Figure 4.5. The H/L=3 position is widely used as near-field data for the input of subsequent propagation analysis, such as during the AIAA Sonic Boom Prediction Workshop.

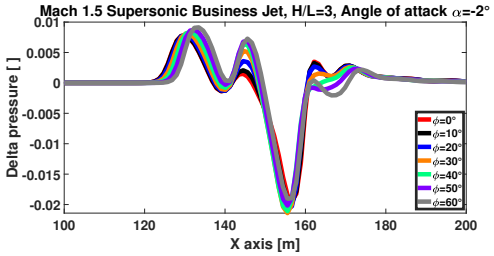

(a) Extracted H/L= 3 pressure signature, α= -2°

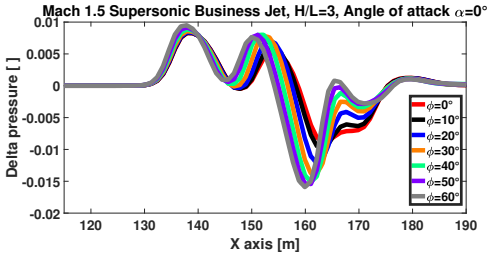

(b) Extracted H/L= 3 pressure signature, $\alpha = 0^\circ$

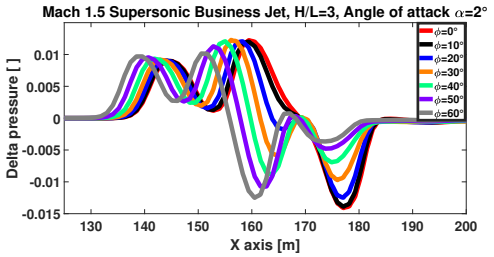

(c) Extracted H/L= 3 pressure signature, $\alpha = 2^\circ$

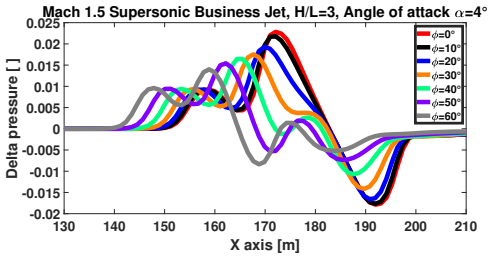

(d) Extracted H/L= 3 pressure signature, $\alpha = 4^\circ$

Fig. 4.5 Extracted pressure signature H/L=3 Mach 1.5 Supersonic Business Jet

The shape of the extracted pressure signature does not vary significantly between the first and second extraction point. In particular, for the flight conditions with an angle of attack α lower than the nominal cruise phase, the shape remains essentially unaltered at H/L = 3. This indicates that the shock waves generated by the aircraft have not yet merged, making it plausible to obtain a shaped waveform at ground level. Conversely, for the flight condition at $\alpha = 2^\circ$, noticeable differences arise, particularly for lower azimuthal angles ϕ_{CFD}. Specifically, the differences observed at H/L = 1 between azimuth angles of 0°, 10°, and 20° further intensify at H/L = 3. In these directions, an additional shock is present before the pressure returns to the free-stream value. Lastly, for the flight condition at $\alpha = 4^\circ$, a similar trend is observed. The shocks visible at H/L = 1 begin to merge already within the near-field region, and—as in the $\alpha = 2^\circ$ case—the pressure signatures extracted at 0°, 10°, and 20° differ substantially from those obtained at higher ϕ_{CFD} values. At low angles of attack, the weaker pressure gradients reduce nonlinear steepening, delaying the merging of shocks and preserving a multi-peaked structure over larger distances. As α increases, stronger lift-induced compressions promote earlier coalescence, leading to a more N-wave-like signature even at moderate extraction distances.

The previous findings are evident from the on-track extracted pressure signature, corresponding to a radial extraction angle $\phi_{CFD} = 0^\circ$ and shown in Figure 4.6.

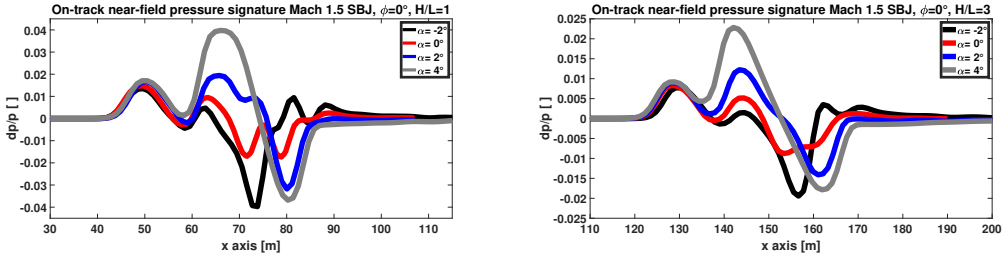

(a) On-track extracted pressure signature, H/L=1, $\phi_{CFD} = 0°$

(b) On-track extracted pressure signature, H/L=1, $\phi_{CFD} = 0°$

Fig. 4.6 On-track extracted pressure signature, $\phi_{CFD} = 0°$, Mach 1.5 SBJ

Noticeable variations in the signature shape occur with changes in the simulated angle of attack, highlighting the influence of flight conditions on the flow field and shock interactions. The case with $\alpha = -2°$ at both extraction points exhibits a similar structure, with shock merging between the engine nacelle and horizontal tail in the trailing portion of the signature. A comparable behavior is also observed for $\alpha = 0°$ and $\alpha = 2°$. Conversely, at $\alpha = 4°$ the signature shows two dominant contributions: the first generated by the nose, and the second by the wing, nacelle, and horizontal tail, which have already merged near the aircraft. This behavior originates from the aft displacement of the effective aerodynamic center with increasing angle of attack, which intensifies the pressure gradients over the rear fuselage and lifting surfaces. The resulting modification of the local flow topology promotes earlier shock coalescence and alters the relative phase between the primary and secondary compression waves, thereby reshaping the ground-perceived pressure signature.

4.1.2 Mach 2 Concorde-like

A similar approach evaluates the CS1 Concorde-like configuration. The mission profile and angle of attack variations were previously presented in Figures 2.7a and 2.7b. The reference cruise design point is defined with a Mach number of 2.0, angle of attack α at 4°, and altitude of 18,000 m (59,000 ft). Table 4.3 lists the simulated Mach-angle of attack flight conditions, with the on-design cruise point highlighted by a green solid ✓, similarly to the previous case study.

Table 4.3 CS1 off-design simulations, green ✓ reference design point

Mach	**-2°**	**0°**	**2°**	**4°**
1.50	✓	✓	✓	✓
1.75	✓	✓	✓	✓
2.00	✓	✓	✓	✓

As for the previous case study, Table 4.4 presents the details of the three grids employed for each Mach number. As in the previous case, due to the solely variations of the structured Mach cone μ aligned grid, the major variations in the number of the elements of the grid regard the hexa elements.

Table 4.4 Supersonic Business Jet grid detail

	Mach 1.50	Mach 1.75	Mach 2.00
Nodes	6,243,813	6,742,182	7,113,494
Elements	11,874,374	12,948,413	14,114,943
Tetra	7,613,848	7,749,227	7,894,193
Hexa	4,248,374	5,113,842	6,021,134
Tri	559,987	564,134	571,294
Penta	0	0	0
Quad	224,953	231,495	244,022
Pyra	47,949	49,533	51,134

The total computational time for each simulation spans between 25 and 27 hours on the HPC cluster of Politecnico di Torino with 48 processors, and between 9 to 11 with HiPerGator cluster by using 108 processors. The contour of the increase in the static pressure for the CS1 configuration at Mach 2 are highlighted in Figure 4.7.

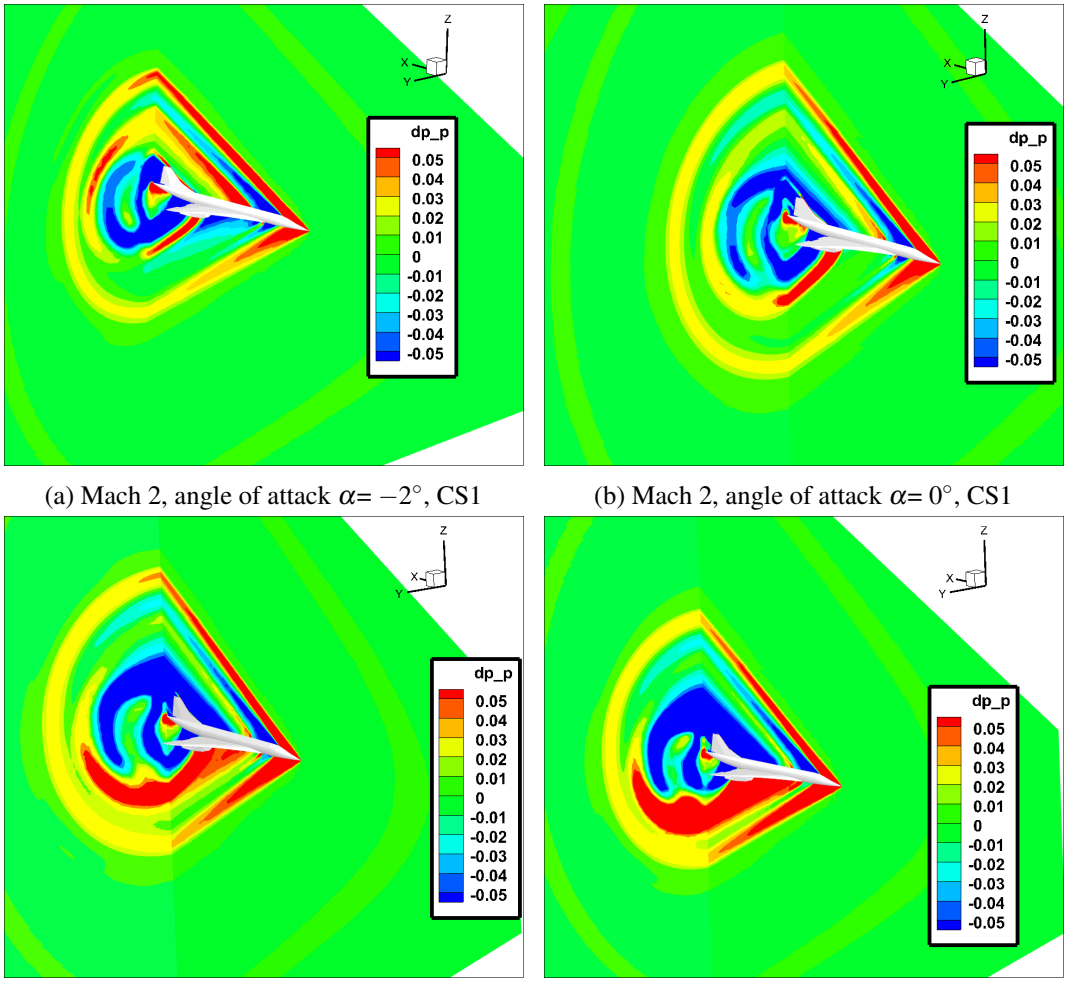

(a) Mach 2, angle of attack α= -2°, CS1

(b) Mach 2, angle of attack α= 0°, CS1

(c) Mach 2, angle of attack α= 2°, CS1

(d) Mach 2, angle of attack α= 4°, CS1

Fig. 4.7 Increase of static pressure contour CS1 configuaration, flight Mach number 2.0

For the CS1 configuration, the effect of increasing the angle of attack is clearly evident. A similar behavior compared to the previous Mach 1.5 Supersonic Business Jet is visible. At -2° of incidence three distinct shocks are visible: the first generated by the nose, followed by a small one at the start of the wing section and a third one near the end of the wing. In addition, a strong expansion region is visible between the fuselage and the final shock. At 0° the wing shock notably strengthens, while the expansion region previously described is not visible anymore with the current scale of dp/p. Finally, the last two simulations shows that the wing shock is visibly stronger, interacting with other shocks and causing stronger compressions. As in the previous case study, the nose shock remains largely unaffected, showing only minor

deviations. Due to the specific geometry of the configuration, the flow field below the aircraft differs significantly from that above it, influencing shock propagation.

This trend is also visible for the Mach number contours, highlighted in Figure 4.8, which confirms the findings previously written.

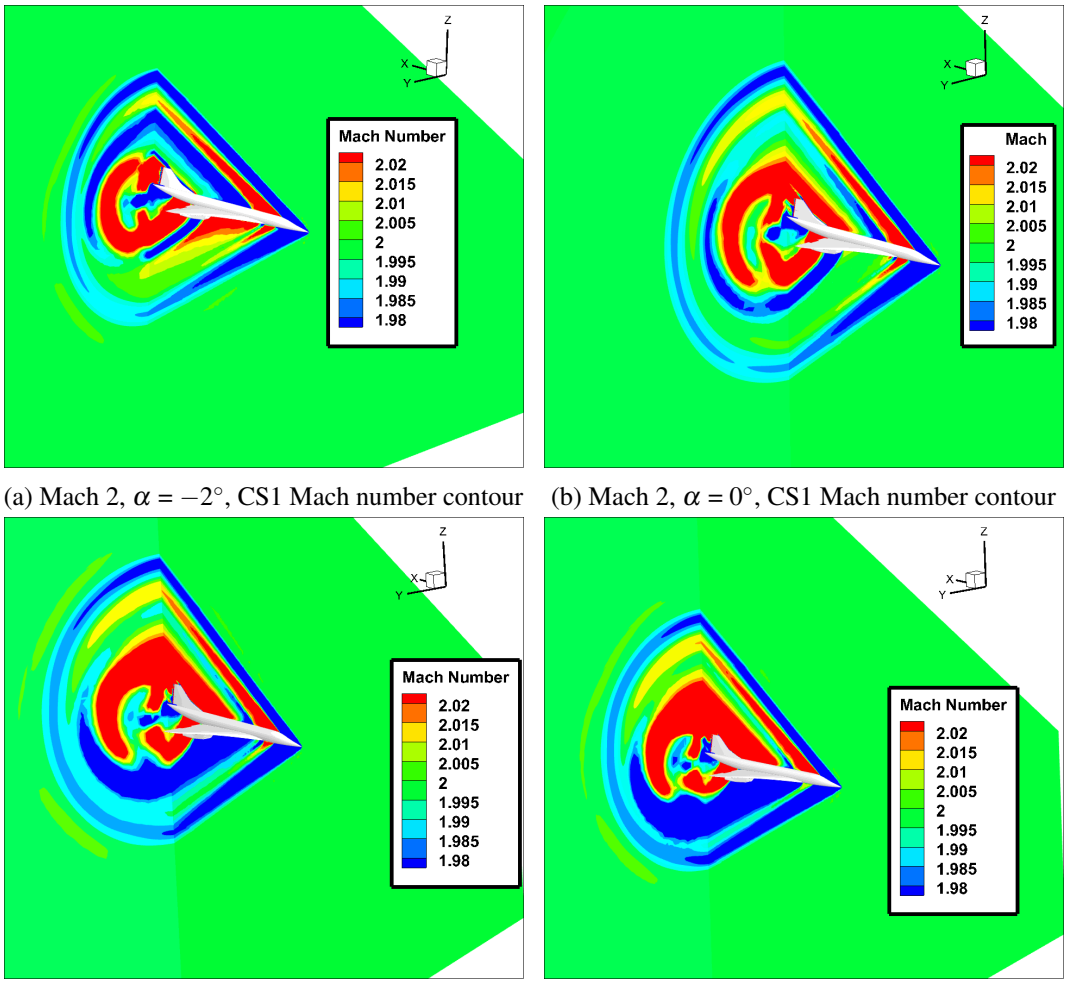

(a) Mach 2, $\alpha = -2°$, CS1 Mach number contour

(b) Mach 2, $\alpha = 0°$, CS1 Mach number contour

(c) Mach 2, $\alpha = 2°$, CS1 Mach number contour

(d) Mach 2, $\alpha = 4°$, CS1 Mach number contour

Fig. 4.8 Mach number contour CS1

As in the previous case, the extracted near-field pressure signature were computed at H/L=1 and H/L=3. Figure 4.9 highlights the results for the Mach 2 flight conditions at the closest extraction point.

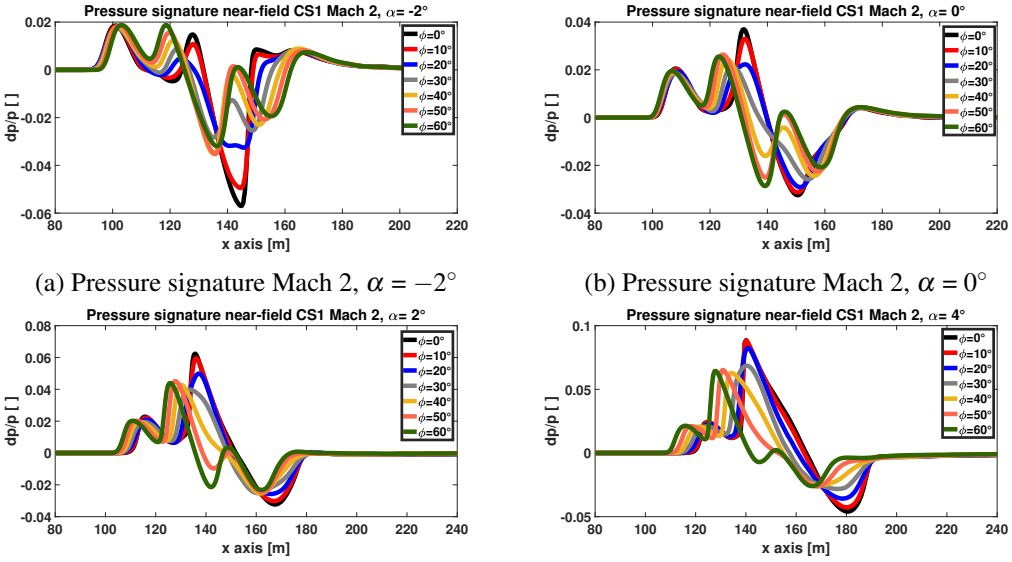

(a) Pressure signature Mach 2, $\alpha = -2°$

(b) Pressure signature Mach 2, $\alpha = 0°$

(c) Pressure signature Mach 2, $\alpha = 2°$

(d) Pressure signature Mach 2, $\alpha = 4°$

Fig. 4.9 Near-field extracted pressure signature CS1, Mach 2, H/L=1

Figure 4.9 shows clear differences in the near-field pressure signature as a function of angle of attack, and it also confirms the previous findings based on contours visualization. At -2°, multiple peaks are clearly visible. In particular, the expansion region is highly sensitive to the radial extraction angle: 0&10° show a strong expansion, whereas 20° exhibits a relatively flat pressure variation. For extraction angles of 30° and above, an additional shock appears, which increases with higher azimuth angles. At α 0°, azimuth angles of 0&10° also display strong compression in the wing region, while the differences in the expansion region are greatly attenuated, resulting in similar signature shapes. The flight conditions at 2° and 4° exhibit similar trends. In particular, the pressure signature closely resembles an N-wave shape, with an additional shock wave generated by the nose. However, the shape of the signature in the expansion region still varies depending on the radial extraction angle. The azimuth angles of 0° and 10° show the highest dp/p values, along with the largest expansion peaks toward the trailing part of the signature. These results demonstrate that increasing the angle of attack strengthens the shocks and accelerates their coalescence, confirming its significant influence on near-field shock interactions and subsequently far-field signature and noise metrics.

As for the previous configuration, the near-field pressure signature is extracted also at the vertical ratio of H/L=3, and visible in Figure 4.10.

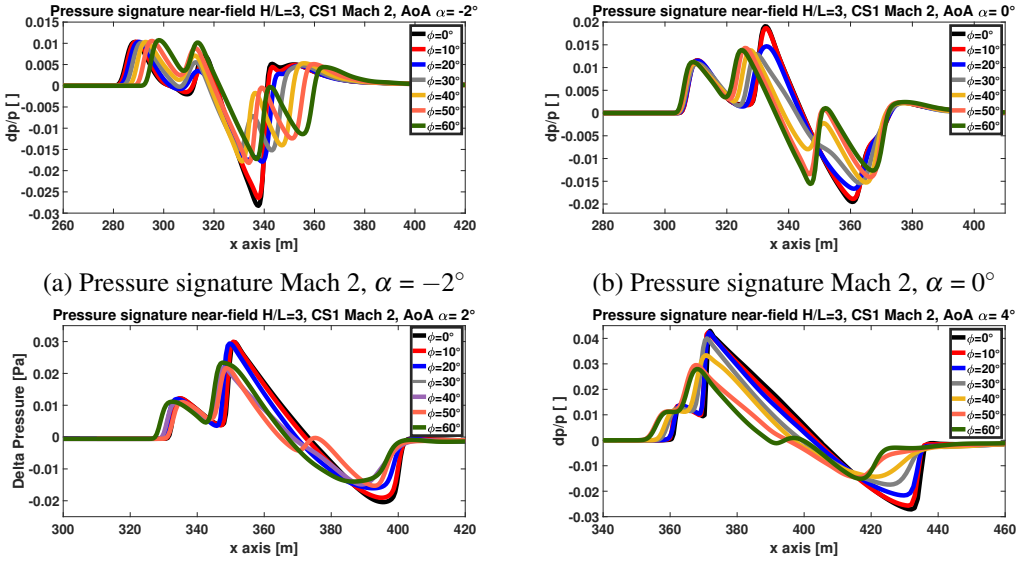

(a) Pressure signature Mach 2, $\alpha = -2°$

(b) Pressure signature Mach 2, $\alpha = 0°$

(c) Pressure signature Mach 2, $\alpha = 2°$

(d) Pressure signature Mach 2, $\alpha = 4°$

Fig. 4.10 Near-field extracted pressure signature CS1, Mach 2, H/L=3

The shape of the pressure signature varies across most of the numerical simulations between the first and second extraction points. For the flight condition at $\alpha = -2°$, the three characteristic peaks observed at H/L = 1 are still visible. However, the discrepancies between the extraction angles of $0°$ and $10°$ and the other ϕ_{CFD} values further increase. In addition, the pressure signature, extracted at $20°$ becomes more aligned with those at higher azimuthal angles, whereas, in the previous extraction point, it exhibited a flatter portion with multiple weak, barely noticeable shocks. At $0°$, the shape of the near-field waveform remains consistent with that obtained at H/L = 1, still showing three distinct shocks. Compared to the previous extraction, these shocks appear closer to merging, suggesting the onset of nonlinear coalescence. For the flight condition at $\alpha = 2°$, a similar trend is observed: the wing-induced shock moves closer to the nose-generated one, indicating stronger nonlinear steepening and early interaction between the two compression regions. Finally, for the flight condition at $\alpha = 4°$, the near-field pressure signature exhibits an almost complete N-wave structure, as the wing and nose shocks have nearly merged. This behavior is consistent with the expected nonlinear propagation effects, where increased lift and stronger pressure gradients at higher incidence promote earlier shock coalescence and a faster transition toward an N-wave shape.

Similarly to the Mach 1.5 Supersonic Business Jet, the on-track pressure signature has been evaluated for the simulations conducted. The on-track condition at H/L=1 is visible in Figure 4.11a, while the H/L=3 is highlighted in Figure 4.11b.

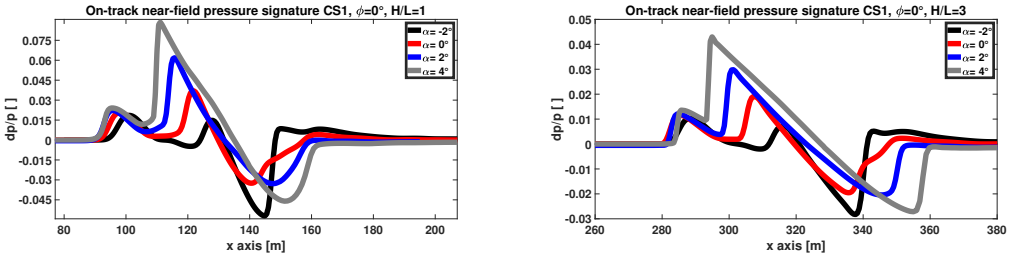

(a) On-track extracted pressure signature, H/L=1, $\phi_{CFD} = 0°$

(b) On-track extracted pressure signature, H/L=1, $\phi_{CFD} = 0°$

Fig. 4.11 On-track extracted pressure signature, $\phi_{CFD} = 0°$, CS1

Compared with the previous configuration, the pressure signature shape remains consistent across the analyzed angles of attack. All on-track signatures exhibit an initial shock generated by the aircraft nose, followed by a second compression associated with the wing. The intensity of this secondary shock depends on the angle of attack and the corresponding lift distribution along the wing. Moreover, increasing the angle of attack brings the two shocks closer together. The extraction at $H/L = 3$ reinforces these observations. At further distance for the noise source, the pressure signatures at $\alpha = 2°$ and $\alpha = 4°$ display an N-wave-like shape, with minimal spacing between the two shocks. Conversely, the other flight conditions preserve the same signature structure observed previously.

4.1.3 Mach 1.8 Supersonic Business Jet

The last configuration to be investigated is the Mach 1.8 Supersonic Business Jet. Compared to the previous case studies, the amount of simulations performed is reduced to just twelve, as it investigates the effects of including turbulence modeling in the CFD domain. While Euler equations are often favoured during the conceptual design phase for their lower computational cost and efficiency, they inherently neglect interactions between the boundary layer and shock waves. To validate the accuracy of the Euler-based results described in the previous sections, a comparative study was conducted on an internal project, comparing Euler simulations with those using the k$-\omega$ and Spalart-Allmaras turbulence models. Accurate modeling of turbulence

in the boundary layer is essential for reliable flow predictions. Neglecting boundary layer could lead to inaccurate predictions of shock-boundary layer interactions, resulting in deviations in both the intensity and position of the ground shock wave. A comparison between the Euler and RANS grids employed is visible in Table 4.5. A grid sensitivity assessment has been conducted. In particular, for the inviscid solution, a coarser grid of 13 million of elements is initially employed and subsequently verified with one of 20.3. Similarly, for the viscous cases, a coarser one of 19 million of elements is adopted. It highlights that Euler grids solve inviscid flow equations, whereas RANS grids include turbulence effects by solving additional transport equations for the Reynolds stresses.

Table 4.5 Grids adopted in this work

	Euler coarse	Euler fine	viscous coarse	viscous fine
Elements	13,251,269	20,350,562	18,840,587	27,099,384
Tetra	3,813,408	8,266,408	3,728,374	9,979,127
Hexa	8,942,732	13,512,484	8,942,732	14,512,484
Tri	207,108	212,156	205,113	210,490
Penta	0	0	5,674,121	6,030,260
Quad	198,894	254,880	200,134	254,880
Pyra	89,127	96,989	90,113	128,715

From Table 4.5, it can be observed that the structured mesh employed consists of the same number of hexahedral elements. In addition, the Reynolds-Averaged Navier-Stokes (RANS) grid incorporates an additional 6.0 million prism elements to properly model the boundary layer. As previously mentioned, 38 prism layers were generated with a first-layer height of 10^{-5} m and a height ratio of 1.18. This mesh yields a turbulent boundary-layer thickness of approximately 5.4 cm, consistent with the expected values for the simulated Reynolds-number conditions. The wall-clock time on the High-Performance Computing (HPC) cluster at Politecnico di Torino is approximately 23 hours for the Euler simulations, 45 hours for the Spalart–Allmaras simulations, and 58 hours for the k–ω simulations.

The test matrix of the simulation for the selected configuration is highlighted in Table 4.6, and just two mission points were analyzed due to time constrain.

Table 4.6 Test matrix employed Mach 1.8 Supersonic Business Jet

Test	Turbulence	angle of attack α	Mach	altitude [m]
#1	Euler	0°	1.8	15,760
#2	k$-\omega$	0°	1.8	15,760
#3	Spalart-Allmaras	0°	1.8	15,760
#4	Euler	4°	1.8	15,760
#5	k$-\omega$	4°	1.8	15,760
#6	Spalart-Allmaras	4°	1.8	15,760

The increase in static pressure contours across the Euler, k-ω, and Spalart–Allmaras simulations is visible in Figure 4.12 for the flight condition at 0° of angle of attack α.

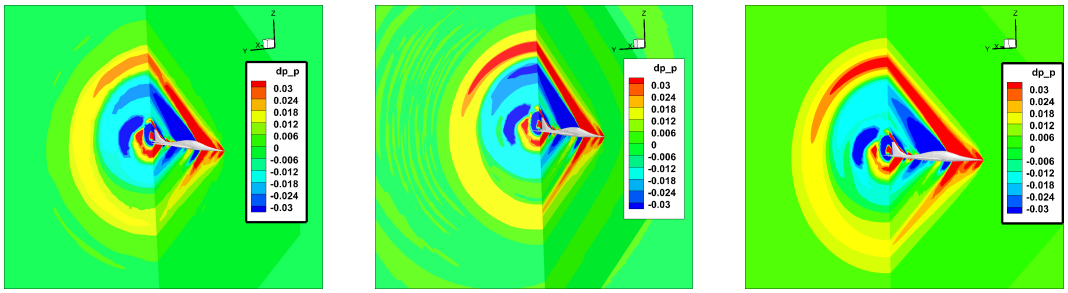

(a) Increase of static pressure contour Euler

(b) Increase of static pressure contour k-ω

(c) Increase of static pressure contour S-A

Fig. 4.12 Increase of static pressure contour Mach 1.8 SBJ, Mach 1.8

The RANS simulation contours show noticeably stronger shocks than those from the Euler simulation. This occurs because RANS models account for viscous effects in the boundary layer, which strongly influence how shocks interact with the flow near the surface. These interactions increase shock strength and also shift their positions slightly. By contrast, the Euler simulation neglects viscosity, resulting in weaker shocks and consequently they underestimate the ground-level pressure signatures and perceived loudness. In particular, the RANS static-pressure contours reveal a stronger shock in the wing region when comparing the two analyzed models. Stronger shocks also appear at azimuthal angles between 90° and 180°. Minor differences occur between the two RANS models in the 0°–90° range, whereas noticeable discrepancies arise elsewhere in the domain. Specifically, the expansion region near the wing section shows visible variations, especially around 180°. The

Spalart–Allmaras model underpredicts the expansion compared to both the Euler and k–ω simulations. Conversely, in the compression region near 90°, it produces the strongest pressure contours. The same behavior could be visible in the Mach number contour in Figure 4.13.

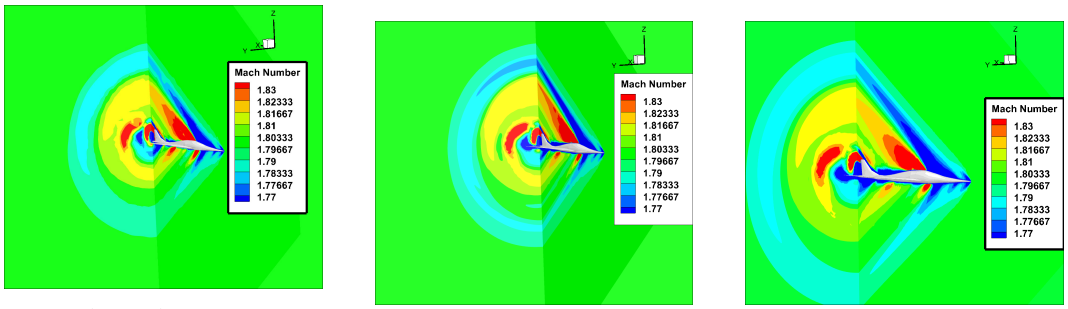

(a) Mach number contour Euler

(b) Mach number contour k-ω

(c) Mach number contour S-A

Fig. 4.13 Mach number contour Mach 1.8 SBJ configuration

The results of the Mach number contours further demonstrates the findings previously written from the increase of static pressure. As in the previous two case studies, the near-field pressure signature is extracted. The grid and solver independence study is highlighted in Figure 4.14. The deviations between the two solvers and grid are negligible, ensuring an adequate resolution of the flow-field.

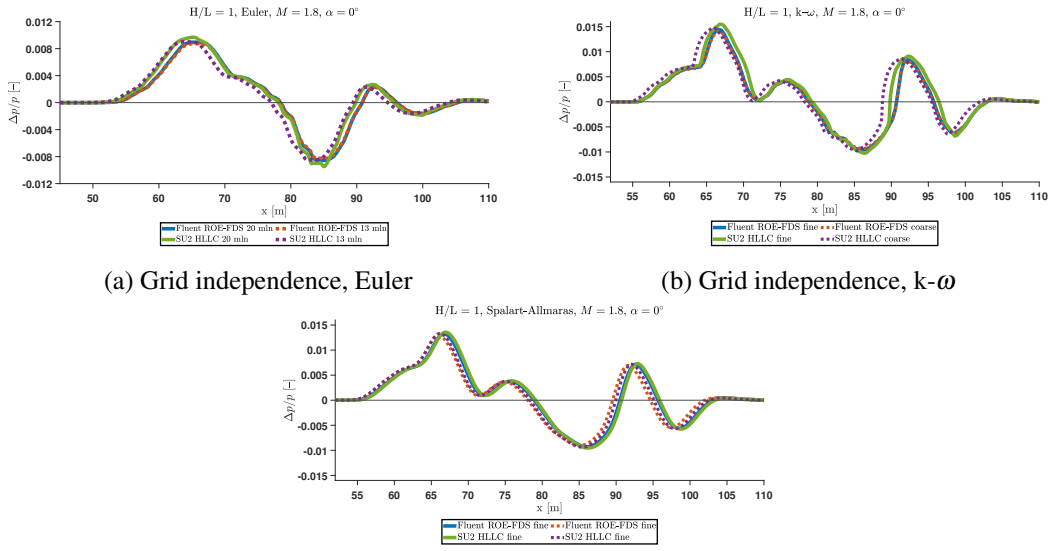

(a) Grid independence, Euler

(b) Grid independence, k-ω

(c) Grid independence, S-A

Fig. 4.14 Grid and solver independence study

A similar shape between the two viscous signatures is visible for both solvers. The coarser grid shows minimal discrepancies in the inviscid and viscous studies across the two solvers, highlighting its grid independence.

The comparison between the Euler, k-ω and Spalart-Allmaras turbulence model at a vertical distance of extraction of H/L=1 for the radial ϕ_{CFD} angle of 0° is visible in Figure 4.15.The differences in the shape of the extracted signature between the k-ω and Spalart–Allmaras turbulence models are negligible. However, the k-ω extraction has slightly higher peak values due to its tendency to predict sharper shock gradients and a more energetic near-wall flow, which in turn enhances the strength of the pressure perturbations that are subsequently propagated to the ground. In addition, the final peak in the pressure signature—associated with the engine nacelle—shows a marked discrepancy between the inviscid and viscous simulations. In both the k-ω and Spalart–Allmaras models, this shock is clearly resolved and constitutes the second-largest contribution to the overall signature, whereas in the Euler simulation it is barely discernible. Similarly, within the expansion region, the viscous models capture an additional shock primarily attributed to the wing. The slope of the expansion region differs substantially between the viscous and inviscid predictions. Although these observations were obtained using ANSYS FLUENT, SU2 simulations employing the HLLC scheme yield analogous results.

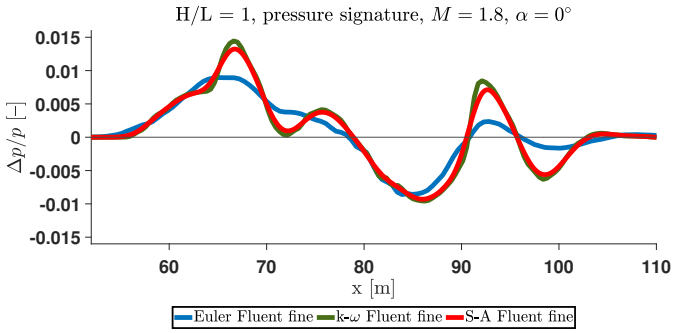

Fig. 4.15 Comparison inviscid and turbulent near-field signature

The comparison between the Euler, k-ω, and Spalart–Allmaras simulations for different radial extraction angles is shown in Figure 4.16. For clarity, the extractions at 0,30 and 60° are presented.

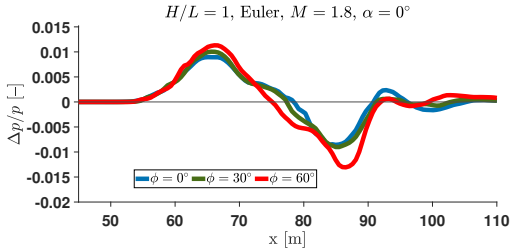

(a) Extracted near-field Euler pressure signature H/L=1

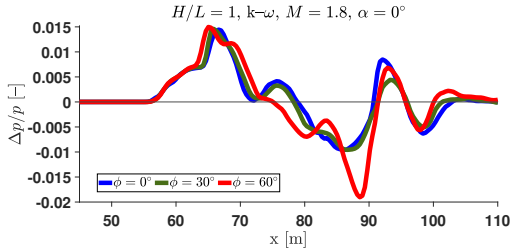

(b) Extracted near-field k$-\omega$ pressure signature H/L=1

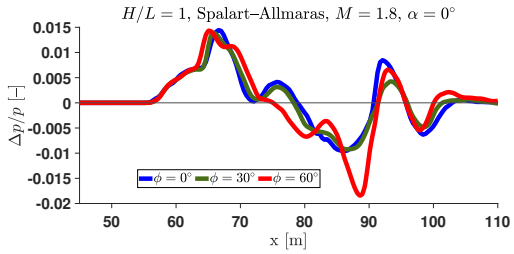

(c) Extracted near-field Spalart-Allmaras pressure signature H/L=1

Fig. 4.16 Near-field pressure signature comparison Euler, k-ω & Spalart-Allmaras, H/L=1

Across all extracted radial angles, the differences between inviscid and viscous simulations are negligible. The viscous solution exhibits a pronounced expansion at higher radial angles that is absent in the Euler solution. Furthermore, the viscous simulations display noticeable variations in waveform shape with increasing ϕ, whereas the Euler predictions remain largely invariant across the examined angular range. These results point out the important role of turbulence in shaping the near-field flow. The impact on the ground pressure signature and noise metrics are examined in the following sections, but it is already clear that the flow field predicted by the RANS simulation differs markedly from that of the Euler model. A similar analysis has been conducted for the flight condition at 4° of angle of attack α, and visible in Figure 4.17.

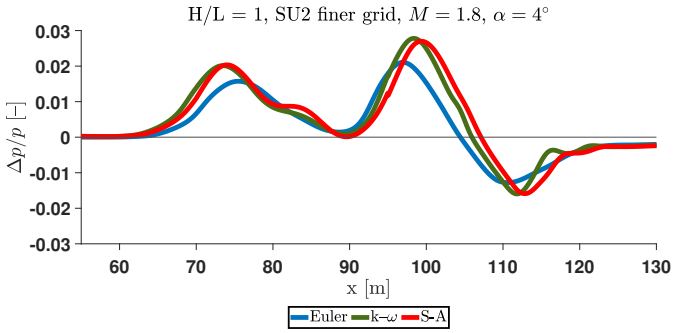

Fig. 4.17 Near-field pressure signature comparison Euler, k-ω, angle of attack $\alpha = 4°$

At a 4° incidence, differences between the inviscid and viscous on-track signatures remain noticeable. The higher lift at this condition reduces discrepancies in waveform shape, as the multiple shocks captured by the viscous model at lower incidence have already merged. The nose and canard shocks exhibit similar structures in both simulations, although intensity differences persist. The SU2 results also show shape variations relative to the FLUENT predictions. An additional shock appears in the expansion region between the nose and wing shocks, and the final shock at the end of the signature is more pronounced. The coarse-grid simulations reproduce the same trends, confirming grid independence for this case. Furthermore, the shock structure across the simulated radial angles indicates that the shape of the extracted signature remains essentially unchanged.

Finally, the extracted radial assessments are presented in Figure 4.18. For the representative extraction angle, the inviscid and viscous signatures exhibit similar overall shapes, showing a trend opposite to that observed in the previous flight condition. At 30° and 60°, both the k–ω and Spalart–Allmaras simulations display a distinct peak, attributable to the engine-nacelle shock. This feature is not present in the Euler solution.

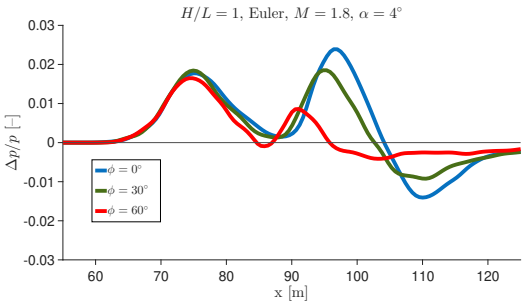

(a) Extracted near-field Euler pressure signature H/L=1

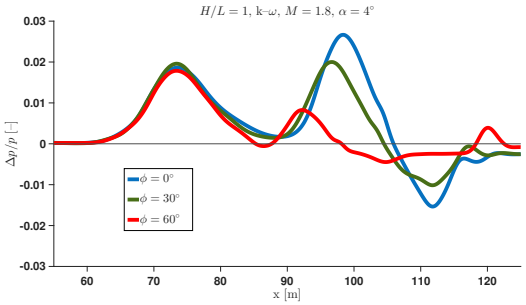

(b) Extracted near-field k$-\omega$ pressure signature H/L=1

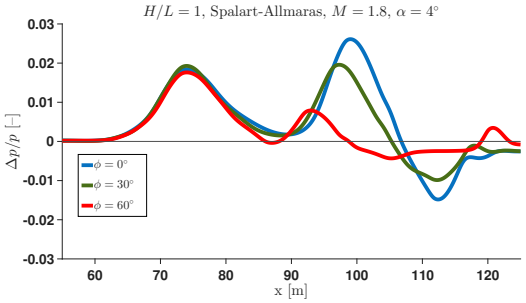

(c) Extracted near-field Spalart-Allmaras pressure signature H/L=1

Fig. 4.18 Near-field pressure signature comparison Euler, k-ω & Spalart-Allmaras, H/L=1

4.2 Far-field result

The near-field pressure signature extracted in the previous Section has to be propagated from the reference altitude to the ground within a non-uniform atmosphere to assess the community impact. As stated in the Methodology & Tools Chapter 3, two different propagation solvers are used. PCBoom version 7.1 has been used for the Mach 1.5 and Mach 1.8 Supersonic Business Jet (Section 4.2.1 & 4.2.3). On the other hand, PropaBoom solver has been used for the CS1 configuration (Section 4.2.2) and for the case studies in the Appendix B. Previous studies by Graziani et al. [243] suggested minimal discrepancies between PCBoom and PropaBoom solver for a selected case study.

4.2.1 Mach 1.5 Supersonic Business Jet

Coherently with the near-field results, the first aircraft analyzed is the Mach 1.5 Supersonic Business Jet, for which PCBoom solver has been employed. For this and the subsequently aircraft evaluated the sample frequency adopted is 200 KHz, which is in line with the value used across the different sonic boom prediction workshop. The propagation of the extracted pressure signatures from the reference cruise altitude to the ground is performed using the atmospheric profile described in Section 3.2.3. Figure 4.19 shows the ground pressure signature for the selected atmospheric profiles at cruise Mach number of 1.5 and 1.35, with a reference angle of attack α equal to 2°.

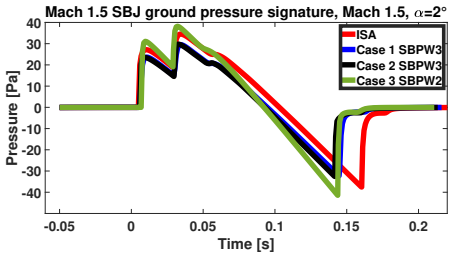

(a) Ground pressure signature Mach 1.5, AoA α = 2°

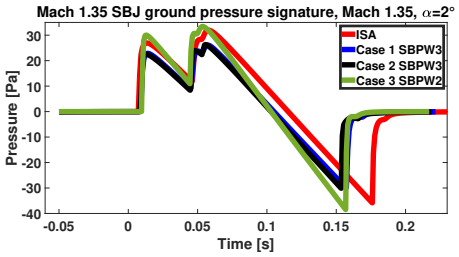

(b) Ground pressure signature Mach 1.35, AoA α = 2°

Fig. 4.19 Ground pressure signature Mach 1.5 SBJ, AoA α =2° Mach 1.35 & Mach 1.5

Figure 4.19 shows that the qualitative shape of the ground pressure signature remains broadly similar across the tested atmospheric profiles and Mach numbers. The waveform displays a characteristic pattern: an initial peak, followed by a roughly linear expansion, and then a second shock. As expected, the spacing between the two shocks tends to be larger for the Mach 1.35 flight condition, and the total duration of the ground pressure signature is slightly longer for the slower flight. Quantitatively, however, noticeable variations in peak overpressure appear even when the nominal flight conditions are the same. In colder atmospheres, the combination of higher ambient density and lower sound speed tends to enhance nonlinear attenuation during propagation, which in turn reduces the peak overpressure, and lower noise metrics. The ISA profile produces the longest ground signal, in agreement with its temperature gradient and sound-speed profile, which effectively increase the propagation path length. Variations with Mach number follow the expected trends:a lower Mach number generally reduces the peak overpressure by up to 10 Pa and diminishes

the relative strength of the wing shock. In contrast, the intensity of the nose shock appears largely unaffected by Mach number, a behavior consistent with the trends shown in Figure 4.3.

Figure 4.20 shows the influence of angle of attack variations in the ground pressure signature with a flight Mach number of 1.5, for both International Standard Atmosphere [244] and realistic atmospheric profile [196].

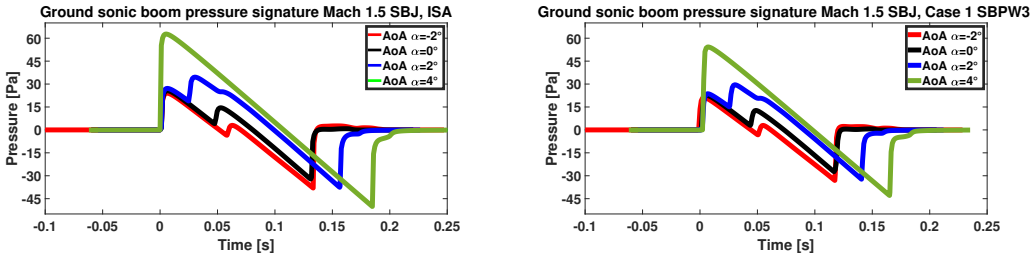

(a) Ground pressure signature ISA atmosphere (b) Ground pressure signature real atmosphere

Fig. 4.20 Effect of incidence variations in ISA and realistic atmospheric profiles on ground-level pressure signature.

Figure 4.20 illustrates the effect of small variations in the angle of attack α on the ground-level pressure signature. The analysis compares the International Standard Atmosphere (ISA) (Subfigure 4.20a) with a realistic atmospheric profile from the Third Sonic Boom Prediction Workshop (Subfigure 4.20b). As shown in the figure, at a flight condition of 4° of incidence, the ground waveform exhibits a characteristic N-wave shape, resulting in higher peak overpressure and a moderately extended signal duration. The implications of this waveform on noise metrics are discussed in the following section. A reduction in angle of attack weakens the secondary shock, primarily associated with the contributions from the wing and engine nacelle. Conversely, increasing the angle of attack modifies the lift distribution, enhancing flow compression and intensifying shock interactions. These observations are consistent with static pressure contours and near-field signature extractions. Furthermore, higher angles of attack reduce the separation between the nose shock and the shocks originating from additional lift-generating components. However, under typical cruise conditions, the resulting ground signature does not exhibit a N-wave shape signature.

Figure 4.21 highlight the ground pressure signature for both the on-track and off-track condition. While Figure 4.21a focuses solely on the ISA atmosphere due to

the symmetric primary carpet, Figure 4.21b and 4.21c focuses on the first atmosphere model of the third sonic boom prediction workshop. To improve Figure visibility, an angle step resolution of 10° is considered, while in the proximity of the limiting azimuth angle a step size of 5° is adopted.

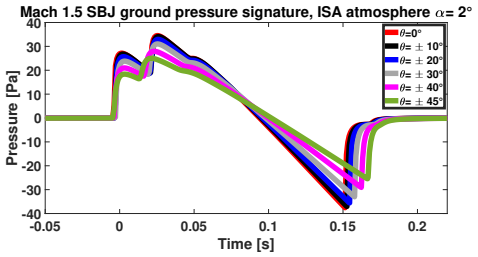

(a) ISA radial ground pressure signature, Mach 1.5 SBJ, $\alpha = 2^\circ$

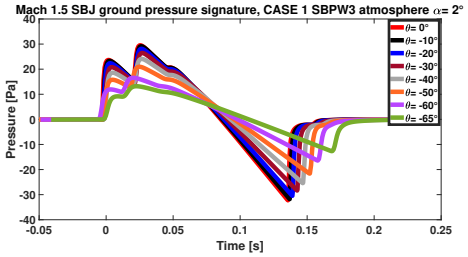

(b) Case 1 SBPW3 negative off-track, Mach 1.5 SBJ, $\alpha = 2^\circ$

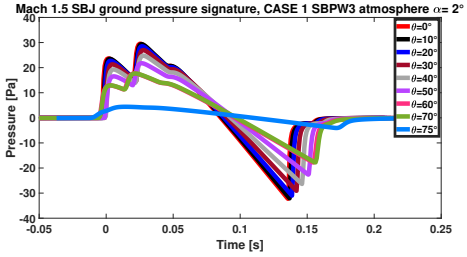

(c) Case 1 SBPW3 positive off-track, Mach 1.5 SBJ, $\alpha = 2^\circ$

Fig. 4.21 ISA & Case 1 SBPW3 radial pressure signature, Mach 1.5 SBJ, $\alpha = 2^\circ$

The figure highlights a slightly different trend between the ISA and the realistic atmospheric profiles. In the first profile considered, the reduction in peak overpressure is less pronounced, with comparable values observed near the limiting azimuth angle θ_{LIM}. Conversely, the realistic atmospheric profile exhibits a more significant variation between the maximum and minimum overpressures, along with a noticeable increase at both negative and positive azimuth angles. This behavior can be attributed to the different extents of the primary carpet. As discussed in Section 4.4, the International Standard Atmosphere profile generally produces a narrower ground footprint, whereas the realistic atmosphere was chosen from an existing database of atmospheric profiles. It is an extreme atmospheric profile that resulted in the angularly widest carpet across 5 years of data for the SBPW3 case for an eastward-flying aircraft. In particular, Figure 4.21c shows the pressure signature at an azimuth angle of 75°, which is close to the limiting value (75.08°). A marked reduction in peak overpressure can be observed at this position.

4.2.2 Mach 2 Concorde-like

Similar to the previous analyzed case study, the near-field extracted pressure signatures are propagated to the ground using the selected atmospheric profiles. Being this configuration part of the MORE&LESS project, the propagation was performed with in-house tool propaBoom. The sample frequency adopted is coherent with the one used in PCBoom, and equal to 200 KHz. Variation in the peak overpressure and noise metrics between PCBoom and propaBoom are limited, as stated in [243].

Figure 4.22 illustrates the variation in the ground pressure signature as the Mach number changes from 1.5 to the ideal cruise value of 2.0.

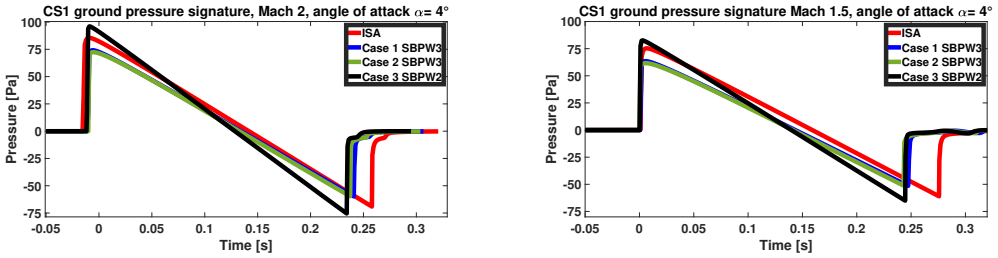

(a) Ground pressure signature Mach 2, AoA 4° (b) Ground pressure signature Mach 1.5, AoA 4°

Fig. 4.22 Ground pressure signature CS1, incidence of 4°, Mach 2 & Mach 1.5

Figure 4.22 shows that the configuration produces a fully developed ground N-wave signature at the reference angle of attack across the range of simulated Mach numbers. While the overall N-wave shape is maintained, atmospheric conditions noticeably affect both the peak overpressure and the signal duration, due to variations in sound speed, air density, and nonlinear propagation effects. Consistent with the previous case study, the International Standard Atmosphere yields the longest ground signal, whereas a colder realistic atmosphere results in the lowest peak overpressure. A reduction in Mach number primarily decreases the peak overpressure up to 20 Pascal and increases the signal duration of 0.05 seconds, while the general waveform shape remains largely unchanged.

Figure 4.23 compares the ground-level pressure signatures obtained using the previously described atmospheric profiles across the selected range of angles of attack. Figure 4.23a shows the results for the ISA profile, while Figure 4.23b highlights the one of a realistic profile.

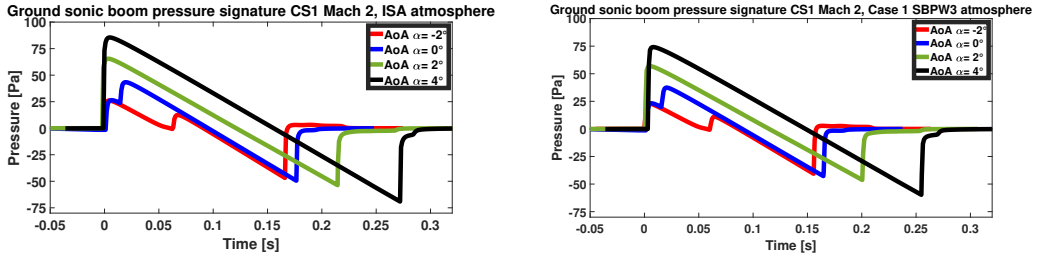

(a) Ground pressure signature Mach 2 ISA atmosphere

(b) Ground pressure signature Mach 2 realistic atmosphere

Fig. 4.23 Ground pressure signature CS1, ISA & realistic atmosphere, angle of attack α variations

Simulations indicate that, at flight conditions of -2° and 0°, the configuration produces a shaped ground waveform. Although outside the operational flight envelope, these conditions highlight the contribution of lift to ground N-wave formation without altering the aircraft layout. Increasing the angle of attack from -2° to 0° reduces the separation between the nose shock and the wing shock, indicating an imminent coalescence of shocks. This increase also significantly prolongs the signal duration for both the ISA and the realistic atmosphere. While peak overpressure and signal duration vary between the two atmospheric profiles, the overall waveform shape remains unchanged.

As for the previous configuration, the pressure signature has been evaluated across the primary carpet for the International Standard Atmosphere and for a realistic atmosphere, and reported in Figure 4.24.

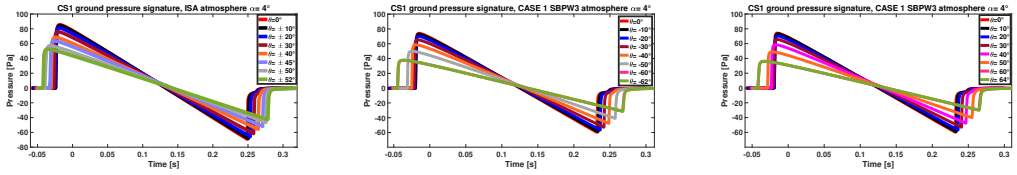

(a) ISA radial ground pressure signature, CS1, $\alpha = 4°$

(b) Case 1 SBPW3 negative off-track, CS1, $\alpha = 4°$

(c) Case 1 SBPW3 positive off-track, CS1, $\alpha = 4°$

Fig. 4.24 ISA & Case 1 SBPW3 radial pressure signature, CS1, AoA $\alpha = 4°$

From Figure 4.24, trends similar to those observed for the Mach 1.5 Supersonic Business Jet can be identified. As will be discussed later, the limited extent of the ISA primary carpet leads to smaller variations in the pressure signature in the off-track condition. In contrast, the realistic atmospheric profile produces more

pronounced variations, mainly due to the larger source-to-observer distance at higher azimuth angles. Nevertheless, for the selected atmospheric profile, the overall shape of the pressure signature remains consistent across the primary carpet, maintaining an N-wave form. As expected, increasing azimuth angles correspond to lower peak overpressures and longer signature durations.

4.2.3 Mach 1.8 Supersonic Business Jet

Lastly, the Mach 1.8 Business Jet signal is propagated for the two flight conditions simulated. As for the previous business jet configuration, the propagation has been performed with the NASA developed PCBoom solver. Previously described near-field results highlight marked differences in the extracted pressure signature between the Euler and RANS simulations. To assess the effects of the grid and solver independency, the near-field data extracted are firstly propagated for the two atmospheric profiles adopted. Figure 4.25 shows the propagated signals to the ground with the ISA profile for the on-track condition. Subfigure 4.25a shows the Euler inviscid results, while Subfigure 4.25b and 4.25c highlights the k-ω and Spalart-Allmaras ground signature, respectively. Similar results were obtained when Case 1 SBPW3 profile has been employed. As in the near-field region, negligible differences are visible between the coarser and finer grid as well as between Fluent with ROE-FDS and SU2 with HLLC. As in the previous case, the SU2 solver slightly overpredicts the maximum pressure in the resulting signature.

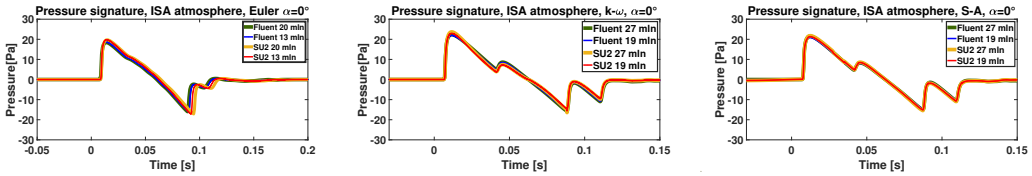

(a) Ground signature, Euler, $\alpha = 0°$ (b) Ground signature, k–ω, $\alpha = 0°$ (c) Ground signature, S–A, $\alpha = 0°$

Fig. 4.25 Ground pressure signature, $\alpha = 0°$, ISA atmosphere

The comparison between the Euler and viscous ground signatures at $\alpha = 0°$ is shown in Figure 4.26. Subfigure 4.26a reports the results obtained with the ISA profile, while Subfigure 4.26b presents those based on a realistic profile.

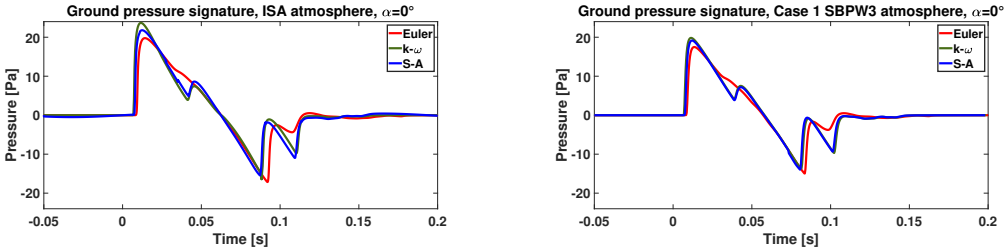

(a) Ground signature, ISA, $\alpha = 0°$ (b) Ground signature, Case 1 SBPW3, $\alpha = 0°$

Fig. 4.26 Ground pressure signature, $\alpha = 0°$

The ground-level pressure signatures exhibit marked differences between the Euler and RANS simulations. In particular, the k–ω and Spalart–Allmaras models show multiple peaks in the ground waveform that are not present in the Euler signature. This behavior is consistent with the near-field results, where the inviscid simulation shows a negligible contribution from the wing and engine nacelle, whereas the RANS models accurately capture these shock features, as previously illustrated in Figure 4.16. Moreover, the viscous simulations identify a small shock within the expansion region, attributed to the canard surface, which is not visible by the Euler model. Overall, the Euler simulations predict lower peak overpressures and shorter signal durations . In the far-field, however, the differences due to turbulence considerations are less evident than in the near-field region. The ground pressure signatures obtained from the two turbulence models also show strong agreement. Both the k–ω and Spalart–Allmaras models yield very similar waveform shapes and peak overpressures, with only minor discrepancies between them.

Figure 4.27 evaluates the deviation in the ground signature across the considered atmospheric profiles. Within a given turbulence model, differences in the resulting signature are minimal, whereas noticeable variations arise from the different atmospheric gradients. Consistent with Figure 4.26, only limited discrepancies are observed between the k–ω and Spalart–Allmaras turbulence models.

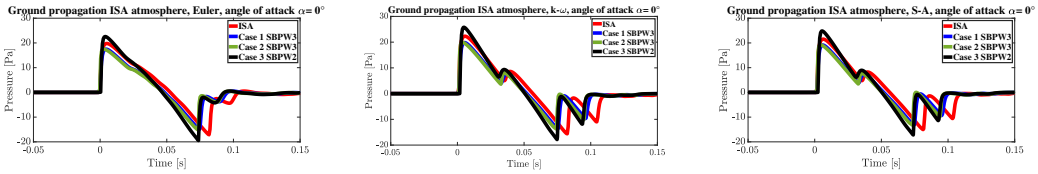

(a) Ground waveform from Euler simulation, $\alpha = 0°$ (b) Ground waveform from k-ω simulation, $\alpha = 0°$ (c) Ground waveform from S-A simulation, $\alpha = 0°$

Fig. 4.27 Comparison of ground waveforms from Euler , k-ω and Spalart–Allmaras simulation, AoA $\alpha = 0°$

To accurately assess the performance of the different turbulence models, the ground-level pressure signatures were analyzed over the entire extent of the primary carpet. Owing to the perfect symmetry of the International Standard Atmosphere, only half of the carpet was evaluated. Figure 4.28 presents results for azimuth angles θ ranging from 0° to 50°, with a step of 10°. Although the actual computation was performed with a 5° step, a coarser spacing was adopted in the plot to improve visual clarity.

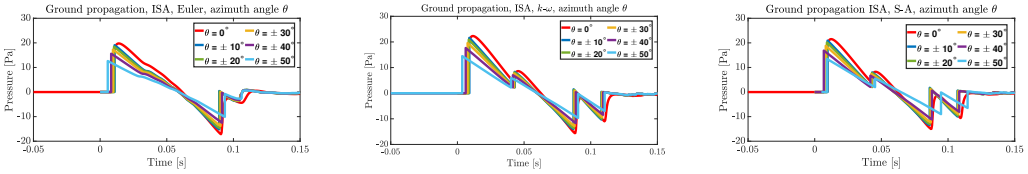

(a) Azimuth ground waveform from Euler simulation, $\alpha = 0°$ (b) Azimuth ground waveform from k-ω simulation, $\alpha = 0°$ (c) Azimuth ground waveform from S-A simulation, $\alpha = 0°$

Fig. 4.28 Comparison of azimuth ground waveforms from Euler, k-ω and Spalart-Allmaras simulation, AoA $\alpha = 0°$

As for the previously described on-track signature, the off-track signals of the viscous simulations exhibits multiple distinct shock for the simulated azimuth angles. Similarly, the Euler simulation exhibit the shape of on-track signature, with a single shock, followed by a linear expansion. Peak pressure values from the Euler simulations are consistently lower than those predicted by the k–ω and Spalart–Allmaras models across the azimuth angles. The limiting azimuth angle—the maximum angle at which shocks intersect the ground—differs slightly between the models, with 51.6 ° for the Euler simulation, 53.1 ° for the k–ω and 52.8° for Spalart-Allmaras.

The analysis is then extended to a realistic atmospheric profile, specifically Case 1 from the Third Sonic Boom Prediction Workshop (SBPW3)[196], as in the other

case studies. These features make it a particularly relevant scenario for evaluating the influence of turbulence modeling in the CFD domain and subsequent ground-level propagation. Ground pressure signatures for off-track negative azimuth angles are shown in Figure 4.29, while those for positive angles are presented in Figure 4.30.

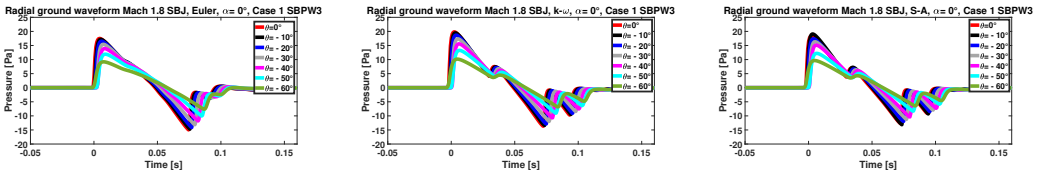

(a) Azimuth ground waveform from Euler simulation, AoA $\alpha = 0°$, off-track negative angles

(b) Azimuth ground waveform from k-ω simulation, $\alpha = 0°$, off-track negative angles

(c) Azimuth ground waveform from S-A simulation, $\alpha = 0°$, negative angles

Fig. 4.29 Comparison of azimuth ground waveforms from Euler, k-ω and Spalart-Allmaras simulation, off-track negative angles

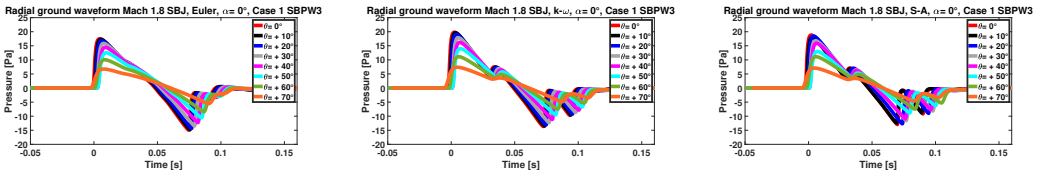

(a) Azimuth ground waveform from Euler simulation, $\alpha = 0°$, off-track positive angles

(b) Azimuth ground waveform from k-ω simulation, $\alpha = 0°$, off-track positive angles

(c) Azimuth ground waveform from S-A simulation, $\alpha = 0°$, Positive angles

Fig. 4.30 Comparison of azimuth ground waveforms from Euler, k-ω and Spalart-Allmaras simulation, off-track positive angles

Figures 4.29 and 4.30 compare the ground-level pressure signatures predicted by the two RANS simulations and the Euler one across the evaluated azimuth angles. Both k–ω and Spalart-Allmaras models produce similar results, while the Euler simulation consistently predicts lower pressures throughout the sonic boom carpet. As the International Standard Atmosphere case, the shape of the pressure signature remains consistent across the carpet even for a realistic atmosphere, for both positive and negative azimuth angles. The k–ω model generally exhibits peak overpressures that are slightly higher—by approximately 0.5 to 2 Pa—than those predicted by the Spalart–Allmaras model, while the Euler model exhibits even reduced values, even if it is comparable.

A comparable analysis was performed for the flight condition at 4° angle of attack. Due to the reduced differences demonstrated for the flight condition at

0° between k–ω and Spalart-Allmaras model, just the first has been used in the following analysis. The on-track ground pressure signature for this condition is shown in Figure 4.31.

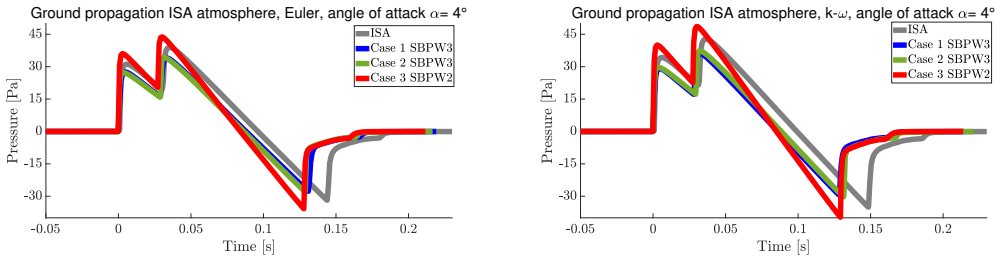

(a) Ground pressure signature Euler simulation, AoA $\alpha = 4°$

(b) Ground ground pressure signature k-ω simulation, $\alpha = 4°$

Fig. 4.31 Ground pressure signature Euler and k–ω simulation, AoA $\alpha = 4°$

The selected flight condition reveals a trend different from that observed in the previous flight condition. The distinct shock structures identified between the Euler and RANS simulations are no longer evident under this condition. This change is primarily attributed to shock interactions occurring during propagation from the reference altitude to the ground. The wing shock in the k–ω simulation appears noticeably stronger, resulting in non-negligible variations in peak overpressure across the analyzed azimuth angles. Furthermore, the signal duration is slightly longer when adopting the k–ω turbulence model in near-field simulations.

Figure 4.32 illustrates the off-track trend for the ISA atmosphere. The results demonstrate that the Euler and viscous simulations exhibit similar behavior across all evaluated azimuth angles.

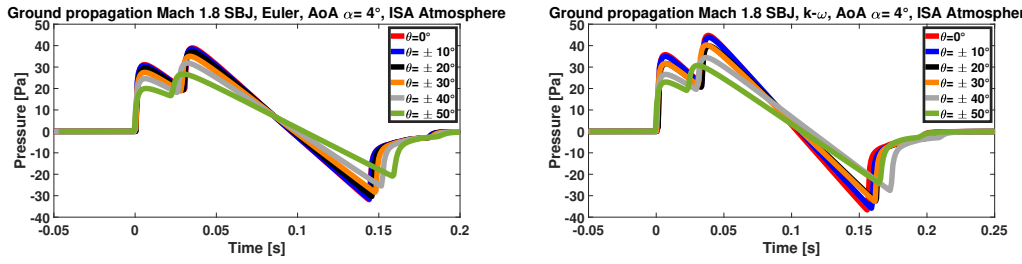

(a) Azimuth ground pressure signature Euler simulation, AoA 4°

(b) Azimuth ground pressure signature k-ω simulation, AoA 4°

Fig. 4.32 Azimuth ground pressure signature Eulerian and RANS simulation, AoA $\alpha = 4°$

Similarly to the previous case, the effects of a realistic atmospheric profile is considered, with the Case 1 SBPW3 [196] profile employed. The ground pressure signature for off-track negative azimuth angles is evaluated in Figure 4.33 in the range 0-60° range. As in the previous case, the step-size adopted in equal to 5° is considered, even if a 10° has been adopted in the plot for better visualization.

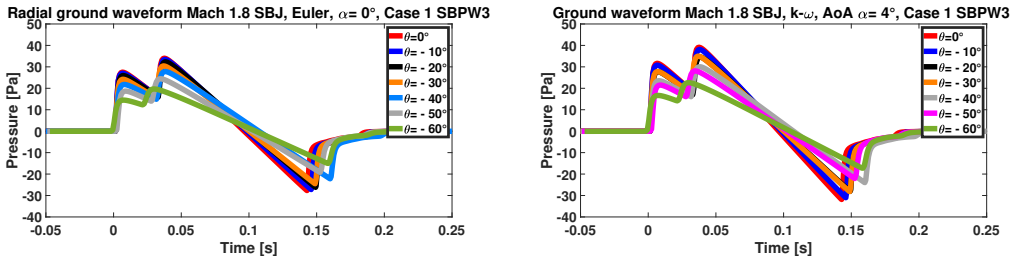

(a) Negative azimuth ground pressure signature Euler simulation, AoA $\alpha = 4°$, Case 1 SBPW3

(b) Azimuth ground pressure signature k-ω simulation, AoA $\alpha = 4°$, Case 1 SBPW3

Fig. 4.33 Negative azimuth ground pressure signature Eulerian and RANS simulation, AoA $\alpha = 4°$, Case 1 SBPW3

As the case of the International Standard Atmosphere, the shape of the pressure signature remains consistent between the two models employed. However, as stated in the previous atmospheric profile analyzed, the second shock is visibly stronger in the RANS simulation. The same analysis is performed for the positive azimuth angles in the range 0-70°, and visible in Figure 4.34, adopting the same step-size.

The previous findings related to the negative azimuth angles could be translated in the positive portion of the primary carpet. The trend visualized is similar across the simulated azimuthal angles, showing a general reduced impact compared to the previous findings highlighted in the near-field region. While not reported to better visualization, the Spalart-Allmaras results strongly aligns with the k–ω one for both the ISA and realistic atmospheric profile adopted.

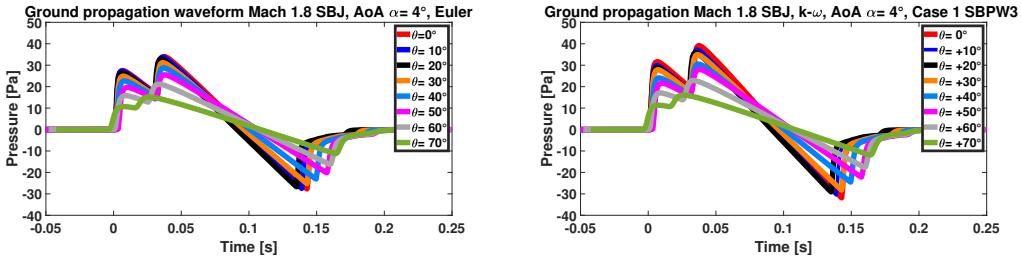

(a) Positive azimuth ground pressure signature Euler simulation, AoA $\alpha = 4°$, Case 1 SBPW3

(b) Positive azimuth ground pressure signature k-ω simulation, AoA $\alpha = 4°$, Case 1 SBPW3

Fig. 4.34 Positive azimuth ground pressure signature Eulerian and RANS simulation, AoA $\alpha = 4°$, Case 1 SBPW3

4.3 Noise Metrics

The previously obtained far-field pressure signatures are then used to quantify the psychoacoustic and energy-based metrics previously described. Future overland civil certification standards are expected to rely on threshold values of specific noise metrics to assess the perceptual annoyance experienced by ground observers. Although there is still international debate regarding the most appropriate metric to be adopted for certification purposes, this thesis focuses on noise metrics that have been previously adopted by the scientific community. The development or proposal of new or improved metrics lies beyond the scope of this work and will be addressed in the candidate's future research.

4.3.1 Noise metrics Mach 1.5 SBJ

The first aircraft simulated is the Mach 1.5 Supersonic Business Jet, coherently with the previous Sections. The selected metrics are computed across varying flight parameters and atmospheric conditions to accurately assess their influence and to provide insight for future regulatory frameworks. Although this aircraft was not specifically designed for sonic boom minimization, future high-speed configurations are expected to exhibit similar payload capacities and mission profiles. Table 4.7 summarizes these metrics for the four atmospheric profiles considered at the design cruise condition of Mach number equal to 1.5 and angle of attack equal to 2°. The reported noise metrics are based on the data extracted at the vertical ratio H/L=1.

Table 4.7 Mach 1.5 SBJ cruise design point metrics

Metric [dB]	ISA	Case 1 SBPW3	Case 2 SBPW3	Case 3 SBPW2
PL	95.27	91.94	95.26	98.67
ISBAP	102.78	100.62	102.12	105.64
ASEL	81.54	77.55	82.31	84.38
BSEL	90.63	88.87	90.71	92.86
CSEL	99.41	98.21	98.62	100.92
DSEL	90.41	88.58	90.38	92.71
ESEL	87.89	85.51	88.33	90.45

The perceived levels (PL) under on-design conditions range from 91.94 dB for the Case 1 SBPW3 atmosphere to 98.67 dB for Case 3 SBPW2, indicating a nearly 7 dB difference. Similarly, the Indoor Sonic Boom Annoyance Predictor (ISBAP) varies between 100.62 dB and 105.64 dB, reflecting approximately a 5 dB change. The acoustic energy-based metrics—ASEL, BSEL, CSEL and ESEL—exhibit consistent trends across the atmospheric cases, confirming that atmospheric variations influence the total acoustic energy of the ground-level signature. These results confirm the non-negligible impact of atmospheric conditions on the evaluated noise metrics, and it also highlight the need for future high-speed aircraft certification frameworks to account for potential deviations due to atmospheric variability.

An assessment of the sensitivity of noise metrics to near-field extraction positions was conducted. Specifically, results obtained at H/L=3 closely match those reported at H/L=1, with differences below 0.5 dB for the selected metrics, indicating that the choice of position of extraction has a negligible effect on the predicted ground-level noise. Based on the obtained results, the computational cost of the near-field simulations can be reduced by limiting the simulation domain, without introducing significant deviations in the ground results.

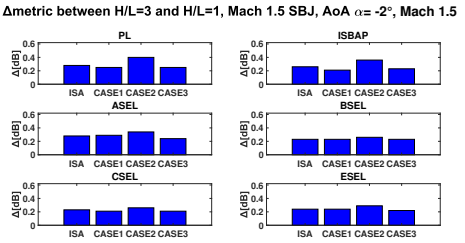

(a) Δmetrics between H/L=3 & H/L=1, $\alpha = -2°$

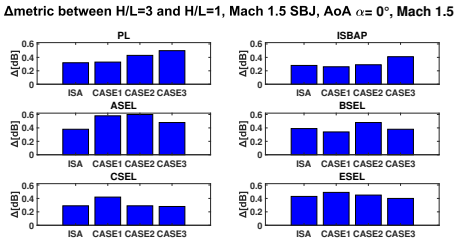

(b) Δmetrics between H/L=3 & H/L=1, $\alpha = 0°$

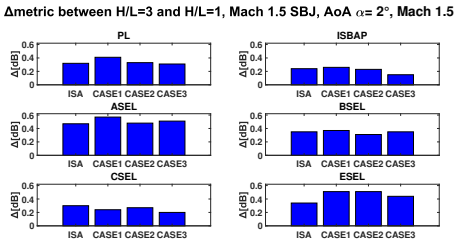

(c) Δmetrics between H/L=3 & H/L=1, $\alpha = 2°$

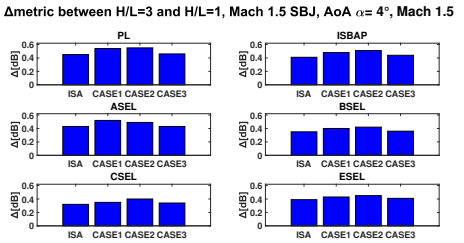

(d) Δ metrics between H/L=3 & H/L=1, $\alpha = 4°$

Fig. 4.35 Mach 1.5 SBJ Δ metrics between H/L=3 & H/L=1 extraction, Mach 1.5

Based on these findings, no specific flight condition or noise metric appears to be particularly sensitive to the extraction position. These results also support the possibility of reducing the computational domain in future numerical simulations.

The variation in the metrics due to changes in Mach number at a constant angle of attack α is depicted in Figure 4.36. The analysis maintains the incidence at 2°, corresponding to the nominal condition during the cruise flight phase, with the nominal flight condition at Mach 1.5 highlighted by a wider bar. Although some of the reported conditions fall outside the nominal mission profile, those informations are valuable for assessing the behavior of the studied metrics across different flow-field regions.

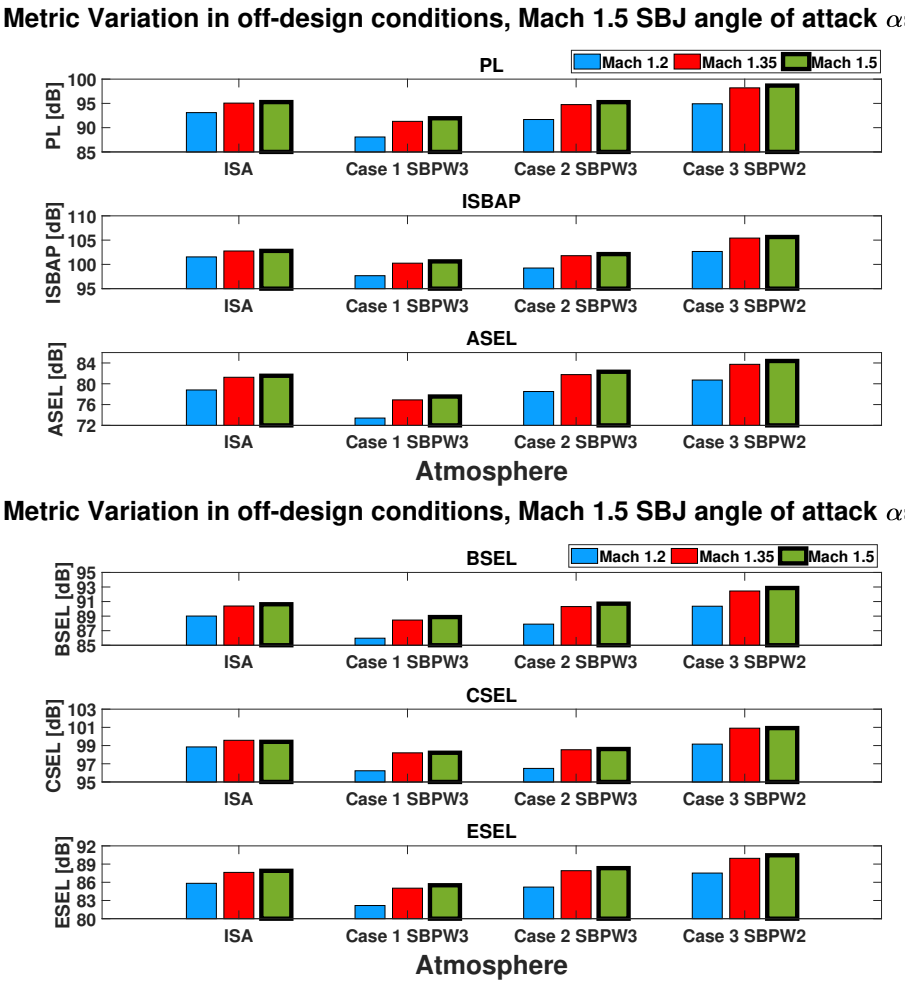

Fig. 4.36 Noise metrics variations with Mach number for the Mach 1.5 SBJ configuration, AoA $\alpha = 2^\circ$

The Figure shows that variations in Mach number have a limited effect. Reducing the Mach number slightly from the reference cruise value of 1.50 to 1.35 results in less than a 1 dB decrease across all atmospheric conditions considered. Larger deviations appear when the Mach number is lowered further to 1.20, with differences reaching up to 4 dB. This behavior is associated with the aircraft operating near the transonic regime and close to the Mach cut-off condition. The reduced flight condition strongly modifies the shock pattern and, consequently, the acoustic signature and perceived loudness. The shocks produced by the configuration are weaker, with reduced coalescence. Comparing a realistic atmospheric profile with the International Standard Atmosphere (ISA) shows that the first amplifies the variations in noise metrics. However, the amplification visible is less than 1 dB. Among the

metrics, the response to Mach number changes differs: psychoacoustic metrics such as PL and ISBAP exhibit deviations up to 4 dB, primarily because of their dependence on high-frequency content. Energy-based metrics remain relatively steady, as they primarily quantify total acoustic energy and are less sensitive to fluctuations in high-frequency content induced by atmospheric absorption; their weighting curves are level-independent. In contrast, the weighting curve used for PL varies with level to better approximate the response of the human ear.

A similar analysis evaluates the effect of variations in the angle of attack α in Figure 4.37. The results reported are based on a flight Mach number equal to 1.5. Understanding how small changes in the mission profile influence the ground-level noise metrics is essential for assessing trade-offs between aerodynamic performance and sonic boom impact on populated areas. As in the previous Figure, the on-design condition is marked by a wider bar width.

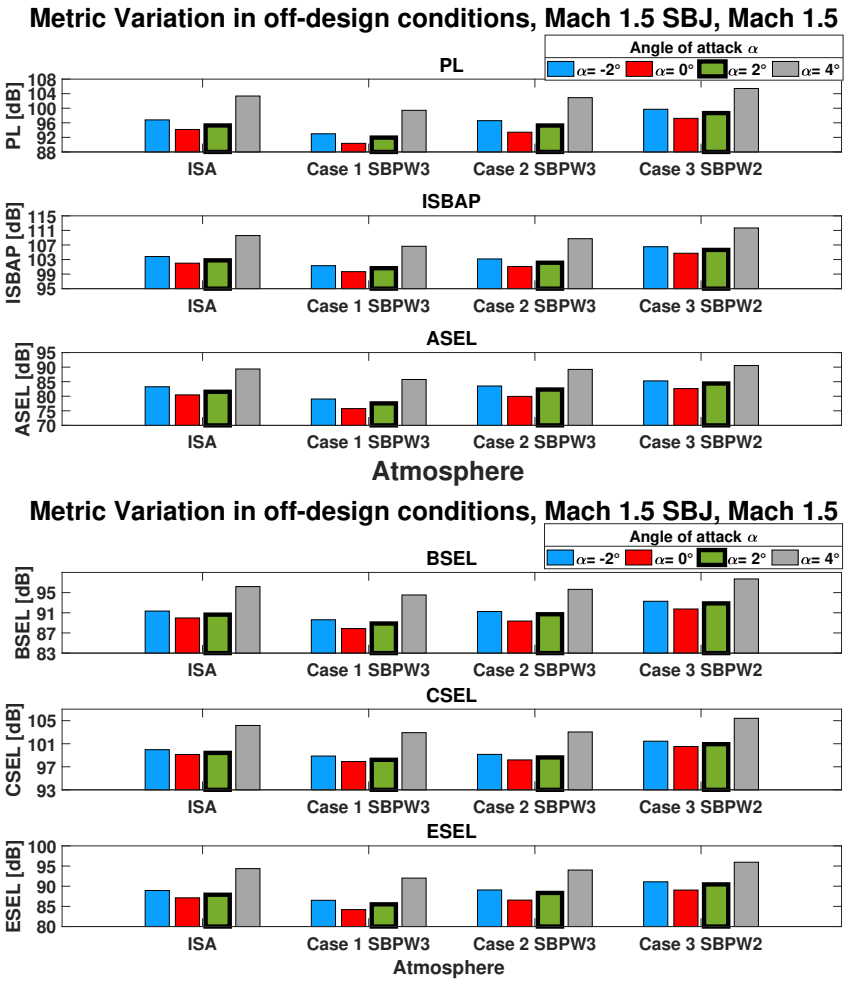

Fig. 4.37 Metrics variation with angle of attack α Mach 1.5 SBJ, Mach number 1.5

The Figure highlights a clear trend at 4° angle of incidence. It is evident that the values of the noise metrics increase significantly across all atmospheric models. At this flight condition, the ground pressure signature of the aircraft transitions from a shaped waveform to a N-wave signature, characterized by sharp shock fronts and elevated peak overpressures. These characteristics increase both energy-based metrics (e.g., SEL) and psychoacoustic metrics (e.g., PL, ISBAP), indicating potentially greater perceived annoyance. Conversely, shaped pressure signatures, such as those presented in Figure 4.20, correspond to lower noise levels and reduced psychoacoustic responses. Variations up to 7 dB occurs in the metrics between the flight condition at 2° of incidence ad 4. Avoiding flight conditions that produce a ground N-wave signature throughout the entire mission profile is therefore critical for

reducing sonic boom impact on populated areas for the next generation of supersonic civil aircraft's.

The evolution of the PL and DSEL noise metrics across the primary carpet for the simulated atmospheric profiles is shown in Figure 4.38. The flight condition reported is the on-design flight at $M_\infty = 1.5$ and $\alpha = 2°$.

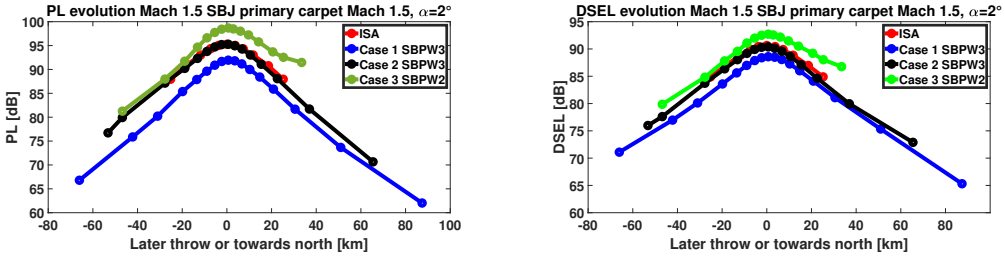

Fig. 4.38 PL and DSEL distribution at on-design conditions for different atmospheric profiles

PL distribution is strongly influenced by the atmospheric profile. The International Standard Atmosphere has a symmetric lateral profile, while the SBPW3 profiles (Case 2 and Case 1) generate lower PL values, reduced by approximately 1–3 dB, respectively. The warmer atmospheric profile instead produces higher PL values across the carpet, with increments up to 4 dB for positive lateral throw. In the realistic profiles, vertical and horizontal wind profiles alter shock refraction, which lowers amplitude and introduces asymmetry in the lateral distribution. At higher temperature, the molecular relaxation absorption of O_2 and N_2 is reduced, leading to weaker attenuation of the high-frequency components of the boom signature. This sustains higher peak amplitudes during propagation and results in increased PL.

The evolution of the D-weighted Sound Exposure Level (DSEL) across the primary carpet exhibits trends similar to PL but with reduced sensitivity to atmospheric variations. As an energy-based metric, DSEL integrates the total acoustic energy over the shock waveform rather than emphasizing instantaneous peak levels. Consequently, variations in shock amplitude and high-frequency content caused by wind-induced refraction or temperature-dependent molecular absorption have a smaller relative impact.

4.3.2 Noise metrics Concorde-like

Similarly to the Mach 1.5 business jet configuration, the ground level pressure signature is evaluated using the same set of noise metrics. Table 4.8 highlights the results of the on-design cruise condition for the CS1 case study, at a Mach number of 2, angle of attack of 4° and reference cruise altitude of 59,000 ft.

Table 4.8 CS1 cruise design point psychoacoustics and energy-based metrics

Metric [dB]	ISA	Case 1 SBPW3	Case 2 SBPW3	Case 3 SBPW2
PL	107.52	102.30	105.40	109.36
ISBAP	113.37	109.46	111.34	115.26
ASEL	93.02	88.7	91.6	94.09
BSEL	99.34	97.88	98.58	100.72
CSEL	106.96	105.74	105.76	108.16
DSEL	100.31	98.02	99.32	101.32
ESEL	97.83	95.72	97.22	99.28

Compared to the results for the Mach 1.5 Supersonic Business Jet reported in Table 4.7, the CS1 configuration shows an increase of approximately 10 dB across the selected metrics in his cruise design point. Perceived Loudness (PL) ranges from 102 to 109 dB, exhibiting variations similar to those observed in the previous configuration. Consistent with the earliest scenario, the metrics most robust to atmospheric changes are the B-, C- and D-weighted sound exposure levels. The B-weighted SEL applies a filter approximating the human ear's sensitivity to mid-frequency sound, while CSEL features a flatter frequency response at low frequencies, as shown in Figure 3.9. However, CSEL statistically correlates poorly (R_s^2) across different studies, particularly when comparing indoor and outdoor measurements [46]. In contrast, PL and A-weighted SEL exhibit the highest sensitivity to both configuration and atmospheric variations.

Figure 4.39 illustrates the influence of the near-field extraction position on the predicted noise metrics. The overall trends closely resemble those observed for the previous configuration. Differences in both psychoacoustic and energy-based metrics remain within 0.75 dB across all cases. Psychoacoustics metrics PL and ISBAP are more sensitive, with notable differences visible at the 4° flight condition Therefore, within the considered range of distances and configurations, the choice

of near-field extraction point does not critically affect the assessment. However, for this configuration, the discrepancy between position of extraction is larger than that observed for the business jet. Therefore, position of extraction of H/L=1 should be used preliminary to obtain quantitative results, since H/L=3 is preferred for higher quality results.

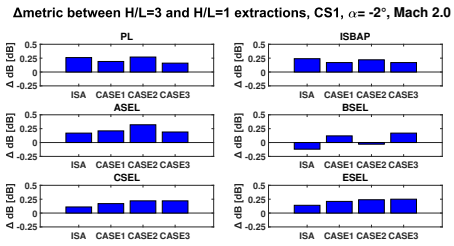

(a) CS1 Δmetrics between H/L=3 & H/L=1, $\alpha = -2°$

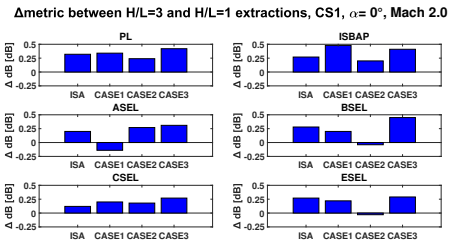

(b) CS1 Δmetrics between H/L=3 & H/L=1, $\alpha = 0°$

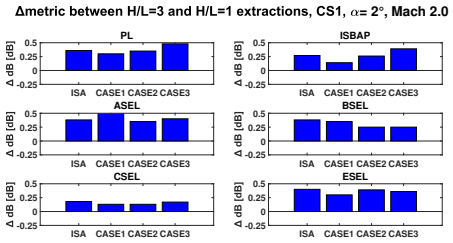

(c) CS1 Δmetrics between H/L=3 & H/L=1, $\alpha = 2°$

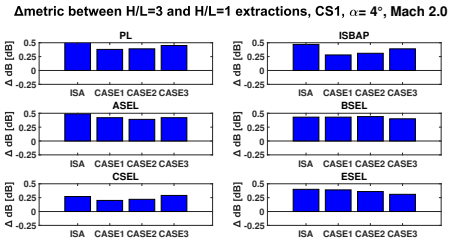

(d) CS1 Δ metrics between H/L=3 & H/L=1, $\alpha = 4°$

Fig. 4.39 CS1 Δ metrics between H/L=3 & H/L=1 extraction, Mach 2.0

As for the previous case study, the deviations in noise metrics with Mach number variation are evaluated in Figure 4.40. In this analysis, the angle of attack is set to 4°, corresponding to the cruise condition (Figure 2.7b). The nominal scenario is highlighted by a wider bar.

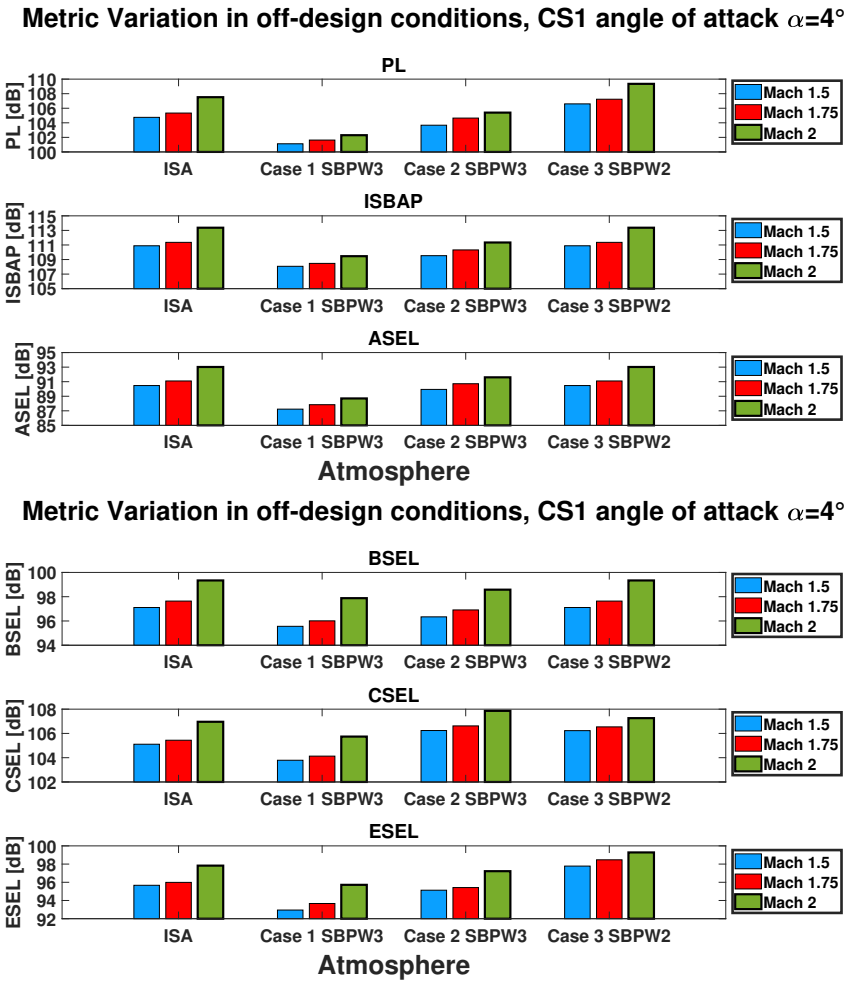

Fig. 4.40 Noise metrics variation with Mach number, $\alpha = 4°$

For the CS1 configuration, the variation of both psychoacoustic and energy-based metrics with Mach number exhibits distinct behavior. For the previous configuration, the reduction of the Mach number to 1.20 led to variations in the metrics of up to 4 dB, which can be attributed to flow conditions approaching the transonic regime.

In contrast, the CS1 aircraft exhibits smaller deviations in the evaluated metrics, with variations limited to approximately 2.5 dB between the flight condition at Mach 1.5 and Mach 2. This reduced sensitivity is due to the cruise angle of attack of 4°, which consistently produces a ground N-wave shape signature, maintaining the overall shock structure. Consequently, both psychoacoustic and energy-based metrics remain relatively stable. This behavior underscores the strong influence of

near-field shock formation and coalescence on the robustness of the ground-level acoustic signature.

A similar analysis is conducted for the variation of the angle of attack in Figure 4.41, with the on-design cruise point marked with a wider black bar.

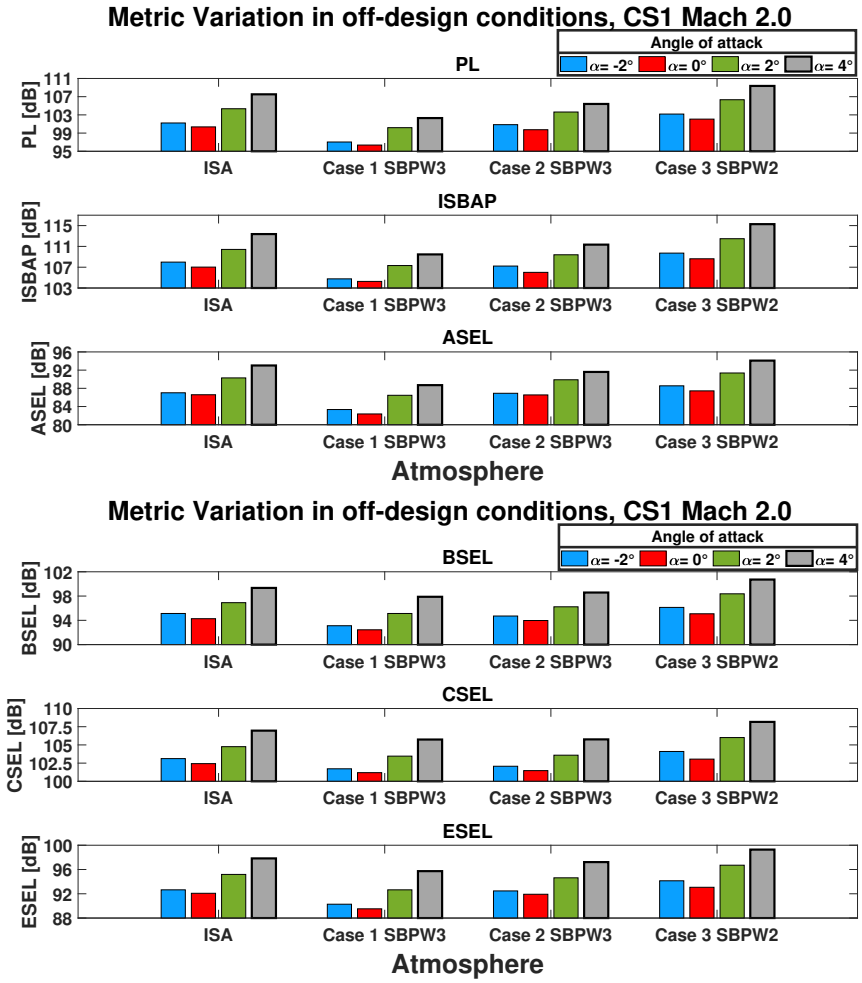

Fig. 4.41 Noise metrics variation with angle of attack CS1, Mach 2

The Figure shows a noticeable reduction in both psychoacoustic and energy-based metrics at angles of attack of $-2°$ and $0°$. These differences are primarily linked to the shape of the ground-level pressure signature: at these angles, the near-field shock interactions do not produce a N-wave signature, unlike other flight conditions. As illustrated in Figure 4.23, this occurs for both the International Standard Atmosphere and the realistic atmospheric profiles evaluated. The absence of a ground N-wave

leads to lower peak overpressures and altered pressure gradients, which in turn influence both energy-based and psychoacoustic metrics.

The PL and DSEL distribution across the primary carpet for the CS1 aircraft is shown in Figure 4.42, with a step size of 5° in the azimuth angle.

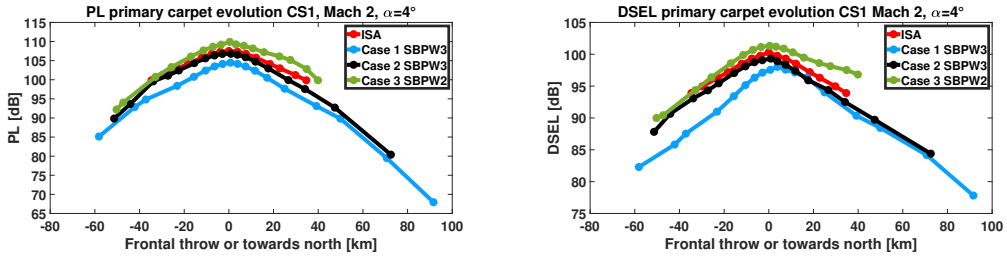

Fig. 4.42 PL and DSEL distribution at on-design conditions for different atmospheric profiles, CS1 aircraft.

As for the previous configuration, the PL distribution for CS1 is strongly influenced by the atmospheric profile. The ISA profile produces a symmetric lateral distribution, whereas realistic atmospheres exhibit deviations due to wind shear. Consistent with the on-track results, the Case 1 profile [196] generates lower PL values, although the reductions are smaller than those observed for the previous configuration.

In a realistic atmospheric profile, vertical and horizontal wind gradients modify shock refraction, reducing peak overpressures and introducing asymmetry in the lateral distribution. The warmer atmospheric profile sustains higher PL values across the carpet, though the increase relative to ISA is smaller than for the previous configuration. These trends confirm that PL is sensitive to both thermodynamic (temperature) and kinematic (wind) atmospheric variations, with the magnitude of the effect depending on vehicle speed, altitude, and shock formation.

The evolution of D-weighted Sound Exposure Level (DSEL) across the primary carpet follows trends similar to PL, reflecting the influence of atmospheric profiles. Because DSEL integrates the total acoustic energy of the shock waveform, it is generally less sensitive to localized amplitude variations caused by wind-induced refraction or temperature-dependent absorption, as already visible in the first configuration. Nevertheless, in regions of negative frontal throw, DSEL deviations are more pronounced for the Case 1 SBPW3 profile, reaching reductions of up to 5 dB.

4.3.3 Noise metrics Mach 1.8 Supersonic Business Jet

Similarly to the previous case studies, the noise metrics for the simulated flight conditions are evaluated. This section specifically examines the influence of CFD turbulence modeling on the variation of these metrics, providing guidance for future simulation activities. The values obtained for the selected metrics at a simulated angle of attack of 0° is shown in Figure 4.43.

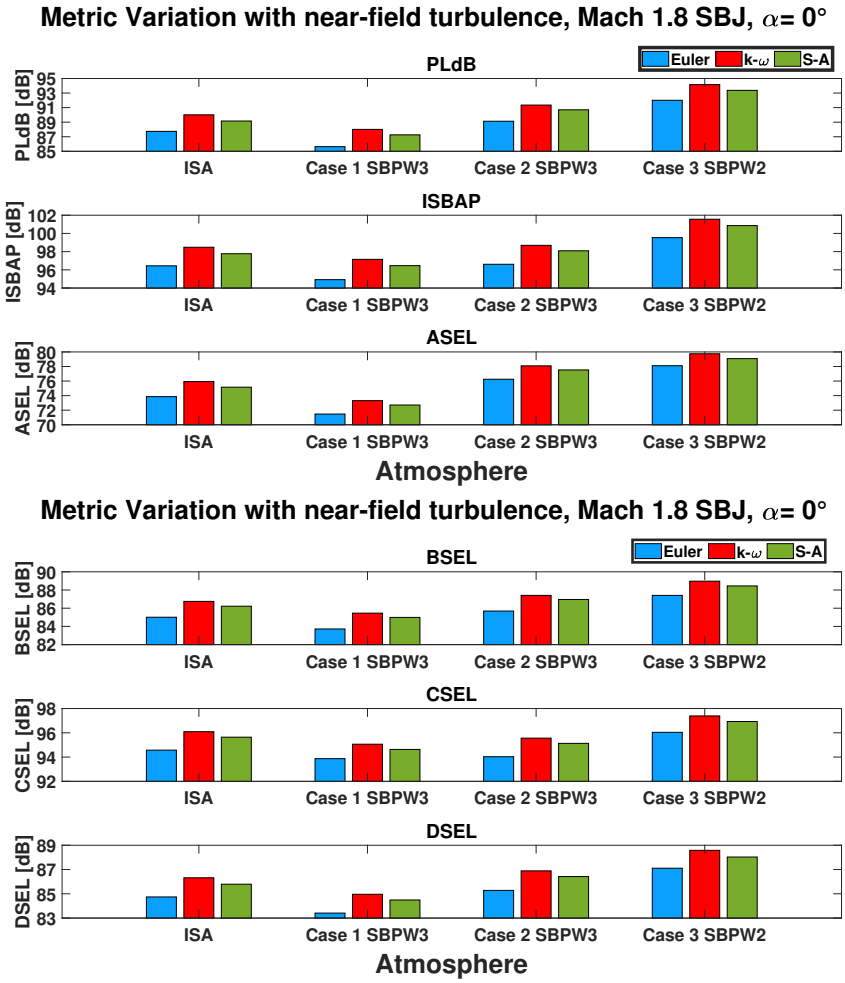

Fig. 4.43 Noise metrics variation with turbulence Mach 1.8 SBJ, angle of attack $\alpha = 0°$

It can be observed that the variation resulting from the inclusion of different turbulence models within the near-field region remains within 2 dB. Turbulent simulations account for boundary layer effects and viscous interactions, which introduce additional high-frequency content and secondary shock structures, contributing to

an increase in the metrics. Furthermore, the ISA atmosphere exhibits slightly larger variations compared to realistic atmospheric profiles, although these deviations remain limited. The differences between the two turbulence models considered—k–ω and Spalart–Allmaras—are negligible, on the order of 0.5 dB.

This configuration exhibits low-boom characteristics, with a ground-level PL below 90 dB for three of the four selected atmospheric profiles. Compared to the Mach 1.5 Supersonic Business Jet and CS1 configurations, it predicts lower PL for an observer on the ground, with reductions of 7 dB and 15 dB relative to their respective reference cruise points. Notably, it is the only configuration that produces a shaped sonic boom ground pressure signature at a 4° angle of attack, reducing perceived annoyance during the non-nominal flight phases. Although transient simulations would be required to fully verify this observation, this effect is clearly absent in the other configurations.

The values of the selected psychoacoustic and energy-based metrics at a flight condition with angle of attack $\alpha = 4^\circ$ are shown in Figure 4.44. As observed for the flight condition at $\alpha = 0^\circ$, variations in the noise metrics remain within 1.5 dB between the Euler and RANS simulations. Similarly, differences between the k–ω and Spalart–Allmaras models are negligible, with variations up to 0.3 dB. These results are consistent with the findings from the far-field analysis, indicating that at an angle of incidence of 4° the deviations are reduced compared to the other flight condition simulated. This confirms that, despite differences in the near-field flow, the choice of turbulence model has a limited effect on the predicted ground-level sonic boom for the flight conditions considered.

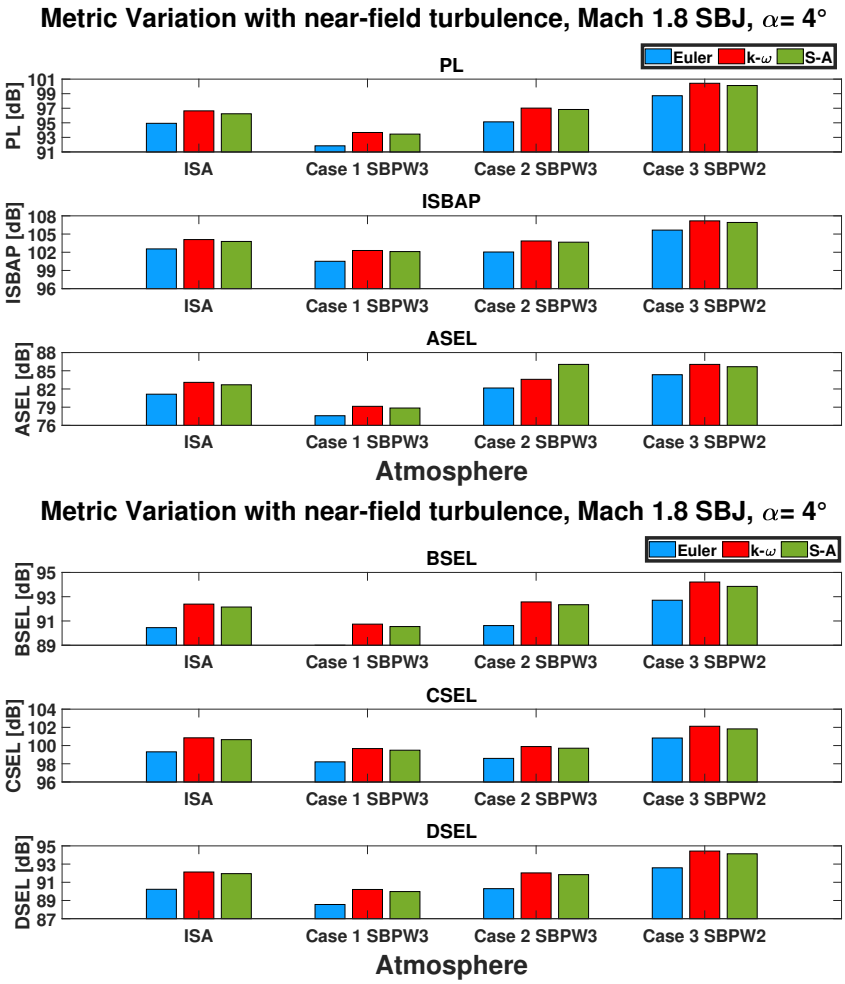

Fig. 4.44 Noise metrics variation with turbulence Mach 1.8 SBJ, angle of attack $\alpha = 4^\circ$

The results presented in Figure 4.44 demonstrate that this configuration produces lower values of noise metrics across all flight conditions compared to the business jet discussed in Section 4.1.1. These differences are amplified at $\alpha = 4^\circ$ due to the shaped pressure signature of the current configuration relative to the previous case studies.

As observed for the previous configurations, Figure 4.45 illustrates the influence of different near-field extraction positions on the predicted noise metrics for both Euler and RANS simulations.

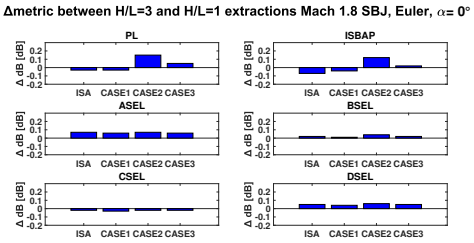

(a) Variation in the metrics Euler simulation

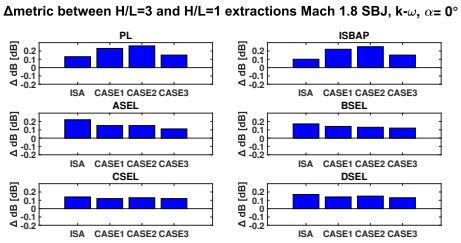

(b) Variation in the metrics k-ω simulation

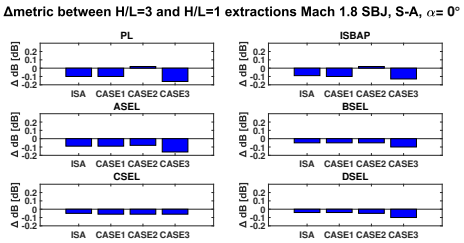

(c) Variation in the metrics Spalart-Allmaras simulation

Fig. 4.45 Δ noise metrics between H/L=3 & H/L=1 extractions, Mach 1.8 SBJ

At the design points considered, the selected noise metrics vary by less than 0.4 dB for both the Euler and RANS simulations. The agreement in the metrics with different extraction positions demonstrates that the mesh resolution is adequate to capture the main flow features for both cases, even with different physical models employed. In addition, the agreement suggests that numerical errors due to grid generation are negligible.

Similarly to the previously analyzed configurations, the Perceived Level (PL) and DSEL values were compared across the primary carpet for both the International Standard Atmosphere and a realistic atmospheric profile. Figure 4.46 illustrates the PL distribution, with Figure 4.46a detailing the flight condition at 0° and Figure 4.46b presenting the simulation at 4°.

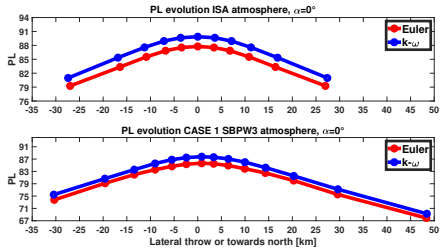

(a) Mach 1.8 SBJ PL distribution, $\alpha = 0°$

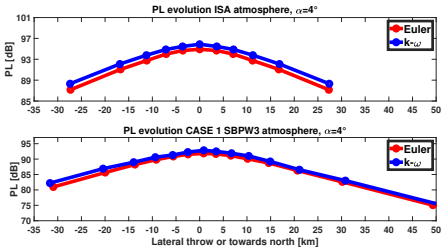

(b) Mach 1.8 SBJ PL distribution, $\alpha = 4°$

Fig. 4.46 PL distribution for the Mach 1.8 Business Jet at angles of attack $\alpha = 0°$ and $\alpha = 4°$.

It can be observed that the discrepancies between the Euler and k–ω results are more pronounced for the flight condition at 0° incidence. This behavior is consistent with the previous findings indicating smaller differences in the ground pressure signature at 4° of incidence, due to the domination of shock interactions. The ISA atmosphere leads to slightly larger deviations between the two turbulence models, reaching up to 2.5 dB. Conversely, the adoption of a realistic atmospheric profile reduces these differences to below 1 dB, which can be considered negligible, while decreasing the overall computational cost up to 60%. While the simulations performed are reduced in number, they provide valuable suggestion for future analysis.

A similar consideration can be made for the energy-based metric DSEL, shown in Figure 4.47. In particular, the largest discrepancies between the Euler and k–ω simulations occur at 0° incidence under the International Standard Atmosphere, consistent with the trend observed for the PL metric.

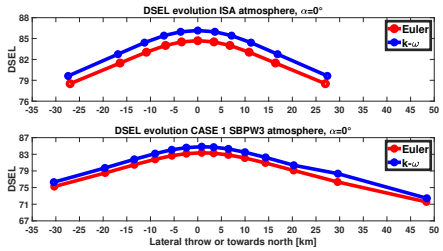

(a) Mach 1.8 SBJ DSEL distribution, $\alpha = 0°$

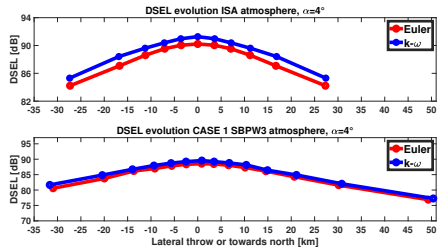

(b) Mach 1.8 SBJ DSEL distribution, $\alpha = 4°$

Fig. 4.47 DSEL distribution Mach 1.8 Business Jet, angle of attack $\alpha = 0$ & 4°

4.4 Sonic boom primary carpet evaluation

As previously discussed, the simulation of ground-level sonic boom footprints begins with a ray-tracing algorithm that accounts for atmospheric refraction in a non-uniform medium. For all simulated aircraft, the flights are assumed to be heading east.

Under the International Standard Atmosphere (ISA), which assumes no wind, this eastward heading has no effect on the lateral spread of the sonic boom. However, when realistic atmospheric profiles with wind are considered—such as those from the Second and Third Sonic Boom Prediction Workshops (SBPW2 and SBPW3)—the eastward heading interacts with atmospheric asymmetries. In these cases, the port-side lateral throw is deflected northward, while the starboard-side throw is deflected southward. High-fidelity simulations of the primary carpet extension are essential for regulatory authorities. Since ground-level sonic boom disturbance may be subject to noise metric thresholds, it is crucial to accurately determine both the spatial extent and the intensity of the disturbance across the entire affected area.

4.4.1 Mach 1.5 Supersonic Business Jet

The first configuration for which the primary carpet was assessed is the Mach 1.5 Supersonic Business Jet. Figure 4.48 illustrates the on-design conditions for the four selected atmospheric profiles, with the aircraft assumed to be positioned at the origin $(0,0)$ of the reference axial system.

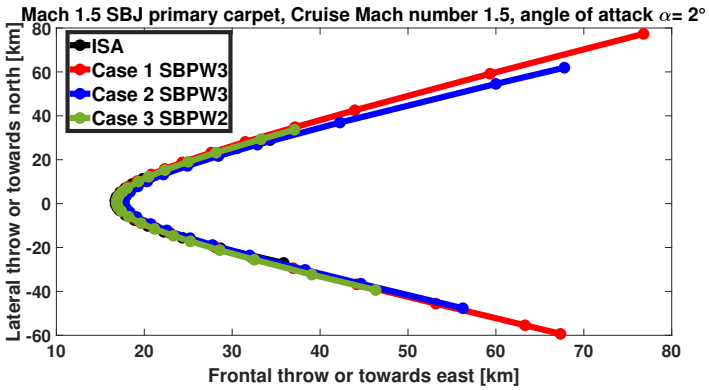

Fig. 4.48 Mach 1.5 Supersonic Business Jet on-design primary carpet

The results indicate that variations in the primary carpet width—both lateral and frontal—are significant across different atmospheric conditions. As expected, the atmospheric profiles from SBPW3 produce noticeably wider carpets, particularly in the eastward direction. Specifically, the lateral extent of the primary carpet for the SBPW3 Case 1 atmospheric profile reaches approximately 140 km in the on-design condition for the selected aircraft.

Figure 4.49 shows the influence of Mach number variation on the primary carpet, while keeping the angle of attack constant to 2°. It is also pointed out the limiting azimuth angle θ_{LIM}.

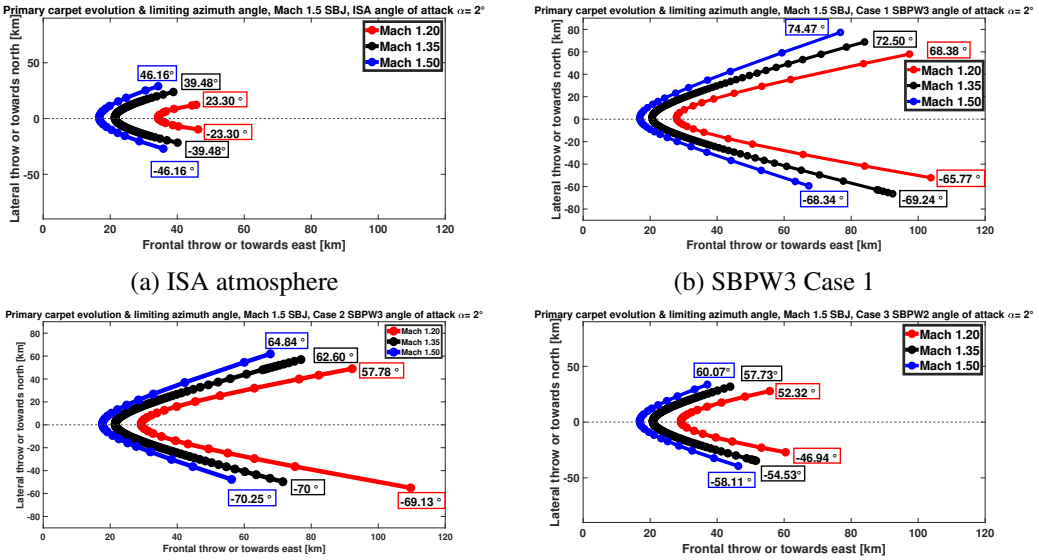

(a) ISA atmosphere

(b) SBPW3 Case 1

(c) SBPW3 Case 2

(d) SBPW2 Case 3

Fig. 4.49 Primary carpet variation and limiting azimuth angles with Mach number, ISA & realistic atmosphere

The effect of Mach number appears clearly across the atmospheric profile studied. In particular, higher speeds produce a narrower Mach cone, causing rays to propagate at smaller angles relative to the aircraft's axis, and this decreases the frontal boom throw while increasing lateral dispersion at ground level. The increase in the limiting azimuth angle with Mach number arises from the Mach cone geometry: as the Mach number increases, the cone angle decreases, causing the shock waves to propagate more obliquely relative to the flight path and thereby allowing the shocks to reach the ground at larger lateral angles.

In contrast to the noise metrics, which show noticeable sensitivity to changes in angle of attack, the primary carpet is relatively insensitive to such variations. This is because the carpet's lateral and longitudinal extent is primarily determined by the overall Mach cone geometry and the aircraft's flight Mach number, which dictate the directions along which shocks reach the ground. Small changes in angle of attack α slightly modify local shock strengths and pressure signatures, affecting the noise metrics, but they do not significantly alter the large-scale propagation angles of the shocks, leaving the footprint's spatial extent largely unchanged. Figure 4.50 shows the influence of angle of attack for both the ISA and the workshop-derived atmospheric profiles. Across all cases, the variations induced by changes in angle of attack are negligible.

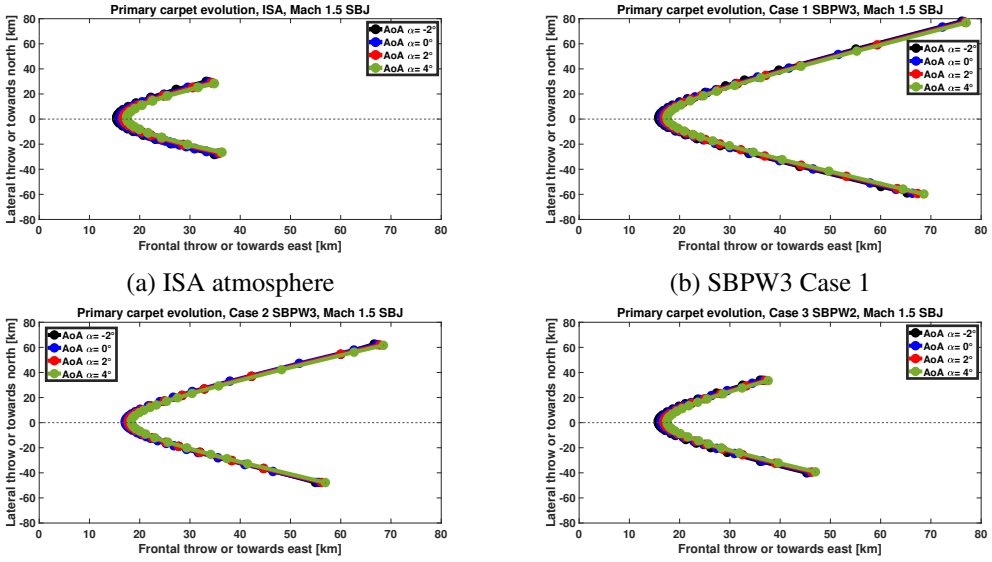

(a) ISA atmosphere

(b) SBPW3 Case 1

(c) SBPW3 Case 2

(d) SBPW2 Case 3

Fig. 4.50 Primary carpet variation with angle of attack, ISA & realistic atmosphere

4.4.2 Concorde-like

Similarly to the previous configuration, the primary carpet extension has been assessed also for the CS1 aircraft. Figure 4.51 shows the on-design primary carpet obtained for the four selected atmospheric profiles. Owing to the higher cruise altitude, the lateral extent of the carpet is increased. Conversely, due to the higher Mach number the frontal throw is partially reduced compared to the previous configuration.

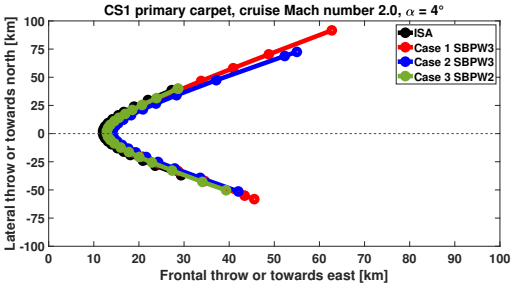

Fig. 4.51 Primary carpet extension Concorde-like CS1 configuration for the on-design conditions.

As previously observed in Figure 4.48, the width of the primary carpet is significantly influenced by the atmospheric profile. In particular, under the Case 1 SBPW3 profile, the lateral extent reaching nearly 175 km. In contrast, for the International Standard Atmosphere (ISA), it remains around 85 km, and highlights the strong sensitivity of the sonic boom footprint to atmospheric conditions. The extension of the primary carpet is particularly important for coastal buffer and regulatory entities for the definition of appropriate mission profiles. Figure 4.52 illustrates the influence of Mach number on the primary carpet for the selected atmospheric profile, highlighting also the limiting azimuth angle.

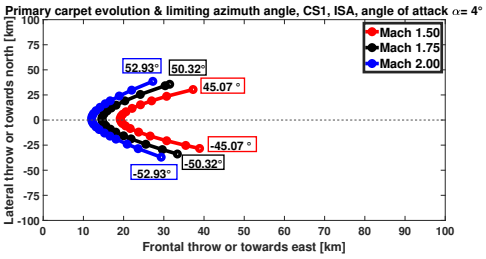

(a) ISA atmosphere, Mach variation

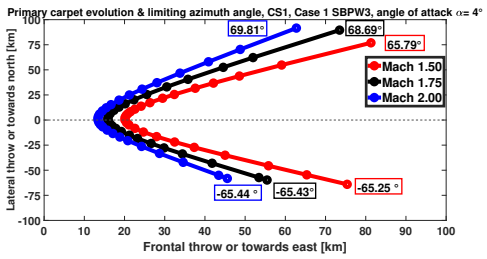

(b) SBPW3 Case 1, Mach variation

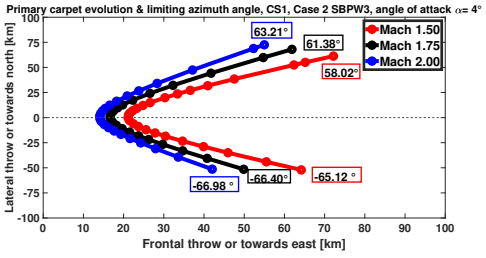

(c) SBPW3 Case 2, Mach variation

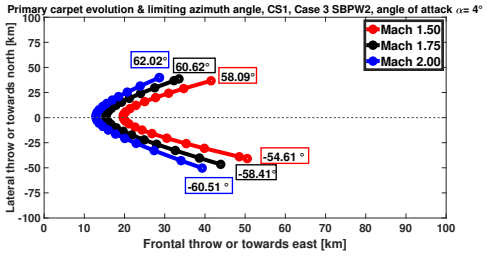

(d) SBPW2 Case 3, Mach variation

Fig. 4.52 Primary carpet variation and limiting azimuth angles with Mach number, ISA & realistic atmosphere

Similar to the previous configuration, increasing the Mach number narrows the Mach cone, as the aircraft emits shock waves at smaller angles relative to the flight direction. This change in propagation geometry shifts the primary carpet farther along the flight path while simultaneously increasing its lateral spread on the ground.

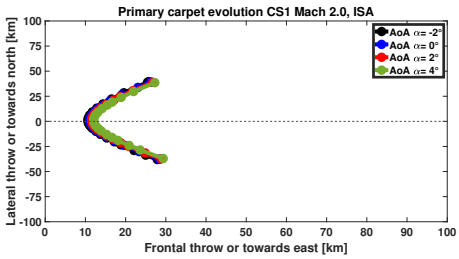

(a) ISA atmosphere

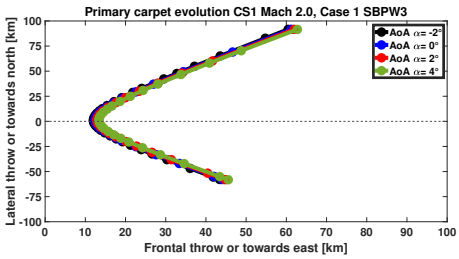

(b) SBPW3 Case 1

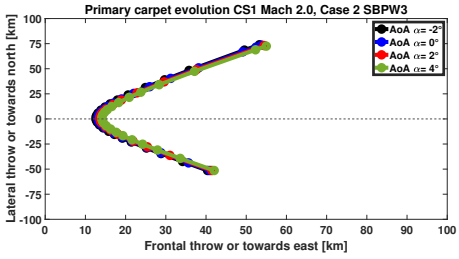

(c) SBPW3 Case 2

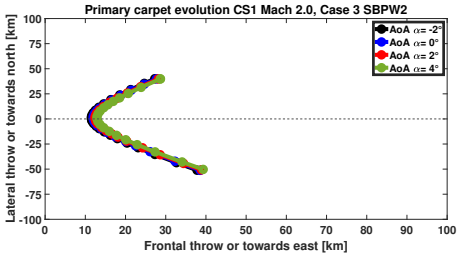

(d) SBPW2 Case 3

Fig. 4.53 Primary carpet variation with angle of attack, ISA & realistic atmospheric profile

The variations in the primary carpet resulting from changes in angle of attack are minimal, as observed in the previous case study.

4.4.3 Mach 1.8 Supersonic Business Jet

Lastly, the primary carpet of the Mach 1.8 Supersonic Business Jet has been analyzed. The analysis of the primary carpet shows that including turbulence modeling in the near-field domain does has negligible influence in the shape or lateral extent on the ground. Figure 4.54 presents the results for different flight conditions and atmospheric modeling.

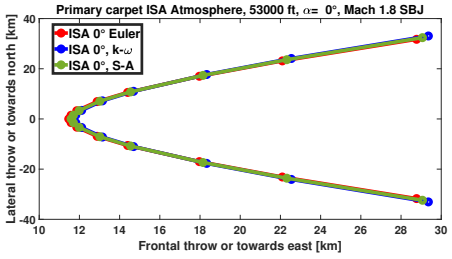

(a) Primary carpet comparison ISA, 0°

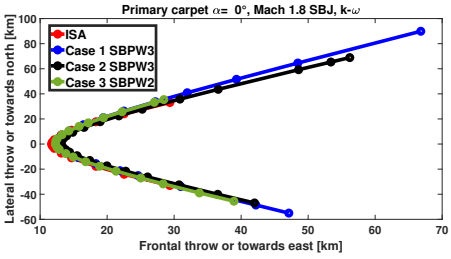

(b) Primary carpet 0° k-ω

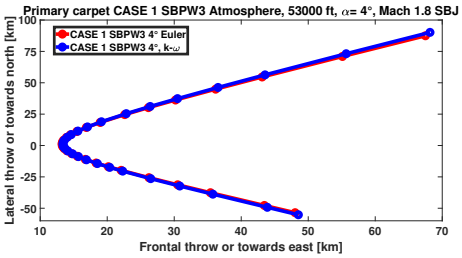

(c) Primary carpet comparison CASE 1 SBPW3, 4°, Euler and k-ω

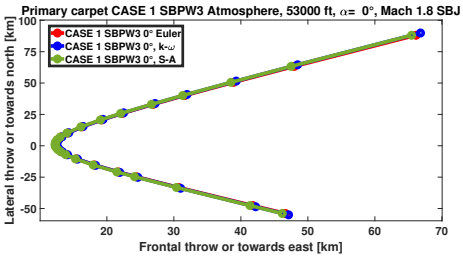

(d) Primary carpet comparison CASE 1 SBPW3, 0°

Fig. 4.54 Comparison of the primary carpet extension

Subfigures 4.54a and 4.54d show how the primary carpet changes between the inviscid and viscous simulations at 0° angle of attack. While Figure 4.54a focuses on the ISA atmosphere, Figure 4.54d presents the result for a realistic atmospheric profile. The deviation between the three turbulence model are unnoticeable, leading to the assumption that only the noise metrics are affected by the inclusion of turbulence model in the CFD domain. Subfigure 4.54c shows a similar comparison at 4° under realistic atmospheric conditions, with similar findings in terms of unnoticeable differences between the models. Lastly, Subfigure 4.54b shows the primary carpet extension with the different atmospheric profiles for the flight condition at 0° of angle of attack. Further detail of the primary carpet for the flight condition at angle of attack of 0° is visible in Table 4.9.

Table 4.9 Parameters of sonic boom primary carpet angle of attack 0°

Atmosphere	AoA	Turb. Model	Min. Azimuth [°]	Max. Azimuth [°]	Starboard Throw [km]	Portside Throw [km]	Frontal Throw [km]
ISA	0°	$k-\omega$	−52.49	52.49	33.06	−33.06	29.36
ISA	0°	S-A	−52.47	52.47	33.08	−32.88	29.31
ISA	0°	Euler	−52.49	52.49	33.12	−33.12	29.33
SBPW3 Case 1	0°	$k-\omega$	−67.90	76.84	87.88	−55.03	66.81
SBPW3 Case 1	0°	S-A	−67.87	76.82	87.95	−54.95	66.83
SBPW3 Case 1	0°	Euler	−67.89	76.85	87.92	−54.98	66.79

A similar analysis has been performed for the flight condition at a 4° angle of attack, which accentuates the differences in the primary sonic boom carpet resulting from turbulence modeling in the near-field domain.

Table 4.10 Parameters of sonic boom primary carpet angle of attack 4°

Atmosphere	AoA	Turb. Model	Min. Azimuth [°]	Max. Azimuth [°]	Starboard Throw [km]	Portside Throw [km]	Frontal Throw [km]
ISA	4°	$k-\omega$	−51.64	51.64	32.76	−32.76	29.84
ISA	4°	S-A	−51.59	51.59	32.77	−32.77	29.79
ISA	4°	Euler	−51.62	51.62	32.71	−32.71	29.82
SBPW3 Case 1	4°	$k-\omega$	−67.65	77.03	87.84	−54.81	67.46
SBPW3 Case 1	4°	S-A	−67.59	77.09	87.78	−54.77	67.33
SBPW3 Case 1	4°	Euler	−67.53	77.05	87.73	−54.69	67.39

4.5 Numerical validation of experimental test

As previously stated in Chapter 3, the experimental test campaigns enabled the validation of the numerical methodology employed up to Mach 5. The following section details the post-processing of the measured data and the characterization of the launch system and its associated acoustic phenomena. The data collected from the two different test campaigns described in Section 3.3 needs to be post-processed and converted into a specific format. This process includes the correct evaluation of each flight and environmental condition, as well as projectile speed profile. The measurement of the environmental conditions were obtained thanks

to an ISL weather station placed in the proximity of the firing line, approximately five meters behind the launcher. The evolution of the roll angle was made by CIRA [207, 209] and described in Appendix A. It was a necessary activity for the correct computation and analysis between numerical and experimental results.

During the tests, a conventional firearm was used employing a confined explosive charge to push the model composed by projectile and sabot out of the gun barrel. In this class of launch system, the projectile acts as a plug within the barrel, retaining the pressurized propellant gases until its exit. Once leaving the barrel, these gases are released at supersonic velocities, generating a shock waves as they interact with the ambient atmosphere. The sound generated by these shock waves is denominated muzzle blast, and it is related to the weapon's configuration and geometry of the gun muzzle.

Figure 4.55a provides insights of the different pressure signature captured by a single microphone during one of the tests. In chronological order, the first sonic boom captured by the microphone is the one from the projectile, followed by those from the pusher plate, while the final one is related to the muzzle blast.

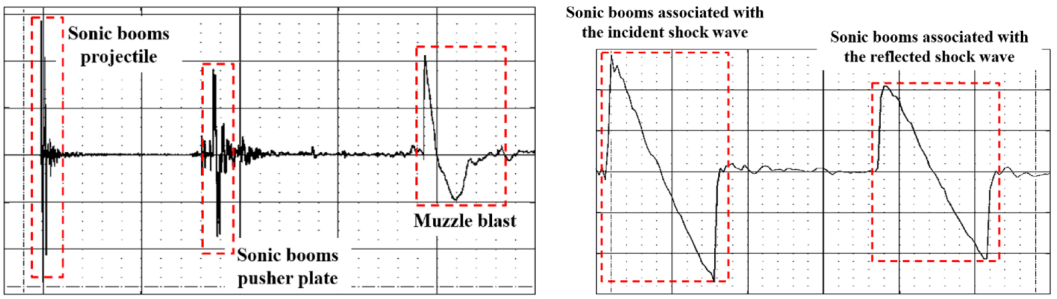

(a) Time-history of the acoustic signature [209]

(b) Direct and reflected shock waves

Fig. 4.55 Time history of a general sonic boom data acquisition

Conversely, Figure 4.55b highlight that two distinct signals are visible from the recorded sonic boom projectile. The first is the one generated by the projectile, while the second one is the ground reflected shock wave. The latter occurs because, in the presence of solid surfaces such as the ground, the shock wave is partially absorbed and reflected. The pressure signature of the reflected sonic boom exhibits a reduced amplitude, attributable to both ground absorption and the extended propagation distance through the air. Considering the flight altitude of just a couple of meters, the microphone detects both the direct and reflected pressure signature. The time delay

between the two recorded pressure signature is solely function of the differences in the acoustic ray paths.

The intervals between signals recorded in separate tests are not consistent. This discrepancy is caused by variations in the speed of sound—resulting from changes in temperature and humidity—as well as differences in the initial velocity, which alter the propagation time of the waves.

4.5.1 CS3 mock-up

To ensure an accurate validation of the experimental findings, a dedicated numerical investigation of the case study was conducted. The results obtained are consistent with those reported in Section 4.5.2. A key distinction, however, lies in the Mach number: in the present simulation it is set to 4.7, corresponding to the projectile velocity near the cannon exit, whereas in Section 4.5.2 it is fixed at 4.58, and equal to the one at the end of the aeroacoustic zone.

Experimental results

The pressure signatures for shots Nr. #1 and #5, recorded by the four CIRA microphones, are shown in Figure 4.56. These tests correspond to horizontal and vertical projectile trajectories, respectively. Numerical simulations were carried out for both configurations; however, only the horizontal case is presented in this thesis.

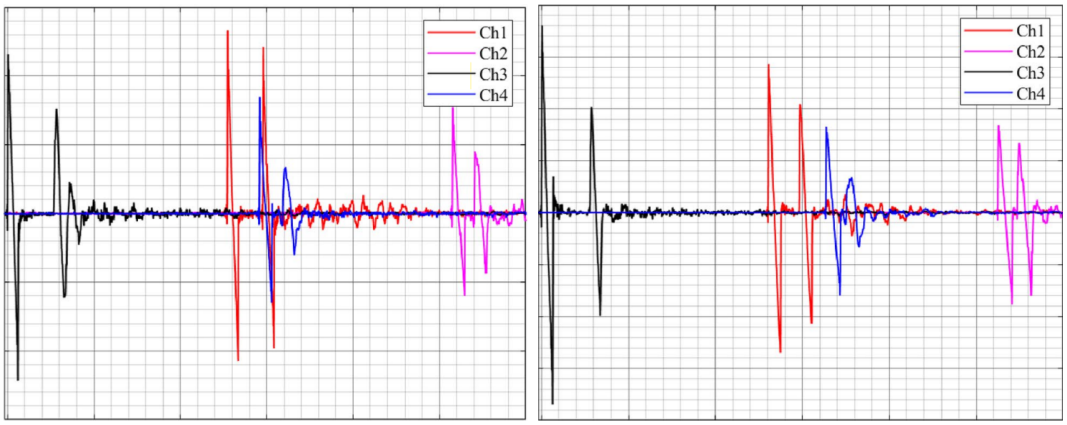

(a) Time-history pressure signature shot #1 [209] (b) Time-history pressure signature shot #5

Fig. 4.56 Time history pressure signature shot #1 and #5

Figure 4.56 presents a detailed depiction of the sonic boom time histories captured by the recording system during a single shot. The pressure signature highlight firstly the arrival of the direct shock waves generated by the supersonic projectile at the measurement points. The reflected component of the sonic boom captured afterwards shows a modest reduction in amplitude, as previously discussed.

Differences in peak overpressure and the overall duration of the acoustic signatures are largely influenced by geometric spreading, as well as by the combined effects of the projectile's rotational motion and its non-axisymmetric geometry. According to classical sonic boom theory, the maximum overpressure of N-waves diminishes with increasing distance from the flight path, while the time duration between the leading and trailing N-waves increases correspondingly. Moreover, both the peak overpressure and the duration of the acoustic signature are affected by variations in the projectile's volume and the distribution of lift along its longitudinal axis, which depend on the observer's position relative to the trajectory. Nevertheless, by comparing the signals recorded at the same microphone across different tests, the effects of geometric spreading can be effectively isolated from other influencing factors.

The results confirm that the shock wave characteristics recorded by the sensors are significantly affected by both the projectile's non-axisymmetric configuration and its flight attitude, particularly its roll angle. Ground and drones microphones were compared with Whitham's theory for both N-wave peak pressure level in dB and duration in Figure 4.57. The measure of peak pressure are in dB, with a reference of 20 μPa, and durations in milliseconds as functions of the distance from the trajectory for each microphone deployed during the firing.

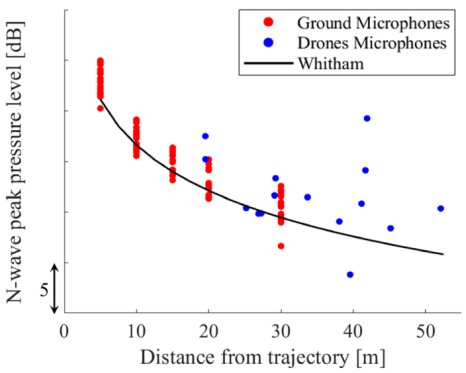

(a) Comparison between experimental and theoretical N-wave peak pressure

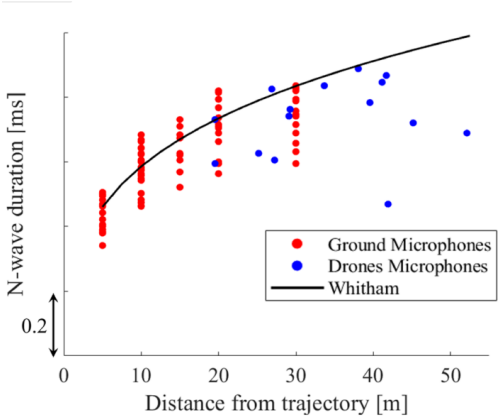

(b) Comparison between experimental and theoretical N-wave time duration

Fig. 4.57 Comparison of experimental and theoretical N-wave properties as a function of distance from trajectory

Figure 4.57 reveals a noticeable dispersion in the ground-based experimental measurements when compared with theoretical predictions, with variations up to 8dB. This variability is solely attributed to the projectile's roll during flight and its non-axisymmetric geometry. For instance, measurements taken at the same closest point of approach (CPA) may correspond to different projected area distributions across tests and microphone positions. Additional environmental factors, such as wind, turbulence, and humidity, may also contribute to the observed spread; however, the measured variations in temperature and humidity are insufficient to fully explain the differences found in the recorded microphones. Furthermore, the same Figure shows that sonic boom measurements obtained using the drone platform exhibit significant deviations, particularly at locations farther from the projectile's flight path. These discrepancies cannot be explained solely by the projectile's roll, indicating that the drone-based measurements should be excluded from numerical validation. Several additional sources of uncertainty further complicate the drone-based measurements, including noise from the motor and propellers, interactions between the shock waves and the drone body, rotor-wash-induced wind effects, and vibrations transmitted through the airframe. As a result, achieving high-precision sonic boom measurements using drone platforms remains particularly challenging.

To address the variability observed in the ground experimental data, the mean value of measurements was considered for further comparison [209] in Figure 4.58. A further comparison among the microphone recordings was performed using

Whitham's analytical approach. His theoretical framework provides a means to estimate the pressure jump across the bow shock produced by an axisymmetric body traveling at supersonic speed. The formulation assumes a steady, homogeneous, irrotational, inviscid, and supersonic flow around a smooth body of revolution with a pointed nose. Under these conditions, Whitham's analytical expressions for shock strength and duration are given by Equation 4.3:

$$\Delta p = \frac{2^{\frac{1}{4}} \gamma \, p_0 \, (M^2-1)^{\frac{1}{8}}}{(\gamma+1)^{\frac{1}{2}}} \sqrt{\int_0^{y_0} F(y) \, dy \, r^{-\frac{3}{4}}} \tag{4.2}$$

$$\Delta t = 2 \frac{2^{\frac{1}{4}} (\gamma+1)^{\frac{1}{2}} \, M}{a \, (M^2-1)^{\frac{3}{8}}} \sqrt{\int_0^{y_0} F(y) \, dy \, r^{\frac{1}{4}}} \tag{4.3}$$

At Mach 4.7, the application of the supersonic area rule to the CS3 mock-up model highlights a major limitation: the F-function becomes negative across much of the domain, indicating a predominantly overexpanded flow. This finding is consistent with prior studies, which note that the classical formulation of the supersonic area rule loses accuracy at high Mach numbers—especially for moderately slender configurations or during steady climb conditions. In contrast, the conventional volume-based area distribution is generally preferred for axisymmetric or blunt geometries. The area contribution due to volume was obtained by calculating the cross-sectional area at 200 uniformly spaced positions along the model. The corresponding equivalent area contribution due to lift was then estimated using the following approximation:

$$B(x) = \frac{\beta \, W \cos(\alpha) \cos(\theta)}{1.4 \, p_v \, M^2 \, S} \int_0^y b(x) \, dx \tag{4.4}$$

The formula reduces to a function that depends exclusively on the x-coordinate.

Despite some discrepancies in the absolute values, the analytical procedure reliably reproduced the average sonic boom signature generated by the CS3 mock-up model across the entire range of roll angles. Predicted peak overpressure deviate from the mean measured values by 0.8 %.

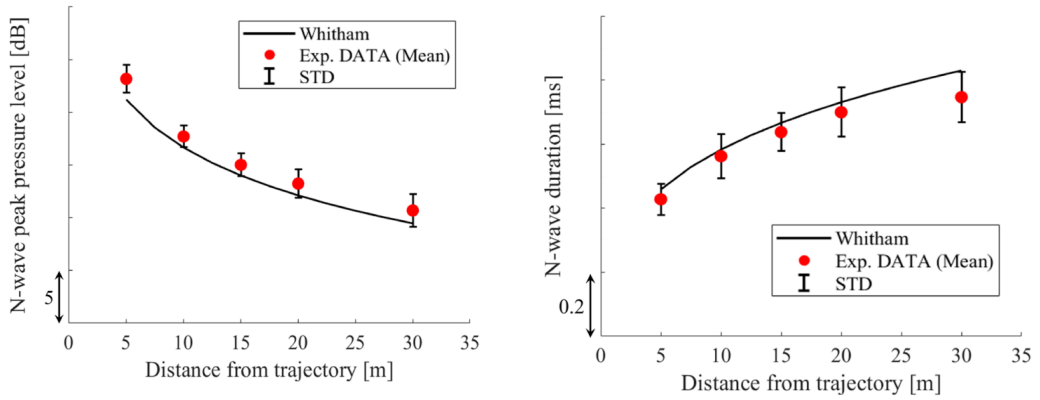

(a) N-Waves peak pressure level

(b) N-waves duration

Fig. 4.58 Comparison of experimental mean N-waves peak pressure and duration with theoretical predictions

Numerical results

Numerical simulations were carried out using a static grid, without accounting for the inherent dynamics of the projectile. Given the relatively limited motion of the CS3 mock-up during its flight, this assumption can be considered reasonable. Shot #1 and shot #5 of Table 3.1 were simulated to account for both the horizontal and vertical shots taken. The contours of the increase of static pressure and Mach number distribution are presented for the horizontal flight in Figure 4.59a and Figure 4.59b, respectively.

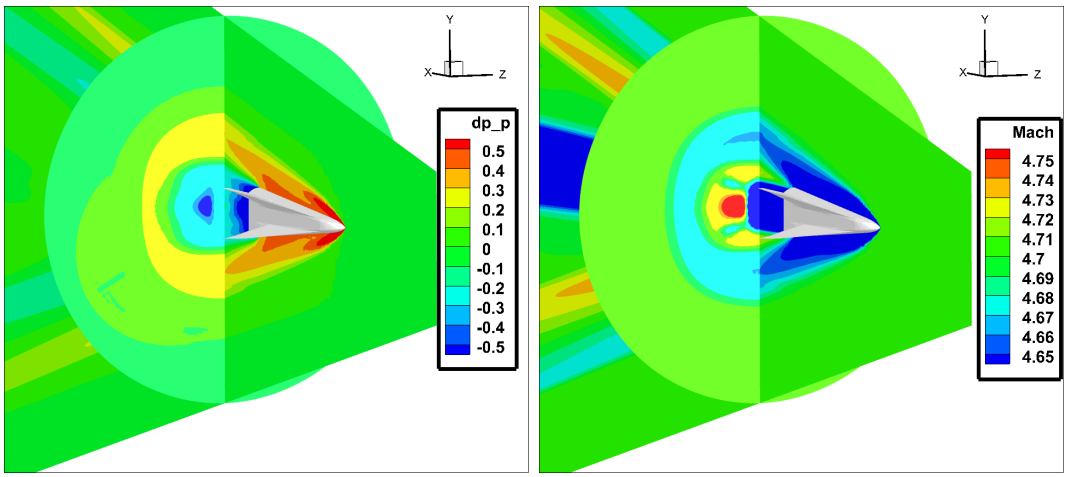

(a) Static pressure contour CS3 mock-up (b) Mach number contour, CS3 mock-up

Fig. 4.59 Static pressure and Mach number contour, CS3 mock-up, Mach 4.7

The shock structures generated around the CS3 mock-up are clearly identifiable, with significantly variations in the dp/p parameter compared to the previous case studies analyzed. As shown in Figure 4.59a, two dominant shocks emerge from the configuration. The first originates at the projectile nose, where the incoming hypersonic flow is abruptly compressed, forming a strong bow shock. The second arises at the wing section, produced by the local acceleration and subsequent compression of the flow around the lifting surface. These two shock systems interact to define the overall flow field around the configuration. Moreover, due to the geometric symmetry of the configuration and the angle of attack equal to 0°, the flow field above and below the body is identical. In addition, the contours in Figure 4.59a highlight that the radial evolution of the static pressure differs between the on-track and off-track conditions.

The pressure distributions were extracted at three non-dimensional vertical positions, namely H/L=1, H/L=3 and H/L=5. A CFD extraction sensitivity of 7.5° was applied to ensure adequate angular resolution. Figure 4.60a illustrates the near-field signature at H/L=1, whereas Figure 4.60b presents the corresponding result at H/L=3. The angular deviation reported in the plot is equal to 15° to ensure adequate visibility of the extracted angles.

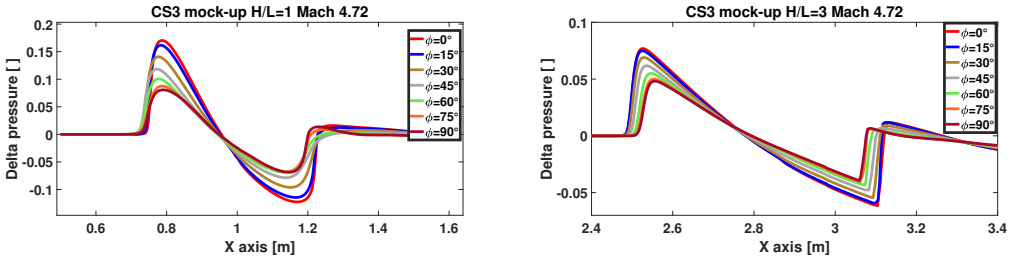

(a) H/L=1 extracted near-field pressure signature (b) H/L=3 extracted near-field pressure signature

Fig. 4.60 Extracted near-field pressure signature H/L=1 & H/L=3, CS3 mock-up

The highest noise levels are observed below the configuration, and this was confirmed by the static pressure contour previously reported. Notably, the overall shape of the pressure signature remains essentially invariant with respect to the extraction angle. At H/L=3 the pressure signature already exhibits the N-wave shape for all radial angles, highlighting that the two visible shocks in the contours already merged.

A systematic procedure was adopted to guarantee consistency between the numerical predictions and the experimental observations. As discussed previously, pressure signatures were extracted up to a distance of five characteristic lengths of the model, corresponding to approximately 1.01 m. To enable a meaningful comparison with the measurements, however, the simulated waveforms needed to be propagated to the distance of the microphones used in the experimental campaign. The extracted pressure signals were treated as far-field N-waves, an assumption justified by their shape in the extraction near-field signature. Under this condition, the acoustic divergence laws formulated by Whitham [245] could be applied to scale both amplitude and duration:

$$\Delta p \propto r^{-\frac{3}{4}},$$
$$\Delta t \propto r^{\frac{1}{4}}.$$

It is important to note that Whitham's formulation holds under the hypothesis of a homogeneous medium, which is a reasonable approximation given the relatively short distances between the trajectory of the projectile and the microphone locations. The scaling procedure began with the definition of a reference or fictitious N-wave.

This waveform was constructed by taking the peak overpressure of the compression phase from the near-field signatures. The N-wave duration was then determined as the interval between the compression and expansion peaks.

Comparison of the results

Finally, the analysis focused on the directivity of the model's acoustic emissions and their impact on both the peak overpressure and the duration of the resulting N-waves. The roll angles for each shot and microphone were computed by CIRA using the methodology described in Appendix A.

To facilitate a consistent comparison, all measured peak overpressures and time durations at a given closest point of approach (CPA) were projected to a standard reference distance of 30 meters. As already stated, the experimental signatures were assumed to satisfy far-field conditions, exhibiting the characteristic N-wave shape. Following Whitham's theory, the scaling relations applied are:

$$\Delta p(30\text{ m}) = \Delta p(r)\left(\frac{30}{r}\right)^{-\frac{3}{4}} \tag{4.5}$$

$$\Delta t(30\text{ m}) = \Delta t(r)\left(\frac{30}{r}\right)^{\frac{1}{4}} \tag{4.6}$$

The near-field numerical data, extracted at H/L=5 were propagated to the 30-meter reference distance using Equation 4.6. The resulting comparison as a function of the roll angle between the numerical and experimental data is presented in Figure 4.61.

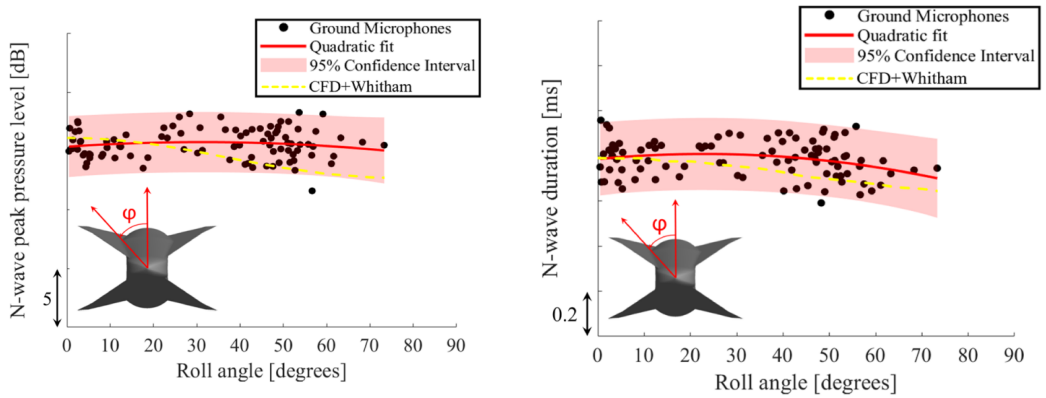

(a) N-wave peak pressure level

(b) N-wave time duration

Fig. 4.61 Comparison between numerical and experimental results with 95& confidence interval

Numerical simulations show that increasing the projectile's roll angle leads to a reduction in both the peak overpressure and the duration of the corresponding pressure signature. This trend is evident in the static pressure contours, as previously illustrated in Figure 4.59a. The effect can be explained by the decrease in the effective cross-sectional area at a roll angle of 90° compared to the 0° configuration. A smaller cross-section results in a smoother variation of the area along the projectile's axis, producing a less pronounced N-wave. Some of the observed variability may also stem from factors such as rapid angular acceleration of the projectile and the difficulty of maintaining a constant rotational speed within the acoustic measurement zone.

Furthermore, a quadratic fit of the experimental data supports this observation, although the reduction in peak pressure and duration is less pronounced than those predicted by the numerical simulations. A likely explanation for this discrepancy is that the rolling motion, combined with the model's non-axisymmetric geometry, produces shock wave fronts that merge into a time-varying envelope—a phenomenon not captured by the numerical model. Consequently, the sonic booms recorded by the microphones represent a superposition of multiple shock waves. The strongest shock, associated with the 0° roll orientation, may not fully dissipate before interacting with the weaker shocks produced at higher roll angles. This interaction limits the overall reduction in N-wave intensity within that region.

Average values are therefore adopted, which allows the directivity effect to be disregarded and enables a comparison between predicted and measured data

as a function of the distance from the trajectory. The mean acoustic pressure is obtained from the squared peak pressures. The procedure begins with the collection of peak pressure values, organized according to the Closest Point of Approach (CPA). Each peak is then squared, and the results for a given CPA are summed and normalized by the number of measurements. The square root of this quantity yields the mean acoustic pressure. The same method is applied to the numerical predictions performed with different solvers and numerical scheme.

Figure 4.62 compares the discrepancies in N-wave peak pressure (expressed in dB) and time duration between the averaged microphone measurements and the corresponding CFD results. The peak pressure estimation shows a mean absolute error of 0.9 dB with a standard deviation of 0.4 dB. For the N-wave duration, the mean error is 0.039 ms with a standard deviation of 0.019 ms. In addition, the numerical simulations performed neglect viscosity. As stated in Section 4.1.3, this assumption can lead to small but not negligible deviations, with variations up to 2 dB in the selected noise metrics. These results demonstrate that the adopted numerical procedure, even with the simplified Whitham propagation law, is able to accurately reproduce the mean sonic boom characteristics of the CS3 mock-up configuration.

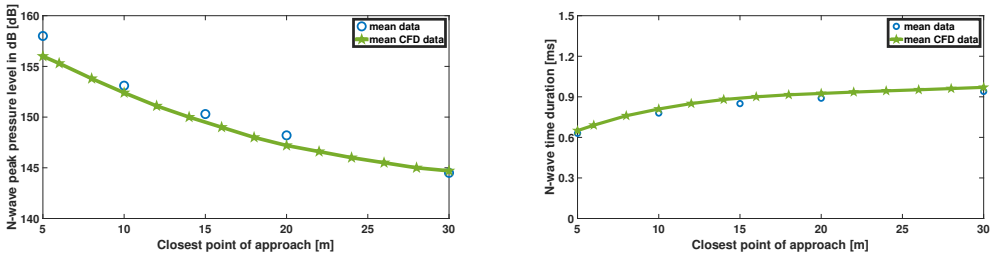

(a) Comparison peak pressure dB, CS3 mock-up (b) Comparison N-wave duration, CS3 mock-up

Fig. 4.62 Comparison numerical and experimental test results, CS3 mock-up

4.5.2 Inverse estimation of flight dynamics via shock wave recordings

Parallel to the numerical validation of the experimental test campaign, within the first sonic boom outdoor test an innovation procedure of inverse estimation of flight dynamics via shock wave recordings has been developed. Reconstructing flight dynamics from shock wave recordings presents significant challenges due to the nonlinearity of supersonic shock propagation and limited measurement data. This

work develops and applies a computational framework that integrates high-fidelity CFD simulations with experimental sensor recordings to estimate the trajectory, velocity, and roll angle of a supersonic projectile. Space-time pressure signatures for the forward solution of the free-flight shock emission are calculated at a vertical distance of H/L=5, and subsequently are used for the inverse estimation of the roll angle, given a set of shock wave field measurement.
The pressure field has been model by adopting the mixed grid approach presented in Section 3.1.3 paired with the equivalent multipole approach (see Section 3.3.4), where the equivalent sources align with the shock wave detachment points of the trajectory for the respective sensors.

The first step in the inverse estimation of the flight dynamics consists of evaluating the Computational Fluid Dynamics results. In this study, the Advection Upstream Splitting Method (AUSM) is adopted as numerical scheme. No turbulence model is applied, and the flow is resolved by means of the Euler equations for the selected projectile. The reference ambient pressure measured during the experimental tests was 995.4 hPa. The simulation was carried out at a Mach number of 4.58, which is lower than the value reported in Section 4.5.1. It corresponds to the projectile velocity at the end of the aeroacoustic region and is slightly reduced with respect to that in the cannon area, owing to aerodynamic drag. The contours of increase of static pressure and Mach number are visible in Figure 4.63.

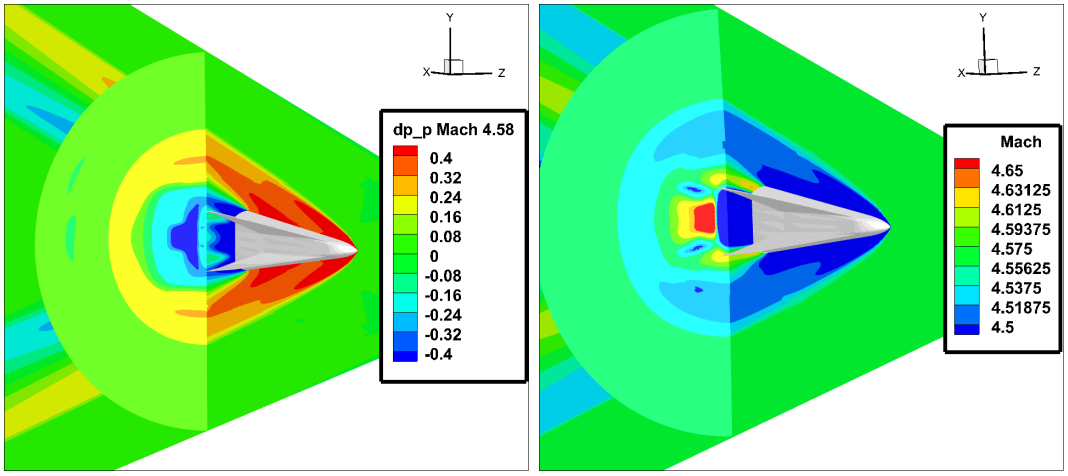

(a) Increase of static pressure contour

(b) Mach number contour

Fig. 4.63 Increase of static pressure and Mach number contour projectile

As for the simulation at Mach 4.72, the strength of the emitted shock differs greatly with the radial angle ϕ_{CFD}. Due to the symmetric shape of the projectile, the pressure signature extracted from the near-field simulation was obtained over the 0–90° azimuthal range.

The pressure signature at H/L = 5 was used as input for the equivalent acoustic multipole formulation, with space–time boundary conditions defined at 2.5° increments. The requirement of a fully developed N-wave guided the choice of the vertical distance extraction of the computational fluid dynamics results.

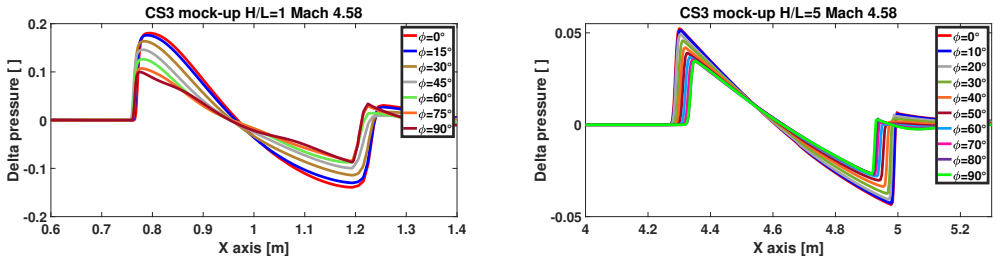

(a) Extracted pressure signature, H/L=1 (b) Extracted pressure signature, H/L=5

Fig. 4.64 Extracted pressure signature CS3 projectile Mach 4.58 H/L=1, H/L=5

The results shown in Figure 4.64 illustrate the directivity of the shock wave as a function of the roll angle θ. In particular, at a position five body lengths below the aircraft, the characteristic N-wave shape of the pressure signature is clearly visible. The highest peak pressure occurs at an azimuthal angle of 0°, i.e., directly below the configuration, and decreases as the azimuthal angle increases toward 90°. This trend is further confirmed by the static pressure contours shown in Figure 4.63a. Owing to the configuration's geometry and the reference flight condition, the shocks merge near the aircraft, resulting in a classic N-wave shape.

Shock Wave Recordings

During the test campaign, dedicated instrumentation positioned behind the cannon recorded the atmospheric conditions (see Section 3.3.1). The first shot of the experimental campaign, denoted as Shot 1 and reported in Table 3.1, was selected for the inverse flight dynamics estimation. The recorded ambient conditions were: a pressure of 995.4 hPa, humidity equal to 69%, and temperature of 19.0°C. The measured launch velocity was 1616 m/s, corresponding to approximately Mach 4.72

under the selected boundary conditions. The measurements of the sonic boom signal using the sensor array provided by ISL are visualized in Figure 4.65.

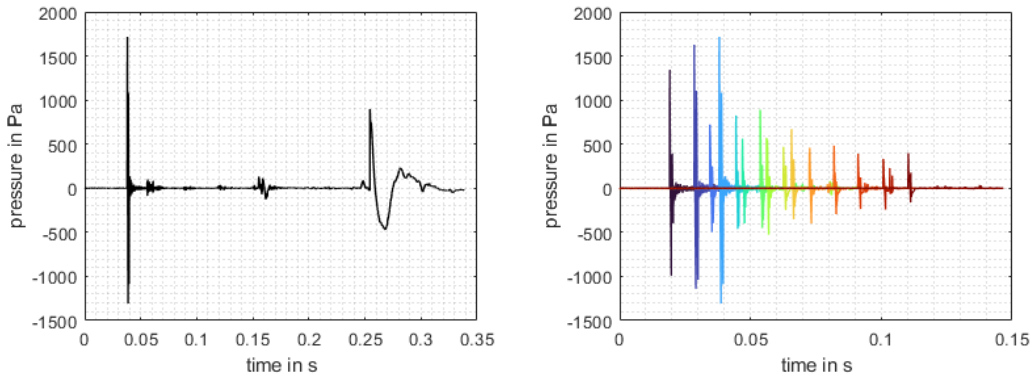

(a) Pressure curve for a single s^{th} acoustic sensor

(b) Time synchronized shocks

Fig. 4.65 Time pressure curves of the ISL sensor array

Subfigure 4.65a highlights the different shock waves captured by the single acoustic sensor. The measured sonic boom shock is visible between 0.03 s and 0.05 s, while the shocks from the sabot and pusher plate propagate more slowly and are recorded later by the microphone. Lastly, the muzzle blast wave from the cannon fire reaches the microphone at 0.23 s.
Subfigure 4.65b highlights the time synchronized N-wave shocks recorded by the ISL 15-sensor array.

Pressure estimation and alternative measurements

Different snapshots were taken of the projectile during the free-flight test, and are visible in Figure 4.66.

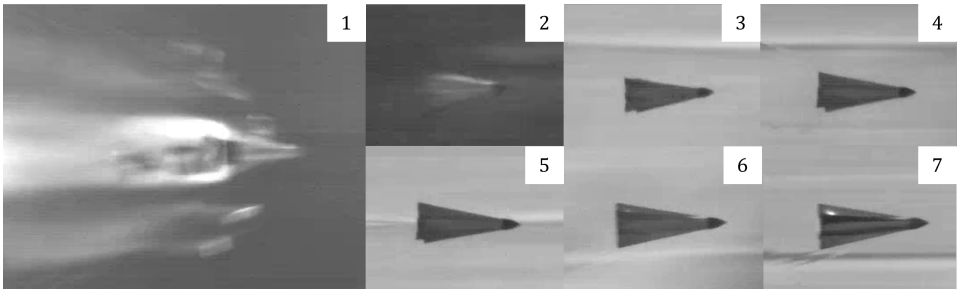

Fig. 4.66 Projectile snapshots in free-flight

In 1 the sabot separates from the projectile shortly after launch, with the pusher plate following soon after. Between 2 and 7, the projectile travels from the cannon toward the sand bay area, rolling slowly in a clockwise direction. Picture 7 shows the shock waves clearly. Looking across 2-7, the clockwise roll is visible along the trajectory and in the area where acoustic measurements are taken, with little or no change in pitch or yaw.

The convergence of the Nelder-Mead optimization [246] is depicted in Subfigure 4.67a. Subfigure 4.67b presents a comparison between the RADAR measurements and the inverse acoustic estimation of velocity and radar position. Using cardboard penetration measurements, an estimated trajectory vector

$$\mathbf{d}_{\text{pen}} = [0.1828, 0.9831, -0.0008]^{\text{T}}$$

was determined. This is compared with the acoustic estimation based on the TDOA approach, as given in Equation 3.26, which converged to a trajectory vector of

$$\mathbf{d}_{\text{ac}} = [0.1812, 0.9834, 0.0016]^{\text{T}}$$

The following angular differences were found in the the direction vectors: an overall deviation of 0.17°, 0.09° in the XY-plane, 0.78° in the XZ-plane, and 0.14° in the YZ-plane. Notably, the largest deviation is in the vertical direction and lowest in the horizontal direction. The vertical angle was slightly overestimated by the developed methodology.

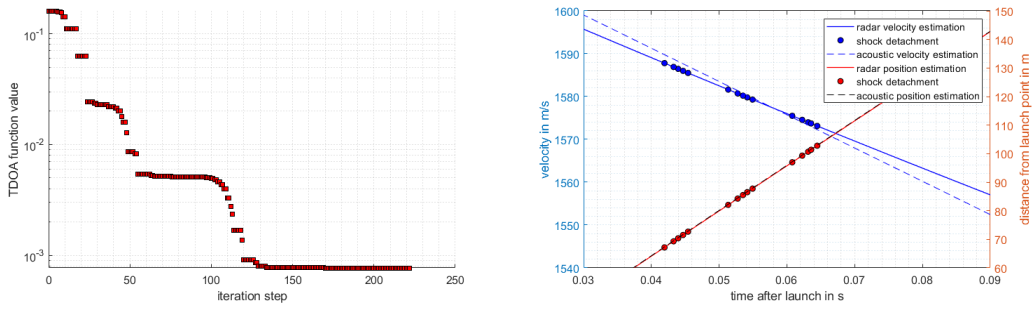

(a) Convergence of the Nelder Mead algorithm for TDOA

(b) RADAR measurement and inverse acoustic estimation of velocity and position

Fig. 4.67 Acoustic TDOA estimation of the velocity and position of the prototype

In the acoustic measurement zone, the velocity deviations between the acoustic-based estimations and the RADAR measurements remain within 6 m/s. Furthermore, the accuracy of the acoustic estimation with respect to the RADAR measurements decreases as the distance from the sensor array increases.

The computed cost functions and results of the acoustic roll angle estimation and cardboard penetration are shown in Figure 4.68. Subfigure 4.68a presents the cost function for the roll angle based on the Wasserstein distances (red) and the shock strength differences (blue). The cost functions exclude large roll angles and exhibit a similar trend. The minimum of the Wasserstein distance-based cost function is observed at 18°, whereas the minimum of the shock strength difference cost function occurs at 29°. For the selected shot, the aircraft penetrated the cardboard at the entry frame after 52.4 meters of trajectory with a roll angle of 0.46° clockwise, and at the exit frame after 122 meters with a roll angle of 18.60° clockwise. Assuming linear roll movement between the cardboard penetrations the roll angle was estimated to be 9.3° at the mean shock detachment point, leading to an overall deviation of 19.7° and 10.7° of the acoustic methods with the penetration estimate. Subfigure 4.68b visualizes the entry and exit penetration angles as well as the roll angle estimates.

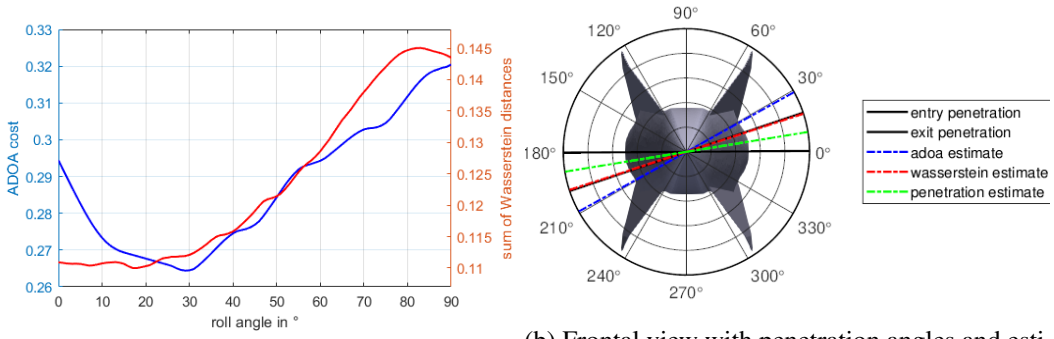

(a) Roll angle cost function

(b) Frontal view with penetration angles and estimates

Fig. 4.68 Roll angle estimation and measurements

4.5.3 CS2 mock-up

As for the previous mock-up model, the numerical validation of the experimental test has been performed for the CS2 configuration. The Mach number for the test is similar to the one of the CS3 mock-up test, set to 4.7. The workflow and the procedure of the experimental setup is equal to the one of the previous campaign.

Additional equipment has been adopted, including a Head and Shoulder Unit (HSU). This equipment provide valuable data on the psychoacoustic metrics for a human subject positioned 150 meters away from the trajectory, studying both the left and right ear. However, within this thesis, solely the numerical validation has been reported.

Experimental results

As already stated in Section 3.3.3 four different shots were performed at Mach 4.7. While for the CS3 mock-up case study the shots were performed both horizontally and vertically, the ones in this case were just performed horizontally.

ISL deployed fifteen microphones at three lines distances of 70, 85 and 100 meters from the canon muzzle and at closest point of approach (CPA) of 5,10,15,20 and 30 meters. The mean values of their experimental results match the theoretical one obtained with the Whitham's theory for an equivalent caliber of 30 millimeters. The estimated standard deviation at each CPA distance reaches a peak value of 167 μs for the N-wave pressure signature duration, and a maximum of +3.6 dB peak value for the pressures estimates.

Table 4.11 Mean peak pressure and shock wave duration

CPA [m]	5	10	15	20	30
mean duration [μs]	549.9	636.3	677.1	754.3	822.9
STD duration [μs]	83.3	104.6	105.6	130.6	167.6
mean peak pressure [dB]	154.0	149.7	147.1	146.2	143.1
STD peak pressure [dB]	2.6	3.6	2.1	2.1	2.2

The analysis of the gunshot recording for the CIRA's microphones is highlighted in Figure 4.69.

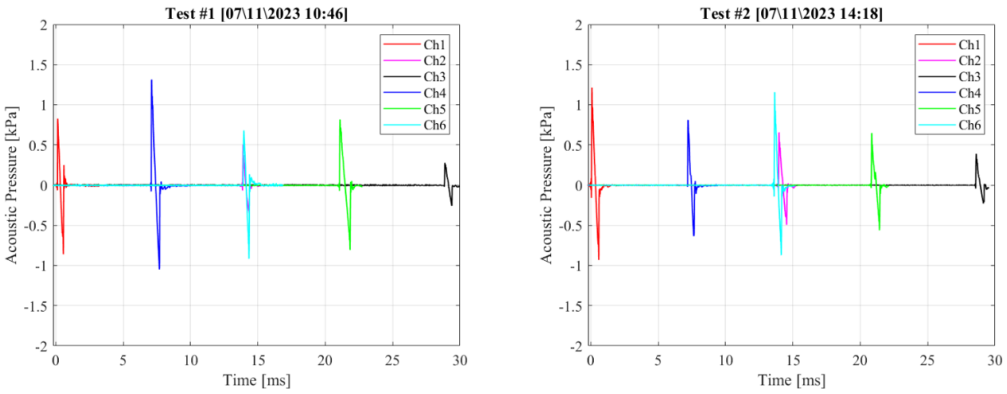

(a) Analysis of gunshot recording, test #1

(b) Analysis of gunshot recording, test #2

Fig. 4.69 Analysis of the gunshot recording, CIRA, CS2

The analysis of the results highlights the differences in the N-wave signatures recorded by the six microphones. The sequence of detections follows the expected order, namely $Ch_1 \rightarrow Ch_4 \rightarrow Ch_6$ & $Ch_2 \rightarrow Ch_5 \rightarrow Ch_3$, which is consistent with the spatial arrangement of CIRA's microphone array. This confirms the correct synchronization between the shock wave propagation and the sensor positions. Furthermore, even under identical initial conditions, a significant standard deviation is observed across the tests for the peak overpressure and signal duration, as visible.
This variability indicates the presence of experimental uncertainties and environmental effects that influence the propagation and measurement of the acoustic field. The observed dispersion is therefore a relevant factor to consider when assessing the reliability of the measurements. The meteorological instrumentation also indicates minimal variations in temperature, humidity and winds, supporting additional experimental uncertainties in the recorded results. By comparing the pressure signature of a single shot or a single CPA, it is possible to identify consistent trends in the results obtained from both CIRA's and ISL's instrumentation. Specifically, Figure 4.70a illustrates the results for the third shot recorded by CIRA's microphones. For microphones #1 and #2, a secondary peak is visible in the pressure signature, indicating a feature that is not observed in the other recordings. While these peaks are weak compared to the maximum overpressure, they suggest a localized or transient phenomenon captured only by these sensors. The fact that ISL's microphones also recorded this trend further indicates that it is not related to microphone calibration or tuning.

Conversely, Figure 4.70b shows the results from ISL's instrumentation at the closest point of approach of 5 meters. The data reveal a noticeable standard deviation across the different recordings, highlighting variability in the measurements that may arise from environmental or flight conditions. As for the previous recorded test, the microphone capture both the direct and reflected wave, with a reduced intensity for the latter one.

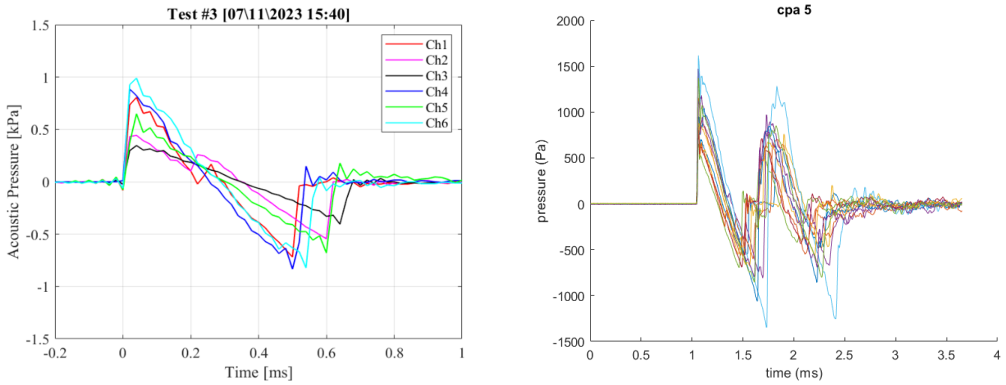

(a) CIRA's results shot #3

(b) ISL's results CPA 5 meters

Fig. 4.70 CIRA's and ISL's experimental results

Numerical results

For the CS2 mock-up configuration, numerical simulations were conducted to support and validate the experimental data recorded. Multiple runs examined variations in initial conditions, including Mach number, ambient static pressure, and humidity, to accurately replicate the four tests conducted. Small differences in these environmental and flight conditions can influence the sonic boom signatures, affecting both the amplitude and shape of the N-wave. Comparison of results across different conditions enables interpretation of the experimental data and evaluation of the sensitivity of the acoustic response to realistic operational parameters. Figure 4.71 presents the contours of static pressure and Mach number for the CS2 mock-up configuration.

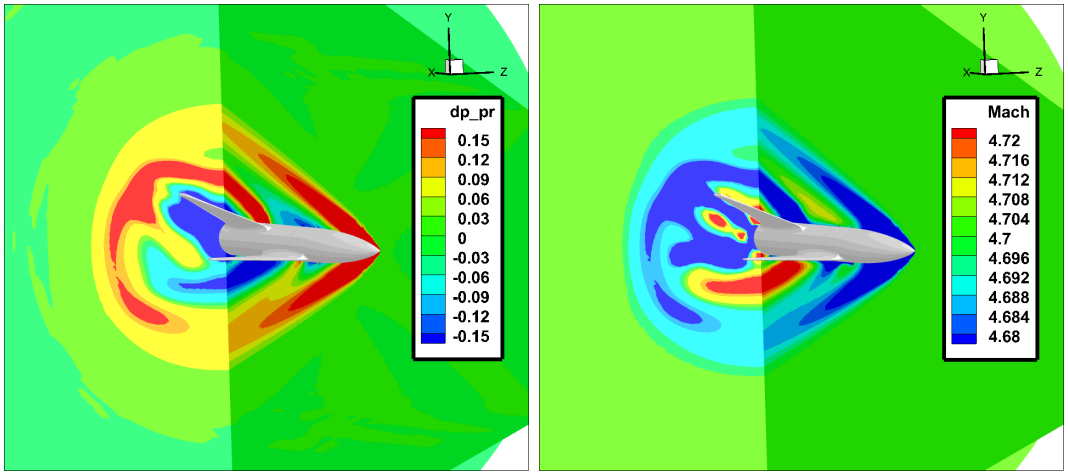

(a) Static pressure contour, CS2 mock-up (b) Mach number contour, CS2 mock-up

Fig. 4.71 Static pressure and Mach number contour, CS2 mock-up

In particular, Figure 4.71a highlights three distinct shock waves generated by the configuration. The first and most intense shock originates at the nose of the model, the second forms along the wing section, while the third is generated at the vertical fin. Additionally, it is evident that the shock waves from the nose and wing begin to coalesce already in the near-field region, indicating early interaction of the pressure disturbances. These shock interactions confirms that the aircraft does not have low-boom characteristics. In contrast to the CS3 mock-up configuration, the flow field below the aircraft differs significantly from the flow above. This asymmetry arises from the more conventional geometry and projectile shape of the model, unlike the double axisymmetric layout observed in the previous mock-up. These geometric differences strongly influence the spatial distribution and interaction of the shock waves. The Mach number contours of Figure 4.71b confirms the findings described in the static pressure contour.

The extracted pressure signature at H/L=2 and H/L=5 is visible in Figure 4.72, with a 15° step in the radial extraction.

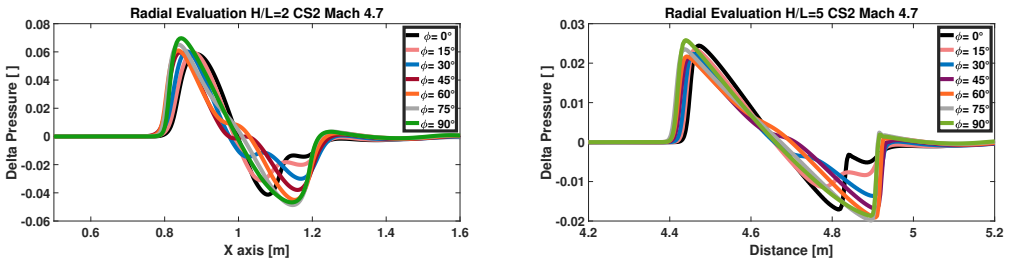

(a) Extracted pressure signature H/L=2, mock-up (b) Extracted pressure signature H/L=5, mock-up

Fig. 4.72 Extracted near-field pressure signature, CS2 mock-up

From the extracted pressure signatures, it is evident that at both H/L = 2 and H/L = 5, the shape of the waveform corresponds to a N-wave shape signature. In the H/L = 2 pressure signature, for extraction angles between 0° and 45°, a secondary, smaller shock is visible, which can be attributed to the contribution of the vertical fin. The results shown in Figure 4.72 are subsequently employed as input for Whitham's analogy, enabling a direct comparison between numerical predictions and experimental measurements.

Comparison of the result

Finally, as for the CS3 mock-up configuration, the analysis of the model's acoustic emissions and impact on peak overpressure and duration of the N-waves has been assessed. The procedure applied to the previous mock-up configuration has been applied, with results visible in Figure 4.73.

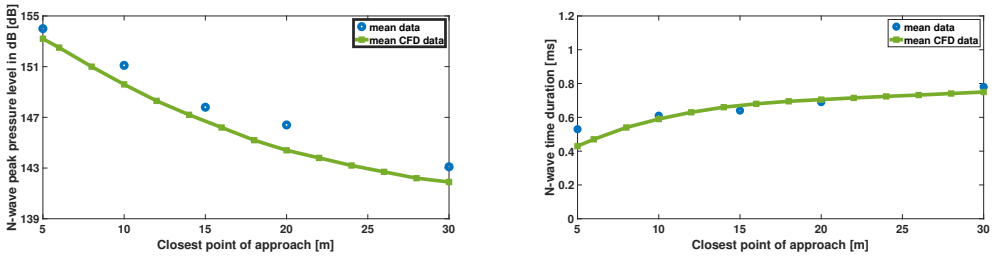

(a) Comparison peak pressure dB, CS2 mock-up (b) Comparison N-wave duration, CS2 mock-up

Fig. 4.73 Comparison numerical and experimental test results, CS2 mock-up

While for the CS3 mock-up configuration the mean absolute error between numerical and experimental tests was below 1 dB, for this case study it reaches 2.2

dB. Similar considerations can be made for the time signature duration. In fact, the absolute error for the CS3 mock-up configuration is equal to 0.039 ms, while for the CS2 mock-up is 0.11 ms.

A detailed analysis of the weak correlation was carried out. Using the two trajectory trackers in combination with the high-speed cameras, the flight path of the mock-up configuration was reconstructed from the moment of sabot separation up to its impact in the sand bay. In particular, a yaw-induced roll phenomenon and a small incidence, and a downward deviation on impact are observed. Figure 4.74 highlights four snapshots of the mock-up configuration in free-flight.

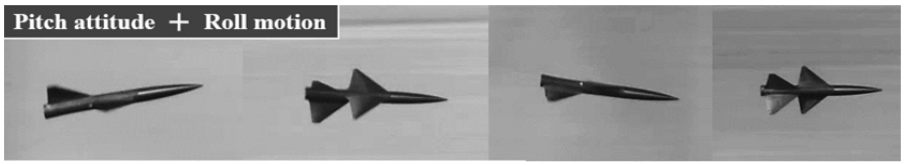

Fig. 4.74 Dynamics of the CS2 mock-up configuration in free-flight

The dynamics shown in Figure 4.74 differ significantly from the steady-state flight assumed in the numerical simulations. While the CS3 mock-up exhibited negligible rotation along the 200 m fireline, the CS2 configuration experienced rotation that affected both the peak pressure and the duration of the pressure signature. In accelerated flights, cusp formation occurs, leading to pressure levels higher than those in steady conditions. Furthermore, shock folding produces multiple booms in the recorded signatures, as illustrated in Channels 1 and 2 of Figure 4.71a. These observations, confirmed by the two experimental campaigns, indicate that steady-state simulations are valid only when flight dynamics are limited or negligible. For configurations such as the CS2 mock-up, however, transient simulations that account for rotational motion are required to achieve accurate characterization.

4.6 Sonic boom preliminary estimation methodologies and tools results

The accurate evaluation of sonic boom during the conceptual design phase is essential to ensure compliance with future regulatory standards, minimize environmental impact, and support aerodynamic shaping decisions. High-fidelity simulations, such as

Computational Fluid Dynamics with detailed shock-wave modeling, provide highly accurate predictions and a comprehensive understanding of the sonic boom signature. However, these methods are computationally expensive and time-consuming, making them unsuitable for rapid design iterations. Conversely, low-fidelity models and surrogate-based approaches offer more efficient alternatives, enabling first-order estimations of sonic boom characteristics. These tools can guide preliminary design choices, identify relevant trends, and prioritize configurations for subsequent high-fidelity analyses.
Low- to mid-fidelity tools can be seamlessly integrated into a multidisciplinary design framework to enable rapid evaluation of sonic boom characteristics alongside aerodynamic and propulsion performance. Their integration facilitates iterative trade-off analyses and design-space exploration, allowing designers to efficiently identify configurations that balance boom mitigation with overall vehicle performance objectives.
Section 4.6.1 presents the new sonic boom requirements implemented within the Matching Chart tool, while Section 4.6.2 introduces the refined analytical formulation. Both methodologies are included into the ASTRID-H 2.0 framework to enable rapid assessment of future high-speed configurations.

4.6.1 Sonic boom preliminary estimation methodologies and tools results

The inclusion of acoustic constraints in the Matching Chart tool is an important requirement for system designers, especially those without expertise in aeroacoustics, to incorporate sonic boom considerations early in the design process. This thesis develops initial constraints based on high-fidelity simulations to guide the conceptual design of supersonic conventional configurations flying at Mach 2 or lower. Such configurations represent a realistic step toward reintroducing commercial supersonic flight.

The case study used to derive the constraint involves a generic 80-passenger configuration cruising at Mach 1.5, selected for its balanced trade-off between performance, capacity, and feasibility for future supersonic transport. This case study, together with the target maximum peak overpressure, provides a clear context to demonstrate the applicability of the methodology developed in this work. As will

be exploited later, future regulations for overland high-speed flights are expected to be based on specified noise metrics. In this work, thresholds defined in terms of peak overpressure have been conceived to guide and support designers who may not have expertise in aeroacoustics.

The design iteration is performed using the proprietary tool ASTRID-H 2.0 and follows the high-level requirements outlined below:

- Cruise Mach number 1.50
- Payload 80 passengers
- Range 6,500 km
- Cruise altitude 18,000 m
- Maximum positive peak overpressure at ground level $\Delta p < 1.05$ psf ≈ 50 Pa
- Minimum negative peak expansion at ground level $|\Delta p| < |1.05 \text{ psf}| \approx 50$ Pa

This work implements a peak overpressure requirement of 50 Pa to demonstrate the applicability of the methodology. Future regulations will likely replace peak overpressure with a specific target of one of the previously selected metrics, such as PL. However, including a physical quantity threshold helps to support designers who are not experts in acoustics, enhancing clarity and accessibility in the use of the Matching Chart tool. The lateral and plan views of the sketch, derived using ASTRID-H 2.0, are shown in Figure 4.75.

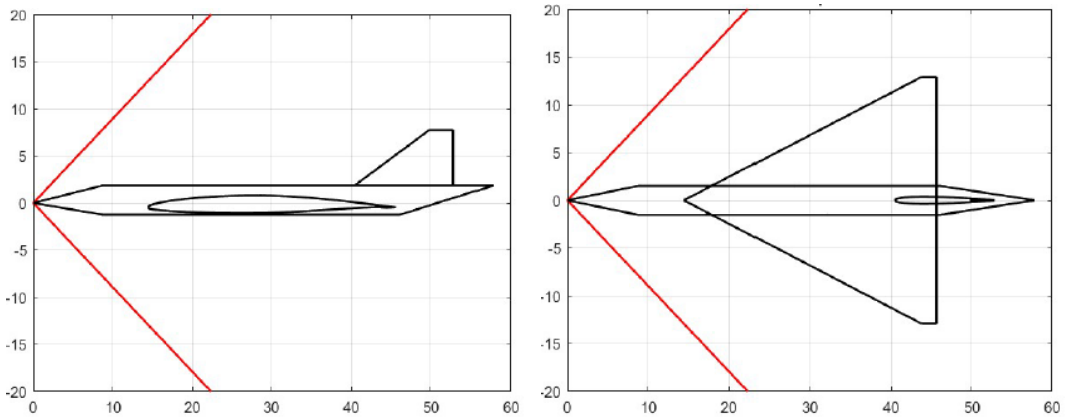

(a) Lateral view sketch

(b) Plan view sketch

Fig. 4.75 Lateral and plan view sketch from ASTRID-H 2.0

Table 4.12 highlight the results given by ASTRID-H 2.0 at the end of the iteration process related to the mass and geometry of the new configuration to be studied.

Table 4.12 Sketch characteristics

Characteristics	Value
MTOW	148,970 $[kg]$
Payload	9,660 $[kg]$
OEW	66,485 $[kg]$
Wing area	358.79 $[m^2]$
Wingpsan	25.85 $[m]$
Aspect ratio	1.86 $[-]$
MAC	20.88 $[m]$
Sweep angle	64.24 $[deg]$
Root chord	31.22 $[m]$
Tip chord	1.87 $[m]$
Tail area	70.77 $[m^2]$
Fuselage length	57.78 $[m]$
Fuselage width	3.01 $[m]$
Required Thrust	493. 6 $[kN]$

Figure 4.76 presents the results of the Matching Chart tool for the converged solution, corresponding to a thrust-to-weight ratio of 0.34 and a wing loading of 415 kg/m^2. The solution is selected at the minimum feasible thrust-to-weight ratio, which corresponds to the maximum allowable wing loading that satisfies the landing requirements. In practice, a slightly higher thrust-to-weight ratio is often chosen as a safety margin. These results do not yet incorporate any sonic-boom constraints and are based solely on aerodynamic and propulsion considerations.

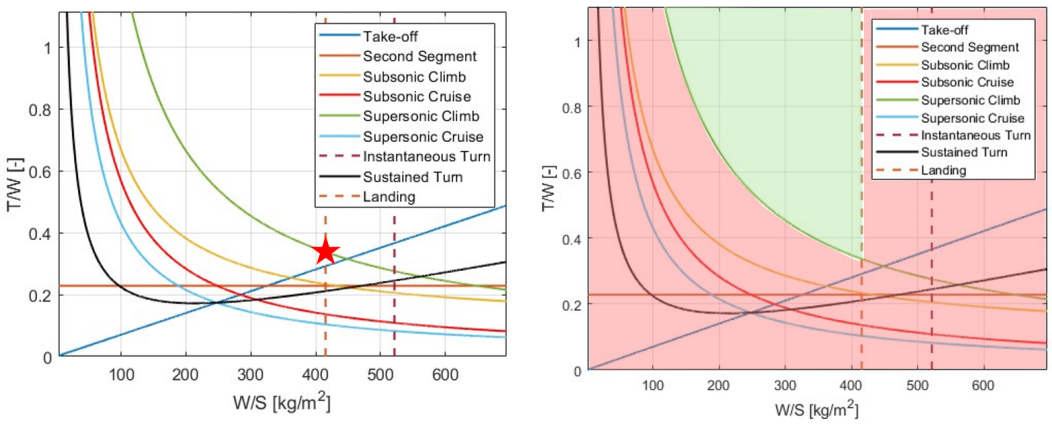

(a) Matching chart constraint

(b) Initial feasible area

Fig. 4.76 Initial Matching Chart of the configuration

At this stage, the previously defined constraints are applied. A key indicator of the model's performance is the coefficient of determination, R_S^2, which quantifies the agreement between the model predictions and the reference data. In this case, the model achieves an R_S^2 value of 0.97 for the positive peak, and R_S^2 value of 0.93 for the negative one, indicating an excellent fit. This result validates the model's accuracy and strengthens confidence in its predictive capability.

These equations provide critical insights into the system behaviour, and their precision is crucial for any further analysis or practical applications. The equation for the positive portion of the pressure signature is highlighted in Equation 4.7:

$$\Delta p = 1.1149 + 0.2792 \cdot \mathrm{M} - 0.0537 \cdot \mathrm{h} + 0.1876 \cdot \alpha + 6.764 \cdot 10^{-4} \cdot \mathrm{S} \qquad (4.7)$$

Conversely, the one for the negative portion of the pressure signature is written in Equation 4.8:

$$\Delta p = -1.8677 - 0.1046 \cdot \mathrm{M} + 0.0670 \cdot \mathrm{h} - 0.0579 \cdot \alpha - 4.463 \cdot 10^{-4} \cdot \mathrm{S} \qquad (4.8)$$

In Equations 4.7 and 4.8, M is the Mach number [-], h is the altitude [km], α is the angle of attack [deg], and S is the wing area [m^2], with the Δp values given in [psf]. Each explicit number represents a coefficient of the vectors $b_{1linear}$ and $b_{2linear}$, respectively. The numerical values obtained by inserting the data related to supersonic cruise and the final wing surface of the case study are as follows:

- Δp_1= 47.75 Pa $\approx$ 1 psf
- Δp_2 = -49.66 Pa $\approx$ 1.04 psf

To effectively integrate the evaluation of the requirement within the performance-oriented design space of the Matching Chart, the equation should be reformulated to be a function of the wing loading W/S. Equation 4.7 and 4.8 are rearranged to express the wing surface, and then formulation introduces wing loading by inverting the expression and multiplying by the aircraft weight. The weight appears on one side of the equation as the MTOW and on the other as W, solely to reflect the notation used in the Matching Chart, and although expressed differently, both terms represent the same value. This adjustment ensures compatibility with the Matching Chart. Accordingly, the following formulation defines a sonic boom requirement tailored for the Matching Chart, focusing on the peak overpressure.

Using the correlation model, Equation 4.9 relates wing loading to the requirement on maximum overpressure peak for the positive portion of the signature:

$$\frac{\mathrm{W}}{\mathrm{S}} = \frac{\mathrm{MTOW} \cdot 6.764 \cdot 10^{-4}}{\Delta p - (1.1149 + 0.2792 \cdot \mathrm{M} - 0.0537 \cdot \mathrm{h} + 0.1876 \cdot \alpha)} \tag{4.9}$$

As it is currently formulated, this equation implies that the wing loading is exactly equal to the value for which a specific overpressure peak is obtained. Considering that the requirement indicates that the peak amplitude must be strictly lower than the initial prescribed value, wing loading for the selected case study shall exceed the value resulting from the right side of the equation. This condition introduces a new constraint on the lower bound of the x-axis in the Matching Chart tool. Unlike the upper wing loading limit imposed by landing or stall requirements, this new boundary represents a sonic boom constraint and defines a previously unconsidered design limit. Parallelly, the same considerations could be applied for the equation related to the negative peak expansion.

The deviations in the feasible design space region for the selected case study in the Matching Chart tool is visible in Figure 4.77.

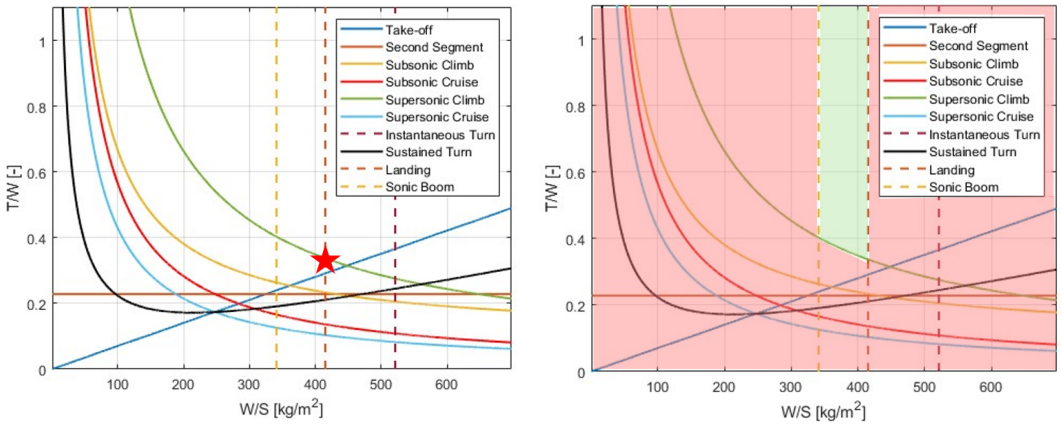

(a) Matching Chart final requirements

(b) Final feasible area

Fig. 4.77 Final Matching Chart of the configuration

As shown, the feasible area varies predictably with the application of a sonic boom constraint. The design point remains unchanged since the initial constraint is satisfied; however, a more restrictive constraint would result in a different design point or an area composed entirely of unfeasible regions. The integration of the sonic boom constraint into the Matching Chart tool allows aircraft designers to incorporate acoustic environmental limitations while evaluating aerodynamic and performance trade-offs. Moreover, the addition of the upper limit of peak overpressure enhance the traditional design space by considering community noise impact, which is a critical factor in future supersonic generation of civil aircraft. While peak overpressure is not a noise metric, and would not be used for future civil overland regulations, it provide a first-order estimation of the sonic boom characteristics of the aircraft. This approach lays the groundwork for integrating the methodology into a multidisciplinary optimization framework, allowing designers to balance aerodynamics, propulsion, structure, and acoustics when developing next-generation sustainable supersonic aircraft.

4.6.2 Evaluation of current analytical formulation

Similarly, refined analytical formulations are proposed to better incorporate sonic boom analysis of future high-speed civil configurations within a holistic multidisciplinary design framework. Leveraging the extensive high-fidelity numerical simulations and experimental campaigns conducted as part of the MORE&LESS

project, a refined Carlson-based analytical formulation has been developed and subsequently validated.

Evaluation of existing methodology

One of the outcomes of this PhD thesis was the inclusion, based on high-fidelity simulations, of new and refined analytical formulations in ASTRID-H 2.0 software. Prior to this step, the existing methodologies were systematically evaluated to determine their suitability for application at the conceptual design stage. This evaluation also ensured that the selected approaches could be consistently validated across a range of flight conditions and aircraft configurations. As discussed in Section 4.6.1, the initial stages of the design process require well-defined requirements and appropriate tools, particularly for designers who are not yet familiar with the physics of sonic booms. In this context, the simplified Carlson method [104], already discussed in Section 1.5, was chosen as the first analytical model to be included and extended in ASTRID-H 2.0. The simplified analytical Carlson method has several practical advantages. It allows fast calculations, which is very useful for early-stage trade-offs, without the need of heavy numerical simulations or expensive post processing data acquisition. It can also be applied to a variety of supersonic and hypersonic configurations, including altitudes up to 76 km, which is above the ceiling considered in the case studies of this thesis. Another benefit is that the method relies on charts and propagation factors, making the estimation process simpler and more straightforward. Finally, the results from the method have been compared with measured sonic boom data from a range of first-generation supersonic aircraft, showing that it is both reliable and broadly applicable.

An initial comparison between Carlson's original formulation and the high-fidelity bi-domain methodology developed in this PhD thesis was carried out for the Concorde-like case study [178]. In this context, the near-field simulations were performed using an Euler approach, without activating a turbulence model, employing the SU2 solver, and selecting the Harten–Lax–van Leer–Contact (HLLC) numerical scheme. The operating conditions for the comparison are highlighted in Table 4.13.

Table 4.13 Simulation condition CS1

Operating condition	Value
Mach number	2.0
Angle of attack α [deg]	0
Altitude [m]	15760
Free-stream pressure [Pa]	10684
Free-stream temperature [K]	216.6

The conditions are similar to one of previous simulations analyzed in Section 4.1.2, with the main difference related to the flight altitude of the configuration. The contour of increase of static pressure and Mach number are visible in Figure 4.7b and 4.8c.

Pressure signature in the radial direction across the geometry was extracted at radial angles ϕ_{CFD} from 0° (below the aircraft) to 180° (above it), with a 5° step. In Figure 4.78, the pressure signature and the corresponding noise levels in decibels are shown for specific radial angles. The angles considered range from 0° to 180° in 30° increments. The noise level in decibels is calculated as $20 \cdot \log_{10}(p_s/p_{\text{ref}})$, where $p_{\text{ref}} = 20\ \mu$Pa. The results highlight that there not evident differences in the radial extracted pressure signature.

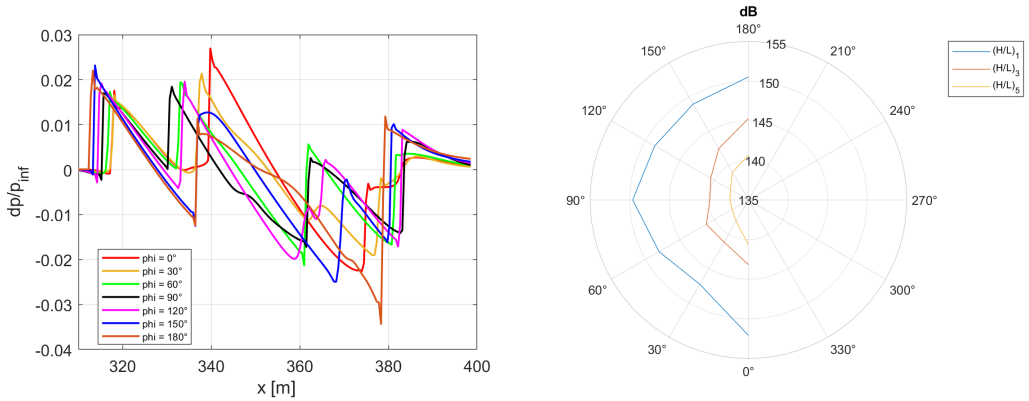

(a) Radial pressure signature at H/L=3

(b) Radial N-wave noise in dB

Fig. 4.78 H/L=3 radial pressure signature and N-wave noise in dB

The propagation of the near-field simulation was performed using the MORE&LESS in-house developed propaBoom software [164]. To maintain consistency with the

Carlson methodology, a windless atmosphere with zero relative humidity was assumed, while temperature and pressure profiles were taken from the ICAO Standard Atmosphere. At the end of each signature, a slight fading was applied to enforce a return to zero, and zero-padding was used by adding additional zeros prior to propagation to avoid numerical artifacts. The raw and processed pressure signatures for the three extraction positions are shown in Subfigure 4.79a, corresponding to a radial angle of 0°. In these plots, dashed lines represent the original signatures, which do not naturally decay to zero, whereas solid lines show the modified signatures adjusted to return to zero at the end of the signal. The effects of non-linear propagation between H/L = 1 and H/L = 5 are evident: positive shocks shift toward the beginning of the signal, while negative shocks move toward the end. Finally, the propagated edited near-field signatures are shown in Subfigure 4.79b. Those were calculated with a sampling frequency of 200 kHz, a ray step size of 0.1 s or less toward the ground, and including a ground reflection factor of 2.

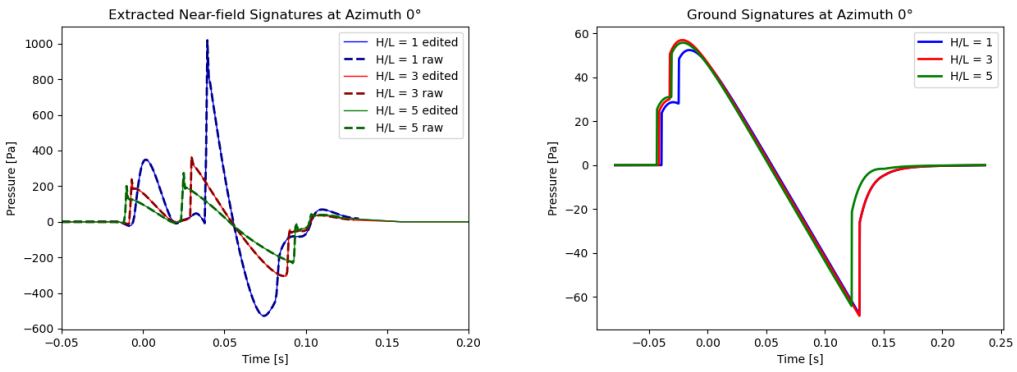

(a) Radial pressure signature at H/L=3

(b) Ground pressure signature

Fig. 4.79 Edited near-field signal and ground sonic boom waveform

In particular, the use of SU2 solver, a slightly modified ISA atmosphere and a reduced flight altitude does not varies the shape of the pressure signature, compared to the one highlighted in Section 4.2.2. The determination of radial distance entails a trade-off between modeling accuracy and atmospheric assumptions: smaller distances minimize the effect of near-field refraction, while larger distances require treating the atmosphere as effectively uniform.

The comparison of the bow-shock overpressure between simplified and high-fidelity simulation is highlighted in Figure 4.80 and Table 4.14 for azimuth angles between 0° and 50°, with a 10° step.

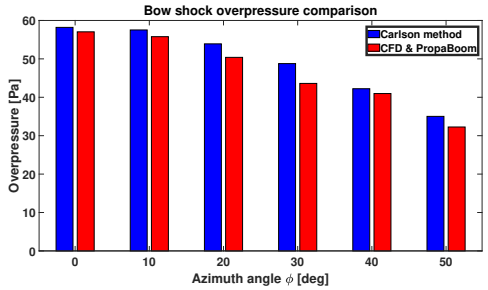

Fig. 4.80 Bow shock overpressure comparison azimuth angle θ

Azimuth ϕ	Carlson	propaBoom
0°	59.44 [Pa]	57.04 [Pa]
10°	58.53 [Pa]	55.78 [Pa]
20°	54.11 [Pa]	50.39 [Pa]
30°	48.77 [Pa]	43.61 [Pa]
40°	43.33 [Pa]	40.97 [Pa]
50°	35.03 [Pa]	32.26 [Pa]

Table 4.14 Numerical comparison bow shock overpressure

In particular, the comparison between the low- and high-fidelity models shows a good correlation for both on-track and off-track conditions, with differences up to 5 Pa. For the selected azimuth angles, the low-fidelity method is conservative compared to the high-fidelity one. However, as discussed in Section 4.2, large variations can still occur due to changes in the atmospheric profile and small deviations in the angle of attack. At the same time, the original formulation of the Carlson method was developed for the first generation of supersonic aircraft, which were not designed with sonic boom minimization, and for which the ground signature consisted of a fully developed N-wave. For this reason, updated formulations are required to take into account low-boom ground waveform shapes and to improve the reliability of sonic boom predictions at conceptual design stage.

Figure 4.81 and Table 4.15 highlight the comparison for the time signature duration with the same range of azimuth angles.

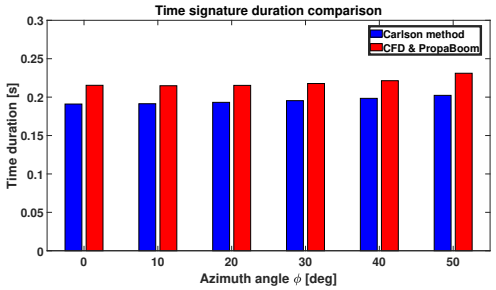

Fig. 4.81 Time signature duration comparison azimuth angle θ

Azimuth ϕ	Carlson	propaBoom
0°	0.1905 [s]	0.21539 [s]
10°	0.1911 [s]	0.21482 [s]
20°	0.1924 [s]	0.21529 [s]
30°	0.1951 [s]	0.21771 [s]
40°	0.1978 [s]	0.22139 [s]
50°	0.2019 [s]	0.23108 [s]

Table 4.15 Numerical comparison time signature duration

The comparison between low- and high-fidelity methods shows a different trend compared to the previous analysis. The low-fidelity method predicts a shorter signature duration, and the gap between the two approaches is larger than in the bow-shock case. In addition, the variation with azimuth angle is more pronounced, reaching a deviation up to 0.03 seconds. As discussed in Section 4.2, the International Standard Atmosphere (ISA) slightly overestimates the duration of the pressure signature compared to more realistic atmospheric profiles.

Figure 4.82 highlights the differences between the methodologies used to estimate the primary sonic boom carpet. Greater discrepancies are observed when different atmospheric profiles are considered, affecting both frontal and lateral propagation. Minor differences also appear in the off-track angle at which the cut-off phenomenon occurs: in the simplified methodology, the azimuth angle beyond which the signal does not reach the ground is approximately 51.5°, whereas in the high-fidelity methodology it is 54.89°.

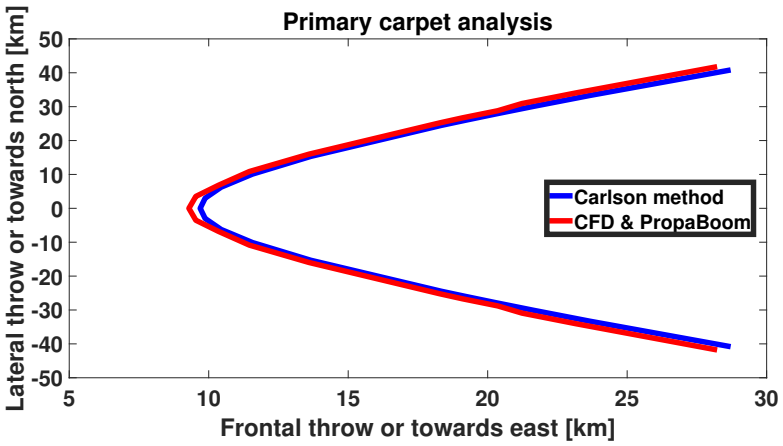

Fig. 4.82 Primary carpet comparison low, high-fidelity simulations

4.6.3 Refined analytical methods

Section 4.6.2 demonstrated that existing analytical methodology provides accurate estimates of sonic boom overpressure and primary carpet extension under the International Standard Atmosphere (ISA) at 0° of angle of attack.
Nevertheless, developing an upgraded methodology is essential for next-generation supersonic aircraft, particularly to account for low-boom configurations without a N-wave shape or varying flight conditions. To address the limitations of current analytical approaches, the model described in Section 3.4.4 was applied to the Mach 1.8 supersonic business jet, as detailed in Section 2.2. High-fidelity RANS simulations, beside assessing the influence of boundary-layer shock waves interactions in the noise metrics, provide valuable data for the validation of the proposed methodology.

A comparative analysis was performed between the original Carlson methodology the refined formulation, and high-fidelity simulations. The high-fidelity simulations employed both inviscid and Navier–Stokes solvers; as discussed in Section 4.3.3, differences between the k–ω and Spalart–Allmaras turbulence models were negligible, so only k–ω results are presented. Comparisons were conducted for flight conditions at angles of attack of 0° and 4°, while keeping the Mach number equal to 1.8.

Peak Overpressure Comparison

For the validation case study, the reference curve chosen to evaluate the shape factor parameter K_S in Figure 3.30 corresponds to the Mach 1.5 Supersonic Business Jet. Although the cruise Mach number differs slightly (1.5 vs. 1.8), the aircraft's maximum take-off weight, length, and wing surface area are comparable. Results are reported for both the original Carlson methodology and the refined formulation, considering variations in azimuth angle θ (0°–50°) and angle of attack α. Figure 4.83 presents the ground peak pressure for angle of attack $\alpha = 0°$ (Figure 4.83a) and $\alpha = 4°$ (Figure 4.83b).

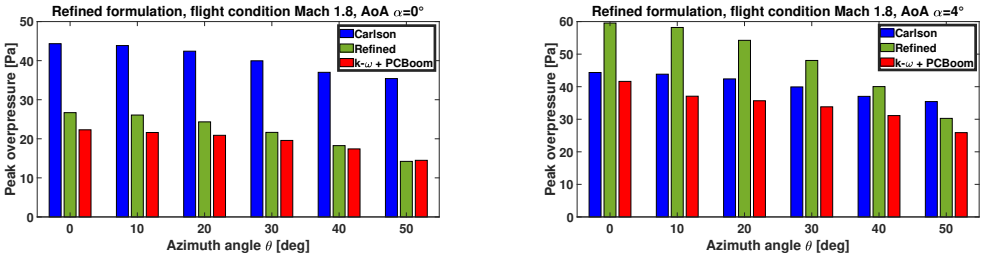

(a) angle of attack $\alpha = 0°$

(b) angle of attack $\alpha = 4°$

Fig. 4.83 Comparison of peak overpressure between the original and refined Carlson formulations

In the original methodology, variations in angle of attack have minimal influence, whereas changes in azimuth angle produce visible effects. As would be later exposed in Table 4.16 and 4.17, differences due to angle of attack in the original methodology are minimal. The refined methodology, in contrast, is significantly more sensitive to the angle of attack α, a trend also observed in the high-fidelity sensitivity study of Section 4.3. Examining the high-fidelity results, a N-wave shape is absent at incidence $\alpha = 0°$ for both configurations (Figure 4.20a and Figure 4.27a). At $\alpha = 4°$, the Mach 1.8 aircraft exhibits a shaped pressure signature, whereas the supersonic business jet displays a N-wave ground signature. The deviation for the refined methodology at 4° of incidence is attributed to the tuning of the model. Specifically, the configuration for which the refined approach has been used exhibits a developed N-wave at the selected flight condition, which noticeably increases the predicted peak overpressure. As visible in Section 4.2, small deviations in the flight condition that bring the ground waveform from a shaped signature to a N-wave strongly increase the maximum overpressure recorded by an ideal ground-based microphone. These

trends and observations suggest that a single aircraft may not be sufficiently accurate to discretize a complete family of configurations, even at the low-fidelity conceptual design stage.

The two methods also differ in the attenuation of peak overpressure across the primary carpet: the original formulation predicts only minor reduction, whereas the refined methodology indicates a substantially stronger decrease, which is in line with high-fidelity numerical simulation findings.

Primary Carpet Comparison

Similar to the bow shock analysis, primary carpet extension was evaluated for azimuth angles θ ranging from 0° to 50°. Under the assumptions of the original methodology, the ISA atmospheric profile without humidity was used as reference. In Carlson's original formulation, the primary carpet does not include the aircraft shape factor parameter K_S, so the comparison is between the simplified methodology and high-fidelity simulations.

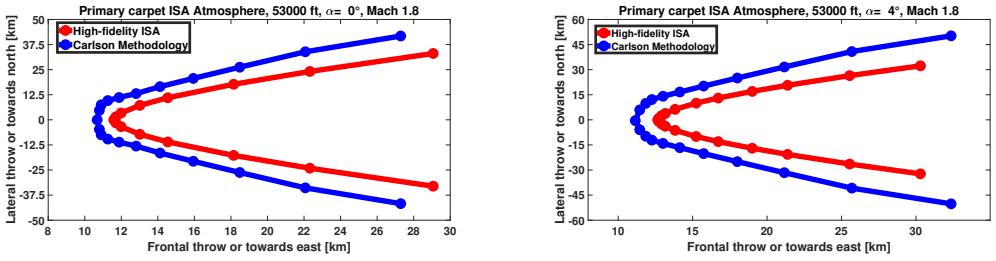

(a) $\alpha = 0^\circ$ (b) $\alpha = 4^\circ$

Fig. 4.84 Comparison of primary carpet extension between high-fidelity and Carlson methods

Overall, there is good agreement between analytical and high-fidelity methods, though Carlson's method tends to slightly overestimate the primary carpet extent. At $\alpha = 4^\circ$, the lateral throw is approximately 20 km wider and the frontal throw 3 km higher than PCBoom results; at $\alpha = 0^\circ$, lateral overestimation is reduced to 11 km and the frontal throw is underestimated by less than 3 km.

Analysis of Results

Comparing high-fidelity and simplified methods highlights the respective strengths and limitations of each approach. The refined Carlson formulation significantly improves peak overpressure predictions while preserving low computational cost, providing reliable first-order estimates under both operating conditions. Its main advantage lies in the rapid evaluation of maximum peak pressure over the primary carpet at the selected azimuth angle θ, without executing all steps required within the original method. It requires neither a detailed CAD model nor costly preprocessing of equivalent areas due to volume or lift. However, as discussed in Section 4.2 and 4.3, realistic atmospheric profiles can significantly affect primary carpet extension, noise metrics, and peak overpressure.

Table 4.16 summarizes the peak pressure across azimuth angles at $\alpha = 0^\circ$ for the original and refined methodologies alongside high-fidelity simulations using ISA conditions. Both Euler and k-ω simulations are reported.

Azimuth angle	**Carlson [Pa]**	**E. Carlson [Pa]**	**Euler [Pa]**	***k*-ω [Pa]**	**% var. Carlson**	**% var. Refined**
0°	44.34	26.69	19.76	22.30	22.04	4.39
10°	43.86	26.08	19.07	21.61	22.25	4.47
20°	42.42	24.33	18.04	20.89	21.53	3.44
30°	39.96	21.64	17.27	19.58	20.38	2.06
40°	37.01	18.25	15.59	17.41	19.60	0.84
50°	35.41	14.22	12.62	14.49	20.92	-0.27

Table 4.16 Peak pressure comparison in Pascal for the angle of attack $\alpha = 0^\circ$ flight condition including variations relative to *k*-ω simulation

At incidence $\alpha = 0^\circ$, the refined methodology closely matches high-fidelity results, whereas the original method assumes a fully developed ground N-wave, explaining the larger deviations. Errors in the original Carlson formulation increase with azimuth angle, reflecting limited lateral attenuation modeling, while the refined approach shows only minor deviations.

Similarly, table 4.17 presents the results for angle of attack $\alpha = 4°$, where deviations are more pronounced due to differences in ground pressure signature development.

Azimuth angle	**Carlson [Pa]**	**E. Carlson [Pa]**	**Euler [Pa]**	k-ω **[Pa]**	**Δp Carlson**	**Δp refined**
0°	44.32	59.56	38.92	41.63	2.69	17.93
10°	43.84	58.19	34.52	37.08	6.76	21.11
20°	42.39	54.24	33.38	35.68	6.71	18.55
30°	39.93	48.06	31.48	33.82	6.11	14.24
40°	37.03	40.03	28.68	31.13	5.90	8.90
50°	35.43	30.27	23.72	25.89	9.54	4.38

Table 4.17 Peak pressure comparison in Pascal for the angle of attack $\alpha = 4°$ flight condition including variations relative to k-ω simulation

The deviations observed in the refined Carlson formulation were previously discussed and attributed to differences in the shape of the ground pressure signature between the aircraft's tuned configuration and the reference case used for the method's validation. To improve the quality of the model, additional case studies for each aircraft category should be included in future work.

Finally, Table 4.18 compares primary carpet extension. Significant differences are observed in lateral spread on both sides, indicating that simplified methods may overestimate the affected area, which could influence sonic boom impact assessments.

Table 4.18 Comparison of primary carpet extension

Case	Angle of Attack	Turb. Model	Starboard [km]	Portside [km]	Frontal [km]
ISA high-fidelity	0°	k-ω	33.06	-33.06	29.36
ISA high-fidelity	0°	Euler	33.12	-33.12	29.33
Carlson	0°	/	41.75	-41.75	27.29
ISA high-fidelity	4°	k-ω	32.76	-32.76	29.84
ISA high-fidelity	4°	Euler	32.71	-32.71	29.82
Carlson	4°	/	50.21	-50.21	32.33

The results provided by Table 4.18 highlights that the original Carlson method strongly overpredict the Starboard and Portside extension of the primary carpet.

Chapter 5

Discussion

This chapter presents the main results, findings, uncertainties, and limitations of this doctoral thesis. It interprets the key outcomes, evaluates the limitations and uncertainties of the employed methods, and discusses their implications for future supersonic aircraft design and regulation. Particular attention is given to how sonic boom characteristics change under off-design conditions, the effectiveness of both high- and low-fidelity tools, and the practical relevance of different noise metrics. By linking numerical predictions, experimental validation, and design-oriented tools, this chapter provides an integrated analysis aimed at helping aircraft designers and regulatory bodies make informed decisions for the next generation of supersonic transport.

5.1 Summary of main findings

This section presents a summary of the main findings of the PhD thesis. The discussion follows the key areas of investigation, while the limitations and uncertainties are addressed in Section 5.2.

A comprehensive numerical framework was developed, combining near-field Computational Fluid Dynamics simulations with propagation through a non-uniform, stratified atmosphere. This approach allowed for accurate predictions of sonic boom ground pressure signatures and related noise metrics from Mach 1.5 to Mach 5.0 (as discussed in Appendix B). It also delivered consistent results across a range

of configurations, including low-boom business jet, supersonic aircraft concepts, experimental projectiles, and hypersonic vehicles.

A key outcome concerns the sensitivity of sonic boom noise metrics to small off-design conditions. Distinct trends were observed between a Mach 1.5 Supersonic Business Jet and a Concorde-like configuration. For both cases, the angle of attack varied between -2° and 4° with a 2° step, while the Mach number ranged from 1.2 to 1.5 for the business jet and from 1.5 to 2.0 for the Concorde-like aircraft. Four atmospheric profiles were assessed, including the International Standard Atmosphere and three realistic cases proposed at the Sonic Boom Prediction Workshop [196–198]. Furthermore, modest deviations of 2° in flight conditions that transformed the ground pressure signature from a shaped profile to a N-wave shape led to a marked increase in noise metrics. For the business jet, noise metrics variations reached up to 7 dB when a N-wave pressure signature occurred, emphasizing the importance of designing for robustness across the entire mission envelope, rather than focusing solely on cruise conditions. Similar results were obtained for the Concorde-like Mach 2 airliner. While no experimental tests were conducted on human subjects in this thesis, a detailed evaluation of psychoacoustic metrics, including PL and ISBAP, has been included. Energy-based metrics, though useful for quantifying total acoustic energy, fail to represent the temporal structure of the signal. Two waveforms with identical energy but different rise times or sharpness can produce markedly different levels of perceived annoyance. In contrast, time-domain and loudness-based metrics account for the steepness, duration, and sharpness of the ground pressure signature—features critical to human auditory perception. While NASA and ICAO-CAEP studies often report a strong correlation between PL and subjective loudness and annoyance, some NASA studies indicate that specific weighted SEL metrics (e.g., BSEL) may achieve similar or higher correlation levels, particularly for indoor perception. Furthermore, psychoacoustic metrics are more sensitive to variations in atmospheric conditions than energy-based metrics, as demonstrated within this work. Under realistic atmospheric profiles, changes in temperature, humidity, and wind can modify the shock steepness and spectral content of the waveform, thereby affecting perceived loudness and sharpness. In contrast, energy-based metrics remain more stable, as they depend primarily on the total acoustic energy. As a result, realistic atmospheric profiles may alter psychoacoustic metrics by up to 5 dB relative to the International Standard Atmosphere (ISA), while leaving energy-based metrics with reduced variations. This finding suggests that future

overland sonic boom certification standards should either include a Δ allowance for atmospheric variability or require flight planning that explicitly accounts for atmospheric conditions throughout the mission.

A second numerical finding of this thesis is the comparison of noise metrics between Euler and RANS simulations. Since inviscid simulations are less computationally demanding, previous studies have relied on them; however, this approach can limit their ability to capture interactions between the boundary layer and shock waves. These interactions, if neglected, may lead to inaccurate predictions of ground pressure signature intensity and locations. With the aim of supporting future definitions of overland high-speed civil flights noise procedure standards, the present work quantifies noise metric deviations for a Mach 1.8 low-boom Supersonic Business Jet. Results indicate a deviation of approximately 1.5 dB between inviscid and viscous simulations. Two turbulence models—k$-\omega$ and Spalart–Allmaras—were tested, but discrepancies were minimal, with variations in noise metrics up to 0.35 dB.

The near-field numerical methodology was validated up to Mach 5.0 through dedicated experimental campaigns at the ISL proving ground, which generated a unique dataset of free-flight sonic boom pressure signatures. Comparisons between scaled projectiles and numerical simulations demonstrated a strong agreement, with deviations of about 1 dB for the CS3 mock-up configuration. The numerical findings not only reproduced but also validated the experimental observations, confirming the reliability and predictive capability of the proposed approach, as well as the setup of the test. Considering the steady-state and Euler assumptions, these deviations are consistent with the trends reported in Section 4.2.3. The experiments further highlighted the substantial influence of atmospheric parameters—temperature, humidity, and wind—on waveform steepening and attenuation. Finally, the use of microdrone-based instrumentation provided an innovative means of capturing sonic boom signatures, though its correlation with ground-based microphones remained limited.

High-fidelity simulations and experimental tests form the backbone for developing design-oriented tools that can be used and integrated since the conceptual design phase. The first tool introduced in this work is a new sonic boom constraint, which has been integrated into the Matching Chart based on peak overpressure. This requirement is based on high-fidelity numerical simulations and has been calibrated against a statistical database to ensure reliability for conventional configurations and

for flight conditions up to Mach 2. While future noise certification standards will rely on specific noise metrics, this study initially focuses on estimating peak overpressure. Although the tool is currently limited to configurations up to Mach 2, it has proven to be a useful low-fidelity guideline for early-stage design and trade-offs. These configurations represent a meaningful step toward the next generation of supersonic civil aircraft. By providing designers with the ability to include peak overpressure thresholds in early trade-offs, alongside conventional aerodynamic and propulsion requirements, this contribution effectively bridges the gap between high-fidelity simulations and practical conceptual design decisions.

The second tool developed in this thesis extends the Carlson analytical simplified method. A new framework was introduced to estimate the aircraft shape factor parameter, K_S, by combining high-fidelity CFD results with experimental data. This approach provides a mid-fidelity estimate of peak overpressure for a given configuration at the conceptual design stage, offering a rapid and low-cost means to assess sonic boom impacts within a multidisciplinary design process. Four new curves were generated, corresponding to different aircraft categories. This tool is integrated at the end of the design iteration loop to ensure that low-fidelity requirements are satisfied before proceeding to high-fidelity, computationally expensive numerical simulations or experimental sub-scaled tests. Comparison of these curves with high-fidelity simulations for the Mach 1.8 supersonic business jet shows good agreement, confirming the method's accuracy and its suitability for reliable integration into multidisciplinary optimization frameworks. Differences at the flight condition of 4° incidence were assessed and are attributed to the different behavior of the ground pressure signature under this specific flight condition compared with the configuration used to tune the model. Following the completion of a design iteration, the expected sonic boom overpressure can be estimated by selecting the appropriate aircraft category and the corresponding K_L lift parameter for the relevant flight condition. This approach enables early-stage evaluation of sonic boom effects without requiring full high-fidelity simulations, facilitating informed trade-offs during preliminary design. Collectively, these tools represent a significant step toward the development of efficient and reliable noise-conscious design methodologies for next-generation high-speed civil aircraft.

Lastly, this thesis addresses the inverse estimation of the flight dynamics of supersonic and hypersonic projectiles. This approach is particularly relevant in applications where the spatio-temporal evolution of the pressure field, including

amplitude variations, contains valuable information about the source. The methodology developed allows amplitude-based inverse estimation of the projectile's flight dynamics by combining linearized wave propagation models with pressure data obtained from CFD simulations on a cylindrical surface surrounding the projectile. The results indicate a high level of accuracy in reconstructing the flight dynamics. Angular deviations in the direction vectors are minimal, with an overall deviation of 0.17°—0.09° in the XY plane, 0.14° in the YZ plane, and 0.78° in the XZ plane. Within the acoustic measurement zone, velocity deviations between the acoustic-based estimations and RADAR measurements remain below 6 m/s, confirming the robustness and reliability of the proposed approach for supersonic and hypersonic flight analysis.

5.2 Limitations and uncertainties

Although the methodologies developed in this work proved effective, several limitations and uncertainties must be acknowledged. The two experimental campaigns introduce significant uncertainties in both results and methodology. A key challenge is reconstructing the aircraft shape for sub-scaled mock-ups. At the ISL proving ground in Baldersheim, as previously described, various considerations regarding the projectile's shape had to be accounted for. Free-flight experiments required projectiles with near-zero lift to ensure safety, which differs from ideal full-scale configurations. This constraint strongly influenced projectile shape, altering sonic boom characteristics relative to the original configuration.

Variations in the projectile shape were noticeable for both the CS3 and CS2 mock-up configurations. For the first concept, most of the geometric changes were focused on the lee-side surfaces, while the windward side—the part responsible for generating shock waves that reach the ground—was kept as close as possible to the original aircraft design. To prevent asymmetric lift during free-flight tests, the lower fuselage contour was mirrored into the upper side, creating symmetry along the longitudinal plane. These adjustments had a significant impact on how shock waves were generated and interacted compared to the original vehicle. Similarly, the CS2 mock-up design was driven by two main considerations: the vehicle needed to withstand mechanical loads during launch and free flight without structural damage, and aerodynamic lift had to be minimized for safety. Structural reinforcements

were added to limit body deformation during launch. For both sub-scaled models, design simplifications were required for manufacturability and safe launch involved removing non-essential aerodynamic features, such as canards and fins. In the CS3 mock-up, the frontal air intake was sealed, which had little effect on sonic boom characteristics. In contrast, the CS2 mock-up had significantly enlarged vertical fins to ensure adequate longitudinal and vertical stability, which in turn affected shock wave generation compared with the original configuration.

The experimental campaigns covered high-supersonic to low-hypersonic regimes, which do not fully match flight conditions expected for future high-speed aircraft. Nevertheless, preserving the overall geometric structure in future experimental campaigns is essential for low-boom configurations, which are designed to mitigate shock wave generation and interactions. The current instrumentation setup and smooth-bore launcher may not be directly applicable to future configurations. In particular, the maximum projectile width is constrained by the smooth-bore launcher, and reproducing low-boom designs while maintaining near-zero lift must be carefully assessed. Although the lift coefficient is generally small for hypersonic configurations due to their high speed, for low-boom and low-Mach concepts the deviation between the ideal cruise lift coefficient C_L and the maximum value permitted during the tests may be non-negligible.

Another source of uncertainty comes from transient flight regimes occurred in the tests. Manufacturing tolerances introduced unexpected dynamic behavior during free flight. For the CS3, these dynamics were minimal, and numerical predictions closely matched the experimental observations. These simulations were performed without activating a turbulence model, confirming the reliability of both the numerical procedure and the experimental setup. In contrast, the second test campaign displayed more noticeable dynamics, resulting in deviations exceeding 2 dB between steady-state predictions and experimental measurements. The use of transient and turbulence-resolving simulations could help reduce this discrepancy, but the additional computational cost and time would be substantially higher. All case studies in this thesis used steady-state simulations. For future work, especially involving off-design or maneuvering flight conditions, transient simulations will be needed to capture unsteady aerodynamic effects, such as those related to climb, descend or maneuvers. Alternative approaches—such as reconstructing Whitham's F-function in near-field analyses or using surrogate-based models—offer promising ways to reduce computational time while still maintaining acceptable accuracy.

Finally, the two design-oriented tools developed in this thesis have different limitations. Both rely primarily on peak overpressure, without accounting for perceptual noise metrics that are expected to play a pivotal role in future overland high-speed civil regulations. The Matching Chart methodology is based on a statistical approach derived from high-fidelity simulations of the Concorde-like and CS2 configurations, which is described later in Appendix B. At present stage, it is mainly applicable to conventional geometries operating up to Mach 2 at small angles of attack. Expanding the simulation database would improve robustness, while extending the formulation to other configuration types would facilitate integration within a multidisciplinary design framework, thus enabling the inclusion of additional aircraft types. The refined analytical method, while effective, also has limitations. Because of the limited dataset, the aircraft family curve is highly sensitive to the reference configuration that tuned the model. For a comparable business jet configuration, results aligned well at 0° angle of attack, but significant discrepancies appeared at 4°. This occurred because the configuration which tuned the model produced a N-wave ground signature, whereas the validated case study exhibited multiple peaks in its ground pressure signature. Although the methodology is already embedded in a multidisciplinary design framework, additional case studies involving different aircraft families are needed to enhance robustness and predictive performance. Moreover, while peak overpressure provides a valid first-order approximation, incorporating perceptually based noise metrics and higher-fidelity requirements will be essential.

5.3 Implications for future aircraft design

The numerous of this thesis have important implications for the design of future supersonic aircraft. These emerge from a combination of high-fidelity numerical simulations, enhanced analytical tools, and experimental validation, which together offer a more complete framework for shaping the next generation of civil high-speed transport. A key insight is that the sonic boom cannot be treated as an afterthought, but instead it must be addressed from the earliest stages of the design process. Traditional approaches, such as the Matching Chart tool, focused mainly on aerodynamic and propulsion considerations. By introducing a simplified requirement based on peak overpressure thresholds, this work extends those methods, making acoustic performance a fundamental driver of design. This represents a significant

shift: aircraft must now be sized and shaped with environmental acceptability treated as a hard boundary. Figure 4.77 shows how the feasible design space reduces when aeroacoustics constraint are applied.

Another important contribution of this thesis is the refinement of the existing analytical method, in particular the Carlson simplified approach. The methodology developed here improves prediction accuracy for both peak overpressure and time-signature duration. This refinement is particularly valuable during the conceptual design phase, when high-fidelity simulations are often impractical because of computational cost, incomplete CAD models, or limited input data. By reducing the gap between low- and high-fidelity predictions, the method developed here allows designers to make more informed decisions early in the process, before committing to detailed simulations or experimental campaigns.

Numerical analyses of two representative supersonic configurations also show that sonic boom performance is highly sensitive to deviations from nominal design conditions. Therefore, future supersonic aircraft should be conceived with operational robustness as a design objective. Their acoustic characteristics must remain within acceptable limits not only at the ideal cruise condition but also across realistic variations in flight scenarios, including changes in atmospheric profiles.

Taken together, these findings suggest that the second generation of supersonic civil transports will differ fundamentally from Concorde. While first-generation aircraft prioritized aerodynamic performance and cruise speed, future designs must operate within a multidimensional design space in which noise, pollutant emissions, and climate impact are equally significant. By incorporating sonic boom requirements from the conceptual design phase, refining analytical models, validating predictions experimentally, and accounting for off-design robustness, a new design philosophy emerges. A proposed workflow for the development of future low-boom, high-speed concepts is presented in Figure 3.2.

The flowchart presents a multi-level design methodology that brings environmental constraints into the development of supersonic aircraft. It combines low-fidelity and high-fidelity tools with experimental validation, gradually refining candidate designs until they meet mission, performance, and environmental requirements. At the centre of this workflow is sonic boom minimization, which must be managed carefully to satisfy regulatory limits and societal expectations when considering future high-speed civil aircraft. The process starts with the definition of high-level

requirements that cover both performance and environmental goals. Balancing those objectives remains a central challenge, as improvements in one area could lead to compromises in the other. Once the requirements are defined, ASTRID-H 2.0 tool generates an optimized preliminary configuration, integrating aerodynamics, propulsion, and weight-and-balance analyses to ensure physical feasibility. The mission definition then establishes the aircraft's operational profile, resulting in a baseline configuration that satisfies performance targets. At this stage, environmental constraints—including the sonic boom ones—have not yet been fully evaluated, underscoring the importance of incorporating acoustic considerations early in the design process.

In parallel, sonic boom requirements are defined in two complementary forms:

- Low-fidelity requirements (in Pascal [Pa]), directly related to peak overpressure values experienced at ground level.
- High-fidelity noise metrics (in PL), which account for human perception of the signal.

The refined Carlson methodology described in Section 3.4.4 is used to rapidly estimate the low-fidelity sonic boom signature from preliminary configurations at the end of the iteration loop. It offers an initial assessment before resorting to high-fidelity simulations or experimental tests. If the resulting predictions do not meet the requirements, the process returns to the sizing and mission definition stage, where design parameters are adjusted to better satisfy both performance and environmental objectives. If requirements are satisfied, the configuration proceeds to high-fidelity and experimental analysis. At this stage, two complementary approaches are employed to validate the previous predictions: (i) high-fidelity bi-domain numerical simulations, and (ii) experimental tests on sub-scaled configurations, which provide ground validation and support model calibration. The dual-path process ensures robustness by cross-verifying numerical and physical evidence, while being both computationally and economically cost-effective.

Following the high-fidelity analysis, the design is evaluated against the corresponding requirements:

- If the high-fidelity requirements are not met, the process loops back to earlier stages, where design parameters are adjusted and the workflow repeated.

- If the high-fidelity requirements are met, the configuration is considered the final one, and can proceed to more in-depth studies.

This iterative process embodies the design–analysis–validation cycle central to aerospace system development, particularly in areas where environmental constraints closely interact with aerodynamic performance.

5.4 Implications for certification metrics and suggestion for regulatory entities

The present analysis of psychoacoustic and energy-based metrics highlights the inherent complexity of evaluating sonic boom signatures and underscores that different parameters can produce markedly contrasting assessments of the same supersonic configuration. While the findings of this thesis may support regulatory bodies in defining internationally validated standards for high-speed overland flight, no independent subject tests or survey-based evaluations were conducted. The results are solely based on numerical simulations and analyses. Among the examined noise metrics, PL remains the most widely adopted choice due to its straightforward interpretation as a measure of perceived loudness, and it has long served as a benchmark for comparison across studies. The results of this thesis indicate that PL is especially sensitive to off-design conditions, such as changes in the angle of attack. Because it reflects perceived loudness, its value can vary with specific waveform features—including rise time, peak sharpness, slope asymmetry, and brief oscillations—that influence how a sonic boom is experienced by listeners.

In contrast, energy-based metrics such as DSEL, along with the weighted derivatives BSEL and CSEL, exhibit greater robustness in capturing the temporal evolution of the pressure waveform. By integrating the waveform's energy over time, these metrics provide a comprehensive measure of acoustic exposure, making them particularly reliable for quantifying the energy content of complex sonic boom events. However, this approach also reveals key limitations. These metrics do not explicitly model perceptually relevant temporal features, such as rise time, peak sharpness, or other transient waveform characteristics; however, these features are indirectly reflected in the frequency content of the signal, so that weighted SEL metrics like BSEL and DSEL respond to them and can correspondingly capture variations re-

lated to human annoyance. Consequently, although these metrics capture waveform dynamics accurately from a physical standpoint, their correlation with subjective human annoyance for low-boom configurations on real flight tests remains to be fully assessed. Laboratory studies on low-boom signatures have shown that some weighted SEL metrics can correlate well with human response indoors, particularly when rattle or vibration is present.

Overall, the findings suggest that no single metric yet offers a complete or universally reliable assessment of sonic boom impact. Upcoming flight tests with low-boom configurations, such as the X-59, are expected to provide both qualitative and quantitative data to better link noise metrics with the perceived annoyance experienced by an ideal observer. As noted by Loubeau [46], three meta-analysis methodologies were applied to evaluate the performance of different metrics. All three methods used R_S^2 to quantify how well each metric explains human annoyance, and in none of the analyses did a single metric clearly outperform the others. The five metrics ultimately recommended were PL, BSEL, DSEL, ESEL, and ISBAP. Notably, the inclusion of outdoor studies led to the exclusion of C-weighted metrics, which are effective only in indoor environments. In addition, the results of this thesis showed minimal deviation in the C-weighted metric for small variations in flight conditions. Furthermore, the present study underscores the critical importance of incorporating atmospheric variability in future guidelines. Propagation effects—such as temperature gradients, wind shear, and humidity profiles—can significantly modify the ground-level pressure signature, causing noticeable changes in both energy-based and psychoacoustic metric results. Ignoring these factors during certification could produce assessments that do not fully reflect real operating conditions, potentially weakening the credibility of the selected metrics and reducing public confidence in supersonic flight. This issue is especially relevant for the next generation of supersonic commercial aircraft, where strict noise certification will be key to achieving both regulatory approval and community acceptance. The findings of this thesis therefore contribute not only to a better scientific understanding of sonic boom evaluation but also to the practical development of reliable, perception-based certification standards.

5.5 Recommendations for future experimental campaigns

The two free-flight test campaigns provided valuable data for numerical analysis and validation, helping refine both the data acquisition procedures and the overall experimental setup. That said, some limitations became evident, offering lessons for future experiments. As shown in Figure 4.57, there is a noticeable dispersion in the recordings from the stationary drones, particularly at locations farther from the projectile trajectory. This scatter is largely due to noise from the drone motors and propellers, as well as vibrations transmitted through the airframe, which decrease correlation with ground-based microphone measurements.

In addition, the campaigns carried out nine launches at Mach numbers between 4.6 and 4.72, which are well above the operational range expected for future supersonic commercial aircraft. Future experiments would benefit from focusing on low-boom, lower-Mach configurations that better reflect the conditions of the emerging supersonic market. Testing at these speeds would provide data that are directly applicable to next-generation vehicle designs and could also help in shaping new noise certification standards and regulatory limits, especially with regard to community acceptance and environmental impact. It would also be useful to conduct tests under a variety of environmental conditions—such as different temperatures, humidity levels, and atmospheric pressures—to understand how these factors affect the sonic boom signatures recorded by the ground microphones.

During the two experimental test campaigns, CIRA and ISL placed their microphones at different heights above the ground. CIRA positioned its instruments about 1–1.5 meters high to reduce overlapping signals, while ISL placed theirs closer to the ground to limit interference between direct and reflected acoustic signals and to capture the direct sonic boom more clearly. These differences in microphone height allow some comparison of measurements as a function of roll angles, but they can also cause discrepancies at certain points of closest approach (CPA) within the same shot. Aligning microphone heights between CIRA and ISL would improve data consistency and strengthen cross-validation of the experimental setup and instrumentation.

Chapter 6

Conclusion

This thesis advanced numerical methodologies for high-fidelity sonic boom simulations, with the primary aim of supporting the development of future overland high-speed civil internationally valid regulations. In parallel, new methodologies and tools for the conceptual design phase of high-speed transport aircraft were introduced, enabling the integration of sonic boom constraints from the earliest design stages of the project. Sonic boom remains the primary limitation for a successful second generation of supersonic civil aircraft. This research validated numerical methodologies up to the hypersonic regime, analyzed vehicle performance under off-design conditions, and proposed innovative reduced-order tools for the conceptual design stage. The numerical and computational results produced in this framework could inform regulatory agencies by providing validated data and methodologies. Environmental issues linked to high-speed aviation must also be considered from the project outset, as they represent key factors in designing aircraft with sustainable performance. Specifically, aspects such as greenhouse gases, pollutant emissions, and noise generation are addressed to give a broad overview of these impacts.

The work was conducted within the EU-funded project MORE&LESS, in collaboration with CIRA (Centro Italiano di Ricerche Aerospaziali [247]), ISL (Institut Franco-Allemand de Recherche Saint-Louis [248]), and TUHH (Technische Universität Hamburg [249]). A six-month research period at the Department of Mechanical and Aerospace Engineering of the University of Florida [250], in collaboration with Dr. S. A. E. Miller and Dr. Sivaramakrishnan Balachandar, provided additional expertise critical to method development and validation. Existing high-fidelity numerical

methodologies were applied to compute near-field analysis of consortium configurations. The first part of the research focused on improved numerical approaches for sonic boom prediction. Computational Fluid Dynamics simulations analyzed the near-field region of various supersonic and hypersonic configurations, while dedicated propagation solvers modeled pressure signature evolution through realistic atmospheric profiles. The inclusion of turbulence modeling, systematic assessment of grid resolution and extraction distances enabled a more reliable characterization of the simulated signatures. Comparison with free-flight experimental campaigns confirmed method quality, with discrepancies limited to approximately one decibel, validating the experimental results. This agreement demonstrates that the developed framework provides a robust predictive tool and it could support both design and regulatory applications.

A central part of the doctoral thesis analyzed off-design conditions for two configurations up to Mach 2. Unlike classical design approaches, which focus solely on ideal cruise points, the results demonstrate that sonic boom noise metrics are highly sensitive to variations in Mach number, angle of attack, and atmospheric stratification. For the configurations studied, small deviations from the design point that produce a N-wave shape ground signature can increase psychoacoustics and energy-based metrics up to 5–6 dB. These findings highlight the importance of accounting for variability in regulatory standards, suggesting that future certification frameworks should include safety margins to accommodate non-nominal flight conditions or atmospheric uncertainties. The use of psychoacoustic and energy-based metrics provided a richer characterization of sonic boom assessment, moving beyond traditional physical descriptors toward measures more representative of human perception. Additionally, the influence of different turbulence models in the near-field domain was assessed, confirming its limited but not negligible effect.

The numerical work was complemented by the introduction of specific design-oriented tools to support designers without aeroacoustic knowledge to include sonic boom constraints. Firstly, the Matching Chart tool, which was traditionally employed for rapid performance evaluation of subsonic and supersonic concepts, was extended with the inclusion of sonic boom constraints. The methodology is valid for conventional configurations up to Mach 2, and allows designers to identify feasible design space that satisfy low-fidelity sonic boom requirements. Furthermore, analytical formulations were refined with the aim of improving accuracy without the need of high-fidelity simulations. A refined Carlson-based methodology was proposed and

validated for a Mach 1.8 business jet, improving low-fidelity tools. This leads to more reliable predictions of peak overpressure and time signature duration at conceptual design stage. These tools bridge the gap between high-fidelity simulations and preliminary design practices, and are included in a multi-disciplinary design optimization framework, ensuring environmental considerations from the earliest stages of the project.

Beyond prediction and design support, this thesis explored inverse methodologies for the estimation of flight dynamics from acoustic measurements. Using experimental data from free-flight campaigns, it is demonstrated that trajectory, velocity, and roll angle of hypersonic projectiles can be reconstructed from numerical simulations. The proposed approach provided results in good agreement with reference measurements, showing the potential of advanced numerical simulations as an alternative to traditional tracking techniques. This opens the way of new validation strategies, particularly in flight regimes where direct measurements are challenging.

Taken together, the results of this work provide a coherent framework spanning the full fidelity spectrum of sonic boom research. At the high-fidelity level, detailed CFD analyses offer accurate prediction of sonic boom generation, and propagation tools account for realistic atmospheric variability. In addition psychoacoustic and energy-based noise metrics are assessed. At the conceptual design stage, analytical formulations and extended Matching Chart requirements embed sonic boom constraints directly into design practice. Finally, the inverse methodologies expand the scope of aeroacoustics into experimental validation and system identification. This approach ensures that consistency is maintained across scales and applications, and that both industry and regulatory entities can rely on a unified set of tools.

While the methodologies developed proved to be accurate and versatile, some limitations should be acknowledged. The numerical high-fidelity CFD simulations, although validated against experimental tests, remain computationally demanding, especially for the RANS case. The experimental datasets, though unique and valuable, are limited in number, and validated mainly for the mock-up case with reduced dynamics. Furthermore, the results from the noise metrics are limited, and require experimental tests on lower Mach number and low-boom configurations. Lastly, the metrics analyzed still require broader consensus and standardization before they can be fully integrated into certification frameworks.

Future research directions can build upon these foundations. Firstly, low-boom configurations should be developed to evaluate their behavior in off-design and transient flight conditions. Secondly, the inclusion of transient simulations that evaluate the dynamic phases of the configuration, such as climb or maneuvers, should be considered to assess variations in noise metrics during these flight phases. Additional experimental campaigns on low-boom and low-Mach concepts, involving both scaled models and flight demonstrators, would provide data to further validate and refine the proposed methods. Finally, closer collaboration with international research centers and regulatory entities will support the definition of internationally validated overland noise limits.

In conclusion, this thesis has demonstrated that accurate, reliable, and computationally efficient sonic boom predictions are achievable, and can be seamlessly integrated into both regulatory processes and aircraft design methodologies. The contributions extend from fundamental numerical research to practical design tools and experimental validation, establishing a comprehensive framework to address the sonic boom challenge. While supersonic civil aviation continues to face significant technical, environmental, and societal obstacles, the advances presented here bring the field closer to realizing a new generation of sustainable high-speed transport.

References

[1] Air Transport Action Group. Waypoint 2050 2nd edition: September 2021, 2021. Accessed: 2025-05-28.

[2] Domenic J. Maglieri, Percy J. Bobbitt, Kenneth J. Plotkin, Kevin P. Shepherd, Peter G. Coen, and David M. Richwine. Sonic boom: Six decades of research, 2014. Document ID 20150006843.

[3] Yusuke Naka. Subjective evaluation of loudness of sonic booms indoors and outdoors. *Acoustical Science and Technology*, 34(3):225–228, 2013.

[4] Samuele Graziani, Francesco Petrosino, Jacob Jäschke, Antimo Glorioso, Roberta Fusaro, and Nicole Viola. Evaluation of sonic boom shock wave generation with cfd methods. *Aerospace*, 11(6):484, 2024.

[5] Gerald Carrier, Olivier Atinault, Patrice Malbequi, Aurelia Cartieri, P Taravel, Pierre-Elie Normand, Didier Dragna, Sébastien Ollivier3 Regis Marchiano, Stephen Rolston, Jochen Kirz, et al. Sts-14-3 sonic boom prediction capabilities: Overview of the project rumble work package 2. *Special Technology Sessions*.

[6] Nicole Viola, Roberta Fusaro, Bayindir Saracoglu, Christophe Schram, Volker Grewe, Jan Martinez, Marco Marini, Santiago Hernandez, Karel Lammers, Axel Vincent, et al. Main challenges and goals of the h2020 stratofly project. *Aerotecnica Missili & Spazio*, 100(2):95–110, 2021.

[7] Johan Steelant et al. Lapcat: high-speed propulsion technology. *Advances on propulsion technology for high-speed aircraft*, 12(1):1e38, 2008.

[8] Johan Steelant, Richard Varvill, Craig Walton, Sebastien Defoort, Klaus Hannemann, and Marco Marini. Achievements obtained for sustained hypersonic flight within the lapcat-ii project. In *20th AIAA international space planes and hypersonic systems and technologies conference*, page 3677, 2015.

[9] Airbus. Zeroe: Our hydrogen-powered aircraft, 2025. Accessed: 2025-05-26.

[10] Roberta Fusaro and Nicole Viola. Design and integration of a cryogenic propellant subsystem for the hypersonic stratofly mr3 vehicle. In *AIAA Scitech 2020 Forum*, page 1106, 2020.

[11] Federal Aviation Administration. 14 CFR § 91.817 - Civil aircraft sonic boom. https://www.ecfr.gov/current/title-14/section-91.817, 1973. Codified at 14 C.F.R. § 91.817.

[12] Ted Budd and Troy Nehls. Budd, nehls introduce legislation to allow flight of supersonic civil aircraft. https://www.budd.senate.gov/2025/05/14/budd-nehls-introduce-legislation-to-allow-flight-of-supersonic-civil-aircraft/, May 2025. Accessed: 2025-05-27.

[13] International Civil Aviation Organization (ICAO). Committee on Aviation Environmental Protection (CAEP). https://www.icao.int/environmental-protection/Pages/Caep.aspx, 2025. Accessed: 2025-05-26.

[14] Horizon2020. Mdo and regulations for low-boom and environmentally sustainable supersonic aviation, 2021.

[15] Bernd Liebhardt and Klaus Lütjens. An analysis of the market environment for supersonic business jets. *DLRK Tagungsband 2011: 60. Deutscher Luft-und Raumfahrtkongress in Bremen*, 2011.

[16] Christoph Klingenberg and Jan Loic Belke. Profitability of supersonic travel. *Journal of Air Transport Management*, 117:102581, 2024.

[17] Matisse DeRoo and Timothy T Takahashi. A study of the economic viability of commercial supersonic flight. In *AIAA SCITECH 2024 Forum*, page 2214, 2024.

[18] Wu Li, Karl Geiselhart, Ryan Palma, Michael Patterson, Samuel Dollyhigh, Zhou Wang, Nicolas Hinze, and Antonio Trani. Using global market demand analysis to guide conceptual design of low-boom supersonic transports. *Journal of Air Transportation*, pages 1–16, 2025.

[19] John D Anderson. Breaking the sound barrier. In *AIAA Scitech 2019 Forum*, page 2194, 2019.

[20] Robin Moret and Jean-Marc Moschetta. Through the sound barrier, a historical and technical survey. *PIR report*, 2000.

[21] MB Morgan. Supersonic aircraft—promise and problems. *The Aeronautical Journal*, 64(594):315–334, 1960.

[22] Richard H Graham. *SR-71 Blackbird: Stories, Tales, and Legends*. Zenith Imprint, 2002.

[23] Paul F Crickmore. *Sr-71 Blackbird*. Bloomsbury Publishing, 2016.

[24] Harvey H Hubbard and Domenic J Maglieri. Sonic boom signature data from cruciform microphone array experiments during the 1966-1967 eafb national sonic boom evaluation program. Technical report, 1990.

[25] John A Walgreen, EH Rastatter, and Arnold B Moore. The economics of the united states supersonic transport. *Journal of Transport Economics and Policy*, pages 186–193, 1973.

[26] Stephen Enke. Government-industry development of a commercial supersonic transport. *The American Economic Review*, 57(2):71–79, 1967.

[27] Egbert Torenbeek. *Essentials of supersonic commercial aircraft conceptual design*. John Wiley & Sons, 2020.

[28] Richard Seebass. Minimum sonic boom shock strengths and overpressures. *Nature*, 221(5181):651–653, 1969.

[29] Wilfried KH Kressner. The 2707 supersonic transport. *Proceedings of the IEEE*, 56(4):682–691, 1968.

[30] Christopher Orlebar. *Concorde*. Bloomsbury Publishing, 2017.

[31] Sebastien Candel. Concorde and the future of supersonic transport. *Journal of propulsion and power*, 20(1):59–68, 2004.

[32] Jonathan Glancey. *Concorde: the rise and fall of the supersonic airliner*. Atlantic Books Ltd, 2015.

[33] Robert A Rivers. *A qualitative piloted evaluation of the tupolev tu-144 supersonic transport*. NASA Langley Research Center, 2000.

[34] Zhonghua Han, Jianling Qiao, Liwen Zhang, Qing Chen, Han Yang, Yulin Ding, Keshi Zhang, Wenping Song, and Bifeng Song. Recent progress of efficient low-boom design and optimization methods. *Progress in Aerospace Sciences*, 146:101007, 2024.

[35] Michael Aftosmis, Marian Nemec, and Susan Cliff. Adjoint-based low-boom design with cart3d. In *29th AIAA applied aerodynamics conference*, page 3500, 2011.

[36] Xiaoqiang Feng, Zhanke Li, and Bifeng Song. Research of low boom and low drag supersonic aircraft design. *Chinese Journal of Aeronautics*, 27(3):531–541, 2014.

[37] Shigeru Horinouchi. Conceptual design of a low boom ssbj. In *43rd AIAA Aerospace Sciences Meeting and Exhibit*, page 1018, 2005.

[38] Wu Li and Karl Geiselhart. Integration of low-fidelity mdo and cfd-based redesign of low-boom supersonic transports. *AIAA Journal*, 59(10):3923–3936, 2021.

[39] Yicheng Sun and Howard Smith. Review and prospect of supersonic business jet design. *Progress in Aerospace Sciences*, 90:12–38, 2017.

[40] Alexandra Loubeau and Juliet Page. Human perception of sonic booms from supersonic aircraft. *Acoustics Today*, 14(3):23–30, 2018.

[41] Jonathan Rathsam, Peter Coen, Alexandra Loubeau, Lori Ozoroski, and Gautam Shah. Scope and goals of nasa's quesst community test campaign with the x-59 aircraft. In *14th ICBEN Congress on Noise as a Public Health Problem*, 2023.

[42] William J Doebler, Sara R Wilson, Alexandra Loubeau, and Victor W Sparrow. Simulation and regression modeling of nasa's x-59 low-boom carpets across america. *Journal of Aircraft*, 60(2):509–520, 2023.

[43] Will Doebler, Sara Wilson, Alexandra Loubeau, and Victor Sparrow. Five-year simulation study of nasa's x-59 low-boom carpets across the contiguous united states of america. In *eForum Acusticum 2020*, pages 1001–1008, 2020.

[44] Todd E Magee, Leonel Serrano, Raul Mendoza, Alejandro Gonzalez, David R Muscalus, Ashley M Jones, Madison Peyton, and Stephen G Shaw. X-59 cfd and wind tunnel data comparisons. In *AIAA Aviation 2023 Forum*, page 4320, 2023.

[45] Jonathan Rathsam. An overview of the nasa quesst community test campaign with the x-59 aircraft. *DATAWorks*, 2023.

[46] Alexandra Loubeau, Sara R Wilson, and Jonathan Rathsam. Updated evaluation of sonic boom noise metrics. *The Journal of the Acoustical Society of America*, 144(3_Supplement):1706–1706, 2018.

[47] NASA. Special report: X-59 makes its public debut, 2024. Accessed: 2025-05-21.

[48] Boom Supersonic. Boomless cruise, 2025. Accessed: 2025-05-20.

[49] Larry J Cliatt, Michael A Hill, and Edward Haering. Mach cutoff analysis and results from nasa's farfield investigation of no-boom thresholds. In *22nd AIAA/CEAS Aeroacoustics Conference*, page 3011, 2016.

[50] Harry W Carlson and Domenic J Maglieri. Review of sonic-boom generation theory and prediction methods. *The Journal of the Acoustical Society of America*, 51(2C):675–685, 1972.

[51] Norman J Mcleod. Flights at cutoff mach number. In *Third Conference on Sonic Boom Research*, volume 255, page 243. Scientific and Technical Information Office, National Aeronautics and Space ..., 1971.

[52] Boom Supersonic. Overture, 2025. Accessed: 2025-10-06.

[53] Bernd Liebhardt, Klaus Lütjens, Atsushi Ueno, and Hiroaki Ishikawa. Jaxa's s4 supersonic low-boom airliner–a collaborative study on aircraft design, sonic boom simulation, and market prospects. In *AIAA Aviation 2020 Forum*, page 2731, 2020.

[54] Junichi Akatsuka, Atsushi Ueno, and Yoshikazu Makino. System noise assessment and prediction methodology uncertainty analysis for jaxa's supersonic conceptual aircraft with variable noise reduction system. In *AIAA SCITECH 2025 Forum*, page 1796, 2025.

[55] European Commission / Deutsches Zentrum für Luft- und Raumfahrt (DLR). (lto) noise and emissions of supersonic aircraft — seneca. CORDIS, EU Project, 2025. Accessed: 2025-10-06.

[56] Muharrem Mane, Samarth Jain, and William Crossley. Market size and design requirements for supersonic passenger transport aircraft. In *AIAA AVIATION 2021 FORUM*, page 2442, 2021.

[57] Laurette Fisher, Sandy Liu, Lourdes Q Maurice, and Kevin P Shepherd. Supersonic aircraft: Balancing fast, affordable, and green. *International Journal of Aeroacoustics*, 3(3):181–197, 2004.

[58] Shigeru Obayashi, Daisuke Sasaki, Yukishiro Takeguchi, and Naoki Hirose. Multiobjective evolutionary computation for supersonic wing-shape optimization. *IEEE transactions on evolutionary computation*, 4(2):182–187, 2000.

[59] Saeed Shokrollahi and Firooz Bakhtiari-Nejad. Limit cycle oscillations of swept-back trapezoidal wings at low subsonic flow. *Journal of aircraft*, 41(4):948–953, 2004.

[60] Yue Gu, Mirjam Wiedemann, Tim Ryley, Mary E Johnson, and Michael John Evans. Hydrogen-powered aircraft at airports: A review of the infrastructure requirements and planning challenges. *Sustainability*, 15(21):15539, 2023.

[61] Subodh K Mital, John Z Gyekenyesi, Steven M Arnold, Roy M Sullivan, Jane M Manderscheid, and Pappu LN Murthy. Review of current state of the art and key design issues with potential solutions for liquid hydrogen cryogenic storage tank structures for aircraft applications. 2006.

[62] Dries Verstraete. The potential of liquid hydrogen for long range aircraft propulsion. 2009.

[63] Eytan J Adler and Joaquim RRA Martins. Hydrogen-powered aircraft: Fundamental concepts, key technologies, and environmental impacts. *Progress in Aerospace Sciences*, 141:100922, 2023.

[64] Johannes Friedrich Pletzer and Volker Grewe. Sensitivities of atmospheric composition and climate to altitude and latitude of hypersonic aircraft emissions. *EGUsphere*, 2023:1–54, 2023.

[65] European Commission. The european green deal. https://commission.europa.eu/strategy-and-policy/priorities-2019-2024/european-green-deal_en, 2019. Accessed: 2025-21-10.

[66] Parash Agarwal, Xiaoxiao Sun, Pierre Q Gauthier, and Vishal Sethi. Injector design space exploration for an ultra-low nox hydrogen micromix combustion system. In *Turbo expo: Power for land, sea, and air*, volume 58608, page V003T03A013. American Society of Mechanical Engineers, 2019.

[67] M Anwar H Khan, Joel Brierley, Kieran N Tait, Steve Bullock, Dudley E Shallcross, and Mark H Lowenberg. The emissions of water vapour and nox from modelled hydrogen-fuelled aircraft and the impact of nox reduction on climate compared with kerosene-fuelled aircraft. *Atmosphere*, 13(10):1660, 2022.

[68] Susanne Becken, Brendan Mackey, and David S Lee. Implications of preferential access to land and clean energy for sustainable aviation fuels. *Science of The Total Environment*, 886:163883, 2023.

[69] Kimberly M Carlson and Rachael D Garrett. Environmental impacts of tropical soybean and palm oil crops. In *Oxford Research Encyclopedia of Environmental Science*. 2018.

[70] International Civil Aviation Organization (ICAO). Annex 16. Environmental Protection - Volume I - Aircraft Engine Emissions, 2023. Available from: https://www.icao.int.

[71] Thomas Rötger, Chris Eyers, and Roberta Fusaro. A review of the current regulatory framework for supersonic civil aircraft: Noise and emissions regulations. *Aerospace*, 11(1):19, 2023.

[72] International Civil Aviation Organization (ICAO). Annex 16. Environmental Protection - Volume I - Aircraft Noise, 2017. Available from: https://www.icao.int.

[73] JA Hay. Concorde-community noise. Technical report, SAE Technical Paper, 1976.

[74] J Jones Berton, SM Jones, JA Seidel, and DL Huff. Noise predictions for a supersonic business jet using advanced take-off procedures. *The Aeronautical Journal*, 122(1250):556–571, 2018.

[75] Michel Nöding and Lothar Bertsch. Application of noise certification regulations within conceptual aircraft design. *Aerospace*, 8(8):210, 2021.

[76] Grazia Piccirillo, Nicole Viola, Roberta Fusaro, and Luigi Federico. Guidelines for the lto noise assessment of future civil supersonic aircraft in conceptual design. *Aerospace*, 9(1):27, 2022.

[77] International Civil Aviation Organization (ICAO). Reduction of noise at source, 2024. Accessed: 2025-05-23.

[78] Victor W Sparrow. Review and status of sonic boom penetration into the ocean. *The Journal of the Acoustical Society of America*, 111(1):537–543, 2002.

[79] Christine M Darden. Sonic-boom minimization with nose-bluntness relaxation. Technical report, 1979.

[80] Henning E von Gierke. Effects of sonic boom on people: review and outlook. *the journal of the Acoustical Society of America*, 39(5B):S43–S50, 1966.

[81] Ragnar Rylander, Stefan Sörensen, Kenneth Berglund, and Carina Brodin. Experiments on the effect of sonic-boom exposure on humans. *The Journal of the Acoustical Society of America*, 51(2C):790–798, 1972.

[82] Alexandra Loubeau, Brenda M Sullivan, Jacob Klos, Jonathan Rathsam, and Joseph R Gavin. Laboratory headphone studies of human response to low-amplitude sonic booms and rattle heard indoors. Technical report, 2013.

[83] David Suisman. The oklahoma city sonic boom experiment and the politics of supersonic aviation. *Radical History Review*, 2015(121):169–195, 2015.

[84] David Artland Hilton, Vera Huckel, DJ Maglieri, and R Steiner. Sonic-boom exposures during faa community response studies over a 6-month period in the oklahoma city area. Technical report, 1964.

[85] Michael B Arkin, Glen M Burdick, and Sam A Joyner. Sonic boom–a legal nightmare. *Okla. L. Rev.*, 19:292, 1966.

[86] Charles W. Nixon and Paul N. Borsky. Effects of sonic boom on people: St. louis, missouri, 1961–1962. *The Journal of the Acoustical Society of America*, 39(5B):S51–S58, 05 1966.

[87] Charles W Nixon and Harvey H Hubbard. *Results of USAF-NASA-FAA Flight Program to study community responses to sonic booms in the Greater St. Louis area*, volume 2705. National Aeronautics and Space Administration, 1965.

[88] Armand Dancer and Pierre Naz. Sonic boom: Isl studies from the 60's to the 70's.

[89] Jack D Leatherwood, Kevin P Shepherd, and Brenda M Sullivan. A new simulator for assessing subjective effects of sonic booms. Technical report, 1991.

[90] Allen J Roth. Sonic boom: A new legal problem. *American Bar Association Journal*, pages 216–276, 1958.

[91] John I Hopkins and John J McIntosh. Is sonic boom an explosion. *Ins. LJ*, page 15, 1957.

[92] CHE Warren. Noise from aircraft at supersonic speeds. *Nature*, 171(4344):214–215, 1953.

[93] T Gold. The 'double bang'of supersonic aircraft. *Nature*, 170(4332):808–808, 1952.

[94] Gerald Beresford Whitham. The flow pattern of a supersonic projectile. *Communications on pure and applied mathematics*, 5(3):301–348, 1952.

[95] F Walkden. The shock pattern of a wing-body combination, far from the flight path. *Aeronautical quarterly*, 9(2):164–194, 1958.

[96] Adolf Busemann. The relation between minimizing drag and noise at supersonic speeds. *Proceedings of High Speed Aerodynamics*, pages 133–144, 1955.

[97] Harry W Carlson. *The lower bound of attainable sonic-boom overpressure and design methods of approaching this limit*. National Aeronautics and Space Administration, 1962.

[98] LB Jones. Lower bounds for sonic bangs. *The Aeronautical Journal*, 65(606):433–436, 1961.

[99] LB Jones. Lower bounds for sonic bangs in the far field. *Aeronautical Quarterly*, 18(1):1–21, 1967.

[100] Richard Seebass and Albert R George. Sonic-boom minimization. *The Journal of the Acoustical Society of America*, 51(2C):686–694, 1972.

[101] AR Seebass and AR George. Design and operation of aircraft to minimize their sonic boom. *Journal of aircraft*, 11(9):509–517, 1974.

[102] LB Jones. Lower bounds for the pressure jump of the bow shock of a supersonic transport. *Aeronautical Quarterly*, 21(1):1–17, 1970.

[103] AR George and R Seebass. Sonic boom minimization including both front and rear shocks. *AIAA Journal*, 9(10):2091–2093, 1971.

[104] Harry W Carlson. Simplified sonic-boom prediction. Technical report, 1978.

[105] HW Carlson and WD Middleton. A numerical method for calculating near-field sonic-boom pressure signatures. Technical report, 1965.

[106] Roberta Fusaro, Grazia Piccirillo, Davide Ferretto, Guido Saccone, Daniel Bodmer, Jacob Jäschke, Michele Cremaschi, and Nicole Viola. Esatto: the holistic framework to support the design of sustainable supersonic aviation. In *34th Congress of the International Council of the Aeronautical Sciences, ICAS 2024*. International Council of the Aeronautical Sciences, 2024.

[107] Bastien Martinez, Myriam Bastide, and Pierre Wey. Free flight measurement technique in shock tunnel. In *30th AIAA aerodynamic measurement technology and ground testing conference*, page 2523, 2014.

[108] Barry M Hellman, John E Bradford, Brad D St. Germain, and Kevin Feld. Two stage to orbit conceptual vehicle designs using the sabre engine. In *AIAA SPACE 2016*, page 5320, 2016.

[109] Richard Varvill, Ignacio Duran, Adrian Kirk, Stuart Langridge, Oliver Nailard, Russ Payne, and Helen Webber. Sabre technology development status and update. In *8th European conference for aeronautics and space sciences (EUCASS)*, 2019.

[110] Davide Ferretto, Roberta Fusaro, and Nicole Viola. A conceptual design tool to support high-speed vehicle design. In *AIAA Aviation 2020 Forum*, page 2647, 2020.

[111] P Roncioni, M Marini, R Fusaro, and N Viola. Aerodatabase development and integration of supersonic/hypersonic cruiser vehicles in more&less project. In *33rd Congress of the International Council of the Aeronautical Sciences*, pages 4–9, 2024.

[112] Grazia Piccirillo, Antonio Gregorio, Roberta Fusaro, Davide Ferretto, and Nicole Viola. Mixed-flow turbofan engine model for the conceptual design of sustainable supersonic airplanes. *Aerospace*, 11(9):740, 2024.

[113] Davide Ferretto, Roberta Fusaro, and Nicole Viola. Innovative multiple matching charts approach to support the conceptual design of hypersonic vehicles. *Proceedings of the Institution of Mechanical Engineers, Part G: Journal of Aerospace Engineering*, 234(12):1893–1912, 2020.

[114] Pietro Roncioni, Marco Marini, Oscar Gori, Roberta Fusaro, and Nicole Viola. Aerodatabase development and integration and mission analysis of a mach 2 supersonic civil aircraft. *Aerospace*, 11(2):111, 2024.

[115] Ali Can Ispir, Pedro Miguel Gonçalves, and Bayindir H Saracoglu. Analysis of a combined cycle propulsion system for stratofly hypersonic vehicle over an extended trajectory. In *MATEC Web of Conferences*, volume 304, page 03001. EDP Sciences, 2019.

[116] Charles E Cockrell Jr, Lawrence D Huebner, and Dennis B Finley. Aerodynamic characteristics of two waverider-derived hypersonic cruise configurations. Technical report, 1996.

[117] Kevin G Bowcutt, John D Anderson, and Diego Capriotti. Viscous optimized hypersonic waveriders. In *25th AIAA Aerospace Sciences Meeting*, page 272, 1987.

[118] Nicole Viola, Roberta Fusaro, Davide Ferretto, Oscar Gori, Bayindir Saracoglu, Ali Can Ispir, Christophe Schram, Volker Grewe, Johannes Friedrich Plezer, Jan Martinez, et al. H2020 stratofly project: From europe to australi in less than 3 hours. In *ICAS 2021 THE 32 nd CONGRESS OF THE INTERNATIONAL COUNCIL OF THE AERONAUTICAL SCIENCES*, 2021.

[119] Nicole Viola, Roberta Fusaro, Davide Ferretto, Oscar Gori, Marco Marini, Pietro Roncioni, Bora Orcun Cakir, Ali Can Ispir, Bayindir Husein Saracoglu, et al. Hypersonic aircraft and mission concept re-design to move from mach

8 to mach 5 operations. In *33rd Congress of the International Council of the Aeronautical Sciences*, pages 4–9, 2022.

[120] Giovanni Fasulo, Luigi Federico, Francesco Petrosino, Samuele Graziani, Nicole Viola, Sebastien Hengy, Bastien Martinez, and Marie Albisser. Sonic boom comparative study between mach 4.7 outdoor experimental tests and numerical simulations. In *34th Congress of ICAS*, 2024.

[121] Giovanni Fasulo, Sébastien Hengy, Bastien Martinez, Luigi Federico, Luciano De Vivo, Marie Albisser, and Andreas Zeiner. Outdoor experimental assessment of sonic boom characteristics for the stratofly mr3 model. *CEAS Space Journal*, pages 1–18, 2025.

[122] Michael A Park, Michael J Aftosmis, Richard L Campbell, Melissa B Carter, Susan E Cliff, and Linda S Bangert. Summary of the 2008 nasa fundamental aeronautics program sonic boom prediction workshop. *Journal of Aircraft*, 51(3):987–1001, 2014.

[123] Michael A Park and John M Morgenstern. Summary and statistical analysis of the first aiaa sonic boom prediction workshop. *Journal of Aircraft*, 53(2):578–598, 2016.

[124] Michael A Park and Marian Nemec. Nearfield summary and statistical analysis of the second aiaa sonic boom prediction workshop. *Journal of Aircraft*, 56(3):851–875, 2019.

[125] Sriram K. Rallabhandi and Alexandra Loubeau. Summary of propagation cases of the third aiaa sonic boom prediction workshop. *Journal of Aircraft*, 59(3):578–594, 2022.

[126] Sriram K. Rallabhandi and Alexandra Loubeau. Summary of propagation cases of the second aiaa sonic boom prediction workshop. *Journal of Aircraft*, 56(3):876–895, 2019.

[127] Peter Constantin and Ciprian Foiaş. *Navier-stokes equations*. University of Chicago press, 1988.

[128] Robert MacCormack and Alvin Paullay. Computational efficiency achieved by time splitting of finite difference operators. In *10th aerospace sciences meeting*, page 154, 1972.

[129] Larry S Caretto, AD Gosman, Suhas V Patankar, and DB Spalding. Two calculation procedures for steady, three-dimensional flows with recirculation. In *Proceedings of the Third International Conference on Numerical Methods in Fluid Mechanics: Vol. II Problems of Fluid Mechanics*, pages 60–68. Springer, 1973.

[130] Antony Jameson. *Computational aerodynamics*, volume 49. Cambridge University Press, 2022.

[131] Antimo Glorioso, Francesco Petrosino, Andrea Aprovitola, Mattia Barbarino, and Giuseppe Pezzella. Sonic boom generation using open source cfd approach. In *AIAA AVIATION 2023 Forum*, page 4168, 2023.

[132] Philip L Roe. Approximate riemann solvers, parameter vectors, and difference schemes. *Journal of computational physics*, 43(2):357–372, 1981.

[133] Philip L Roe. Characteristic-based schemes for the euler equations. *Annual review of fluid mechanics*, 18(1):337–365, 1986.

[134] Meng-Sing Liou and Christopher J Steffen Jr. A new flux splitting scheme. *Journal of Computational physics*, 107(1):23–39, 1993.

[135] Franck Dagrau, Adrien Loseille, and Itham Salah El Din. Computational and experimental assessment of models for the first aiaa sonic boom prediction workshop using adaptive high fidelity cfd methods. In *32nd AIAA Applied Aerodynamics Conference*, page 2009, 2014.

[136] Rei Yamashita and Kojiro Suzuki. Full-field sonic boom simulation in real atmosphere. In *32nd AIAA Applied Aerodynamics Conference*, page 2269, 2014.

[137] David Luquet, Régis Marchiano, François Coulouvrat, Itham Salah El Din, and Adrien Loseille. Sonic boom assessment of a hypersonic transport vehicle with advanced numerical methods. In *21st AIAA/CEAS Aeroacoustics Conference*, page 2685, 2015.

[138] E. F. Toro and A. Chakraborty. The development of a riemann solver for the steady supersonic euler equations. *The Aeronautical Journal*, 98(979):325–339, 1994.

[139] Eiji Shima, Keiichi Kitamura, and Takanori Haga. Green–gauss/weighted-least-squares hybrid gradient reconstruction for arbitrary polyhedra unstructured grids. *AIAA journal*, 51(11):2740–2747, 2013.

[140] Andrej Nikolaevich Kolmogorov. Equations of turbulent motion in an incompressible fluid. In *Dokl. Akad. Nauk SSSR*, volume 30, pages 299–303, 1941.

[141] Philip Geoffrey Saffman. A model for inhomogeneous turbulent flow. *Proceedings of the Royal Society of London. A. Mathematical and Physical Sciences*, 317(1530):417–433, 1970.

[142] DC Wilcox and IE Alber. A turbulence model for high speed flows. In *Proceedings of the 1972 Heat Transfer and Fluid Mechanics Institute*, volume 231, page 252. Stanford University Press, 1972.

[143] David C Wilcox. Reassessment of the scale-determining equation for advanced turbulence models. *AIAA journal*, 26(11):1299–1310, 1988.

[144] David C Wilcox et al. *Turbulence modeling for CFD*, volume 2. DCW industries La Canada, CA, 1998.

[145] Philippe Spalart and Steven Allmaras. A one-equation turbulence model for aerodynamic flows. In *30th aerospace sciences meeting and exhibit*, page 439, 1992.

[146] Rei Yamashita, Yoshikazu Makino, and Philip L Roe. Fast full-field simulation of sonic boom using a space marching method. *AIAA Journal*, 60(7):4103–4112, 2022.

[147] Rei Yamashita and Hiroaki Ishikawa. A semi-adapted space marching method for fast sonic boom prediction. *Journal of Computational Physics*, 487:112170, 2023.

[148] R Yamashita and N Nikiforakis. Three-dimensional full-field simulation of sonic boom emanating from complex geometries over buildings. *Shock Waves*, 33(2):149–167, 2023.

[149] Hiroaki Ishikawa, Yoshikazu Makino, Takeshi Ito, and Fumitake Kuroda. Sonic boom prediction using multi-block structured grids cfd code considering jet-on effects. In *27th AIAA Applied Aerodynamics Conference*, page 3508, 2009.

[150] Mathias Wintzer and Ilan Kroo. Optimization and adjoint-based cfd for the conceptual design of low sonic boom aircraft. In *50th AIAA Aerospace Sciences Meeting including the New Horizons Forum and Aerospace Exposition*, page 963, 2012.

[151] Ariane Emmanuelli, Didier Dragna, Sébastien Ollivier, and Philippe Blanc-Benon. Sonic boom propagation over real topography. *The Journal of the Acoustical Society of America*, 154(1):16–27, 2023.

[152] Didier Dragna, Ariane Emmanuelli, Sébastien Ollivier, and Philippe Blanc-Benon. Sonic boom reflection over urban areas. *The Journal of the Acoustical Society of America*, 152(6):3323–3339, 2022.

[153] Osama Kandil, Zhi Yang, and Percy Bobbitt. Prediction of sonic boom signature using euler-full potential cfd with grid adaptation and shock fitting. In *8th AIAA/CEAS Aeroacoustics Conference & Exhibit*, page 2542, 2012.

[154] Boping Ma, Gang Wang, Jiong Ren, Zhengyin Ye, and Gecheng Zha. Near field sonic boom analysis with huns3d solver. In *55th AIAA Aerospace Sciences Meeting*, page 0038, 2017.

[155] Michael A Park and Melissa B Carter. Nearfield summary and analysis of the third aiaa sonic boom prediction workshop c608 low boom demonstrator. In *AIAA Scitech 2021 Forum*, page 0345, 2021.

[156] Michael A Park and Melissa B Carter. Low-boom demonstrator near-field summary for the third aiaa sonic boom prediction workshop. *Journal of Aircraft*, 59(3):563–577, 2022.

[157] Michael A Park, Richard L Campbell, Alaa A Elmiligui, Susan E Cliff, and Sudheer Nayani. Specialized cfd grid generation methods for near-field sonic boom prediction. In *52nd Aerospace Sciences Meeting*, page 0115, 2014.

[158] Boping Ma, Gang Wang, Jiong Ren, Zhengyin Ye, Zhijin Lei, and Gecheng Zha. Near-field sonic-boom prediction and analysis with hybrid grid navier–stokes solver. *Journal of Aircraft*, 55(5):1890–1904, 2018.

[159] George R Anderson, Michael J Aftosmis, and Marian Nemec. Cart3d simulations for the second aiaa sonic boom prediction workshop. *Journal of Aircraft*, 56(3):896–911, 2019.

[160] J-M Moschetta and J Gressier. The sonic point glitch problem: A numerical solution. In *Sixteenth International Conference on Numerical Methods in Fluid Dynamics: Proceedings of the Conference Held in Arcachon, France, 6–10 July 1998*, pages 403–408. Springer, 1998.

[161] Anatoly Potapkin, Tatiana Korotaeva, Dmitry Moskvichev, Anatoly Shashkin, Anatoly Maslov, Joseph Silkey, and F Roos. An advanced approach for far-field sonic boom prediction. In *47th AIAA Aerospace Sciences Meeting including The New Horizons Forum and Aerospace Exposition*, 2009.

[162] M. J. Siclari and C. M. Darden. Euler code prediction of near-field to midfield sonic boom pressure signatures. *Journal of Aircraft*, 30(6):911–917, 1993.

[163] Isik Ozcer. Sonic boom prediction using euler / full potential methodology. In *45th AIAA Aerospace Sciences Meeting and Exhibit*, 2012.

[164] Jacob Jäschke, Samuele Graziani, Francesco Petrosino, Antimo Glorioso, and Volker Gollnick. Comparison of prediction models for sonic boom ground signatures under realistic flight conditions. *Aerospace*, 11(12):962, 2024.

[165] John E Matsson. *An introduction to ANSYS fluent 2022*. Sdc Publications, 2022.

[166] Thomas D. Economon, Francisco Palacios, Sean R. Copeland, Trent W. Lukaczyk, and Juan J. Alonso. Su2: An open-source suite for multiphysics simulation and design. *AIAA Journal*, 54(3):828–846, 2016.

[167] Armin Wulf and Vedat Akdag. Tuned grid generation with icem cfd. In *Nasa conference publication*, pages 477–477. NASA, 1995.

[168] Robin Olav Cleveland. *Propagation of sonic booms through a real, stratified atmosphere*. The University of Texas at Austin, 1995.

[169] Jongmin Kang. *Nonlinear acoustic propagation of shock waves through the atmosphere with molecular relaxation*. The Pennsylvania State University, 1991.

[170] AD Pierce and J Kang. Molecular relaxation effects on sonic boom waveforms. *Frontiers of Nonlinear Acoustics, Proceedings of the 12th ISNA, Elsevier, Amsterdam*, 1990.

[171] P.W. Hammerton. Effect of molecular relaxation on the propagation of sonic booms through a stratified atmosphere. *Wave Motion*, 33(4):359–377, 2001.

[172] Allan D Pierce. *Acoustics: an introduction to its physical principles and applications*. Springer, 2019.

[173] Sriram K Rallabhandi. Advanced sonic boom prediction using the augmented burgers equation. *Journal of Aircraft*, 48(4):1245–1253, 2011.

[174] Joel B. Lonzaga, Juliet A. Page, Robin S. Downs, Sophie R. Son, Meghan J. Alhearn, Alexandra Loubeau, and William J. Doebler. Pcboom 7 technical reference, 2nd edition, 2025.

[175] Joel B Lonzaga. Recent enhancements to nasa's pcboom sonic boom propagation code. In *AIAA Aviation 2019 Forum*, page 3386, 2019.

[176] Robert S Downs, Sophie R Kaye, and Juliet A Page. Pcboom propagation modeling for the third aiaa sonic boom prediction workshop. *Journal of Aircraft*, 59(3):612–623, 2022.

[177] Joel B. Lonzaga, Juliet A. Page, Meghan J. Ahearn, Sophie R. Son, Robin S. Downs, Alexandra Loubeau, and William J. Doebler. Pcboom version 7.5 user's guide, 2025.

[178] Samuele Graziani, Nicole Viola, Francesco Petrosino, and Jacob Jäschke. Comparison between simplified approach and cfd & propagation tool for sonic boom estimation. In *AIAA AVIATION 2023 Forum*, page 4166, 2023.

[179] Jacob J Jäschke and Bernd Liebhardt. Sonic boom simulation for boom carpet determination. *The Journal of the Acoustical Society of America*, 149(4_Supplement):A74–A75, 2021.

[180] RO Onyeonwu. The effects of wind and temperature gradients on sonic boom corridors. Technical report, University of Toronto, 1971.

[181] Masafumi Yamamoto, Atsushi Hashimoto, Takashi Aoyama, and Takeharu Sakai. A unified approach to an augmented burgers equation for the propagation of sonic booms. *The Journal of the Acoustical Society of America*, 137(4):1857–1866, 2015.

[182] Charles L Thomas. Extrapolation of sonic boom pressure signatures by the waveform parameter method. Technical report, 1972.

[183] K Plotkin and J Cantril. Prediction of sonic boom at a focus. In *14th Aerospace Sciences Meeting*, page 2, 1976.

[184] Kenneth J Plotkin and Fabio Grandi. Computer models for sonic boom analysis: Pcboom4, caboom, boomap, corboom. *Wyle Report WR*, 211, 2002.

[185] Kenneth Plotkin, Juliet Page, and Edward Haering. Extension of pcboom to over-the-top booms, ellipsoidal earch, and full 3-d ray tracing. In *13th AIAA/CEAS Aeroacoustics Conference (28th AIAA Aeroacoustics Conference)*, page 3677, 2007.

[186] SC Crow. Distortion of sonic bangs by atmospheric turbulence. *Journal of Fluid Mechanics*, 37(3):529–563, 1969.

[187] Lance Locey, Victor Sparrow, and Andrew Piacsek. Sonic boom post processing to include atmospheric turbulent effects. In *14th AIAA/CEAS Aeroacoustics Conference (29th AIAA Aeroacoustics Conference)*, page 3035, 2008.

[188] Lance L Locey. *Sonic boom postprocessing functions to simulate atmospheric turbulence effects*. The Pennsylvania State University, 2008.

[189] Kevin A Bradley, Christopher M Hobbs, Clifton B Wilmer, Victor W Sparrow, Trevor A Stout, John M Morgenstern, Kenneth H Underwood, Domenic J Maglieri, Robert A Cowart, Matthew T Collmar, et al. Sonic booms in atmospheric turbulence (sonicbat): The influence of turbulence on shaped sonic booms, 2020.

[190] Trevor A Stout. *Simulation of N-wave and shaped supersonic signature turbulent variations*. The Pennsylvania State University, 2018.

[191] Robert Downs, Michael Barzach, Jacob Klos, Joel Lonzaga, Will Doebler, Peter Parker, and Alexandra Loubeau. Turbulence effects on shaped booms: Finite impulse response filter development. In *184th Meeting of the Acoustical Society of America*, 2023.

[192] ICAO. Manual of the icao standard atmosphere [: extended to 80 kilometres (262 500 feet). *Third Edition, Technical Report Doc 7488-CD*, 1993.

[193] Accredited Standards Committee S1, Acoustics, American National Standards Institute, and Acoustical Society of America Standards Secretariat. *Method for calculation of the absorption of sound by the atmosphere*. Standards Secretariat, Acoustical Society of America, New York, NY, rev edition, 1995.

[194] Sriram K Rallabhandi and Alexandra Loubeau. Summary of propagation cases of the second aiaa sonic boom prediction workshop. *Journal of Aircraft*, 56(3):876–895, 2019.

[195] Sriram K Rallabhandi and Alexandra Loubeau. Summary of propagation cases of the third aiaa sonic boom prediction workshop. *Journal of Aircraft*, 59(3):578–594, 2022.

[196] NASA Langley Research Center. Sonic boom propagation webpage for sbpw3 project. https://lbpw-ftp.larc.nasa.gov/sbpw3/propagation/case1/, 2020. Accessed: September 25, 2024.

[197] NASA Langley Research Center. Sonic boom propagation webpage for sbpw3 project. https://lbpw-ftp.larc.nasa.gov/sbpw3/propagation/case2/, 2017. Accessed: September 25, 2024.

[198] NASA Langley Research Center. Sonic boom propagation webpage for sbpw2 project. https://lbpw-ftp.larc.nasa.gov/sbpw2/propagation/axibody/atmospheric_profiles/atmospheric_profile_3.txt, 2020. Accessed: September 25, 2024.

[199] David A McCurdy, Sherilyn A Brown, and R David Hilliard. Subjective response of people to simulated sonic booms in their homes. *The Journal of the Acoustical Society of America*, 116(3):1573–1584, 2004.

[200] Henk ME Miedema and Henk Vos. Demographic and attitudinal factors that modify annoyance from transportation noise. *The Journal of the Acoustical Society of America*, 105(6):3336–3344, 1999.

[201] Alexandra Loubeau, Yusuke Naka, Brian G Cook, Victor W Sparrow, and John M Morgenstern. A new evaluation of noise metrics for sonic booms using existing data. In *AIP Conference Proceedings*, volume 1685. AIP Publishing, 2015.

[202] Stanley S Stevens. Perceived level of noise by mark vii and decibels (e). *The Journal of the Acoustical Society of America*, 51(2B):575–601, 1972.

[203] Asa/ansi s1.42-2023: Design response of weighting networks for acoustical measurements, 2023. Approved November 6, 2023; provides design information for A-, B-, C-, D-, E-, G-, and U-weighting networks used for acoustical measurements.

[204] JG Callaghan. A feasibility investigation concerning the simulation of sonic boom by ballistic models. Technical report, 1966.

[205] Wilbur Chang. *Design and development of a rectangular supersonic wind tunnel facility for the study of shock/boundary layer interactions*. PhD thesis, University of Illinois at Urbana-Champaign, 2012.

[206] Akshay Raju Kulkarni, Carmine Varriale, Mark Voskuijl, Gianfranco La Rocca, and Leo L. Veldhuis. Assessment of sub-scale designs for scaled flight testing. In *AIAA Aviation 2019 Forum*, 2019.

[207] Graziani S. Fasulo G. Sonic boom comparative study between mach 4.7 outdoor experimental tests and numerical simulations. In *Proceedings of the 34th Congress of the International Council of the Aeronautical Sciences (ICAS)*, page Paper No. 0882, Florence, Italy, 2024.

[208] Specialised Imaging Ltd. High-speed imaging systems. https://specialised-imaging.com/, 2025. Accessed: 2025-06-03.

[209] Giovanni Fasulo, Sébastien Hengy, Bastien Martinez, Luigi Federico, Luciano De Vivo, Marie Albisser, and Andreas Zeiner. Outdoor experimental assessment of sonic boom characteristics for the stratofly mr3 model. *CEAS Space Journal*, 2025.

[210] Hottinger Brüel and Kjær. 4938 - 1/4" pressure-field microphone cartridge, 2025. Accessed: 2025-06-03.

[211] PCB Piezotronics, Inc. Model 377a12 - free-field microphone, prepolarized, 1/2" diameter, 2025. Accessed: 2025-06-03.

[212] HEAD acoustics GmbH. HSU III – Artificial Head for Binaural Recording. https://www.head-acoustics.com/products/artificial-head-binaural-recording/hsu-iii, 2023. Accessed: 2025-06-06.

[213] Matthias Witte, Artur Paszkiewicz, Matthias Wolfram Ospel, Johannes Tobias Rathje, Max Hieke, and Frank-Hendrik Wurm. Design of a hydro sound intensity probe for quantification and localization of acoustic sources—applied to a hubless marine rim drive. *Ocean Engineering*, 267:113227, 2023.

[214] Matthias Wolfram Ospel, Niklas Nolte, Matthias Witte, and Frank-Hendrik Wurm. Global active noise control using simo near-field systems-simulation and technical implementation. In *INTER-NOISE and NOISE-CON Congress and Conference Proceedings*, volume 270, pages 5589–5600. Institute of Noise Control Engineering, 2024.

[215] PA Nelson. A review of some inverse problems in acoustics. *International journal of acoustics and vibration*, 6(3):118–34, 2001.

[216] Sébastien Hengy, Pascal Duffner, Sébastien DeMezzo, Stéphane Heck, Laurent Gross, and Pierre Naz. Acoustic shooter localisation using a network of asynchronous acoustic nodes. *IET Radar, Sonar & Navigation*, 10(9):1528–1535, 2016.

[217] Gerald Beresford Whitham. *Linear and nonlinear waves*. John Wiley & Sons, 2011.

[218] Jean Varnier, Marie-Claire Le Pape, and Frédéric Sourgen. Ballistic wave from projectiles and vehicles of simple geometry. *AIAA Journal*, 56(7):2725–2742, 2018.

[219] Michael James Lighthill. On sound generated aerodynamically i. general theory. *Proceedings of the Royal Society of London. Series A. Mathematical and Physical Sciences*, 211(1107):564–587, 1952.

[220] John E Ffowcs Williams and David L Hawkings. Sound generation by turbulence and surfaces in arbitrary motion. *Philosophical Transactions of the Royal Society of London. Series A, Mathematical and Physical Sciences*, 264(1151):321–342, 1969.

[221] Valana L Wells. Acoustic waveform singularities from supersonic rotating surface sources. *AIAA journal*, 29(3):387–394, 1991.

[222] Zhongjie Huang, Leonidas Siozos-Rousoulis, Tim De Troyer, and Ghader Ghorbaniasl. A time-domain method for prediction of noise radiated from supersonic rotating sources in a moving medium. *Proceedings of the Royal Society A: Mathematical, Physical and Engineering Sciences*, 474(2210):20170089, 2018.

[223] Matthias Ospel, Samuele Graziani, Jacob Jäschke, and Sebastien Hengy. Inverse estimation of the flight dynamics of a hypersonic aircraft prototype via shock wave measurements. *Aerospace Science and Technology*, page 110504, 2025.

[224] Jeffrey C Lagarias, James A Reeds, Margaret H Wright, and Paul E Wright. Convergence properties of the nelder–mead simplex method in low dimensions. *SIAM Journal on optimization*, 9(1):112–147, 1998.

[225] Lexing Ying. A pedestrian introduction to fast multipole methods. *Science China Mathematics*, 55:1043–1051, 2012.

[226] Benedetto Piccoli and Francesco Rossi. On properties of the generalized wasserstein distance. *Archive for Rational Mechanics and Analysis*, 222:1339–1365, 2016.

[227] Astos Solutions GmbH. Astos – analysis, simulation and trajectory optimization software for space applications. https://astos.de/, 2025. Accessed: 2025-10-09.

[228] David G Goodwin, Raymond L Speth, Harry K Moffat, and Bryan W Weber. Cantera: An object-oriented software toolkit for chemical kinetics, thermodynamics, and transport processes. *Zenodo*, 2018.

[229] Volker Grewe and Andrea Stenke. Airclim: an efficient tool for climate evaluation of aircraft technology. *Atmospheric Chemistry and Physics*, 8(16):4621–4639, 2008.

[230] Johannes Pletzer, Volker Grewe, et al. supersonic-effects (version 1.0). *GitHub*, 2025.

[231] Andreas Page Risueño, Jasper Bussemaker, Pier Davide Ciampa, and Bjoern Nagel. Mdax: Agile generation of collaborative mdao workflows for complex systems. In *AIAA Aviation 2020 Forum*, page 3133, 2020.

[232] Brigitte Boden, Jan Flink, Robert Mischke, Kathrin Schaffert, Alexander Weinert, Annika Wohlan, Caslav Ilic, Tobias Wunderlich, Carsten M Liersch, Stefan Goertz, et al. Distributed multidisciplinary optimization and collaborative process development using rce. In *AIAA aviation 2019 forum*, page 2989, 2019.

[233] Daniel Raymer. *Aircraft design: a conceptual approach*. American Institute of Aeronautics and Astronautics, Inc., 2012.

[234] Jan Roskam. *Airplane design*. DARcorporation, 1997.

[235] Egbert Torenbeek. *Synthesis of subsonic airplane design: an introduction to the preliminary design of subsonic general aviation and transport aircraft, with emphasis on layout, aerodynamic design, propulsion and performance*. Springer Science & Business Media, 2013.

[236] Laurence K Loftin Jr. Subsonic aircraft: Evolution and the matching of size to performance. Technical report, 1980.

[237] S Matlab. Matlab (mathworks). *Natick, MA*, 2012.

[238] Israel Cohen, Yiteng Huang, Jingdong Chen, Jacob Benesty, Jacob Benesty, Jingdong Chen, Yiteng Huang, and Israel Cohen. Pearson correlation coefficient. *Noise reduction in speech processing*, pages 1–4, 2009.

[239] Samuele Graziani, Nicole Viola, Roberta Fusaro, Sebastien Hengy, Marie Albisser, and Bastien Martinez. Sonic boom numerical validation of a mach 4.7 experimental test. In *30th AIAA/CEAS Aeroacoustics Conference (2024)*, page 3184, 2024.

[240] Delores Maria Etter, David C Kuncicky, and Douglas W Hull. *Introduction to MATLAB*, volume 4. Pearson Education, 2002.

[241] HPC@PoliTO. Hpc@polito: High performance computing at politecnico di torino. https://hpc.polito.it/, 2025. Accessed: 2025-10-10.

[242] UFIT Research Computing, University of Florida. HiPerGator - Research Computing - University of Florida. http://www.rc.ufl.edu, 2025. Accessed: October 13, 2025.

[243] Samuele Graziani, Jacob Jens Jäschke, Nicole Viola, and Volker Gollnick. Sonic boom velocity and altitude sensitivity analysis of a hypersonic aircraft concept. *SAE technical papers*, 2025.

[244] Mustafa Cavcar. The international standard atmosphere (isa). *Anadolu University, Turkey*, 30(9):1–6, 2000.

[245] David Vernon Ritzel and James Joseph Gottlieb. The overpressure signature from a supersonic projectile. 1987.

[246] John A Nelder and Roger Mead. A simplex method for function minimization. *The computer journal*, 7(4):308–313, 1965.

[247] Centro Italiano Ricerche Aerospaziali (CIRA). Centro italiano ricerche aerospaziali – home page. https://www.cira.it/, 2025. Accessed: 2025-10-29.

[248] Frenchgerman research institute of saintlouis – home page. https://www.isl.eu/, 2025. Accessed: 2025-10-29.

[249] Tuhh – hamburg university of technology. https://www.tuhh.de/tuhh/startseite, 2025. Accessed: 2025-10-29.

[250] University of Florida, Department of Mechanical and Aerospace Engineering. Department of mechanical and aerospace engineering. https://mae.ufl.edu/, 2025. Accessed: 2025-05-23.

Appendix A

Roll angle estimation

Two appendices are included within this PhD thesis. Although the results presented therein were essential to several outcomes discussed in the main body of the work, they do not specifically address innovative aspects.

The first appendix describes the procedure adopted for the accurate computation of the roll angle during the experimental test campaigns. In Section 4.5.1, a direct comparison between experimental and numerical results as a function of the roll angle is presented and validated. Appendix B concerns the numerical simulations of two Mach 5 hypersonic configurations. The results of this numerical campaign were used to refine existing analytical formulations, as discussed in Section 4.6.3. Furthermore, the outcomes presented in Section B.1 were recognized with the Best Student Paper Award at the SAE Noise and Vibration Conference 2025, held in Grand Rapids, Michigan.

Roll angle estimation

As discussed in Sections 4.5.1 and 4.5.3, the non-negligible dynamics of the two tested projectiles required developing a methodology to track the roll angle evolution from cannon release to the sand bay. Accurately determining this parameter was also crucial for validating the numerical CFD results against the pressure signatures recorded by the microphones. The non-axisymmetric shape of the two projectiles significantly influences the pressure signatures recorded and the spatial distribution of the resulting sonic booms, due to the orientation of the configuration with respect

to the microphone array. Additionally, the sound field is highly sensitive to the model's roll angle, as also visible by the extracted static pressure contours in Figure 4.59a and 4.71a. Due to the complexity of precisely determining the roll angle at each microphone position for a given shot, a simplified approximation was developed to estimate the roll angle at each recording location. Figure A.1 illustrates the theoretical approach presented by Fasulo, Graziani et al. [207]. Specifically, the sound captured at the position $C^{'}$ was associated with the shock wave detachment point at B.

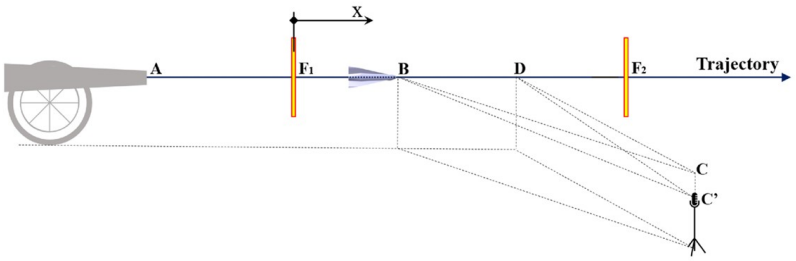

Fig. A.1 Representation of the positioning of roll angle detection targets F_1 and F_2 of the acoustic ray path considered for roll angle estimation $\overline{BC'}$

In addition, the roll motion of the projectile was not predetermined before each test but occurred due to manufacturing uncertainties. The approximation of roll motion is based on the results obtained from the two paper frames positioned at the entrance (F_1) and exit (F_2) of the aeroacoustic measurement zone. The location of the two paper frames has already been described in Section 4.5.1 and 4.5.3. Figure 3.11a highlights the position of the two paper frames involved for the CS3 tests. For the CS3 mock-up test campaign, the first paper frame was positioned 52.4 meters from the launcher, while for the second campaign, accounting for the shorter firing distance, it was placed 36.7 meters from the muzzle.

Interpolating between the first and second paper frames enables evaluation of the roll angle evolution across the measurement zone. Under the assumption of constant angular velocity, the resulting roll angle evolution follows Equation A.1:

$$\varphi(x) = \frac{\varphi_2 - \varphi_1}{\overline{F_1 F_2}} x + \varphi_1 \tag{A.1}$$

As shown in Figure A.1, an accurate determination of the roll angle at a given microphone location requires a precise calculation of the longitudinal coordinate x, which is given by $\overline{AB}$ - $\overline{AF_1}$, with the latter term fixed. The first term is calculated using a geometric acoustic model developed by CIRA [209], and corresponds to the instantaneous shock position across the acoustic measurement zone. The parameter x specifies the shock wave's position relative to the launcher.

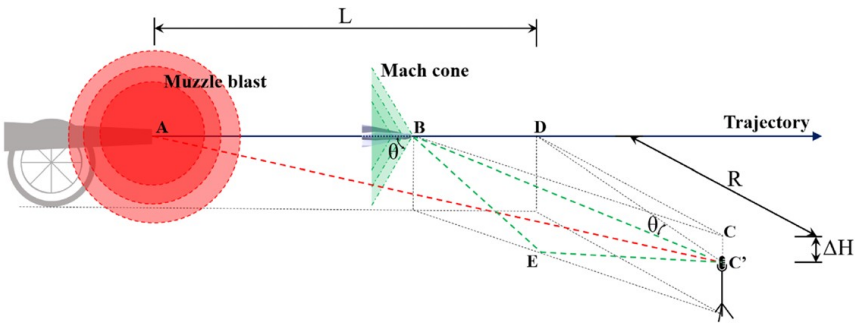

Fig. A.2 Geometric sketch of the test recording, CS3 mock-up [209]

Figure A.2 highlights the geometric layout of the experimental setup, including the firing system and an acoustic sensor for data acquisition. The projectile moves from the cannon at a speed roughly equal to Mach 4.7 towards point D in its trajectory up to the sand bay, where it stops. The system of shock wave generated by the projectile expands behind the model at the speed of sound along a direction $BC^{'}$, which is a function of the Mach angle. A first simplification involves neglecting the small variations in the speed of the projectile due to aerodynamic drag, so a constant speed is considered. By employing this assumption, the distance $\overline{AB}$ can be determined using Equation A.2.

$$\overline{AB} = L - \sqrt{R^2 + \Delta H^2}\tan(\mu) \tag{A.2}$$

In equation A.2, μ represents the Mach angle, L is the distance measured along the projectile trajectory from the probe to the cannon outlet, and R is the perpendicular distance's projection onto the ground plane. Finally, ΔH denotes the altitude difference between the gunshot and the microphone positions.

By accounting for aerodynamic drag, the Mach number and the Mach angle μ varies along the trajectory. The distance $\overline{AB}$ is then determined by solving a system of equations [209], and it is given in Equation A.3.:

$$\overline{AB} = L - \sqrt{R^2 + \Delta H^2} \tan\left[\arcsin\left(\frac{1}{M(\overline{AB})}\right)\right] \tag{A.3}$$

To account for the differences in elevation between the shot trajectory and the recording instrumentation a roll angle adjustment was also introduced [207]. The angle correction was performed using two local coordinate systems to align the roll angle with the orientation of the model relative to the acoustic sensor. The goal is to set the roll angle equal to 0° when the model is perfectly horizontally aligned and equal to 90° when it is vertically.

In Figure A.3, the blue coordinate system adds the angle between the horizontal axis and the line connecting the fire trajectory to the probes to the roll angle φ measured from the vertical upward direction. The second system in green coordinate, subtracts this angle from the calculated φ. The addition of subtraction of the selected angles depends on whether the recording instrumentations were placed to the left or right of the shot trajectory.

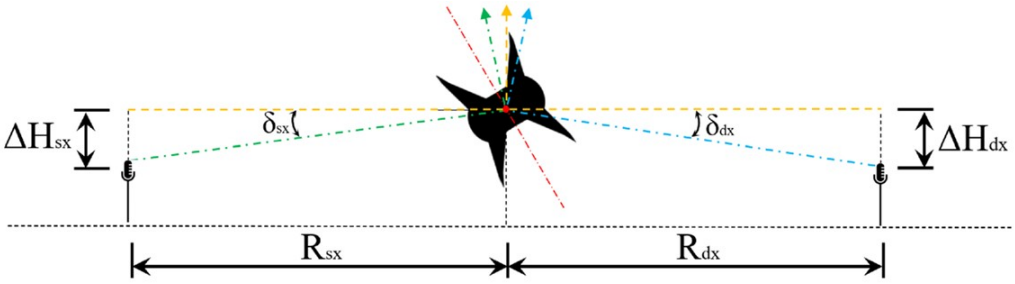

Fig. A.3 Front view of the vertical shot setup CS3 mock-up [207] with roll correction

This could be evaluated numerically with Equation A.4:

$$\varphi_{cor} = \varphi \pm \arctan\left(\frac{\Delta H}{R}\right) \tag{A.4}$$

Due to the geometry of the CS3 mock-up configuration, roll angles were evaluated within the range 0° to 90°, whereas for the CS2 mock-up, the range extended from 0° to 180°. In each case, however, the two sub-scaled models were simulated in the latter range by creating a half-cylinder grid. .

Roll angle first test campaign

As mentioned earlier, the roll angle is measured using two paper frames placed at the start and end of the aeroacoustic zone, denoted as F_1 and F_2, respectively. After each test, a dedicated team replaced these frames and calculated the roll angle at both positions, while other members qualitatively evaluated the recorded data and prepared the smooth-bore launcher for the subsequent test. Table A.1 shows the measured roll angles at each frame, with the last column indicating whether the rotation was anticlockwise or clockwise.

Table A.1 Roll angle at the paper frame, CS3-mock up

Shot	Position	Roll frame 1 φ_1 [°]	Roll frame 2 φ_2 [°]	Rotation
#1	vertical	0.5	18.6	Anticlockwise
#2	vertical	39.8	63.1	Anticlockwise
#3	vertical	122.0	141.8	Anticlockwise
#4	horizontal	-39.5	-50.6	Clockwise
#5	horizontal	9.5	3.5	Clockwise

As shown in Table A.1, the variation in the roll angle between the two frames is not constant across the different shots, indicating uncertainties in projectile manufacturing. As previously mentioned, for the CS3 mock-up configuration, the roll angle data were normalized to the 0–90° range due to dual symmetries. The roll angle values calculated for each microphone in each experimental test with the CS3 mock-up configuration are reported in Table A.2.

Table A.2 Roll angle at the recording instrumentations in degrees [°], CS3-mock up

Microphone	Test 1	Test 2	Test 3	Test 4	Test 5
Mic 1	18.7	61.6	38.6	41.4	11.1
Mic 2	30.2	73.3	27.1	30.7	21.9
Mic 3	4.6	47.6	52.7	55.8	3.2
Mic 4	8.3	51.2	49.0	51.2	1.2
Mic 5	9.2	51.8	48.2	49.4	2.8
Mic 6	14.7	56.6	42.9	39.0	12.4
Mic 7	26.3	68.3	31.3	28.4	23.2
Mic 8	0.8	42.6	56.9	53.4	1.9
Mic 9	4.4	46.1	53.3	48.8	2.5
Mic 10	5.3	46.9	52.4	47.0	4.1
Mic 11	10.9	51.5	47.2	36.6	13.7
Mic 12	22.4	63.3	35.6	26.0	24.5
Mic 13	3.1	37.6	61.1	51.0	0.7
Mic 14	0.5	41.2	57.5	46.4	3.8
Mic 15	1.4	41.9	56.7	44.7	5.4
Ch 1	5.2	47.7	52.3	52.6	0.5
Ch 2	8.0	50.5	49.4	49.6	2.5
Ch 3	17.6	59.1	40.1	34.6	16.6
Ch 4	12.4	53.9	45.4	39.3	11.7
P3O3	61.4	15.2	64.6	70.8	32.3
P3OASyS	47.5	73.2	18.2	72.5	1.4
P4	16.1	85.0	66.9	79.4	61.5

Roll angle second test campaign

As in previous experimental campaign, the roll angle was estimated using the two paper frames, and by employing the same methodology. The first frame was placed 36.7 meters from the gun muzzle, and the second at 112 meters. The roll angles were evaluated clockwise, considering the nominal trajectory of the projectile from the release to the sand bay.

Table A.3 Roll, Y and Z values at 36.7 m and 112 m from the gun muzzle

Shot	**at 36.7 m**			**at 112 m**		
	Roll (°)	Y (m)	Z (m)	Roll (°)	Y (m)	Z (m)
#1	94	0.015	1.86	181	0.07	2.04
#2	30.5	0.015	1.68	310	0.04	1.64
#3	61	0.01	1.67	349.5	0	1.40
#4	102	0.035	1.675	328	0.12	1.61

As visible from Figure 4.74, the configuration undergoes multiple rotations about its axis due to a strong lateral instability and pitching moment.

Appendix B

Mach 5 configurations: CS2 and CS3

The last appendix concerns the numerical investigation of two hypersonic configurations derived from the MORE&LESS project. Although these configurations are not candidates for near-term high-speed civil applications, they provided valuable data for assessing sonic boom behavior in the hypersonic regime. Moreover, the results enabled the refinement of the Carlson simplified methodology for hypersonic configurations. Section B.1 refers to a hypersonic demonstrator developed by the former UK company Reaction Engines, whereas Section B.2 addresses a hypersonic waverider derived from the STRATOFLY project [6].

B.1 CS2 analysis

The bi-domain approach enables the aeroacoustic analysis of high-supersonic to low-hypersonic configurations, and this appendix presents the results for Case Study 2 (Section 2.4). This study conducts a brief sensitivity analysis by varying the Mach number across three flight conditions, from low-supersonic up to Mach 5, to predict the acoustic behavior throughout the whole cruise envelope. The analysis considers two altitudes: 11.3 km, marking the start of supersonic flight, and 28.0 km, the reference cruise altitude of the demonstrator. All simulations assume an angle of attack of 0° and were solved using the inviscid Euler equations. The analyzed mission points are listed in Table B.1.

Table B.1 CS2 mission points

Mission point	Mach	Angle of attack [$^\circ$]	Altitude [km]	Pressure [Pa]
#1	1.20	0	11.3	21481
#2	1.20	0	28.0	1586
#3	2.00	0	11.3	21481
#4	2.00	0	28.0	1586
#5	5.00	0	11.3	21481
#6	5.00	0	28.0	1586

The analysis of the number of grid elements is reported in Table B.2. In particular, as expected, the number of elements for the Mach 5 simulations increases due to the strong variation in the Mach angle μ, and it can be observed that no prism elements are present.

Table B.2 CS2 grid detail

	Mach 1.20	Mach 2.00	Mach 5.00
Nodes	5,504,609	6,547,294	7,535,223
Elements	12,741,913	13,711,274	14,845,595
Tetra	7,910,754	7,924,713	7,955,728
Hexa	3,881,508	4,779,274	5,887,134
Tri	732,580	732,741	733,064
Penta	0	0	0
Quad	184,610	202,913	224,466
Pyra	24,412	30,119	37,026

Near-field results

The contours of the near-field results for the CS2 configuration are highlighted in Figure B.1 for the increase of static pressure ratio dp/p.

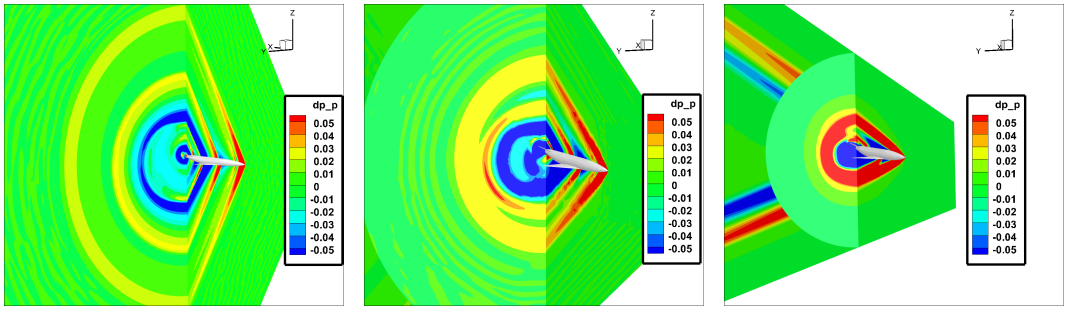

(a) CS2 static pressure contour Mach 1.2

(b) CS2 static pressure contour Mach 2

(c) CS2 static pressure contour Mach 5

Fig. B.1 Increase in static pressure contour CS2

"Figure B.1 highlights how the static pressure increases with Mach number. Notably, Subfigure B.1c shows stronger shocks compared to the lower-supersonic cases. In particular, this flight condition shows that the distinct shocks visible in the other contours have already merged in the near-field region. The corresponding pressure signatures extracted at a vertical ratio of H/L=1 are shown in Figure B.2.

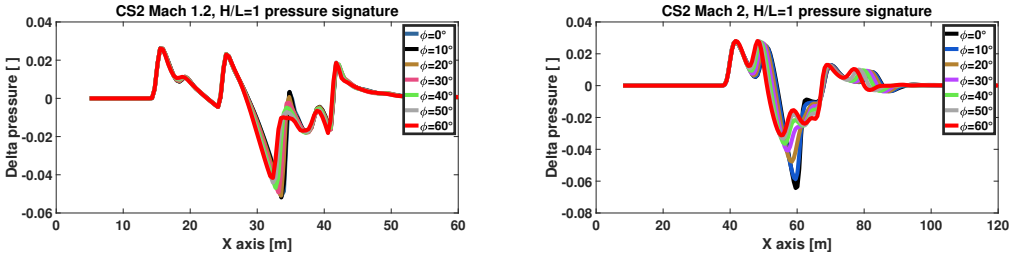

(a) CS2 extracted pressure signature H/L=1 Mach 1.2

(b) CS2 extracted pressure signature H/L=1 Mach 2

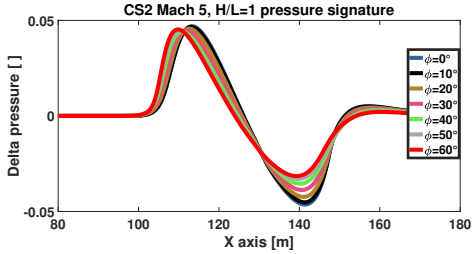

(c) CS2 extracted pressure signature H/L=1 Mach 5

Fig. B.2 Extracted radial pressure CS2 at H/L=1

At the lower Mach number of 1.2 (see Subfigure B.2a), the near-field pressure signature clearly shows four separate shock waves, each linked to different parts of

the aircraft—the nose, canard, wing, and fin. This suggests that the shocks remain fairly distinct at this speed. In contrast, at Mach 5 (Subfigure B.2c), the pressure pattern changes, forming a N-wave shape. This pattern reflects the merging of shock waves, which is typical for hypersonic flow conditions. Lastly, the flight condition at Mach 2 still shows a distinct shock pattern, although the individual shocks are located closer together compared to the Mach 1.2 simulation.

Far-Field and psychoacoustics metrics

The extracted near-field signatures are propagated to the ground using the previously described atmospheric profiles. The resulting ground-level pressure signatures for the three simulated Mach numbers, assuming a flight altitude of 11.3 km, are presented in Figure B.3.

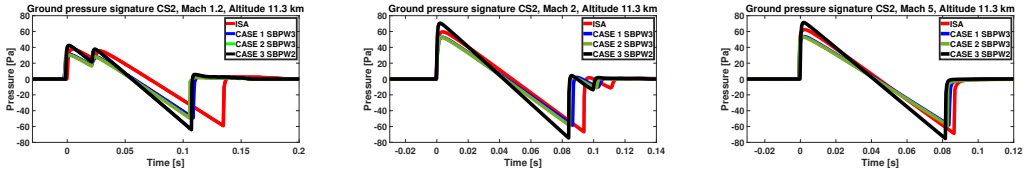

(a) CS2 ground signature Mach 1.2 (b) CS2 ground signature Mach 2 (c) CS2 ground signature Mach 5

Fig. B.3 Ground sonic boom waveform CS2 11.3 km

It can be observed that the Mach 2 and Mach 5 ground pressure signatures exhibit a ground N-wave shape signature, while the Mach 1.2 flight condition has two visible peaks. Moreover, the lower speed flight condition significantly reduces the maximum peak overpressure. The shape of the configuration, while optimized for a Mach 5 cruise, is not dedicated to sonic boom minimization, and subsequently, high values of peak overpressure and related noise metrics are visible. At high speed, the shock waves visible in the near-field region coalesce during their propagation between the reference altitude and the ground.

The psychoacoustics and energy-based metrics for the CS2 aircraft in the three described flight conditions at 11.3 km of altitude are presented in Table B.3.

Table B.3 CS2 noise metrics (in dB) at 11.3 km for different Mach numbers and atmospheric conditions

Metric	Mach 1.2				Mach 2.0			
	ISA	Case 1	Case 2	Case 3	ISA	Case 1	Case 2	Case 3
PL	102.02	98.28	101.77	104.75	105.21	101.62	104.96	108.39
ISBAP	108.62	105.7	107.74	111.14	111.3	108.63	110.85	114.36
ASEL	87.96	84.59	88.1	89.89	91.01	87.74	91.01	93.20
BSEL	95.42	93.71	94.71	97.38	97.54	96.04	97.51	100.05
CSEL	103.67	102.25	102.32	105.09	105.51	104.4	105.03	107.39
DSEL	95.53	93.35	94.87	97.52	97.97	95.76	97.78	100.44

Metric	Mach 5.0			
	ISA	Case 1	Case 2	Case 3
PL	106.38	101.83	105.26	108.97
ISBAP	112.29	108.82	110.94	115.04
ASEL	92.13	88.07	91.31	93.82
BSEL	98.45	96.43	97.48	100.6
CSEL	106.18	104.71	104.84	108.25
DSEL	98.95	96.14	97.82	101.09

Table B.3 shows that the noise metrics vary only slightly—by up to about 5 dB—across the three flight conditions tested. In particular, the differences between Mach 2 and Mach 5 are mostly within 1 dB, indicating only minor changes, which suggest that the Mach number has a relatively small effect.

More variations are visible with the primary carpet within the three simulations for the two selected altitudes, and those are visible in Figure B.4 and B.5.

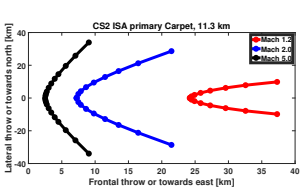

(a) Primary carpet ISA 11.3 km

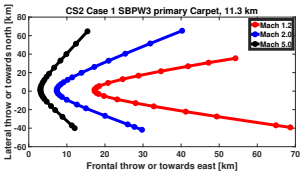

(b) Primary carpet Case 1 SBPW3 11.3 km

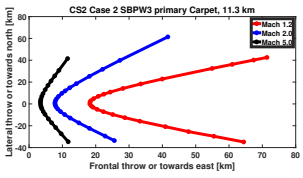

(c) Primary carpet Case 2 SBPW3 11.3 km

Fig. B.4 Primary carpet CS2 flight altitude 11.3 km

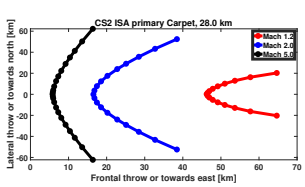

(a) Primary carpet ISA 28 km

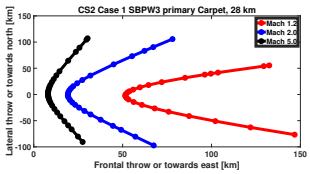

(b) Primary carpet Case 1 SBPW3 28 km

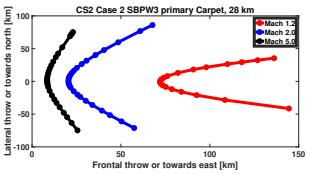

(c) Primary carpet Case 2 SBPW3 28 km

Fig. B.5 Primary carpet CS2 flight altitude 28 km

A clear trend can be observed from the simulations. As the Mach number increases from transonic to hypersonic flight regime, the lateral extent of the primary carpet expands, as visible across all evaluated atmospheric profiles. The Mach 5 propagation exhibits a much broader distribution in the primary carpet due to enhanced shock wave propagation at higher speeds, which intensifies with increasing altitude.

B.2 CS3 analysis

Along with the CS2 case study, this work examines another hypersonic configuration—a waverider design named CS3 or MR5. Unlike CS2's conventional wing-fuselage layout, CS3 features a larger size and follows a different mission profile. While the CS2 was developed as a demonstrator for the SABRE engine, the CS3 design targets long-range antipodal flight, with a sustained cruise at Mach 5. For this case study, the analysis considers two Mach numbers while maintaining a constant angle of attack at 0°, reflecting its mission profile (Figure 2.11b). The simulation altitude is fixed at 31 km for all cases, with the mission points summarized in Table B.4.

Table B.4 CS3 mission points

Mission point	Mach	Angle of attack [$^\circ$]
#1	4.00	0
#2	4.20	0
#3	4.40	0
#4	4.60	0
#5	4.80	0
#6	5.00	0

The analysis of the number of elements in the grids is reported in Table B.5. To ensure adequate resolution, only the two grids corresponding to the extreme flight conditions are reported.

Table B.5 CS3 grid detail

	Mach 4.00	Mach 5.00
Nodes	5,510,493	5,974,132
Elements	12,584,195	13,642,274
Tetra	7,899,336	7,913,241
Hexa	3,977,424	4,916,747
Tri	469,096	472,113
Penta	0	0
Quad	169,056	169,489
Pyra	32,076	32,134

Near-field results

Due to space constraints, this section of the PhD thesis presents only the first and last mission points analyzed. The complete analysis is visible in the work by Graziani et al. [4]. The contour of the increase of static pressure for the CS3 configuration is highlighted in Figure B.6.

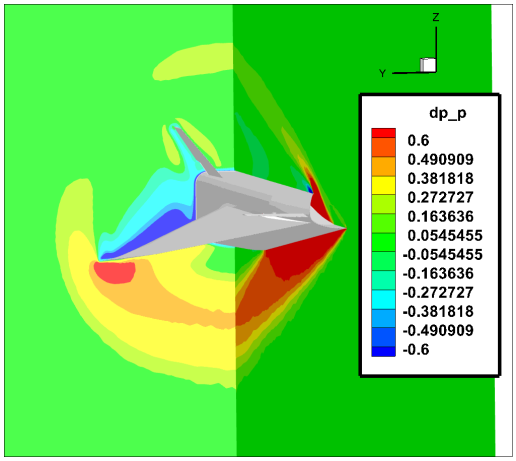

(a) CS3 increase of static pressure contour, Mach 4

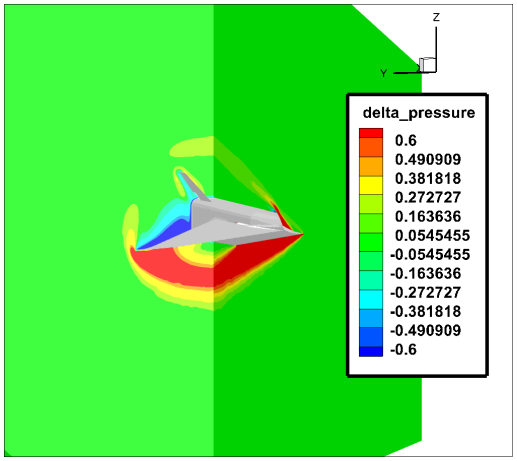

(b) CS3 increase of static pressure contour, Mach 5

Fig. B.6 Increase of static pressure contour CS3 at Mach 4 and Mach 5

Figure B.6b shows that the cruise condition at Mach 5 generates stronger shock waves in the near-field region, even though both mission points exhibit a single strong shock. In both cases, however, the shock wave intensity remains higher than in the other configurations evaluated due to the shape of the configuration, which has not been optimized for sonic-boom minimization.

The extracted pressure signatures at specific vertical-ratio distances are shown in Figure B.7 for the flight conditions at Mach 4 (Subfigure B.7b) and Mach 5 (Subfigure B.7a).

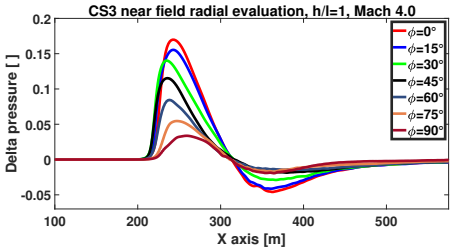

(a) CS3 extracted pressure signature, Mach 4

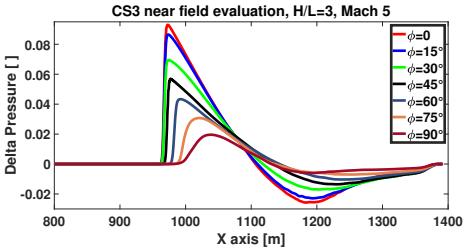

(b) CS3 extracted pressure signature, Mach 5

Fig. B.7 Extracted pressure signature CS3 at Mach 4 and Mach 5

Figure B.7 presents the extracted near-field pressure signature, which displays an N-wave shape within the near-field domain. This behavior is consistent with the

previously described contours, in which a single shock was visible. In addition, it confirms the relatively small expansion region.

Far-field and noise metrics

The study propagates the near-field results from Computational Fluid Dynamics simulations through the previously described non-uniform and stratified atmospheric profiles. The resulting ground-level propagated pressure signatures are presented in Figure B.8, with Subfigure B.8a related to the Mach 4 ground signature and Subfigure B.8b to the Mach 5.

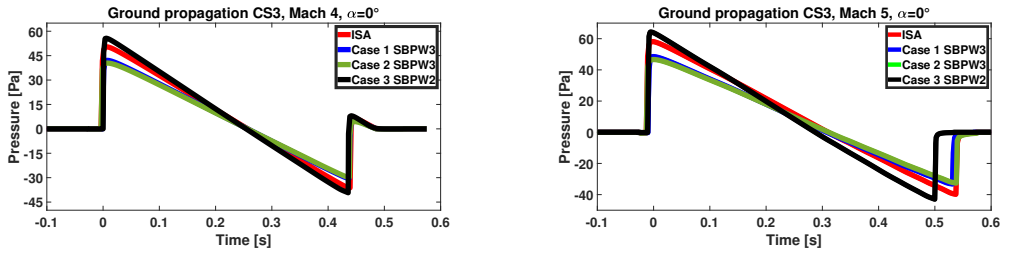

(a) CS3 ground pressure signature, Mach 4

(b) CS3 ground pressure signature, Mach 5

Fig. B.8 Ground propagated pressure signature CS3

Figure B.8 illustrates that the configuration produces a N-wave shape at ground level. Minor differences are evident in the ground pressure signatures between the Mach 5 and Mach 4 flight conditions. In particular the latter signature exhibits a small peak near the trailing edge of the waveform, which is not visible in the Mach 5 pressure signature.

The noise metrics for the CS3 configuration for the flight condition at Mach 4 and 5 are highlighted in Table B.6.

Table B.6 CS3 noise metrics (in dB) for different Mach numbers and atmospheric conditions

Metric	ISA		Case 1		Case 2		Case 3	
	Mach 4	Mach 5	Mach 4	Mach 5	Mach 4	Mach 5	Mach 4	Mach 5
PL	100.91	101.77	96.02	96.95	99.23	100.13	103.21	103.85
ISBAP	107.37	108.07	103.88	104.55	105.51	106.22	109.62	110.16
ASEL	87.26	87.99	82.31	83.24	86.03	86.81	88.59	89.15
BSEL	94.53	95.02	92.13	92.68	93.29	93.76	95.96	96.38
CSEL	102.65	102.98	100.99	101.33	100.98	101.31	103.84	104.16
DSEL	94.55	95.22	91.82	92.38	93.13	93.75	96.19	96.69
ESEL	92.45	93.09	89.27	89.94	91.28	91.89	94.08	94.58

Table B.6 shows that across the four atmospheric profiles, the noise metrics for the CS3 configuration vary by less than 1 dB between the Mach 4 and Mach 5 flight conditions. This further suggests that the Mach number has little impact on the noise metrics at very high speeds. A similar pattern was observed in the CS2 case study (Table B.3). Similarly to the previous case study, the primary carpet for the two flight conditions reported is analyzed in Figure B.9.

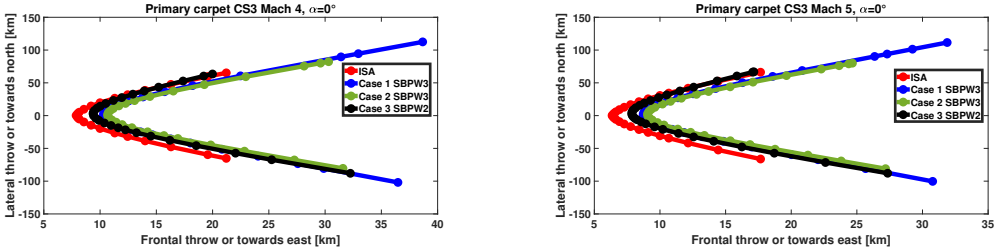

(a) CS3 primary carpet, Mach 4

(b) CS3 primary carpet, Mach 5

Fig. B.9 CS3 primary carpet exposure Mach 4 and Mach 5

Varying the Mach number produces only minimal differences in the shape and extent of the primary carpet. Moreover, due to the cruise altitude of 31 km, the lateral spread of the primary carpet reaches up to 220 km for both flight conditions under the Case 1 SBPW3 atmosphere, which is almost twice the extent of the Concorde-like case study previously presented.